Pontifícia Universidade Católica
do Rio de Janeiro

AmirFarzan Esmaeili Taklimi

Exploring some new aspects of the interactions of cosmic messengers in astroparticle physics

Tese de Doutorado

Thesis presented to the Programa de Pós-graduação em Física of PUC-Rio in partial fulfillment of the requirements for the degree of Doutor em Ciências - Física.

Advisor: Prof. Arman Esmaili Taklimi

Rio de Janeiro
June 2025

Pontifícia Universidade Católica
do Rio de Janeiro

AmirFarzan Esmaeili Taklimi

Exploring some new aspects of the interactions of cosmic messengers in astroparticle physics

Thesis presented to the Programa de Pós-graduação em Física of PUC-Rio in partial fulfillment of the requirements for the degree of Doutor em Ciências - Física. Approved by the Examination Committee:

Prof. Arman Esmaili Taklimi
Advisor
Departamento de Física – PUC-Rio

Prof. Luiz Vitor de Souza Filho
USP

Prof. Ulisses Barres de Almeida
CBPF

Prof. Gero Arthur Hubertus Thilo Freiherr von Gersdorff
Departamento de Física – PUC-Rio

Prof. Thiago Barbosa dos Santos Guerreiro
Departamento de Física – PUC-Rio

Rio de Janeiro, June 6th, 2025

AmirFarzan Esmaeili Taklimi

B.Sc. in Physics (2016) and an M.Sc. in Physics (2019) from Sharif University of Technology.

Bibliographic data

Esmaeili Taklimi, AmirFarzan

Exploring some new aspects of the interactions of cosmic messengers in astroparticle physics / AmirFarzan Esmaeili Taklimi; advisor: Arman Esmaili Taklimi. – 2025.

209 f: il. color. ; 30 cm

Tese (doutorado) - Pontifícia Universidade Católica do Rio de Janeiro, Departamento de Física, 2025.

Inclui bibliografia

1. Informática – Teses. 2. Astropatículas. 3. Abordagem Multimensageiro. 4. Mensageiros cósmicos de alta energia. 5. Neutrino. 6. Raios gama. 7. Raios cósmicos. I. Esmaili Taklimi, Arman. II. Pontifícia Universidade Católica do Rio de Janeiro. Departamento de Física. III. Título.

CDD: 004

To my professors, friends, and family,
whose steadfast support and encouragement
have been my foundation throughout this journey.

Acknowledgments

First and foremost, I extend my deepest gratitude to my advisor, Arman Esmaili. More than a mentor, he has been a guiding force in my academic and personal journey. Long before my PhD, Arman played a pivotal role in nurturing my passion for physics, offering support and encouragement when I needed it most. When I faced challenges in securing a PhD position, he believed in my potential and encouraged me to apply to PUC-Rio, a decision that shaped my path. Over these years, his unwavering support—whether in physics, research, or even navigating life's difficulties—has been invaluable. The countless hours we spent discussing physics, the dedication he brings to his work, and the depth of his insights have left a lasting impression on me. I also had the privilege of taking two astrophysics courses with him, where his clarity, depth, and enthusiasm made complex topics both accessible and fascinating. His ability to teach, to inspire curiosity, and to convey deep physical intuition is truly remarkable. More than just an extraordinary physicist, Arman is an inspiration and a friend, someone whose influence I will carry with me always.

I am also profoundly grateful to Pasquale Dario Serpico, one of the most brilliant physicists I have had the privilege of working with. Collaborating with Arman and Pasquale on our four papers has been one of the most rewarding experiences of my PhD. Their intellectual curiosity, depth of knowledge, and dedication to physics are truly boundless. Our discussions were not just intellectually stimulating but also among the most enjoyable moments of my PhD. The opportunity to learn from them has been an extraordinary privilege—one that has shaped my approach to research and deepened my appreciation for the beauty of physics.

I would also like to extend my sincere gratitude to all the professors who have guided me throughout my academic journey, both at PUC-Rio and beyond. In particular, I am deeply grateful to Prof. Gero Gersdorff for his inspiring lectures, generous support, and the trust he has placed in me.

I would like to express my gratitude to all of my friends, as it is difficult to adequately thank the many wonderful people who have come into my life. To my friends at PUC-Rio and beyond academia: thank you!

Last, but certainly not least, I would like to express my deepest gratitude to my family, especially my parents, whose unwavering support, encouragement, and belief in me have been invaluable throughout my journey in completing this thesis.

Thanks to the financial support by the Fundação Carlos Chagas Filho de Amparo à Pesquisa do Estado do Rio de Janeiro (FAPERJ) scholarship No. 201.293/2023, the Conselho Nacional de Desenvolvimento Científico e Tecnológico (CNPq) scholarship No. 140315/2022-5 and by the Coordenação de Aperfeiçoamento de Pessoal de Nível Superior (CAPES)/Programa de Excelência Acadêmica (PROEX) scholarship No. 88887.617120/2021-00.

This study was financed in part by the Coordenação de Aperfeiçoaento de Pessoal de Nível Superior - Brasil (CAPES) - Finance Code 001.

Abstract

Esmaeili Taklimi, AmirFarzan; Esmaili Taklimi, Arman (Advisor). **Exploring some new aspects of the interactions of cosmic messengers in astroparticle physics**. Rio de Janeiro, 2025. 209p. Tese de Doutorado – Departamento de Física, Pontifícia Universidade Católica do Rio de Janeiro.

Cosmic rays, gamma rays and neutrinos trace extreme astrophysical phenomena across orders of magnitude in energy and distance, yet their interpretation relies on a set of microphysical processes that govern the interactions of these messenger particles both within the astrophysical sources and en route to the Earth. In this thesis we study some of these microphysics processes, spanning in energies from GeV to ZeV and distances from Galactic scales to the high-redshift Universe, with a focus on specific aspects that give rise to observable macrophysical effects and signatures relevant to current and future multi-messenger observations and simulations.

At the ultra-high-energy regime, for both cosmological propagation and source environments, two key topics are addressed. First, an often-overlooked process—pair production with capture—is investigated in the context of ultra-high-energy cosmic rays using a semi-analytical estimation method. The results indicate that, although this process does not significantly alter the ionization state of ultra-high-energy nuclei during their propagation over cosmological distances, heavy and ultra-heavy nuclei may not be fully stripped at acceleration sites. This challenges the commonly adopted assumption that ultra-high-energy nuclei are fully ionized both at their sources and during propagation through astrophysical environments.

Second, we examine a crucial multi-messenger phenomenon: the development of electromagnetic cascades at these energies. We show that cascades in this regime can serve as a source of high- and ultra-high-energy neutrinos, both inside and outside of astrophysical sources. To support this study, we introduce `MUNHECA`, a `Python3` framework for simulating ultra-high-energy electromagnetic cascades and computing the resulting neutrino spectra.

At lower energies, and on Galactic scales, the energy loss processes of cosmic ray protons are carefully re-examined. This study is particularly relevant in the light of recent observational advances (e.g. AMS-02), as experimental

uncertainties in this regime have now surpassed the precision of our theoretical models. Using an analytical approach, our study reveals that certain proton energy loss mechanisms, previously considered negligible, such as elastic proton-proton scattering, can no longer be ignored in accurate cosmic ray propagation modeling.

In the final part of this thesis, we turn to a distinct and yet related study that also benefits from the multi-messenger approach: the observational prospects of primordial black holes through gamma ray and neutrino telescopes. We discuss the unique advantages of neutrino telescopes in detail. Through a numerical and accurate reassessment of the gamma ray and neutrino spectra from evaporating primordial black holes, we quantify the correlated energy and time profiles of both messengers. These correlations are then utilized to enhance the identification of primordial black holes in case of future detection.

Keywords

Astropaticles; Multi-messenger Approach; Ultra-high-energy Cosmic Rays; Neutrino; gamma rays; cosmic ray.

Resumo

Esmaeili Taklimi, AmirFarzan; Esmaili Taklimi, Arman. **Exploração de novos aspectos das interações de mensageiros cósmicos na física de astropartículas**. Rio de Janeiro, 2025. 209p. Tese de Doutorado – Departamento de Física, Pontifícia Universidade Católica do Rio de Janeiro.

Raios cósmicos, raios gama e neutrinos são mensageiros de fenômenos astrofísicos extremos, abrangendo diversas ordens de grandeza em energia e distância. A interpretação desses sinais depende de um conjunto de processos microfísicos que governam as interações dessas partículas tanto nas fontes astrofísicas quanto durante sua propagação até a Terra. Esta tese investiga alguns desses processos microfísicos, cobrindo energias desde GeV até ZeV e distâncias desde escalas galácticas até o Universo em alto redshift, com foco em aspectos específicos que resultam em efeitos macrofísicos observáveis e assinaturas relevantes para observações e simulações multi-mensageiras atuais e futuras.

No regime de energia ultra-alta, tanto na propagação cosmológica quanto nos ambientes das fontes, dois tópicos principais são abordados. Primeiramente, um processo frequentemente negligenciado — a produção de pares com captura — é investigado no contexto dos raios cósmicos de energia ultra-alta, utilizando um método de estimativa semianalítico. Os resultados indicam que, embora esse processo não altere significativamente o estado de ionização dos núcleos durante sua propagação em distâncias cosmológicas, núcleos pesados e ultra-pesados podem não estar totalmente despojados em locais de aceleração, desafiando a suposição comum sobre o estado de ionização desses núcleos nas fontes astrofísicas.

Em seguida, examinamos um fenômeno crucial no contexto multi-mensageiro: o desenvolvimento de cascatas eletromagnéticas nessas energias. Demonstramos que cascatas nesse regime podem servir como fontes de neutrinos de altas e ultra-altas energias, tanto dentro quanto fora das fontes astrofísicas. Para apoiar este estudo, introduzimos o MUNHECA, um framework em Python 3 para simular cascatas eletromagnéticas de energia ultra-alta e calcular os espectros de neutrinos resultantes.

Em energias mais baixas e em escalas galácticas, os processos de perda de energia dos prótons dos raios cósmicos são reexaminados cuidadosamente. Este

estudo é particularmente relevante à luz dos avanços observacionais recentes (por exemplo, AMS-02), pois as incertezas experimentais neste regime agora superaram a precisão de nossos modelos teóricos. Utilizando uma abordagem analítica, nossa pesquisa revela que certos mecanismos de perda de energia dos prótons, anteriormente considerados negligenciáveis, como o espalhamento elástico próton-próton, não podem mais ser ignorados em modelos precisos de propagação de raios cósmicos.

Na parte final desta tese, voltamo-nos para um estudo distinto, mas ainda relacionado, que também se beneficia da abordagem multi-mensageira: as perspectivas observacionais de buracos negros primordiais por meio de telescópios de raios gama e neutrinos. Discutimos em detalhes as vantagens únicas dos telescópios de neutrinos nesse contexto. Por meio de uma reavaliação numérica e precisa dos espectros de raios gama e neutrinos provenientes da evaporação de buracos negros primordiais, quantificamos os perfis de energia e tempo correlacionados de ambos os mensageiros. Essas correlações são então utilizadas para aprimorar a identificação de buracos negros primordiais em caso de detecção futura.

Palavras-chave

Astropatículas; Abordagem Multimensageiro; Mensageiros cósmicos de alta energia; Neutrino; Raios gama; Raios cósmicos.

Table of contents

List of figures

List of tables

List of Abreviations

ADAF – Advection-Dominated Accretion Flow

AGN – Active Galactic Nucleus

CIB – Cosmic Infrared Background

CMB – Cosmic Microwave Background

COB – Cosmic Optical Background

CoM – Center of Momentum

CPPP – Charged Pion Pair Production

CR – Cosmic Ray

CRB – Cosmic Radio Background

CXB – Cosmic X-ray Background

CUB – Cosmic Ultraviolet Background

DCS – Double Compton Scattering

DM – Dark Matter

DPP – Double Pair Production

EAS – Extensive Air Shower

EBL – Extragalactic Background Light

EGB – Extragalactic Gamma-ray Background

EM – Electromagnetic

EoM – Equation of Motion

EMPP – Electron Muon-Pair Production

EPMPP – Electron Pair Muon Pair Production

EPP – Electron Pair Production

ETP – Electron Triplet Production

Fermi-LAT – Fermi Large Area Telescope

GR – Glashow Resonance

GRB – Gamma-Ray Burst

GZK – Greisen–Zatsepin–Kuzmin

HESE – High-Energy Starting Events

IACT – Imaging Atmospheric Cherenkov Telescopes

ICS – Inverse Compton Scattering

IGM – Intergalactic Medium

IGMF – Intergalactic Magnetic Field

IGRB – Isotropic Gamma Ray Background

ISM – Interstellar Medium

IR – Infrared

LHAASO – Large High Altitude Air Shower Observatory

MPP – Muon Pair Production

NPPP – Neutral Pion Pair Production

PAO – Pierre Auger Observatory

PBH – Primordial Black Hole

PMNS – Pontecorvo–Maki–Nakagawa–Sakata

PPC – Pair Production with Capture

QCD – Quantum Chromodynamics

QED – Quantum Electrodynamic

RA – Right Ascension

SFG – Star-forming Galaxy

SHDM – Super Heavy Dark Matter

SM – Standard Model [of particle physics]

SMBH – Super Massive Black Hole

SNRs – Supernova Remnants

TA – Telescope Array

TPP – Triple Pair Production

UHE – Ultra-high Energy

UHECR – Ultra-high Energy Cosmic Ray

UV – Ultraviolet

The first principle is that you must not fool yourself—and you are the easiest person to fool!

Richard Feynman, *"Cargo Cult Science" speech, 1974.*

Thesis Outline

This thesis is divided into 6 chapters:

1. Chapter 1 provides a comprehensive introduction to the topics relevant to the subject of this dissertation. It begins by presenting the different cosmic messengers, their observational characteristics, and the key physical processes governing their behavior. Special attention is given to cosmic-ray nuclei, their propagation, and interactions, culminating in a discussion on the multi-messenger approach, investigating the electromagnetic cascade as one of the most important examples of the multi-messenger in astroparticle physics.

2. Chapter 2 is based on the published paper (33). This chapter investigates the interaction of ultra-high-energy cosmic rays (UHECRs) with background photon fields, focusing on the process of pair production with electron capture (PPC). This mechanism counteracts photo-ionization and plays a crucial role in determining the ionization state of high-energy cosmic ray nuclei, particularly heavy and ultra-heavy species. The analysis considers both extragalactic propagation and source environments.

3. Chapter 3 is based on the two published papers (34, 35), exploring the development of ultra-high-energy electromagnetic cascades, emphasizing the role of muon pair production and other QED processes in shaping cascade evolution. The implications for neutrino production are examined, and a computational tool, `MUNHECA`, is introduced to model these interactions and their resulting neutrino spectra.

4. Chapter 4 presents a precision study of energy loss mechanisms affecting low-energy cosmic ray protons. The analysis addresses nuclear elastic cross sections, the validity of continuous energy loss approximations, and sub-leading effects, refining our understanding of cosmic ray propagation at GeV energies, based on the published work (36).

5. Chapter 5 shifts focus to the evaporation of primordial black holes (PBHs) and their potential observational signatures in gamma-ray and neutrino telescopes in a multi-messenger approach. The detectability of these transient signals is revisited in light of current observational constraints. This chapter is based on (37).

Finally, Chapter 6 provides closing remarks on the broader implications of this work for high-energy astroparticle physics and multi-messenger approach.

1
Introduction

From the dawn of human history, our fascination with the night sky has been an enduring source of wonder and inspiration. Watching the *lights* from the sky, simply, has been driving humanity's relentless quest to unravel the mysteries of the Universe. The *Four-element Theory* of Empedocles, *spherical Universe* of Aristotle and *Atomism* of Democritus reflect not only an early attempt to comprehend the cosmos but also the profound impact that celestial observations have had on shaping our understanding of the natural world. However, it took millennia for humanity to develop the mathematical and technological tools necessary to model the dynamic of the objects. With advancements in the electrodynamic theory, we gained an understanding of the *light*, the only detectable *messenger* until 20th century, coming from the celestial objects. The quantum and relativity revolutions opened a great window of other detectable *messengers*, models for their production in the astrophysical sources and their propagation through the Universe, which led to building new experiments and detectors. The paradigm of scientific studies changed and hence new research fields, although rooted in ancient desires, appeared. In this sense, *astronomy*, *astrophysics*, *particle physics* and *astroparticle physics* can be seen as the continue of humanity's attempt to unravel the mysteries of the Universe. However, they operate within a completely different paradigm compared to the ancient world, known as the *scientific method*, grounded in empirical evidence, systematic observation, and testable hypotheses.

Astrophysics and astroparticle physics both aim to understand the Universe and its fundamental constituents, but they approach this goal from different perspectives and methodologies. Astrophysicists primarily focus on exploring the physics underlying the diverse range of the observed astronomical phenomena, such as the formation and evolution of astrophysical sources like stars and galaxies.

On the other hand, astroparticle physics extends this exploration into the realm of particle physics, governed by the fundamental interactions between cosmic messengers within the astrophysical and cosmological environments. Defined as a multidisciplinary research area, it bridges astrophysics, cosmology, particle physics, nuclear physics, and plasma physics, employing experimental techniques from both particle accelerators and astronomical observatories to study the Universe through multiple cosmic messengers. Therefore, astroparti-

cle physics becomes an essential tool for probing the most fundamental aspects of the Universe. In this context, this dissertation centers on the investigation of very energetic cosmic messengers or more technically *astroparticles at ultra-high energies*. In the following, we outline the key challenges and central features of astroparticles, providing a broad framework for understanding the phenomena that shape this unique field.

Before we go any further, I want to emphasize that this dissertation serves as a detailed presentation of the new results achieved and published by the author during his PhD. Therefore, we assume that the reader is familiar with the fundamentals of particle physics, general relativity, and cosmology. Throughout this thesis, we will use natural units with $\hbar = c = 1$, unless otherwise specified.

1.1 Cosmic Messengers

Putting aside the complexity of the observation processes, by gazing at the sky, we are presented with a tapestry of particles, cosmic messengers, that provide insights into the intricate processes shaping the Universe. Each of these cosmic messengers is produced at different stages of the cosmic evolution through various astrophysical phenomena. Thus, they serve as witnesses to the Universe's history including the formation of cosmic structures, the mechanisms at play within astrophysical sources and their propagation enroute to the Earth. These cosmic messengers, as discussed in this dissertation, are exclusively Standard Model (SM) particles, since they are the only particles our current experiments can detect, either through quantum electrodynamic (QED) or electroweak interactions. Notably, in the current framework of astroparticle physics, Beyond Standard Model (BSM) particles, such as axions or dark matter particles, are often assumed to interact with the SM sector. Consequently, their detection typically relies on observing SM particles as signals.

Astroparticle physics, mostly, hinges on the insights gleaned from three distinct types of particles cosmic messengers: photons, neutrinos, CR including nuclei and electrons[1]. Each of these messengers is a unique signal, shedding light on different facets of astrophysical processes, such as stellar evolution, acceleration mechanisms, cosmic distance propagation, etc. However, extracting information from the observed fluxes at the Earth is complicated because of the extreme-condition and out of control ambient of production and propagation.

[1]Note that the multi-messenger approach in astrophysics also includes gravitational waves. However, as they fall beyond the scope of this dissertation, they will not be discussed here.

Moreover at the detection site, depending on the sensitivity and proficiency of the detector, the systematic errors can be large.

While each messenger provides invaluable insights into astrophysical phenomena, it's crucial to recognize that their production and propagation are intricately connected. Astrophysical processes often involve complex interactions between different types of messengers, creating a rich tapestry of information that astroparticle physicists strive to unravel. This interconnectedness underscores the importance of the *multi-messenger approach*, allowing us to piece together a more comprehensive understanding of the Universe's complexities.

This dissertation focuses on astroparticle physics at ultra-high energies, with particular emphasis on ultra-high energy cosmic rays (UHECRs) and the phenomenon of *electromagnetic cascades*, a pivotal concept in multimessenger astroparticle research. To provide the context, the following sub-sections will review three primary particle messengers, photons, cosmic rays, and neutrinos, highlighting their key characteristics and roles in astrophysics. These messengers form the basis for the investigations in astroparticles. Following this, I will examine conventional electromagnetic cascades in detail. I will then frame the scope of this thesis by defining the ultra-high-energy range and discussing what distinguishes it from lower-energy regimes. Lastly, I will provide a comprehensive overview of our research undertaken over the past four years, presenting its outcomes and implications in detail.

Before we start, let's clarify how the term "cosmic rays" is used in this dissertation. While we'll explore their properties in depth later, the term will appear frequently in connection with the broader network of cosmic messengers. Here, "cosmic rays" refers specifically to the nuclei (e.g. proton, He, Fe, etc.) emitted from astrophysical sources and propagating through Galactic or intergalactic space. Though electrons are sometimes classified as "cosmic rays" or even "electron cosmic rays" in the field of astroparticles, this dissertation will simply refer to them as "electrons" for clarity.

1.2 Photons

Visible light was the first cosmic messenger observed by humanity, long before we understood it as part of the electromagnetic (EM) spectrum or developed the concept of the photon. With the advancement of electrodynamic theory and improvements in observational technology, astronomers extended their exploration beyond optical wavelengths. Today, a global network of highly sensitive instruments continuously scans the sky, detecting photons across the entire EM spectrum, far beyond the capability of the human

eye. This capability has revolutionized our understanding of the Universe, enabling the identification and classification of countless astrophysical sources through their spectroscopic emissions, from low-energy radio waves to high-energy gamma rays. Observations across these bands have revealed a wealth of discoveries, from pulsars in the radio domain to the cosmic microwave background, high-energy emissions from compact objects, and gamma ray bursts. Each wavelength contributes a distinct layer of information about the underlying astrophysical processes. In addition to discrete point sources, observations have uncovered diffuse photon fluxes that cannot be traced back to individual objects but instead stretch across the whole sky. When gazed with relatively wide angular view, focusing on radiation from beyond the Milky Way, these emissions reveal diffuse anisotropies on top of a homogeneous, isotropic background, commonly referred to as the "cosmic background" (CB). This is different from the highly anisotropic emission originating from within our own galaxy. Galactic emissions are predominantly concentrated along the plane of the Milky Way, forming a distinct band across the sky that can be observed in multiple wavebands. However, the focus of this dissertation, mainly, lies on processes and particles originating from beyond our galaxy, although the study of the Milky Way and its constituent objects is of course an interesting topic in its own right.

The sources contributing to the CB range from small-scale like dust grains, to large-scale structures such as stars, galaxies, and galaxy clusters. This background is shaped by various processes, including nuclear fusion, gravitational collapse, thermal and/or non-thermal radiations. Spanning an immense frequency range, from 10^8 to 10^{25} Hz, understanding the cosmic background requires a diverse set of detection techniques and theoretical models. Overall, our measurement of CB, today, ranges from very high energy (γ-ray) (38, 39, 40), to X-ray (41, 42), through optical and infrared (43, 44), and ultimately down to radio (4, 45, 46, 47, 48, 3).

Figure 1.1 presents the current measurements of the extragalactic photon flux. In this plot, the *specific Intensity* of the CB is illustrated with respect to the wavelength, λ, or equivalently the frequency, ν. The specific Intensity, usually denoted by I_ν with units [W.m^{-2}.sr^{-1}.Hz^{-1}], is the power a detector would receive per unit area, per solid angle observed on the sky, per unit frequency, ν, of the light being detected. It is common to multiply I_ν by ν. Since I_ν is proportional to the energy density per unit frequency, plotting νI_ν, of units [W.m^{-2}.sr^{-1}], will give a qualitative view of how the energy density is distributed across the spectrum.

The entire spectrum depicted in Figure 1.1 represents what is termed the

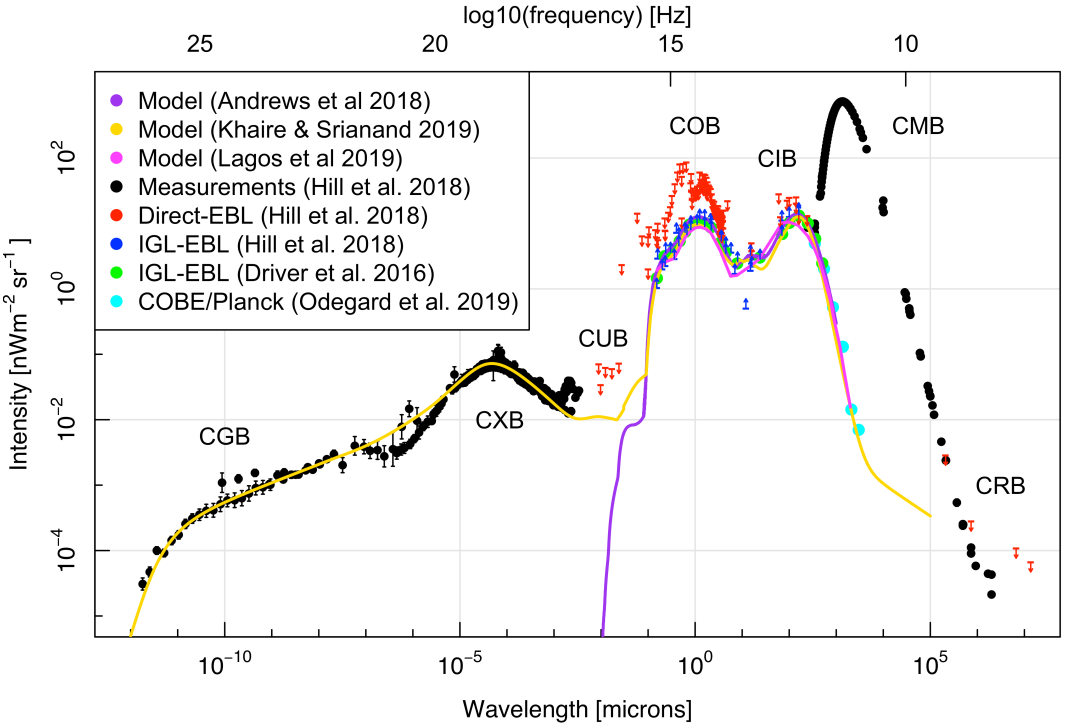

Figure 1.1: Compilation of measurements of the extragalactic photon spectrum. Figure from (1). The reader is referred to the original article for references on the datasets displayed.

extragalactic background light (EBL). This encompasses all radiation reaching Earth from extragalactic sources, excluding the contributions from Diffuse Galactic Light components (49, 50), solar system's *zodiacal* emission (51, 52), and emissions from the Milky Way group (53). In the astronomy literature, it is commonplace to categorize this spectrum into distinct wavebands, including the cosmic gamma ray (CGB), X-ray (CXB), ultraviolet (CUB), optical (COB), infrared (CIB), microwave (CMB), and radio (CRB) backgrounds, each category unique in its detection methods, units and jargon, although the same physical quantity, the isotropic photon background, is being described.

1.2.1 CMB

Among the EBL wavebands mentioned, the Cosmic Microwave Background (CMB) stands out as the only relic radiation from the hot early Universe. These photons decoupled from the hot plasma once it had cooled sufficiently for protons and electrons to combine and form neutral atoms, preventing further scattering. This event is known as the epoch of recombination in standard cosmology. Ever since, these photons have been propagating through the Universe, redshifting into the microwave band as the Universe expanded. Historically, the idea of a relic thermal radiation was outlined qual-

itatively by George Gamow (54), who argued that the hot, early Universe was radiation-dominated and that the photon bath would cool as the Universe expands. Shortly thereafter, Ralph A. Alpher and Robert C. Herman (55), provided the first quantitative estimate, predicting a present-day black-body temperature of about 5 K. In 1965, Arno Penzias and Robert Wilson made the famous accidental detection of this background, identifying a persistent, isotropic noise using the Holmdel Horn Antenna (56). Since then, various missions have mapped the CMB spectrum with great precision, including three landmark efforts: the Far InfraRed Absolute Spectrophotometer (FIRAS) on the COsmic Background Explorer (COBE) satellite (57), WMAP (58), and the Planck mission, which has produced the most detailed full-sky map of the CMB to date (59). Extensive insights into cosmology can be gained from analyzing the spectral anisotropies in the CMB (for instance see (60) for a review). These anisotropies currently provide some of the strongest constraints on cosmological parameters that describe our Universe (59).

The blackbody spectrum of the CMB is given by the Planck intensity function:

$$I_\nu = \frac{2h\nu^3}{c^2}\frac{1}{e^{h\nu/k_\mathrm{B}T}-1}\,, \tag{1-1}$$

where k_B denotes the Boltzmann constant and T is the blackbody temperature. The CMB temperature evolves with redshift, z, following $T_\mathrm{CMB}(z) = T_{0,\mathrm{CMB}}(1+z)$, where $T_{0,\mathrm{CMB}}$ is the CMB temperature at the present time ($z = 0$), measured to be $T_{0,\mathrm{CMB}} = 2.725$ K.

In astrophysics, a central quantity, used extensively throughout this dissertation, is the energy spectrum, $(\mathrm{d}n(E)/\mathrm{d}E)$, where E represents particle energy and n(E) denotes number density. The spectrum is typically expressed in units of $[\mathrm{cm}^{-3}\,\mathrm{eV}^{-1}]$, indicating the number density of particles within the energy interval between E and $(E + \mathrm{d}E)$. Specifically for photons, whose energies are given by $\varepsilon = h\nu$, the photon number-density spectrum $(\mathrm{d}n(\varepsilon)/\mathrm{d}\varepsilon)$ can be derived starting from the specific intensity I_ν. For an isotropic photon distribution, the energy density per unit frequency, u_ν, relates to the specific intensity as $u_\nu = (4\pi/c)I_\nu$. Converting frequency to photon energy via $\nu = \varepsilon/h$, we obtain the energy density per photon energy interval $(u_\varepsilon = u_\nu(\mathrm{d}\nu/\mathrm{d}\varepsilon) = (4\pi I_\nu)/(hc))$. Since each photon carries energy ε, dividing the energy density by ε yields the number-density spectrum, resulting in the relationship

$$\frac{\mathrm{d}n(\varepsilon)}{\mathrm{d}\varepsilon} = \frac{4\pi I_\nu}{h\varepsilon c}\,. \tag{1-2}$$

Integrating the CMB energy spectrum, over all energies yields the photon number density,

$$\bar{n}_{\rm CMB}(z) = \int \frac{{\rm d}n_{\rm CMB}}{{\rm d}\varepsilon}{\rm d}\varepsilon = \int \frac{8\pi\nu^2}{c^3}\frac{1}{e^{h\nu/k_{\rm B}T_{\rm CMB}}-1}d\nu = \frac{2\zeta(3)}{\pi^2}\left(\frac{k_B T_{\rm CMB}}{\hbar c}\right)^3 , \quad (1\text{-}3)$$

where $\zeta(3) = 1.202$ is the Riemann zeta function, giving present-day CMB photon number density of $\bar{n}_{\rm CMB}(z=0) \approx 410$ cm^{-3}. The CMB total energy density, meanwhile, is calculated as

$$U_{\rm CMB} = \int \varepsilon \frac{{\rm d}n_{\rm CMB}}{{\rm d}\varepsilon}{\rm d}\varepsilon = \int \frac{8h\pi\nu^3}{c^3}\frac{1}{e^{h\nu/k_{\rm B}T_{\rm CMB}}-1}d\nu = \frac{\pi^2(k_B T_{\rm CMB})^4}{15(\hbar c)^3} . \quad (1\text{-}4)$$

Thus, the typical CMB photon energy can be estimated as

$$\langle\varepsilon\rangle_{\rm CMB} = U_{\rm CMB}/\bar{n}_{\rm CMB} \approx 2.7 k_{\rm B} T_{\rm CMB} . \quad (1\text{-}5)$$

This means that, for instance, in the local Universe, the CMB photons mostly are of energy $\approx 6.34 \times 10^{-4}$ eV.

The CMB stands out, dramatically, as the most prominent component of the EBL, dominating not only the microwave region ($0.04 - 4$ meV) but also the entire spectrum, with an integrated energy density that is approximately five times greater than the combined contributions of all other backgrounds (61, 62). As we will see in the rest of this dissertation, CMB plays a crucial role in the high energy particles propagation across cosmic distances, and is a key reference of energetic particles interactions especially when going to higher redshifts.

1.2.2 CRB, CIB, COB and CUB: Other prominent low energy photon fields

The remainder of the EBL consists of radiation emitted after the recombination, primarily from sources such as star formation, accretion onto supermassive black holes (e.g., Active Galactic Nuclei), and the reprocessing of ultraviolet and optical light by interstellar dust, which typically results in mid- and far-infrared thermal emission. Two prominent components within this portion of the EBL are the COB and the CIB, which together encompass a significant fraction of the energy emitted by stars and galaxies over cosmic history (44). Consequently, in the literature, the term EBL often refers specifically to the combined COB and CIB emissions. Henceforth, we also employ the term EBL exclusively for referring to the CIB and COB through this dissertation.

The CIB, which contains approximately half of the total energy density produced by stars, is strongly tied to the history of galaxy formation and their evolution. This radiation is largely emitted by interstellar dust that has been heated by starlight within galaxies, with the longest wavelengths corresponding

to the energy output of the earliest, most redshifted galaxies. Directly measuring this component of the cosmic background is particularly challenging due to strong foreground emissions. The strongest of these foregrounds are *(i)* thermal dust emission from the Milky Way and *(ii)* the so-called *zodiacal emission* produced by interplanetary dust in the Solar System. Micron- to millimetre-sized zodiacal grains absorb optical sunlight, reach radiative-equilibrium temperatures, $T \sim 230-280$ K, and re-emit that energy as grey-body radiation peaking in the mid-infrared. Thus, accurate modelling and subtraction of the zodiacal foreground is essential for reliable CIB measurements.

The COB, meanwhile, is dominated by direct starlight and is aligned with the history of cosmic star formation. The COB is a highly studied component, benefiting from the relative accessibility of optical wavelengths to ground-based telescopes, however its direct measurements face substantial challenges. The dominant contaminations are:

(i) **Zodiacal light**—sunlight that is scattered, rather than thermally re-emitted, by the same population of interplanetary dust particles responsible for zodiacal emission. Its broadband optical surface brightness varies smoothly across the sky and typically exceeds the expected COB by factors of 10 - 100.

(ii) **Diffuse Galactic light (DGL)**—a combination of (a) Galactic starlight scattered by interstellar dust in the Milky Way's disk and halo, and (b) the collective, unresolved emission of faint Galactic stars. The DGL inherits the spectral shape of stellar continua modulated by dust albedo and shows strong spatial correlations with interstellar dust column density. Even at high Galactic latitudes its intensity remains well above the COB signal.

Robust COB determinations therefore rely on precise modelling of both zodiacal and DGL components.

To deal with the CIB and COB direct measurement challenges, there are other indirect approaches of measurement, some based on galaxy number counts and flux measurements of resolvable galaxies with extrapolation (for instance, see the method in (47) for the radio galaxies). However, these details are not the subject of this thesis; thus, we will not delve into them.

Unlike CMB, which follows a blackbody spectrum, the EBL is shaped by non-thermal processes that produce radiation spectra deviating from a blackbody profile. In such non-thermal processes, such as synchrotron radiation, inverse Compton scattering, and bremsstrahlung, the photon energy does not correspond directly to the temperatures of the sources, as these processes do

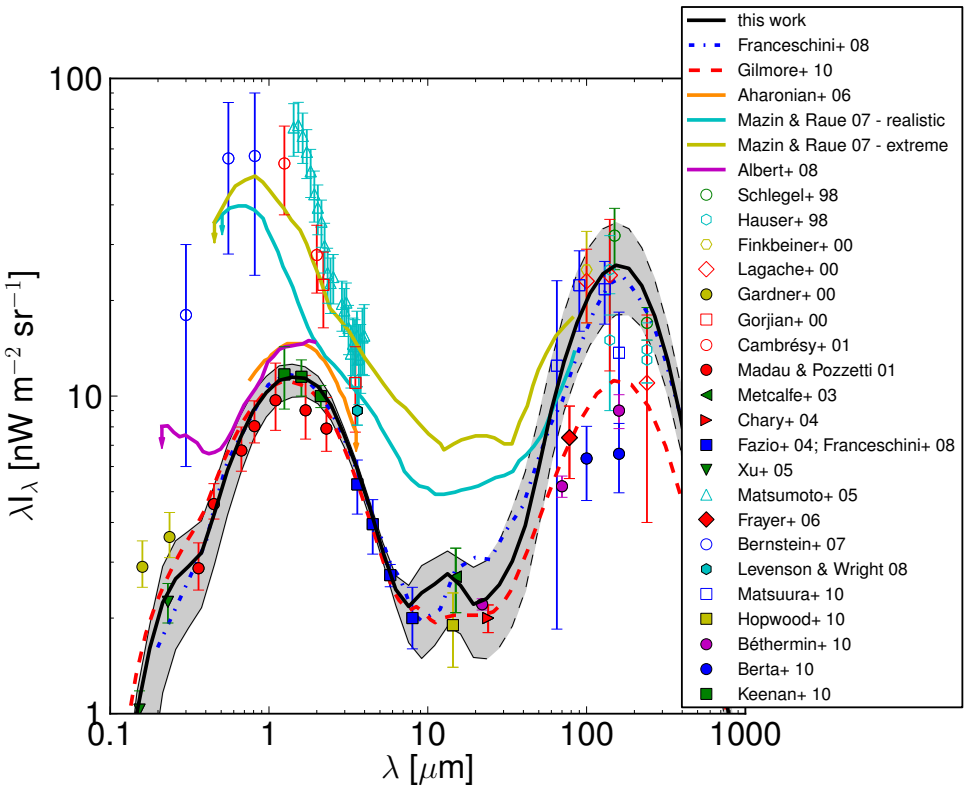

Figure 1.2: Domiguez EBL model. Figure from (2)

not rely on thermal equilibrium. This non-thermal origin characterizes the EBL from infrared to ultraviolet. At redshift $z = 0$, the EBL can be approximated by three blackbody-like peaks: two major peaks near wavelengths of $\lambda \sim 1\mu m$ (COB) and $\lambda \sim 100\mu m$ (CIB), and a smaller peak around $\lambda \sim 10\mu m$. Note that these "three blackbody-like peaks" are purely empirical parametrizations of the complex, non-thermal EBL spectrum and should not be interpreted as arising from actual thermal sources.

Several models have been proposed to reconstruct the EBL intensity, almost all of them showing consistency with one another and with observational data within statistical uncertainties (43, 2, 63). Figures 1.2 and 1.3 illustrate the Dominguez EBL model from (2) and its evolution with redshift, respectively.

The radio spectrum of the Cosmic Background (CB) extends across frequencies below roughly 10^{10} Hz. Current models describe the CRB as a combination of synchrotron radiation from charged particles moving through Galactic and InterGalactic Magnetic Fields (GMF and IGMF), emission from Active Galactic Nuclei (AGN), and contributions from H_I line radiation, in addition to the low-energy end of the CMB (64). The energy of synchrotron radiation is directly linked to the magnetic field strength squared; however, with typical magnetic fields in galaxies on the order of 10^{-9} T (65), the resulting

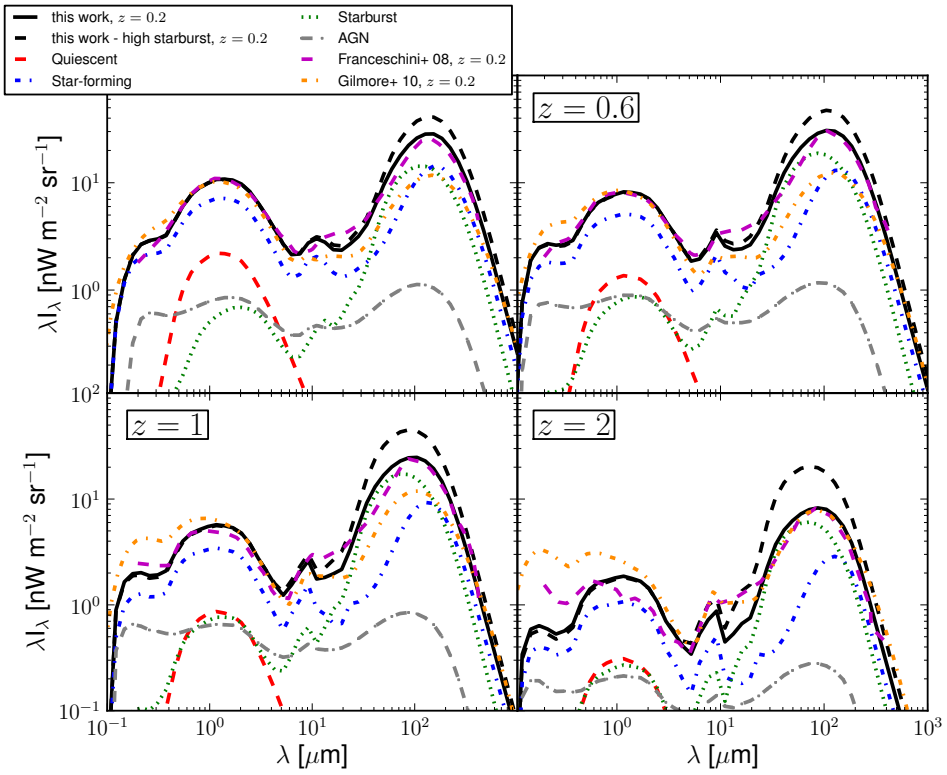

Figure 1.3: Domiguez EBL model redshift evolution. Figure from (2).

photon energies are low.

Detecting the CRB, however, is technically constrained and difficult primarily because of the plasma frequency of both Earth's ionosphere and the interstellar medium (ISM). The plasma frequency is given by

$$\nu_p = \sqrt{\frac{n_e e^2}{\pi m_e}} \ , \tag{1-6}$$

where n_e is the electron number density and m_e the electron mass. This frequency represents the natural oscillation rate of free electrons in a plasma, below which electromagnetic waves are absorbed exponentially over very short distances (66). On Earth, the ionosphere has a plasma frequency of around 10 MHz, limiting ground-based CRB observations, while in the ISM, the plasma frequency is approximately 1 MHz, presenting a constraint even for space-based detectors (67). Additionally, the foreground emission from the Milky Way must be subtracted in order to isolate the extragalactic component.

The CRB has been estimated in (68) using satellite radio measurements and has been modeled in (4, 3) by modeling the radio emission from populations of star-forming galaxies (SFGs) and radio galaxies (RGs). Figure. 1.4 illustrate the CRB estimation by (3, 4).

It's important to note that the intensity of EBL and the CMB behave very differently as redshift increases. The EBL, which originates from astro-

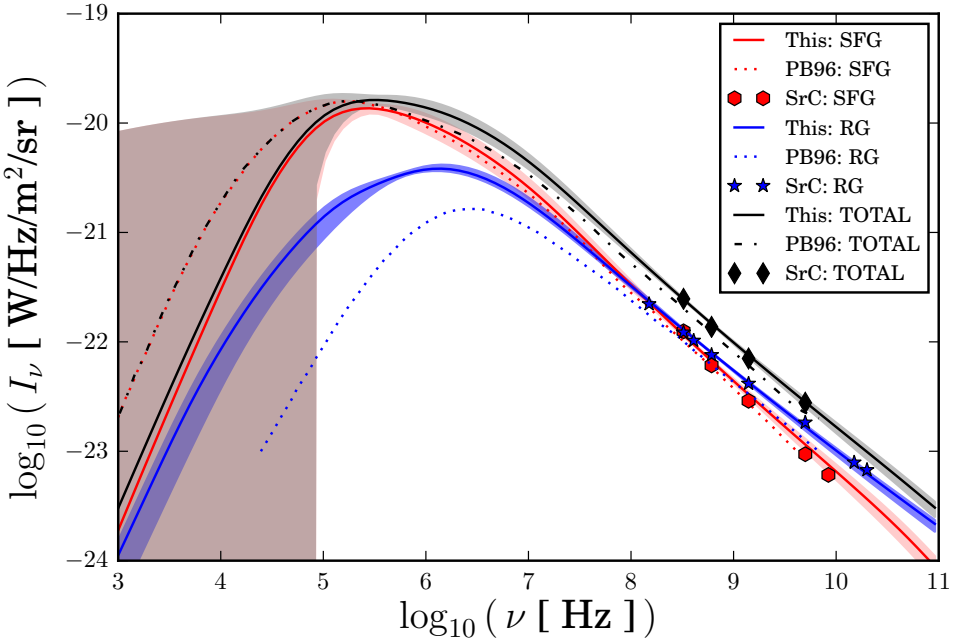

Figure 1.4: The total CRB is shown along with the contributions from SFGs and RGs as calculated in (3) (solid lines) and by (4) (dashed and dotted lines). Observational measurements from radio source-count data (5, 6, 7) are shown as stars, diamonds and hexagons at discrete frequencies. Figure from (3).

physical sources, decreases in intensity at high redshifts (*i.e.* $z \gtrsim 4$) due to the declining number of astrophysical sources as we look farther back in time. In contrast, the CMB intensity actually increases with redshift because its photon number density scales as $(1+z)^3$ and individual photon energies increase by $(1+z)$. Together, this causes the CMB energy spectrum, $\mathrm{d}n_{\mathrm{CMB}}/\mathrm{d}\varepsilon$, to scale as $(1+z)^2$. Thus, while the EBL dims, the CMB becomes more prominent at higher redshifts.

All in all, these pervasive low-energy photon fields, with their relatively high intensity, significantly impact the propagation of high-energy particles across cosmological distances, a topic that will be discussed in detail in the following sections.

1.2.3 CGB

The cosmic gamma ray background (CGB) represents the high-energy frontier of cosmic background radiation, covering frequencies above 10^{19} Hz (or photon energies $E_\gamma \gtrsim 1$ MeV). In gamma ray astronomy's terminology, this background is often referred to as the Extragalactic Gamma-ray Background (EGB). Defined in gamma ray experiments, particularly by the Fermi-LAT

collaboration, the EGB is calculated by measuring the total γ-ray signal within the detector, excluding emissions from our galaxy e.g. the diffuse Galactic emission (DGE) and the solar system.

In our galaxy, diffuse gamma ray emission (DGE) arises mainly from interactions between cosmic rays and the interstellar gas (ISG), which is predominantly hydrogen and helium. Supernova remnants (SNRs) and pulsars are believed to be the principal sources of cosmic ray nuclei, electrons, and positrons. When cosmic ray nuclei, primarily protons and helium, interact with the ISG, they produce neutral pions, π^0, which subsequently decay into gamma ray photons ($\pi^0 \rightarrow \gamma\gamma$). Electrons and positrons, meanwhile, undergo inverse Compton scattering with the interstellar radiation field (ISRF), shooting the low-energy photons to higher energies ($e\gamma_b \rightarrow e\gamma$)[2]. These interactions constitute the main production mechanisms for the DGE, which its intensity is comparable to the EGB at energies $\gtrsim$ 1 GeV even at the Galactic poles. While the DGE has been thoroughly examined in cosmic ray and gamma ray research, an in-depth exploration of DGE models is beyond the scope of this thesis. For a more comprehensive discussion on DGE, we refer readers to (69, 17).

The primary sources contributing to the Extragalactic Gamma-ray Background (EGB) include Active Galactic Nuclei (AGN), star-forming galaxies (SFGs), and γ-ray bursts.

AGN are highly luminous galactic cores powered by matter accreting onto supermassive black holes, converting gravitational energy into radiation across the electromagnetic spectrum—including γ-rays. Some AGN launch powerful relativistic jets that can reach ultra-high energies ($\gtrsim$ PeV) and extend hundreds of kiloparsecs from the host galaxy. The Unified Model of AGN explains the different classes—blazars, radio galaxies, Seyfert galaxies, and quasars—as fundamentally the same engine viewed from different angles relative to the jet and dusty torus (70).

- Blazars have jets pointed almost directly at us (within $\lesssim 10^\circ$). Because the jet material moves at speeds close to light, its emission is strongly enhanced when viewed head-on—a relativistic "beaming" effect that makes blazars appear extremely bright, variable, and γ-ray loud.
- Radio galaxies are those whose jets are oriented at larger angles (typically $\gtrsim 20^\circ$) to our line of sight. In these cases, the beaming effect is weak,

[2]Inverse Compton scattering differs from ordinary Compton scattering in that, in ICS, a low-energy photon gains energy through collision with a relativistic electron (*i.e.*, the photon is "up-scattered"), whereas in Compton scattering a high-energy photon transfers energy to a typically stationary electron and is "down-scattered".

so we observe less bright central emission and instead detect extended radio structures ("lobes") formed where the jet plasma impacts the surrounding medium.

– Seyfert galaxies are less luminous, often found in spiral hosts, and lack large jets. They are identified by their optical emission-line spectra, which include strong features like Hβ and O III[3], generated in gas near the super massive black holes (SMBH).

– Quasars (Quasi-Stellar Objects) represent the most luminous AGN class, often at high redshift. Their optical/ultraviolet spectra display both broad and narrow emission lines, indicating a high-velocity inner gas region coupled with more distant ionized clouds.

In star-forming galaxies (SFGs), hot, massive stars emit intense ultraviolet (UV) light, which is absorbed by interstellar dust and re-emitted as infrared (IR) radiation. Thus a strong IR domination in spectral energy distribution (SED) is a reliable marker of star formation activity. Particularly active regions in starburst galaxies often exhibit extreme IR luminosities, placing many among the brightest infrared galaxies. These massive stars eventually end their lives in supernova explosions, producing supernova remnants (SNRs) and pulsars. Similar to the processes in DGE, gamma rays in SFGs are generated primarily through the decay of neutral pions, π^0, produced by interactions of CR nuclei with the interstellar medium (ISM), and through inverse Compton scattering of electrons and positrons off the ambient photon fields. For more on the gamma ray contribution from SFGs, see (71, 72).

The presence of an all-sky γ-ray emission was first identified in early observations by the OSO-3 satellite, which detected 621 candidate γ-ray events (73, 74). This discovery was followed by the first spectral measurements of an isotropic diffuse background by SAS-2 satellite (75, 76). Later experiments, with improved sensitivity, enabled the detection of individual extragalactic sources and the subtraction of DGE templates to isolate an all-sky residual intensity (77, 78). This isotropic emission, found to be smooth across large angular scales, is commonly termed the isotropic diffuse gamma ray background (IGRB). Today, the Large Area Telescope (LAT) on the Fermi Gamma-ray Space Telescope (Fermi) is one of the most advanced experiments, among others, for detecting the IGRB in the energy range 100 MeV - 820 GeV. With

[3]The Hβ line arises from the Balmer series transition in hydrogen at 4861 Å, produced in relatively dense, lower-velocity gas. The [O III] λ5007 line, a "forbidden" transition of doubly ionized oxygen (O^{2+}), originates in lower-density, more extended regions. These features are essential diagnostics of the ionized gas conditions in AGN narrow-line regions.

a field of view of 2.4 sr and spatial resolution of approximately 1° at 1 GeV, Fermi-LAT has provided deeper insights into the sources of EGB (40).

Other important gamma ray experiments operating in the very-high-energy (VHE) regime include the Major Atmospheric Gamma Imaging Cherenkov (MAGIC) telescopes, a system of two 17-meter diameter Imaging Atmospheric Cherenkov Telescopes (IACTs). MAGIC is designed to observe gamma rays from both Galactic and extragalactic sources in the energy range of 30 GeV to 100 TeV, with high sensitivity (79).

Another experiment working in a similar energy range is the High Altitude Water Cherenkov (HAWC) observatory, a ground-based array located at an altitude of 4100 meters in Mexico. HAWC is designed to detect gamma rays and CRs in the 100 GeV – 100 TeV range using water Cherenkov detectors. Unlike IACTs, which operate only during clear nights, HAWC continuously observes the sky, making it well-suited for studying transient and extended gamma ray sources (80).

The Large High Altitude Air Shower Observatory (LHAASO), located at 4410 meters above sea level in Sichuan, China, is another major facility. LHAASO is designed for ultra-high-energy gamma ray and CR studies, covering the energy range between 10^{11} and 10^{15} eV for gamma rays and 10^{12} to 10^{17} eV for CRs. With its wide field of view (~ 2 sr) and continuous operation, LHAASO provides an unprecedented capability to study the energy spectrum, elemental composition, and anisotropies of CRs, along with the identification of PeVatrons—sources accelerating particles to PeV energies (81).

It is important to note that IGRB intensity measurements are observation-dependent; more sensitive instruments and deeper exposures can resolve fainter extragalactic sources and thus less residual emission remains as IGRB. In contrast, the total EGB intensity, assuming the complete subtraction of all Galactic emissions, is a more fundamental measure of the extragalactic gamma ray background.

In Figure 1.1, we observe a sharp decline in gamma ray flux at frequencies above $\nu \gtrsim 10^{26.5}$ Hz (around 1 TeV). This attenuation does not reflect a limit in the gamma ray production capabilities of the above-mentioned astrophysical sources but instead results from the interactions high-energy gamma rays undergo as they propagate through the intergalactic medium (IGM). Specifically, these gamma rays are absorbed by the pervasive low-energy background photons, especially those from the CMB and EBL and produce $e^{\pm}$ pairs ($\gamma\gamma_b \rightarrow e^+e^-$), leading to a decrease in flux at higher frequencies. Consequently, we can establish the observation horizon for each energy level using the mean free path of photon-photon interaction, representing the average dis-

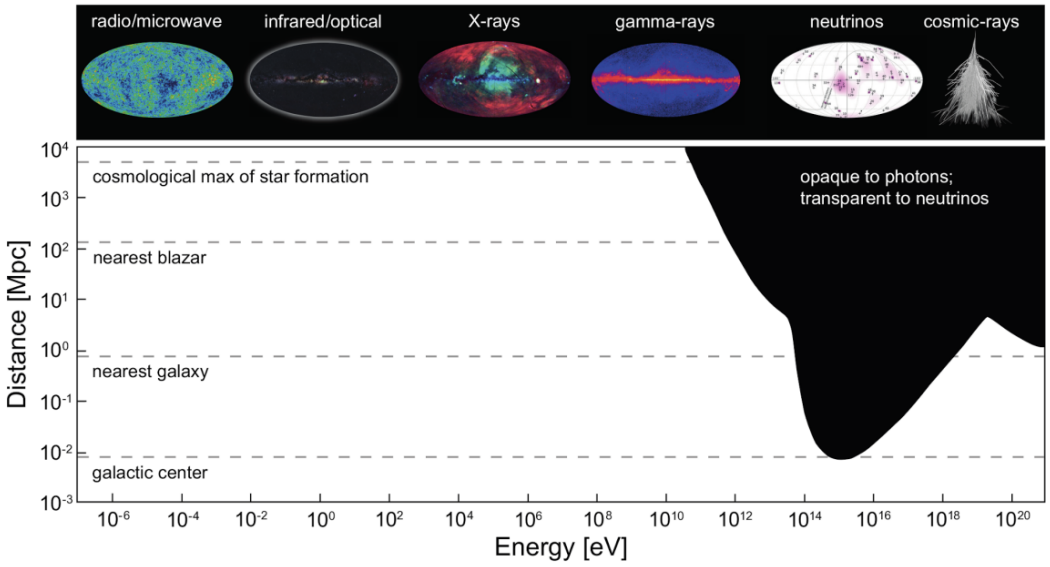

Figure 1.5: Horizon distance for photons as a function of their energy. Black regions indicate distances where γ-rays at those energies cannot reach us before pair-producing with other background photons. Figure from (8).

tance a photon can travel without encountering any interaction. This horizon is depicted in Figure 1.5. As illustrated in this plot, a photon, for instance, with an energy $\gtrsim 10^{13}$ eV cannot traverse distances greater than 1 Mpc without interaction, thus, in the case of detection this photon must have been emitted within the 1 Mpc distance from the Earth. Of course, this statement is true within the standard models of physics and not the exotic ones such as Lorentz invariance violation. Moreover, this attenuation, in fact, is a manifestation of the *electromagnetic cascade*, which we will discuss in details through this dissertation.

1.3 Cosmic Rays (CRs)

The study of cosmic rays (CRs) has a rich history dating back to the early 20th century, although their first signal was noted as early as 1785, when Coulomb observed that charged *electroscopes*[4] gradually lost their charge over time. Initially, the explanation pointed to the existence of charged particles in the air, but it took a century to identify the cause of these charged particles. The discovery of spontaneous radioactivity in 1896 by Henri Becquerel and Marie Curie provided a natural explanation. The radiation from Earth's

[4]An electroscope is a simple charge-detector—classically two thin gold leaves attached to a metal rod inside an insulating jar. When the leaves are given the same electric charge they repel and remain separated. Ionizing radiation, including cosmic-ray–induced secondary particles, produces free electrons and positive ions in the surrounding air; these charge carriers neutralize the leaves, allowing them to collapse.

radioactivity ionizes the air, leading to the discharge of electroscopes. However, it wasn't until 1911-1912 that experiments conducted in the sea and high-altitude balloon flights by Domenico Pacini (82) and Victor F. Hess (83) revealed that this radiation originated from outer space, importantly, the lack of correlation with day or night implied a "galactic" origin, possibly unrelated to solar activity. The nature of CRs was a subject of debate until the 1930s when observations of latitude and East-West effects (84, 85, 86, 87, 88) suggested that the primary CRs reaching Earth are predominantly of positive charge. Further investigations since the 1930s have established that CRs consist predominantly of stable nuclei with lifetimes of approximately 10^6 years or longer, with protons being the dominant constituent.

Cosmic rays are now understood to be predominantly stable, fully ionized nuclei[5] produced by astrophysical sources. As they traverse the cosmos, their paths are deflected by the intergalactic and Galactic magnetic fields (IGMF/GMF), and their energies are drained through interactions with the intergalactic and interstellar media (IGM/ISM) and background photon fields permeating the Universe. Furthermore, these interactions can result in the disintegration or spallation of the nuclei, transforming them into particles that differ from those initially emitted by the sources. Together, these processes obscure the connection between observed CRs and their astrophysical origins. In the contemporary CR research, understanding the arrival directions, energy spectrum, and mass composition remain open challenges and a central focuses. These aspects are key to addressing fundamental questions about the origin and propagation of CRs. Hence, a comprehensive interpretation of the experiments' measurements, along with their energy dependent correlations, is essential for advancing our understanding of CRs and for testing and refining astrophysical models.

In this section, I provide a concise review of cosmic ray research, focusing on aspects most relevant to the scope of this dissertation. While CRs have been a subject of extensive study for over a century, encompassing a wealth of literature, a comprehensive review of all their facets is beyond the scope of this work. To begin, I would like to start with a brief discussion on the galactic and intergalactic magnetic fields, which play crucial roles both in CR acceleration and propagation.

[5]The ionization state of the CRs are discussed in details in Chapter. 2.

1.3.1 Magnetic Fields

Magnetic fields are pervasive across the Universe, detectable in systems ranging from the small scales such as solar system to the galaxy clusters and even the voids of the Large Scale Structure (LSS) (89, 90, 91, 92, 93, 94, 95, 96, 97, 98, 99, 100). These fields are essential to many astrophysical phenomena and have been studied extensively in these environments.

In a well-accepted paradigm, magnetic fields observed in astronomical systems of varying sizes—from stars ($R \sim 10^{11}$ cm) to galaxy clusters ($R \sim 10^{24}$ cm)—are believed to originate from the amplification of weaker seed fields. Two complementary mechanisms drive this growth. *Hydromagnetic dynamos* operate in an electrically conducting, rotating, and often turbulent plasma: chaotic motions stretch, twist, and fold magnetic field lines, steadily converting kinetic energy into magnetic energy and boosting the field by roughly ~ 10 orders of magnitude, depending on the astrophysical setting (101, 102, 103, 104). *Flux-conserving (adiabatic) compression* amplifies the field whenever the gas collapses or shears; because magnetic flux is effectively "frozen" into a highly conducting medium, a contracting cloud drags the embedded field lines with it, intensifying the field as the density rises. These mechanisms, however, rely on the presence of an initial, albeit weak, magnetic field. The generation of this "seed" field predates or coincides with the epoch of structure formation and remains a topic of significant scientific inquiry.

The unresolved nature of the seed field's origin constitutes the "problem of the origin of cosmic magnetic fields" (65, 105, 106). Broadly, two classes of models have been proposed:

1. **Primordial origin:** The seed fields are generated during the early Universe, prior to the formation of large-scale structures.

2. **Astrophysical origin:** The seed fields arise alongside gravitational collapse and structure formation.

To constrain the properties and origins of these fields, it is crucial to study environments where magnetic fields remain largely unaffected by magnetohydrodynamic (MHD) processes, such as the IGM, particularly in the voids of the LSS. As will be discussed in Section 1.5, lower limits on these fields can be derived through the study of electromagnetic cascades.

The primordial nature of weak magnetic fields in LSS voids is not guaranteed. An alternative explanation suggests that these fields may have formed at later cosmic epochs ($z < 10$) as a result of galactic outflows. These outflows could be driven by galactic winds associated with star formation

activity or by relativistic jets produced by active galactic nuclei (AGN) (107, 108). Distinguishing between primordial and astrophysical origins of these fields remains one of the most significant challenges in the study of cosmic magnetism.

Beyond their cosmological importance, magnetic fields are integral to understanding CRs. Being charged particles, CRs are directly influenced by magnetic fields, which govern their propagation and alter their trajectories over cosmic scales. Furthermore, as will be discussed later, strong magnetic fields are necessary to accelerate CRs to the ultra-high energies observed. This underscores the dual significance of magnetic fields as both a tool for probing cosmology and a critical element in high-energy astrophysics.

However, measuring the magnetic fields, remains a significant challenge in astrophysics. It is important to note that we can always constrain the magnetic field within the phase space of (B, λ_B), where λ_B represents the magnetic field correlation length. Loosely, the magnetic field correlation length quantifies the characteristic scale over which a magnetic field maintains its direction and strength before varying due to turbulence or other factors. [6] This is due to the lack of knowledge about λ_B. In fact, there is no formal upper limit on the possible correlation length of the IGMF.

In stellar environments, magnetic fields can be directly inferred from the Zeeman effect, which is responsible for lifting the $(2J+1)$-fold degeneracy of the energy levels, with a shift which is proportional to the magnetic field strength. However, for the interstellar medium (ISM) and extragalactic environments, where fields are weaker, alternative approaches are necessary. One indirect method involves the Faraday rotation. This is based on the fact that left and right-handed circular polarized radio waves have a different refraction index in a magneto-ionic plasma. As a result, a linearly polarized wave, emitted by a source, will see its polarization plane rotate by an angle ϕ as it propagates. This shift depends quadratically on the wavelength.

Observations reveal that Galactic magnetic fields are coherent across kiloparsec (kpc) scales, aligning with major structures like spiral arms. Magnetized halos, extending several kiloparsecs above and below Galactic disks, are inferred to have field strengths of 1–10 μG. On smaller scales, field orientations fluctuate due to ISM turbulence.

Upper bounds on the strength of IGMF are imposed by the non-observation of Faraday rotation of the polarization plane of linearly polarized

[6] Mathematically, it is defined through the two-point correlation function of the magnetic field, which describes how the magnetic field at one point in space relates to the field at another point separated by a distance r.

radio emission from distant quasars. For fields with smaller correlation lengths, the constraint

$$B \lesssim 2 \times 10^{-9} \left(\frac{\lambda_B}{\ell_H}\right)^{-1/2} \text{ G} , \tag{1-7}$$

has been obtained, where $\ell_H = c/H_0$ is the Hubble radius.

Although much can be discussed about magnetic fields, it lies beyond the scope of this thesis. For comprehensive reviews on the subject, the reader is referred to (109, 110, 111).

In the following subsections, I will discuss the CR spectrum and composition, their observations, and associated challenges. I will then delve into the CR acceleration mechanisms inside the astrophysical sources and their propagation in galactic and extragalactic media, where the magnetic field plays the key role in both processes. However, before delving into the details of CR acceleration and propagation, it is worth noting that studies of CRs are generally categorized based on their origin: those originating within the Galaxy and those considered to be extragalactic. This distinction is practical but not absolute, reflecting our limited understanding of the precise conditions required to classify CRs as extragalactic. For Galactic CRs, there is widespread agreement that they originate from supernova explosions, where strong shocks accelerate particles through diffusive processes. Moving beyond the Galactic regime, CRs at ultra-high energies ($E \gtrsim 10^{18}$ eV) are widely considered to be of extragalactic origin. This conclusion is supported by the lack of correlation between the UHECR spectrum and the Galactic plane, as well as the inability of the observed Galactic magnetic fields to confine these particles.

1.3.2 Measurements and Spectrum

Detecting the CRs involves two primary approaches: direct and indirect observations. In principle, any ordinary particle physics detector can be employed to detect and measure the characteristics of CRs, such as energy and direction, outside Earth's atmosphere. This form of observation is termed "direct" detection. Notable examples include AMS-02[7], onboard the International Space Station, and the Voyager spacecraft (112). These instruments are particularly effective for studying CRs at lower energies, since the size and weight of the detectors are crucial considerations. For higher energies, where the CR flux decreases, larger detectors are required, which cannot be transported and set up above the atmosphere. To have an intuition, the arrival of ultra-high energy cosmic rays (UHECRs) at the Earth is so rare, about one event per square

[7]https://ams02.space

kilometer per year, that huge detection areas and long observation times are necessary. However, upon reaching Earth, CRs interact with molecules and ions in the atmosphere, initiating multiplicative cascades known as extensive air showers (EAS). This challenge makes the direct measurements impossible for high/ultra-high cosmic rays ground-based experiments. Therefore, an alternative approach termed "indirect" detection is employed on Earth. In the indirect detection, the ground-based experiments detect the EAS byproduct particles [8], including photons, electrons/positrons and muons. However, determining the energy and composition of the incident CRs requires models of shower development. This task is inherently challenging due to the need for precise knowledge of hadronic interactions within the cascade. While the center-of-momentum (CoM) energies of primary CR collisions with air nuclei at around 10^{17} are comparable to those achieved at the Large Hadron Collider (LHC), significant uncertainties remain. Key details of pion interactions, which are central to cascade development, are poorly understood, and the possibility of unknown processes cannot be ruled out. Additionally, assumptions about the incident mass introduce further systematic uncertainties, making precise interpretation difficult, if not impossible. Tunka (113), High Resolution Fly's Eye (HiRes) (114), IceTop (115), KASKADE (116), Pierre Auger Observatory (PAO) (117) and Telescope Array (TA) (118, 119) are among the most prominent ground-based experiments, have measured the very/ultra-high energy CR flux at Earth. To counter the above-mentioned limitations inherent to indirect detection, these experiments have pioneered techniques that leverage the light emitted by the EAS as they propagate through the atmosphere. Specifically, the detection of Cherenkov and fluorescence radiation enables a calorimetric estimation of the incident CR energy.

Using these techniques, we have been able to measure the CR flux from $\sim$ few GeV up to hundreds of EeV as illustrated in Figure 1.6. In fact, the observed CR spectrum on Earth is bounded by two pronounced cut-offs: the lower limit near $\sim$ few GeV and the upper limit around 10^{20} eV. In the low energies, the expanding magnetized plasma generated by the Sun, known as the solar wind, decelerates and partially shields the CR flux below $\sim$ few GeV. This phenomenon is termed the "solar modulation" (120) and Voyager is the only CR detector that has recently been observing the CR flux below the

[8] In the experimental CR terminology, the incident CRs at the top of Earth's atmosphere are called "primaries", while the EAS byproducts are "secondaries". On the other hand, in discussions of the astrophysical origin of CRs, "primary" CRs are those particles accelerated at and emitted from astrophysical sources, while "secondaries" are those particles produced through the interactions of the primaries with interstellar gas and background photon fields. For clarity, in this dissertation, as we will not delve into the details of CR interactions with the atmosphere, we will adopt the latter definitions of "primary" and "secondary" for CRs.

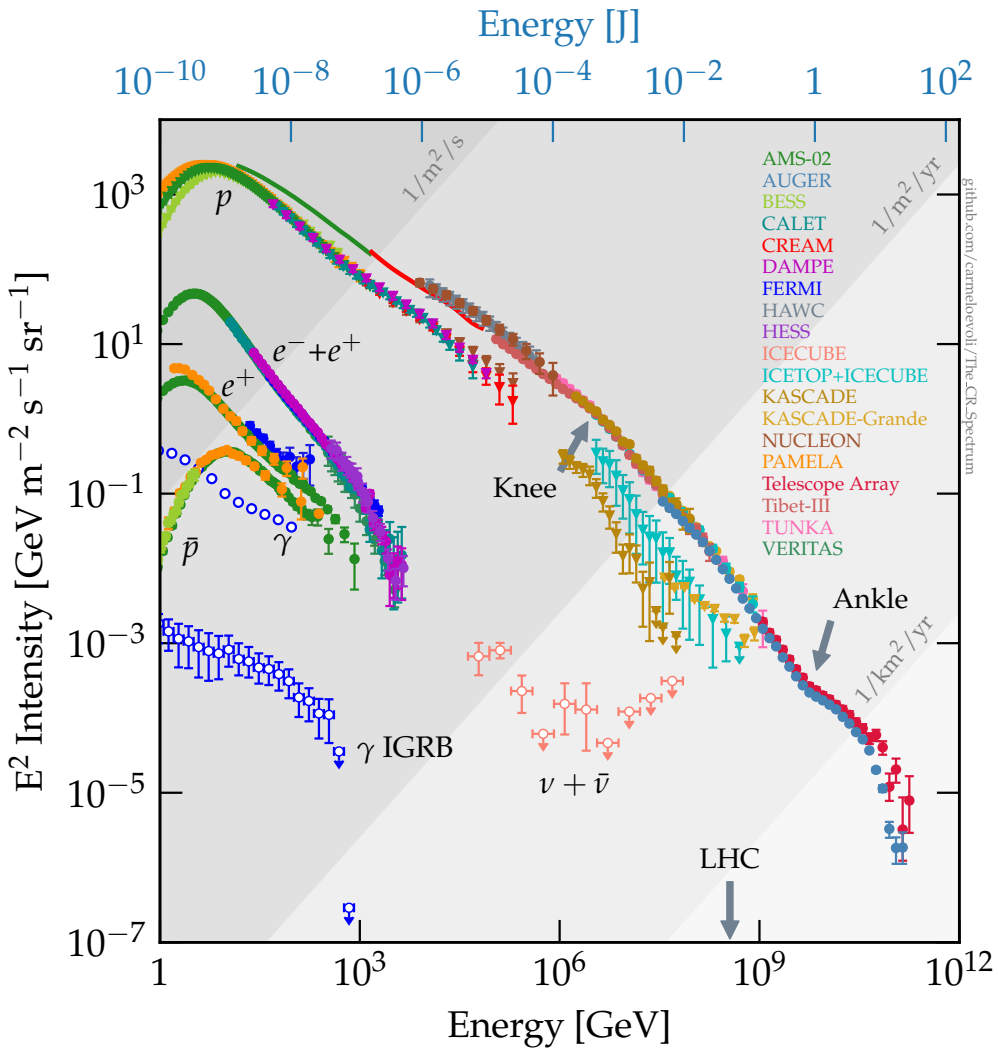

Figure 1.6: Compilation of the cosmic ray spectrum observed on Earth from different experiments, covering the full observable energy range on Earth. Figure from (9)

GeV range beyond the heliosphere, free from this modulation. At the other extreme of the CR spectrum a rapid steepening of the spectrum is evidence. However, it remains unclear whether this feature arises from physical processes during CR propagation or reflects the maximum acceleration capability of their astrophysical sources. Following the discovery of CMB, Greisen, Zatsepin, and Kuzmin (known as GZK cut-off) predicted that the extragalactic proton flux at energies $\sim 6 \times 10^{19}$ eV would be suppressed due to the Δ^+ resonance in the proton-photon ($p\gamma$) interaction cross section (121, 122). In this process, ultra-high energy protons interact with CMB photons through the photopion production process, resulting in the production of either another proton or a neutron at lower energies together with charged or neutral pions.

$$p + \gamma_{\rm cmb} \rightarrow \Delta^{+} \rightarrow \pi^{+} + n \ , \tag{1-8}$$

$$p + \gamma_{\rm cmb} \rightarrow \Delta^{+} \rightarrow \pi^{0} + p \ . \tag{1-9}$$

Alternatively, in the mixed composition model, the photo-dissociation of heavy nuclei also leads to a similar softening at the highest energies of the CR spectrum (123). Additionally, as we mentioned, the ultra-high energy cutoff can always be interpreted as the maximum acceleration capability of astrophysical sources. Cosmic ray events above 10^{20} eV have been detected (124, 125). While various UHECR experiments, including the HiRes fluorescence experiment (126, 127), Auger observatory (128), and Telescope Array (TA) (129), have presented evidence consistent with GZK suppression, recent analyses from Auger (130) challenge this paradigm. Consequently, the ultra-high energy regime remains a subject of debate.

The CR spectrum follows a power-law, $E^{-\alpha}$, with the spectral index α showing slight variations across the entire energy range. These variations carry crucial information about the mass composition and arrival directions of primary particles, serving as key clues to unraveling the mechanisms behind their production and propagation. Notably, interesting features emerge where the spectral index changes. The softening of the spectrum from $\alpha \approx 2.7$ to $\alpha \approx 3.1$ between 10^6 and 10^7 GeV is known as the *knee* of the spectrum. This feature has been observed by all the experiments and in all charged components of the EAS, thus demonstrating its astrophysical origin as opposed to alternative explanations based on possible changes in nucleus-nucleus hadronic interactions, which have been excluded by the first results from LHC (131, 132). This feature is usually interpreted as the maximum energy that protons can get accelerated to inside our galaxy, with the transition towards heavier elements giving the knee its shape (133).

A hardening of the spectrum often termed the "low-energy ankle", just above 10^7 GeV followed by a steepening at $\sim 0.8 - 1 \times 10^8$ GeV, commonly referred to as the "second knee" have been identified in data from three major experiments probing this energy range: KASCADE-Grande, Tunka and IceTop. These observations show remarkable consistency despite the differences in the energy resolution and the systematic uncertainties ($\sim 20 - 30\%$). Notably, these spectral features have also been confirmed by the low-energy extension of the TA experiment (See reference (134) and references therein for a review).

The detection of the ultra-high energy domain of the spectrum, $E \gtrsim 10^{18}$ eV, is mainly covered by PAO and TA experiments. Both collaborations

measure a hardening of the spectrum from $\alpha \approx 3.3$ to $\alpha \approx 2.6$ around $10^{18.5}$ eV which is termed the *ankle* of the spectrum. Possible contributions to the origin of the ankle include a higher energy population of particles overtaking a lower energy population, for example an extragalactic flux beginning to dominate over the Galactic flux (e.g. Ref. (124)). An intriguing explanation connecting the ankle feature to the transition from Galactic to extragalactic CRs involves the interplay of the energy loss mechanisms of UHECR protons on CMB, through pion production and electron-positron pair production ($p\gamma \to p\, e^+e^-$) processes (135). A prominent feature arising in this explanation is the so-called *Berezinski dip* occurring in the energy range $10^{18}-4\times10^{19}$ eV, induced by $p\gamma \to p\, e^+e^-$. The shape and depth of this dip are notably robust against various astrophysical factors and propagation effects, including source distribution discreteness, diverse propagation modes of ultra-high-energy protons (ranging from rectilinear to diffusive regimes), local source overdensities or deficits, large-scale cosmic inhomogeneities, and statistical fluctuations in interactions.

However, certain discrepancies between the UHECR spectra measured by PAO and TA, likely of astrophysical origin, make the situation particularly intriguing. Specifically, TA reports a more intense flux of CRs above $10^{19.5}$ eV and a higher cutoff energy. This is especially noteworthy considering the GZK effect, where the flux of nuclei above 60 EeV is expected to be significantly attenuated due to pion photoproduction interactions (Eqs. 1-8 and 1-9) with the CMB. Observing an intense flux above this energy could indicate the presence of a nearby UHECR source, where nuclei have insufficient time to interact with the background photon field. In technical terms, the photopion mean free path would exceed the source's distance to Earth.

To address these, it is necessary to delve deeper into the details of both PAO and TA experiments: Located in the Southern Hemisphere, PAO observes the sky below a declination of 24.8° (136), while TA, located in the Northern Hemisphere, observes the sky above −15.7° (129). There are therefore large portions of the Northern and Southern Hemispheres that are observed exclusively by TA and PAO, respectively, but there is also a *common declination band*, $-15.7° < \delta < 24.8°$, where the sky is observed by both experiments. Therefore, the measurements from PAO and TA are expected to align in this energy region. However, a systematic difference of approximately 9% in the absolute energy scale persists between the two. This discrepancy has been well-characterized by the TA and Auger Joint Spectrum Working Group, which was formed to investigate variations in spectrum measurements. The difference is attributed to the use of different constants in the reconstruction of fluorescence data, a factor that introduces negligible energy dependence

(137, 138, 139, 140).

Crucially, even after accounting for this energy rescaling, an excess in the TA spectrum remains apparent with 8σ significance (141). TA's data further reveal anisotropy features, including the prominent "Hotspot" (142) and the "Perseus-Pisces supercluster" (PPSC) excess. These anisotropies were detected through oversampling methods applied to intermediate angular scales. Recent analyses demonstrate that removing events associated with these regions eliminates the excess and brings the PAO and TA spectra into alignment (141). This indicates that the excess is likely astrophysical in origin, tied to specific sky regions rather than systematic issues, providing valuable clues about the sources of UHECRs.

1.3.3 Mass Composition

The mass (chemical) composition of CRs incident on Earth is a crucial yet unresolved piece of the puzzle in understanding their origin and propagation. By studying the chemical makeup of CRs across different energy ranges, we can gain insight into the astrophysical processes responsible for their production and their journeys through space. However, the picture remains incomplete, with significant open questions for investigation.

At lower energies, direct measurements of CR composition provide a more detailed picture. Galactic CRs are thought to originate from material similar to the interstellar medium (ISM) and the solar system, mixed with a smaller fraction of stellar wind material expelled by massive stars. Evidence suggests that about 80% of CRs at low energies are derived from interstellar gas, with the remaining 20% coming from ejecta of massive stars, including Wolf-Rayet winds and core-collapse supernovae (143). These CRs predominantly consist of protons, but electrons, positrons, and antiprotons are also present, along with heavier nuclei such as helium, carbon, oxygen, and iron. As shown in Figure 1.7, the notable abundance of nuclei like lithium (Li), beryllium (Be), and boron (B) among CRs is particularly intriguing, given that these elements are not products of stellar nucleosynthesis. From a thermonuclear standpoint, these nuclei are fragile, with low binding energies that make them easily destroyed in stellar environments, leaving them scarce in the ISM. Their prominence in cosmic ray fluxes is instead attributed to the spallation of heavier nuclei, such as carbon (C) and oxygen (O), which are abundant in the ISM. Thus they are largely considered as "secondaries". Given the known ISM density of $\mathcal{O}(1)\text{cm}^{-3}$, the observed abundances of these secondary species imply that CRs spend significantly longer times in the Galaxy than the simple ballistic

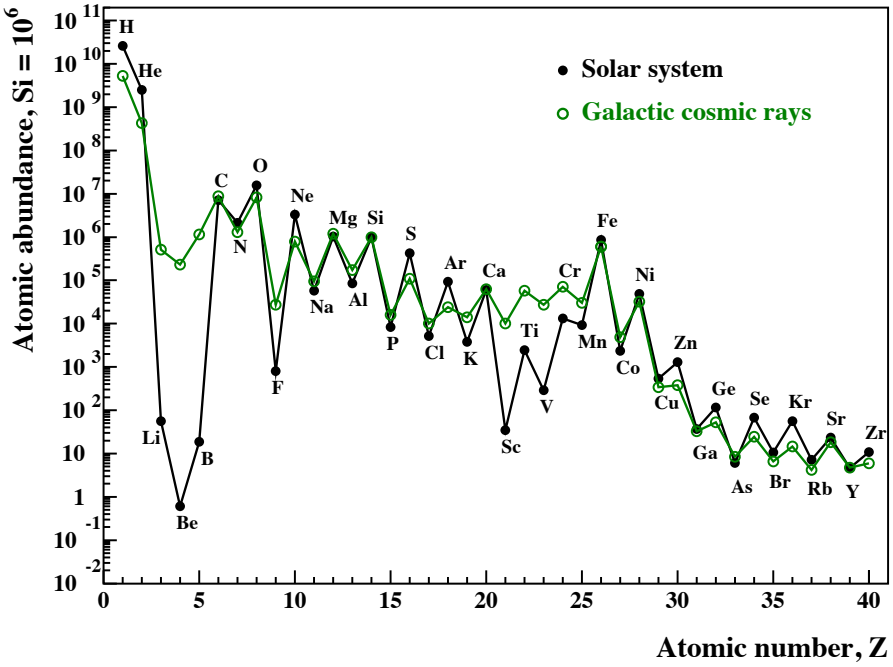

Figure 1.7: Relative abundances of CR species, compared to Solar System values, normalized to Si = 10^6. Figure from (10)

crossing time would suggest. This extended residence time provides some of the earliest and most compelling evidence for diffusive cosmic ray propagation within the Galaxy.

The transition to higher energies, however, complicates the composition studies and indirect detection methods become necessary, as the flux of CRs decreases sharply with energy. At $\sim$ few PeV energy, there is some evidence of change in the chemical composition coincide with the knee. However, the details of this transition remain poorly understood. Some studies suggest it is dominated by light elements (144), while others argue that intermediate-mass elements become predominant (145). This debate underscores the need for further experimental clarity.

At the ultra-high energies ($E \gtrsim 10^{18}$ eV) PAO and TA utilize hybrid detection techniques to study the composition of UHECRs: a surface detector (SD) array measures the charged secondaries that reach the ground level, while fluorescence detectors (FD) measure the longitudinal development of the air showers in the atmosphere in clear moonless nights. A key observable in these studies is $X_{\max}$, the atmospheric depth where the shower reaches its maximum development (146). Both the mean, $\langle X_{\max} \rangle$, and the dispersion, $\sigma(X_{\max})$, provide insights into the primary composition (147, 148). More specifically, the parameter X, known as *grammage*, represents the column density encountered by a particle along its trajectory and it is defined as the path-integrated density: $X = \int \mathrm{d}\ell \rho(\ell)$, where $\rho(\ell)$ is the local density along the

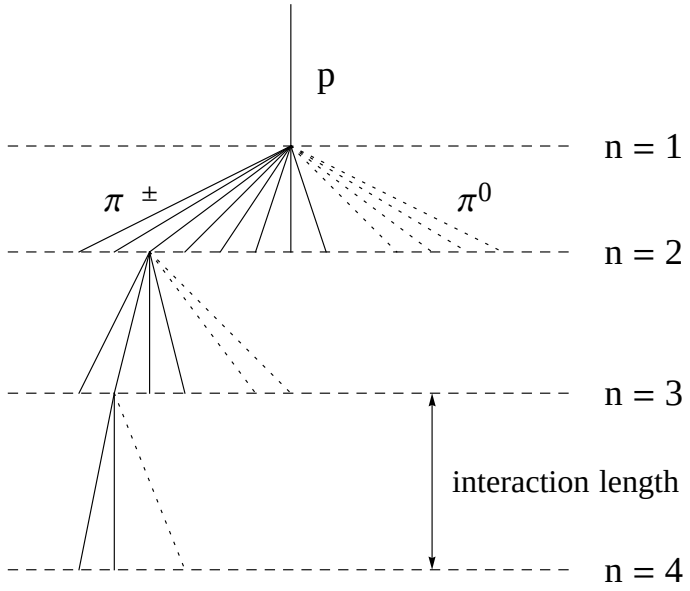

Figure 1.8: The hadronic shower scheme from (11)

path of propagation through the atmosphere. Beginning with a primary nucleus of energy E_0, the CR collides with atmospheric molecules, producing pions (π^0 and $\pi^{\pm}$) among other secondaries. The neutral pions (π^0) decay almost instantaneously into photons, giving rise to electromagnetic sub-showers. In contrast, the charged pions ($\pi^{\pm}$) propagate some distance before undergoing further interactions, generating subsequent generations of pions. This chain of particle multiplication continues until the energies of the pions drop below a critical threshold, E_c, where their decay into muons becomes more probable than other interactions. At this stage, the number of particles in the shower reaches its maximum, corresponding to the maximum grammage, $X_{\max}$. Below E_c, the remaining $\pi^{\pm}$ predominantly decay into muons, which can be detected at ground level. This simplified model of extensive air shower development is visually represented in Figure 1.8.

The interpretation of $\langle X_{\max} \rangle$ and $\sigma(X_{\max})$ can be framed through the "generalized Heitler" model of EAS (149). In this model, $\langle X_{\max} \rangle$ scales linearly with $\log_{10}(A)$, where A is the atomic mass of the incident CR. This relationship provides a practical method for inferring the composition of CRs in ground-based experiments. However, as previously mentioned, converting shower development measurements into the incident CR's characteristics relies on shower simulation codes and assumptions about hadronic interaction models, introducing inherent uncertainties in determining the mass composition. For a detailed discussion, I refer the reader to the extensive body of work on this topic, including (11, 147, 148, 149, 150, 151), and the references therein. Furthermore, some of the state-of-the-art codes for simulating extensive air

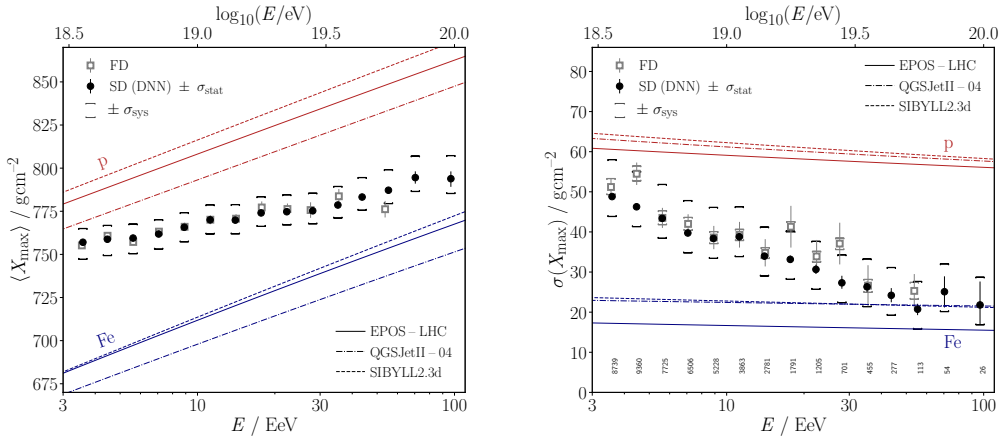

(a) (b)

Figure 1.9: $\langle X_{\max} \rangle$ and $\sigma(X_{\max})$ measurement of UHECRs inferred on an event-by-event level using the SD and FD. Using the depp learning the measurements are extended up to 100 EeV (10^{20} eV). Figure from (12)

showers (EAS) include `CORSIKA` (152), `SENECA` (153), and `CONEX` (154), among others.

Figure 1.9 presents the latest measurements of $\langle X_{\max} \rangle$ and $\sigma(X_{\max})$ for UHECRs observed by PAO using both surface and fluorescence detectors. The plots include reference lines for pure proton (p) and pure iron (Fe) compositions, shown in red and blue, respectively. As evident from these results, at the highest energies, the chemical composition of CRs appears consistent with heavy nuclei. Additionally, some studies suggest that the $\langle X_{\max} \rangle$ values reported by PAO may reflect a heavier mass composition due to potential systematic biases in the shower models (155). Recent analyses from the Telescope Array (TA) also indicate a preference for intermediate to heavy elements at ultra-high energies (156).

Recently, the LHAASO Collaboration provided precise measurements of the all-particle energy spectrum and the mean logarithmic mass, $\langle \ln A \rangle$ of CRs in the energy range from 0.3 PeV to 30 PeV. By combining CR data from space-based experiments such as AMS-02 and DAMPE with ground-based observations from LHAASO and the PAO, they constructed a comprehensive model that reconciles these measurements over a wide energy range, from tens of GeV to tens of EeV. This analysis links the formation of the *second knee* in the CR spectrum, observed around 200 PeV, to the cutoff of galactic iron and potentially the elements within the $Z = 53$ group (157).

All in all, despite the significant advancements in the experiments and their data analysis, the chemical composition of CRs, particularly at the ultra-high energy stage, continues to be an open problem.

1.3.4 Cosmic Ray Propagation

As we discussed, significant advances have been made in CR observations, providing a rich tapestry of data in this field. However, on the theoretical front, it remains crucial to develop models grounded in known physics that not only reproduce existing observations but also predict measurable features for future experiments. In the previous sections, we outlined some of these models, discussing key features of the CR spectrum. In this section, I take a step further to delve into the foundational ideas behind these models. Specifically, addressing the primary aspects of CR studies, *i.e.* chemical composition, spectrum, and arrival direction, requires answering three big questions: 1) How does nature accelerate particles? 2) How do these particles propagate through the complex environments within, around, and beyond their sources? 3) How do these particles lose energy and emit radiation? In this section I will adopt a phenomenological approach to explore these questions.

However, before exploring these questions, let me introduce some key quantities commonly used in CR literature. These include the particle momentum, $p = |\mathbf{p}| = m\beta\gamma$, and the total energy, $E = \sqrt{m^2 + p^2} = \sqrt{A^2 m_N^2 + p^2}$. In the low-energy regime of CRs (GeV – TeV), additional quantities are frequently employed: the *total energy per nucleon*, $E_N = E/A$; the *total kinetic energy*, $K = E - m$; and the *kinetic energy per nucleon*, $K_N = E_N - m_N$. These quantities are particularly useful for analyzing spallation processes, where they remain preserved. Here, A represents the atomic mass number, and m_N is the nucleus mass: $m_p = 938.2$ MeV for the protons and $A \times m_{\rm amu}$ for heavier nuclei, where $m_{\rm amu} = 931.5$ MeV is the atomic mass unit. Another crucial parameter in CR physics is *rigidity*, $\mathcal{R} = p/q$, which reflects the particle's momentum-to-charge ratio. CRs with the same rigidity undergo identical deflections in magnetic fields, making this quantity helpful for studying their transport.

Building on the three fundamental questions mentioned earlier, the first two are closely tied to the complex dynamics of charged particle transport in magnetic fields. But how do we know that CRs undergo such intricate motion? This question is even more fundamental, with its answer rooted in observations and insights gained from our study of the Universe.

Perhaps the clearest and most compelling evidence for the non-trivial motion of CRs lies in the significant abundance of fragile nuclei such as boron (B), lithium (Li), and beryllium (Be) in galactic CRs, as discussed in Section 1.3.3. These elements could not have been synthesized during big bang nucleosynthesis because the Universe cooled too quickly for their production. Additionally, their destruction rates exceed their production rates

in stellar environments, leading to their depletion in the ISM. Yet, their notable abundance in incident CRs implies that they are produced during the spallation processes of primary CRs, such as carbon (C) or oxygen (O), as they propagate toward Earth.

The cross sections for these spallation processes are relatively well-known, $\sigma_{\rm sp} \approx 45A^{0.7}$mb,[9] where A is the atomic mass of the parent nucleus. By requiring that the B/C or B/O ratios match the observed values, one can deduce that the confinement time of primary nuclei in the galaxy must be of the order of the spallation timescale:

$$\tau_{\rm sp} \approx [n_d(h/H)\sigma_{\rm sp}]^{-1} \approx 100 \left(\frac{H}{4\ \rm kpc}\right)\left(\frac{A}{12}\right)^{-0.7}\ \rm Myr\,, \tag{1-10}$$

where n_d is number density of the target nuclei in the ISM, h is the *half-thickness* of the galaxy in the *thin disk* model and H is the galaxy halo size. As one can infer from Eq. 1-10, the Carbon nucleus confinement time inside the galaxy must be around 100 Myr, much longer than its ballistic time $\tau_b \sim H \sim 10^4(H/4\ \rm kpc)$ yr.

Going back to our big questions, the diffusive propagation of CRs can be understood intuitively by considering charged particle motion in a magnetized plasma with a homogeneous magnetic field of strength $B_0 \equiv |\mathbf{B_0}|$ and a perturbation $\delta\mathbf{B}$. In fact, many astrophysical systems, such as astrophysical sources, the interstellar medium, and the intergalactic medium, exist in a very approximate form of Magneto Hydro Dynamic (MHD) plasma with high electric conductivity. Consequently, maintaining large-scale electric fields is often challenging. More precisely, the only electric fields that can be sustained are those associated with the motion of magnetized plasma. Such induced electric fields are of strength $\mathcal{E} \approx \beta_p B$, where $\beta_p = v_p$ is the velocity of plasma motion. In most cases of interest $v_p \ll 1$ and therefore the induced electric fields are small except for the relativistic plasma. Hence, across much of the universe, the absence of electric fields on large scales remains a valid approximation. In this approximation, the trajectory of a particle of charge $q = Z|e|$ and mass m moving with velocity $\mathbf{v}$ (associated to Lorentz factor $\gamma(v)$) in the large-scale magnetic field $\mathbf{B_0}$, is governed by the equation of motion (EoM)

$$\frac{\mathrm{d}(m\gamma\mathbf{v})}{\mathrm{d}t} = q\mathbf{v}\times\mathbf{B_0} = m\gamma\frac{\mathrm{d}\mathbf{v}}{\mathrm{d}t}\ , \tag{1-11}$$

where the last equality arises from the fact that in the absence of electric field the particle's energy does not change with time, thereby γ, velocity modulus v, and momentum modulus p remain constants. Moreover, Eq. 1-11 implies that

[9]The barn (b) is a unit of cross section commonly used in nuclear and particle physics. One barn is defined as $1\mathrm{b} = 10^{-24}\mathrm{cm}^2$. For this case, the cross section is expressed as $4.5\times10^{-26}A^{0.7}\mathrm{cm}^2$.

the velocity component $v_\parallel$ parallel to $\mathbf{B_0}$ remains constant both in modulus and direction. Additionally, it is evident that the cosine of the angle between the velocity vector and the magnetic field direction, $\mu = v_\parallel/v$, dubbed as the *pitch angle*, is a constant of motion. By elaborating on Eq. 1-11 and choosing a coordinate system where $\mathbf{B_0}$ aligns with the $\hat{z}$-axis, one arrives at:

$$v_x(t) = v_\perp \cos(\phi - \Omega t)\,, \tag{1-12}$$

$$v_y(t) = v_\perp \sin(\phi - \Omega t)\,, \tag{1-13}$$

where $v_\perp = \sqrt{v_x^2 + v_y^2} = v\sqrt{1-\mu^2}$, ϕ is an arbitrary phase with no physical significance, and $\Omega = qB_0/m\gamma$ is the gyrofrequency.

These expressions, combined with the condition μ = constant, define what is referred to as the unperturbed trajectory: the motion of a particle in the presence of an ordered magnetic field.

However, this simplistic picture does not resolve the timescale issues we discussed at the beginning of this section, since the motion along the magnetic field occurs at a significant fraction of the ballistic velocity. This would prevent the extended confinement time observed in CR propagation unless μ is exceptionally close to zero. Such a condition, however, applies to only a negligible fraction of particles, making this scenario inadequate for describing realistic CR transport.

In another point of view, the gyration radius of the charged particle around the magnetic field, known as the Larmor radius, is

$$r_L = v/\Omega = \sqrt{1-\mu^2}\frac{\mathcal{R}}{B_0} \approx 10^{-6}\sqrt{1-\mu^2}\left(\frac{\mathcal{R}}{\mathrm{GV}}\right)\left(\frac{\mu\mathrm{G}}{B_0}\right)\mathrm{pc}\,. \tag{1-14}$$

The Larmor radius can be interpreted as an estimate of the confinement scale within the system. Particles with energies corresponding to a Larmor radius larger than the size of the system can potentially escape. Alternatively, from another perspective, in order to accelerate charged particles to ultra-high energies, they must be confined. Therefore, the Larmor radius can be viewed as a measure of the system's maximum acceleration capability. Referring to equation 1-14, the maximum energy corresponding to the Larmor radius is given by

$$E_{\max} \approx qRB_0 \quad \text{or} \quad \mathcal{R}_{\max} \approx RB_0\,, \tag{1-15}$$

known as the "Hillas criterion"(158). This implies that to confine particles with higher energies, a source must possess either a stronger magnetic field or a larger size. For instance, considering a mean Galactic magnetic field strength

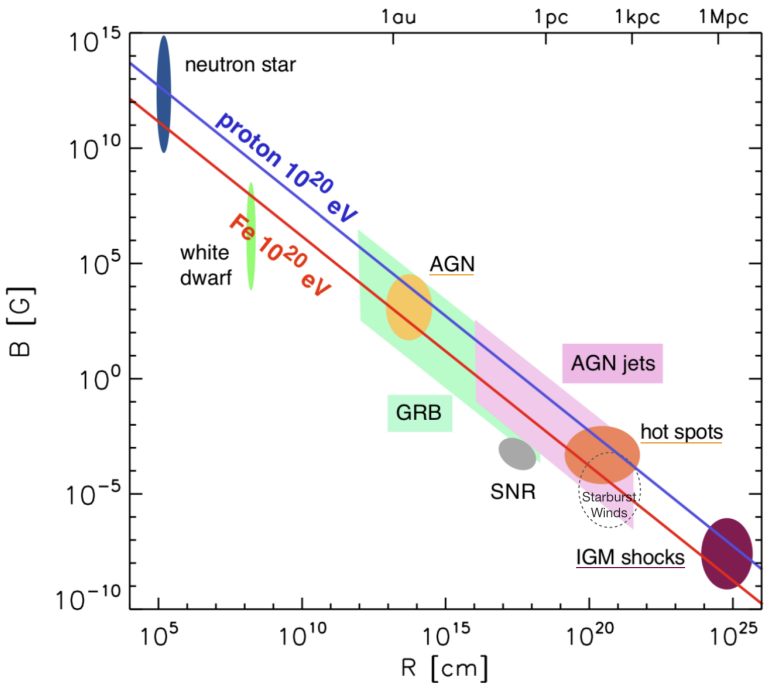

Figure 1.10: An updated Hillas diagram, illustrating the constraint that the Larmor radius of a 10^{20} eV particle must be smaller than the characteristic source size, R. The blue curve marks the threshold for protons, while the red curve delineates the limit for iron nuclei. Various types of astrophysical sources that can meet the requirements are also shown. Figure from (13).

of $B \sim \mu$G, the Milky Way (with $R \sim 10$ kpc) can only confine protons up to $\sim$ few $\times\, 10^{18}$ eV. However, this rather intuitive criterion represents a highly optimistic estimate of the maximum energy, a condition seldom met in astrophysical scenarios. The primary reason is that the induced electric field cannot maintain coherent either over the age or over the spatial size of the acceleration region. Hence, the Hillas criterion should be considered as an absolute upper bound to the maximum energy of a generic accelerator. A modern version of the Hillas diagram is presented in Figure 1.10. It is constructed by requiring the Larmor radius of a 10^{20} eV particle to remain smaller than the characteristic source size, R.

Now let us introduce small-scale stochastic perturbations, $\delta\mathbf{B}$, to the magnetic field. For simplicity we assume the perturbations be perpendicular to $\mathbf{B_0} = B_0\hat{z}$ which occurs when the perturbations take the form of Alfvén waves propagating along $\mathbf{B_0}$. Thus, $\delta\mathbf{B} = (\delta B_x, \delta B_y, 0)$. In this case, the "no electric field assumption" requires a more precise discussion because the magnetic field of the Alfvén wave is associated with an electric field of strength $\delta\mathcal{E} = v_A B_0$, where $v_A = B_0/\sqrt{4\pi\rho}$ is the Alfvén velocity of the wave in a medium with density ρ. As v_A is typically non-relativistic, the electric field is small. Therefore, the equations of motion can be interpreted either as

approximate ones or, more accurately, as the equations of motion of the particle in the reference frame in which the wave is at rest, known as the "wave frame". In the wave frame, $\delta\mathbf{B}$ implies a perturbation in the $x-y$ plane trajectory with μ being the only parameter that changes in time.

For the simplicity we can assume that the perturbation is circularly polarized and have a purely spatial wave dependence with wavenumber k and phase ψ. Therefore we can write:

$$\delta B_y = \delta B \cos(kz + \psi)\,, \tag{1-16}$$

$$\delta B_x = \pm\delta B \sin(kz + \psi)\,, \tag{1-17}$$

thus the EoM for the μ writes

$$\frac{\mathrm{d}\mu}{\mathrm{d}t} = \frac{q\delta B\sqrt{1-\mu^2}}{m\gamma}\cos[\phi \pm \psi \pm (k\mu v \mp \Omega)t]\,. \tag{1-18}$$

Equation 1-18 reveals two key properties: First, its periodic dependence on time ensures that the average pitch angle μ vanishes over sufficiently long periods:

$$\lim_{T\gg\Omega^{-1}}\langle\mu\rangle = \int_0^T \frac{\mathrm{d}\mu}{\mathrm{d}t}\,\mathrm{d}t = 0\,. \tag{1-19}$$

Second, while the average vanishes, the variance of μ does not:

$$\lim_{T\gg\Omega^{-1}}\langle\Delta\mu\Delta\mu\rangle = \pi(1-\mu^2)\left(\frac{\delta B}{B_0}\right)^2 T\delta(k\mu v - \Omega)\,, \tag{1-20}$$

where $\delta(k\mu v - \Omega)$ is the Dirac delta function. Notably, the variance grows linearly with time T, signaling the onset of a diffusive behavior. Together, Eqs. 1-19 and 1-20 illustrate that, over time, the particles undergo a gradual loss of directionality, ultimately leading to complete *isotropization*. Another characteristic of Eq. 1-20 is it's (semi)resonant behaviour as manifested by $\delta(k\mu v-\Omega)$ term. Assuming $\mu \sim 1$, the resonance condition becomes $k \sim \Omega/v = 1/r_L$, indicating that the resonance condition is met only when k^{-1} approaches the scale of the Larmor radius, r_L. More specifically, if the perturbation length scale (wavelength) is much larger than the Larmor radius ($k^{-1} \gg r_L$), the particles perceive the perturbations locally as a large-scale magnetic field and begin to gyrate around them. Conversely, if the Larmor radius is much larger than the perturbation wavelength ($r_L \gg k^{-1}$), the particles barely interact with the perturbations and predominantly follow the large-scale magnetic field ($\mathbf{B_0}$). However, when the perturbation wavelength is comparable to the Larmor radius ($r_L \sim k^{-1}$), the particles' trajectories are significantly influenced by the perturbations, as schematically illustrated in Figure 1.11.

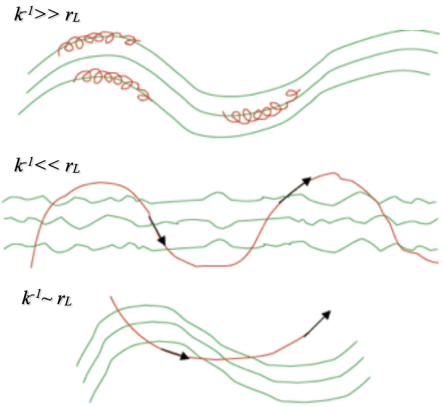

Figure 1.11: Sketch of the resonant CR diffusion mechanism. The direction of the CR is significantly affected when the Larmor radius marches the wavelength of the perturbation (bottom panel); otherwise the CR just 'surfs' the wave if its Larmor radius is very small (top panel) or "ignores the perturbation", if its Larmor radius is very large (middle panel). Figure from the lecture of Pasquale D. Serpico at PUC-Rio.

Analogous to Brownian motion[10], we can define the diffusion coefficient for the cosine of the pitch angle as:

$$D_{\mu\mu} = \frac{1}{2}\left\langle \frac{\Delta\mu\Delta\mu}{T} \right\rangle = \frac{\pi}{2}(1-\mu^2)\left(\frac{\delta B}{B_0}\right)^2 \Omega |k_{\rm res}| \delta(k - k_{\rm res})\,. \tag{1-21}$$

Physically, Eq. 1-21 indicates that particles change their pitch angle by interacting with magnetic field perturbations in the plasma, but only if the resonance condition is satisfied.

However, one could rightly argue that considering only a single wavenumber is not entirely realistic. This derivation can, in fact, be easily generalized to account for an ensemble of perturbations with varying wavenumbers:

$$D_{\mu\mu} = \frac{\pi}{2}(1-\mu^2)\Omega \int {\rm d}k \left(\frac{\delta B(k)}{B_0}\right)^2 |k_{\rm res}| \delta(k - k_{\rm res}) = \frac{\pi}{2}(1-\mu^2)\Omega \mathcal{F}(k_{\rm res})\,, \tag{1-22}$$

where $\mathcal{F}(k_{\rm res}) = |k_{\rm res}|(\delta B(k_{\rm res})/B_0)^2$ is the power spectrum of the perturbations at the resonant scale and is a dimensionless quantity.

To quantify the implications of the concepts discussed so far, let us estimate some relevant orders of magnitude. Starting with ${\rm d}\mu = {\rm d}(\cos\theta) = (1-\mu^2)^{1/2}{\rm d}\theta$, the angular diffusion coefficient can be written as:

[10]In a random walk, the variance of the particle displacement after time t can be expressed as $\langle X^2 \rangle(t) = Dt$, where D is the diffusion coefficient.

$$D_{\theta\theta} = \frac{1}{2}\left\langle \frac{\Delta\theta\Delta\theta}{T} \right\rangle = \frac{\pi}{2}\Omega\mathcal{F}(k_{\rm res})\,, \tag{1-23}$$

where $D_{\theta\theta}$ has units of radians per unit time. The timescale for an angular deflection of order one radian is then:

$$\tau \sim \frac{1}{D_{\theta\theta}} = \frac{2}{\pi}\Omega^{-1}\mathcal{F}^{-1}(k_{\rm res})\,. \tag{1-24}$$

Since $\mathcal{F} \ll 1$ (perturbation assumption), a substantial change in direction requires numerous gyrations. The distance a particle travels before such a deflection, $\lambda_D = v\tau$, corresponds to the diffusion path length. This allows us to define the spatial diffusion coefficient as:

$$D_{zz}(p) = \frac{1}{3}v\lambda_D = \frac{2}{3\pi}\frac{r_L(p)}{\mathcal{F}}v\,. \tag{1-25}$$

From the observed secondary-to-primary abundance ratios (e.g., B/C, B/Be), it is inferred that the galactic halo extends to approximately $H \sim 5\,\mathrm{kpc}$, with a confinement time for $\sim 1\,\mathrm{GeV}$ particles estimated as $H^2/D \sim 80$ Myr. Assuming $B_0 = 1\,\mu\mathrm{G}$ to compute the Larmor radius and using Eq. 1-25, we estimate $\mathcal{F}(1\,\mathrm{GeV}) \approx 10^{-6}$. This indicates that even a small perturbation, with $\delta B/B_0 \sim 10^{-3}$, is sufficient to transform ballistic motion ($\sim 10^4$ yr) into diffusive motion ($\sim$ 80 Myr): although the perturbation is minor, its macroscopic effects are significant.

So far, we have demonstrated, phenomenologically, that small perturbations in a large-scale magnetic field lead to the diffusive motion of charged particles. While this provides a valuable phenomenological insight for understanding CR propagation in the interstellar or intergalactic medium, it is important to recognize its limitations. The diffusion coefficients derived earlier are suitable for obtaining orders of magnitude but fall short in facilitating quantitative calculations for CR propagation. Indeed, the propagation of CRs in magnetized plasma presents considerable complexity, as evidenced by the observations.

The formal approach to studying CR propagation is through the Vlasov equation, which governs the dynamics of a distribution function in phase space. Assuming the dominance of the Lorentz force and neglecting electric fields, the Vlasov equation can be written as:

$$\frac{\partial f}{\partial t} + \vec{v}\cdot\vec{\nabla}f + q(\vec{v}\times\vec{B})\cdot\frac{\partial f}{\partial \vec{p}} = 0\,, \tag{1-26}$$

where $\vec{p}$ is the particle momentum, related to the velocity $\vec{v}$ by $\vec{p} = m\gamma\vec{v}$, and f is the particle phase-space density. The number density of particles at any point $(\vec{x}, t)$ can be obtained from f as:

$$n(\vec{x}, t) = \int \mathrm{d}^3\vec{p}\, f(\vec{x}, \vec{p}, t)\,. \tag{1-27}$$

In Eq. 1-26, the magnetic field $\vec{B}$ represents the total field in the environment, which typically comprises a regular component, $\vec{B}_0$, and small perturbations, $\delta\vec{B}$. Maxwell's equations, with source terms for charge and current densities, govern this field, incorporating contributions from both the background plasma and non-thermal particles. Importantly, Eq. 1-26 inherently describes the collective dynamics of particles, including their interactions with self-generated perturbations, making it a powerful theoretical framework.

To simplify the problem, we linearize the Vlasov equation by introducing perturbations into both the magnetic field and the distribution function, such that $\vec{B} = \vec{B}_0 + \delta\vec{B}$ and $f = f_0 + \delta f$, where f_0 is the solution corresponding to the uniform field $\vec{B}_0$.

Solving the full Vlasov equation, especially for realistic CR propagation scenarios, requires significant computational resources and advanced numerical techniques. While such detailed solutions are beyond the scope of this thesis, I outline the transport equation's simplified form and explain the physical significance of its terms to provide the necessary context for the analyses in Chapter 4.

Starting from the perturbed forms of f and $\vec{B}$ in Eq. 1-26 and transitioning from pitch-angle diffusion to spatial diffusion (as described earlier), we arrive at the CR transport equation. A key point to consider is that the perturbations to the magnetic field are not static—they propagate at finite speeds in the Galactic (or Lab) frame. This dynamic nature introduces additional effects that we will discuss further. By assuming the "scattering centers" move with velocity $\vec{u}$ and transforming the particle momenta to a frame comoving with these scattering centers, the transport equation writes:

$$\frac{\partial f_0}{\partial t} - \frac{\partial}{\partial x_i}\left(D_{ij}\frac{\partial f_0}{\partial x_i}\right) + u_i\frac{\partial f_0}{\partial x_i} - \frac{1}{3}\frac{\partial u_i}{\partial x_i}\left(p\frac{\partial f_0}{\partial p}\right) = \frac{1}{p^2}\frac{\partial}{\partial p}\left(p^2 D_{pp}\frac{\partial f_0}{\partial p}\right) , \quad (1\text{-}28)$$

where now p is the momentum measured in the scattering center frame and D_{pp} denotes the diffusion in the momentum space. Although we have not provided the details of the calculation, we can gain deeper insight by examining the physical meaning of each term in Eq. 1-28:

– The term $u_i\frac{\partial f_0}{\partial x_i}$ describes advection, which accounts for the transport of CRs driven by large-scale flows, such as Galactic winds. These flows are generally directed perpendicular to the Galactic plane and are often modeled as antisymmetric, with $u(z) = -u(-z)$. For typical wind velocities of $u \sim 10$ km.s^{-1}, advection significantly influences CR propagation at

energies around 1 GeV. However, its contribution becomes less important at higher energies, where other transport mechanisms dominate.

– The term, $-\frac{1}{3}\frac{\partial u_i}{\partial x_i}\left(p\frac{\partial f_0}{\partial p}\right)$, describes adiabatic energy changes. When the flow is diverging, particles experience adiabatic energy losses, whereas converging flows result in energy gains. This mechanism becomes particularly significant in models with non-uniform Galactic winds, where spatial variations in the flow velocity influence particle propagation. Furthermore, in certain scenarios this term plays a crucial role in accelerating particles and can effectively produce a source term, Q.

– The reacceleration term, $\frac{1}{p^2}\frac{\partial}{\partial p}\left(p^2 D_{pp}\frac{\partial f_0}{\partial p}\right)$, describes the diffusion of particles in momentum space. This process arises when the motion of scattering centers is incoherent, such as in a turbulent distribution of waves moving in various directions. In this scenario, the residual velocity of these waves relative to the plasma frame generates magnetic perturbations associated with electric fields. These fields drive stochastic interactions with CRs, characterized by the momentum diffusion coefficient D_{pp}. This term is particularly relevant for shaping the spectrum of CRs at energies below a few GeV and may also contribute significantly to particle acceleration at their sources.

In Chapter 4, we present a more comprehensive form of the CR transport equation, including source terms from astrophysical objects and nuclear spallation processes, which with some approximation will be used to gauge the sub-dominant energy loss processes for CRs at low energies (0.1 – 5 GeV), the central focus of that chapter.

Indeed, Eq. 1-28 serves as a remarkably versatile tool for describing a wide range of physical phenomena involving CRs. Two of the most significant applications are the transport of CR protons within the Milky Way (or other galaxies) and the diffusive particle acceleration at non-relativistic shock fronts. In this section, we have outlined the fundamental concepts of galactic CR propagation. In the next section, we will briefly discuss the basics of models for CR acceleration within astrophysical sources, shedding light on their origins.

1.3.5 Cosmic Rays Origin or How to Accelerate the Cosmic Rays

To this point, we have focused on what CRs reveal to us upon reaching Earth and explored their propagation through the galactic and intergalactic medium. Yet, the pivotal question remains: *Where do cosmic rays originate?*

This question is far from straightforward, as CR production must satisfy several critical conditions: *i*) there must be a source of immense energy—be

it the kinetic energy of supernova remnants (SNRs), the rotational energy of pulsars, or the gravitational energy harnessed by an accretion disk surrounding a supermassive black hole. *ii*) An efficient mechanism must exist to transfer this energy to CRs, one fundamentally rooted in electromagnetic interactions, as CRs are charged particles. Crucially, this mechanism must be non-thermal, capable of generating the characteristic power-law energy spectrum observed in CRs. *iii*) The particles require sufficient time to be accelerated to their observed energies, which means that they must remain confined within the acceleration region long enough to complete this process. *iv*) The acceleration must outpace energy losses; otherwise, the particles would lose energy faster than they gain it, rendering the entire process ineffective.

For the conditions (*i*), (*iii*), and (*iv*), there is no shortage of astrophysical objects that provide the necessary large-scale environments, sufficient confinement times, and rarefied conditions required for particle acceleration. For example, see Figure 1.10, illustrating the Hillas condition. Therefore, the central challenge lies not in identifying potential sites, but in understanding the mechanisms at play.

In fact, the acceleration of charged particles relies on electric fields, but in astrophysical plasmas, large-scale electric fields are effectively neutralized. Exceptions occur in rare regions, such as the magnetospheres or winds of neutron stars and near black holes or their accretion disks, where significant voltage drops may accelerate particles. Magnetic fields, on the other hand, are ubiquitous in astrophysical environments. While they cannot directly perform "work", coherent electric fields can arise when magnetic disturbances propagate coherently through the plasma, such as during shock acceleration.

When a magnetic field remains approximately constant over a single Larmor gyration, a particle conserves its magnetic moment, $\mu = p_\perp^2/B$, where $p_\perp$ is the momentum component perpendicular to the magnetic field. Since magnetic fields cannot perform work, the total momentum, $p^2 = p_\perp^2 + p_\parallel^2$, is also conserved. If a particle enters a region with a stronger magnetic field (B), its $p_\perp$ increases, leading to a decrease in $p_\parallel$. If the magnetic gradient is steep enough, the particle may reverse its motion after coming to rest along the magnetic field direction, a phenomenon known as magnetic mirroring.

Such magnetic mirrors, also referred to as magnetic clouds or magnetic irregularities, provide an effective mechanism for scattering particles in regions with non-uniform magnetic fields. Building on Alfvén's insight into the prevalence of these magnetic irregularities in the interstellar medium (ISM), Enrico Fermi proposed that repeated scattering against such magnetic clouds could naturally lead to particle energization (159, 160).

In the rest frame of the magnetic cloud, particle interactions are elastic. However, if the cloud itself is in motion, particles can gain or lose energy: head-on interactions lead to energy gain, while tail-on interactions result in energy loss. This energy exchange arises from the motional electric field generated by the moving cloud. On average, particles gain energy because head-on interactions are statistically more frequent than tail-on ones. The interaction rate depends on the relative velocity between the particle and the magnetic cloud, encapsulated by the so-called "flux factor". For a particle moving with velocity $\vec{v}$ and interacting with a cloud moving with velocity $\vec{\beta}$ (both measured in the lab or Galaxy frame), the probability of interaction per solid angle is given by:

$$P(\mu) \propto \frac{v - \beta\mu}{1 - v\beta\mu} = (1 - \beta\mu) + \mathcal{O}(\beta^2)\,, \tag{1-29}$$

where $\mu = \cos\theta$ is the cosine of the angle between the particle and cloud velocities, with $\mu = -1$ corresponding to a head-on interaction. In the approximation shown, $v \to 1$ (relativistic particle) and $\beta \ll 1$ (non-relativistic cloud). Equation 1-29 illustrates that head-on interactions ($\mu = -1$) are more probable, statistically biasing the process toward energy gain.

If the particle's initial energy in the lab frame is E_i, its energy in the cloud frame is given by $E_i' = \gamma E_i(1 - \beta\mu)$, where γ is the Lorentz factor associated with the cloud's velocity. Since the interaction in the cloud frame is elastic, the particle's final energy in the cloud frame is the same as its initial energy: $E_f' = E_i'$. Transforming back to the lab frame, the particle's final energy is:

$$E_f = \gamma E_f'(1 + \beta\tilde{\mu}) = \gamma^2 E_i(1 - \beta\mu)(1 + \beta\tilde{\mu})\,, \tag{1-30}$$

where $\tilde{\mu}$ is the exit angle of the particle in the cloud frame. Assuming $\tilde{\mu}$ is isotropically distributed (i.e., uniformly distributed between -1 and 1), the average fractional energy change is:

$$\left\langle \frac{E_f - E_i}{E_i} \right\rangle_{\tilde{\mu}} = \gamma^2(1 - \beta\mu) - 1\,. \tag{1-31}$$

The net energy gain of particles, averaged over all possible cloud-particle interactions, is then:

$$\xi = \left\langle \frac{\Delta E}{E} \right\rangle_{\mu} = \int_{-1}^{1} \mathrm{d}\mu \frac{(1 - \beta\mu)}{2} \left[\gamma^2(1 - \beta\mu) - 1\right] \approx \frac{4}{3}\beta^2 + \mathcal{O}(\beta^4)\,. \tag{1-32}$$

The scaling of the energy gain per cycle with the square of the cloud velocity (β^2) defines the mechanism known as *second-order Fermi acceleration*. Nevertheless, with ISM magnetic fluctuations on the order of the Alfvén speed, $\beta \approx v_A \approx 10^{-5} - 10^{-4}$, approximately 10^{10} collisions would be required to

merely double the particle's energy. As a result, the process remains highly inefficient.

However, if all collisions were head-on, the energy gain would scale linearly with β, making the process far more efficient. This is the foundation of what is known as *diffusive shock acceleration* or *first-order Fermi acceleration*. Contrary to its name, this mechanism was not proposed by Fermi but was independently developed by Axford et al. (161), Bell (162), and Blandford and Ostriker (163) in the 1970s. They demonstrated that applying the Fermi process to shock waves alters the geometry of the problem compared to second-order Fermi acceleration, inherently enhancing the acceleration efficiency.

Shock waves represent propagating disturbances that travel faster than the local sound speed, resulting in abrupt changes in macroscopic variables such as density, pressure, and velocity. They are a physical realization of a mathematical discontinuity, *i.e.*, sharp transitions in macroscopic quantities achieved over microscopic distances. The key idea behind diffusive shock acceleration is that if particles can be scattered repeatedly across the shock front, they will undergo a sequence of head-on collisions. This iterative process allows the particles to gain energy efficiently.

Consider an infinite one-dimensional shock front propagating along the $\hat{z}$ direction. In the shock front frame, the unshocked plasma (referred to as the "upstream") moves towards the shock with velocity u_1 from $z = -\infty$. At the shock location, the gas is compressed, heated and slowed down to velocity u_2. As the plasma crosses the shock into the "downstream" region, most of the particles lose a significant portion of their kinetic energy to internal motion, resulting in a temperature increase downstream. However, a few particles, those at the tail of the thermal distribution with a Larmor radius larger than the shock thickness, may cross the shock if they are moving in a favorable direction, thus initiating the acceleration process. An analysis analogous to the one for second-order Fermi acceleration allows us to derive the energy gain per cycle in this mechanism:

$$\left\langle \frac{\Delta E}{E} \right\rangle \approx \frac{4}{3}(u_1 - u_2)\,. \tag{1-33}$$

A schematic picture of the Fermi acceleration mechanisms is shown in Figure. 1.12.

The spectrum of particles accelerated by the Fermi process can be obtained by solving the transport equation (Eq. 1-28), but here we will focus on the key features. The most important property of diffusive shock acceleration is that it accelerates particles into a power-law spectrum potentially spanning an unlimited range of energy that does not depend on the specifics of particle

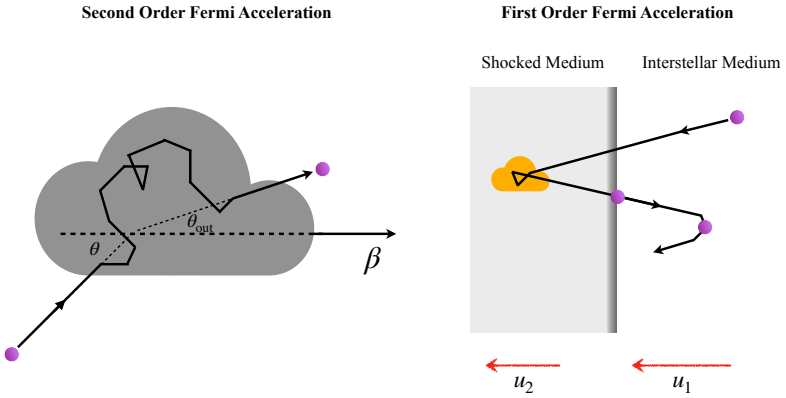

Figure 1.12: Schematic picture of diffusive shock acceleration (First order Fermi acceleration) in the right panel and second order Fermi acceleration in the left panel.

scattering. Bell (162) demonstrated this elegantly. Let us consider N_0 test particles with initial energy E_0 injected into a generic acceleration mechanism. Define $G = \Delta E/E$ as the fractional energy gain per cycle, and $1 - P$ as the probability that a particle leaves the accelerator after each cycle. After one cycle, $N_0 P$ particles will have energy GE_0. After k cycles, the number of particles will be $N_k = N_0 P^k$ and their energy will be $E_k = E_0 G^k$. By eliminating $k = \ln(N_k/N_0)/\ln P = \ln(E_k/E_0)/\ln G$, we arrive at

$$N_k = N_0 \left(\frac{E_k}{E_0}\right)^{-Q}, \tag{1-34}$$

where $Q \equiv -\ln P/\ln G$.

Supernova Remnants (SNRs) are believed to be the primary astrophysical sources responsible for the acceleration of galactic CRs via the first-order Fermi mechanism. Among extragalactic sources, radio-loud and jetted Active Galactic Nuclei (AGNs) provide multiple sites for efficient particle acceleration. These include regions near the black hole (e.g., "vacuum" gaps), the inner (pc-scale) and outer (kpc-scale) jets, the jet termination shock ("hot spots") in powerful sources, the back-flowing region, and the jet-inflated lobes (see, e.g., Figure 1.13). In these environments, a range of acceleration mechanisms can be active, including both first- and second-order Fermi acceleration.

A distinct mechanism for CR acceleration is categorized as "one-shot" mechanism. In this mechanism the particle's acceleration occurs predominantly in a single event rather than through repeated cycles. Astrophysical sources with strong magnetic fields, such as pulsars, provide necessary condition for this single-event process. Neutron stars exhibit extremely strong surface

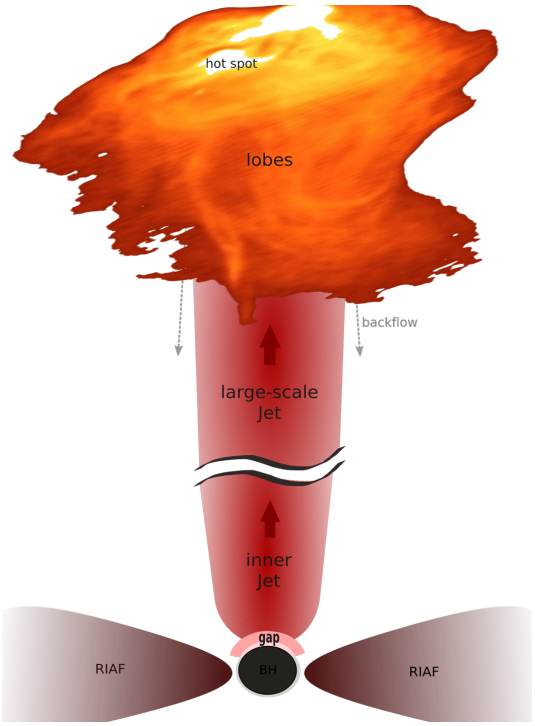

Figure 1.13: Schematic representation of a radio galaxy or jetted AGN, highlighting potential sites for cosmic particle acceleration. These include the black hole vicinity (gaps), the inner and outer jets, the jet termination shock (hot spot), the back-flow region, and the large-scale lobes. The dominant acceleration mechanism varies across these regions, depending on the local conditions. Figure from (13).

magnetic fields ($\mathcal{O}(10^{12})$ G) confined within small radii (a few kilometers) and rotate rapidly ($\mathcal{O}(10)$ s^{-1}). These conditions create a powerful induced electric field between the equator and the pole, capable of accelerating nuclei to high energies in a single event. Another site for this mechanism to occur is near supermassive black holes (SMBHs) under conditions of very low accretion rates, where an advection-dominated accretion flow (ADAF) forms. In such systems, relativistic electrons emit soft gamma rays via Bremsstrahlung, and some MeV photons interact to produce electron-positron pairs in the magnetosphere. Normally, these pairs screen electric fields along magnetic field lines. However, when the accretion rate is sufficiently low, the pair density becomes inadequate to fully screen the fields. This results in a charge-starved magnetosphere where an electric field arises along the magnetic field lines, enabling the acceleration of charged particles.

There is much to be discussed regarding acceleration mechanisms, various models, and their consistency with observations across different astrophysical sources. However, such discussions are beyond the scope of this dissertation. For a comprehensive review, the reader is referred to works such as (13, 164, 165).

The remainder of our discussion on CRs will form the core of this thesis. In the next section, I will examine the energy loss processes of CRs, both within and outside astrophysical sources. These processes not only influence CR acceleration and propagation but also offer a unique avenue for studying them through the detection and analysis of other standard model particles.

1.3.6 Cosmic Ray Energy loss and Multi-Messenger Approach

To this point, we have discussed the CR propagation using a statistical approach, with the Boltzmann-Vlasov equation serving as the foundation for modeling it. In this approach, electromagnetic inhomogeneities and magnetic irregularities are encapsulated within the *collisionless* term of the equation, giving rise to spatial and momentum diffusion.

That said, *collisional* effects, the right-hand side of the Boltzmann-Vlasov equation, are far from negligible. They determine fundamental properties such as the maximum energy CRs can attain, $E_{\max}$, as well as their spectral shape and chemical composition. Additionally, collisional interactions of CRs produce γ-rays and neutrinos. Unlike charged cosmic rays, photons and neutrinos are unaffected by electromagnetic deflection, making them valuable probes for studying CR acceleration and propagation.

Before delving into CR interactions, it is essential to establish the key quantities of an interaction that underpin our analysis. Among these are the kinematic parameters of an interaction e.g. Mandelstam variables, *total cross section*, σ, *differential cross section with respect to energy*, $\mathrm{d}\sigma/\mathrm{d}E_{\mathrm{out}}$, *interaction length* or *mean free path*, λ, *optical depth*, τ, *stopping power*, $-\mathrm{d}E/\mathrm{d}x$ and *inelasticity*, η.

The total cross section of a process is a measure of the probability of that process occurring. It is a Lorentz-invariant quantity, making it a fundamental parameter in describing interactions. However, calculating the total cross section can be highly nontrivial, depending on the type of interaction. For a few QED processes, analytical calculations are possible. For most other QED processes, however, numerical methods become indispensable. This challenge is even greater for QCD processes. The fundamental theory describing strong interactions among quarks and gluons is only perturbatively applicable to high-momentum transfer processes, such as those studied at the LHC. In the processes of interests to us, however, quarks and gluons within nucleons are not resolved, and QCD enters a strongly coupled regime where perturbative methods fail. Instead, nuclear interactions can be effectively described using Yukawa theory, in which nucleons exchange strongly coupled, massive media-

tors (pions). This framework explains the short range and intensity of nuclear forces. Since the Yukawa interaction range is comparable to or smaller than the size of nuclei, nuclear cross sections, dominated by inelastic processes at energies above 1 GeV/nucleon, scale approximately with the geometric size of the nuclei. For nuclei with mass number A, the radius scales as $R \sim 1.2A^{1/3}$ fm, leading to cross sections proportional to $A^{2/3}$. Ultimately, the most reliable method for determining cross sections is the experimental measurement, followed by the development of empirical fitting functions to represent the data.

In $\mathrm{d}\sigma/\mathrm{d}E_{\mathrm{out}}$, the energy E_{out} denotes the energy of one of the outgoing particles from the process, typically the most energetic one. This quantity characterizes the energy distribution of the outgoing particle in the interaction.

The mean free path, or interaction length, quantifies the average distance a particle travels before undergoing an interaction with a particle from the surrounding target field. This quantity is inherently tied to the density of targets in the environment and their energy distribution, as these factors directly influence the probability of collisions. The corresponding collision rate, Γ, is similarly dependent on these conditions. For a target number density $\bar{n}$, a process with cross section σ, and a particle with velocity β, the mean free path and interaction rate can be expressed as:

$$\lambda \equiv \frac{1}{\bar{n}\sigma}\,, \tag{1-35}$$

and

$$\Gamma \equiv \bar{n}\beta\sigma = \frac{\beta}{\lambda}\,. \tag{1-36}$$

Having the energy spectrum of the target particles, $n(\epsilon) = \mathrm{d}N/\mathrm{d}^3X\mathrm{d}\epsilon$ (ϵ denotes the energy) the interaction length can be obtained as a function of the initial particle energy E by:

$$\lambda(E) = \frac{1}{\int \mathrm{d}\epsilon \int \mathrm{d}\mu\, P(\mu)\, n(\epsilon)\, \sigma(s)}\,, \tag{1-37}$$

where s is the squared CoM energy (Mandelstam variable s), and $P(\mu)$ is the flux factor as we discussed in Eq. 1-29.

The optical depth of a medium over a distance l represents the *expected* average number of interactions that a particle *could* undergo while traversing that distance, assuming that its energy and direction remain unchanged. Mathematically, it is expressed as:

$$\tau = l/\lambda\,. \tag{1-38}$$

In this context, the survival probability of the particle in the medium can be expressed as $e^{-\tau}$. Accordingly, the medium is considered optically *thick* if

$\tau \gg 1$ or optically *thin* if $\tau \sim 1$.

The stopping power, $-\mathrm{d}E/\mathrm{d}x$, quantifies the average energy lost by a particle per unit distance traveled. It is expressed as

$$-\frac{\mathrm{d}E}{\mathrm{d}x} = -\frac{1}{\beta}\frac{\mathrm{d}E}{\mathrm{d}t} = n\int \mathrm{d}W\, W \frac{\mathrm{d}\sigma}{\mathrm{d}W}\,, \tag{1-39}$$

where $W = E_{\mathrm{out}} - E_{\mathrm{in}}$ represents the *energy transferred* in an interaction with E_{in} denoting the energy of the incoming particle.

The inelasticity is defined as the fraction of the energy of the incoming leading particle ($E_{\mathrm{in}}^{(L)}$) that is transferred to an outgoing particle i ($E_{\mathrm{out}}^{(i)}$). The *leading particle* L is defined as the particle with the maximum energy in the Lab frame, i.e., $E_{\mathrm{in}}^{(L)} = \max_j\{E_{\mathrm{in}}^{(j)}\}$. This concept is particularly meaningful in the limit where $E_{\mathrm{in}}^{(L)} \gg E_{\mathrm{in}}^{(i)}$, and thus the inelasticity is most appropriately defined and interpreted in the Lab frame. We define the inelasticity of the outgoing i-th particle, $\eta^{(i)}$, as:

$$\eta^{(i)}(s) = \frac{1}{\sigma}\int_{E_{\mathrm{min}}}^{E_{\mathrm{max}}} \frac{E_{\mathrm{out}}^{(i)}}{E_{\mathrm{in}}^{(L)}} \frac{\mathrm{d}\sigma}{\mathrm{d}E_{\mathrm{out}}^{(i)}}\,\mathrm{d}E_{\mathrm{out}}^{(i)}\,, \tag{1-40}$$

where $\mathrm{d}\sigma/\mathrm{d}E_{\mathrm{out}}^{(i)}$ is the cross section of the process, differential with respect to the i-th outgoing particle energy and E_{min} and E_{max} represent the allowed energy range of the outgoing particle.

With the key quantities defined, we now focus on the energy loss mechanisms of CRs. In principle, CRs can lose energy through both elastic and inelastic collisions with target nuclei. However, the forward-peaking nature of elastic cross sections in CR kinematics results in negligible energy loss, so these processes are typically disregarded. That said, the extent to which they are negligible depends on the precision of the observations, a topic discussed in detail in Chapter 4 of this dissertation. Additionally, elastic interactions of nuclei with photons are also insignificant. This can be estimated as follows: For a nucleus of atomic number Z and atomic mass A (mass $m = Am_{\mathrm{amu}}$ and charge Ze), the cross section analogous to the Thomson cross section, σ_{T}, scales as $\sigma(m, Z) \propto Z^4 A^{-2}(m_e/m_{\mathrm{amu}})$. Numerically, this evaluates to approximately $\sigma(m, Z) \sim 3 \times 10^{-7}(Z^4/A^2)\sigma_{\mathrm{T}}$, rendering its contribution negligible.

Inelastic processes dominate the energy loss mechanisms for nuclear kinetic energies above a few hundred MeV per nucleon, and these will be the focus of the subsequent discussion.

Photohadronic interactions, particularly proton-photon ($p\gamma$) interactions, are among the most significant processes to consider specifically at the ultra-high energies of the cosmic rays. These processes can occur both inside astrophysical sources, where CRs interact with background photon fields, or during CR propagation through intergalactic space, where interactions with

the CMB or the EBL become relevant. Photohadronic interactions span a broad range of photon energies in the nucleus rest frame, ε'_γ, [11] where distinct physical processes dominate at different energy scales. At low energies, $\varepsilon'_\gamma \sim 1$ MeV, hadronic processes are suppressed, and energy losses occur primarily through electromagnetic mechanisms, such as *Bethe-Heitler pair production* of electron-positron pairs.

$$p + \gamma \to p + e^+ e^- \,. \tag{1-41}$$

The threshold energy for the Bethe-Heitler process is determined by the condition $s > (m_p + 2m_e)^2$. In the Lab frame, this condition translates to:

$$s = m_p^2 + 2\varepsilon_\gamma E_p(1-\mu) > (m_p + 2m_e)^2 \Rightarrow E_p \gtrsim \frac{m_p m_e}{\varepsilon_\gamma} \,, \tag{1-42}$$

where ε_γ is the photon energy, E_p is the proton energy, and μ is the scattering angle cosine in the Lab frame. For interactions with CMB photons, which have a typical energy of $\varepsilon_{\rm CMB} \approx 6.3 \times 10^{-4}$ eV, this condition implies a proton energy threshold of $E_p \gtrsim 2 \times 10^{18}$ eV.

At leading order, the Bethe-Heitler interaction involves three vertices in the corresponding Feynman diagram, which results in a cross section of order $\mathcal{O}(\alpha^3)$, where $\alpha = 1/137$ is the fine structure constant. A rough estimate of the Bethe-Heitler cross section at high energies is given by:

$$\sigma_{\rm B-H} \simeq \frac{\alpha^3 Z^2}{m_e^2} \left[\frac{28}{9} \ln\left(\frac{2\varepsilon'_\gamma}{m_e} \right) \right] \,. \tag{1-43}$$

Despite its relatively large cross section, the inelasticity of this process is small, approximately $2m_e/m_p \simeq 10^{-3}$, which limits the energy transfer to the produced electron-positron pair. For further details on the Bethe-Heitler process, the reader is referred to (166).

As the photon energy approaches the nuclear binding scale, $\varepsilon'_\gamma \sim 8$ MeV, the resonant motion of nucleons within the nucleus is triggered, leading to nuclear disintegration through the excitation of the Giant Dipole Resonance (GDR). Assuming a nucleus of atomic mass A,

$$A + \gamma \to (A-1) + n + \gamma \,, \tag{1-44}$$

$$A + \gamma \to (A-1) + p + \gamma \,, \tag{1-45}$$

are the predominant reactions. This process, known as *photodisintegration*, is widely modeled using parametrizations like those by Puget-Stecker-Bredekamp (PSB) (167, 168), or with nuclear event generators such as TALYS (169),

[11] I adopt the notation that quantities with a prime ($'$) refer to the nucleus rest frame, while unprimed quantities correspond to the Lab frame.

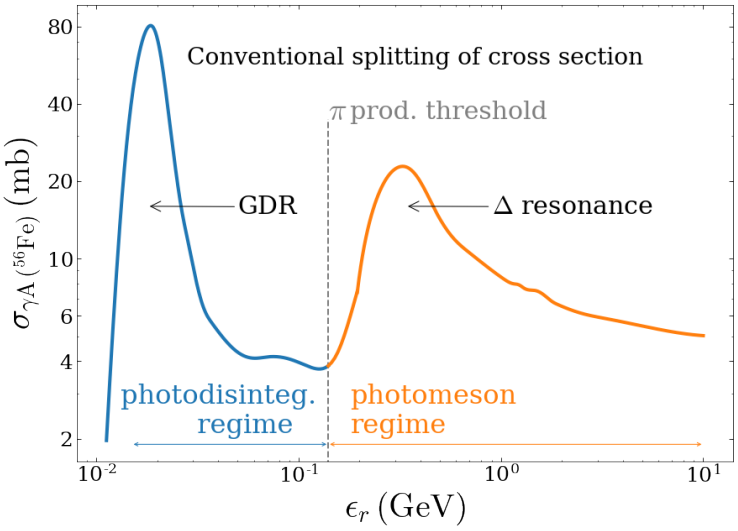

Figure 1.14: The total photodisintegration and photomeson cross section as a function of $\epsilon_r = \varepsilon'_\gamma$. Figure from (14).

GEANT4 (170), and FLUKA (15). Similar to Eq. 1-42, the photodisintegration threshold can be determined, with its value depending on the binding energy of the nucleus. For light nuclei, the threshold lies around $E_A \gtrsim 10^{19}$ eV, while for heavier nuclei, such as those in the iron group where the binding energy is higher, the threshold increases to approximately $E_A \gtrsim 10^{20}$ eV. Here, E_A denotes the total energy of the nucleus.

At higher photon energies, $\varepsilon'_\gamma \gtrsim 140$ MeV, hadronic processes dominate, giving rise to the excitation of baryonic resonances, such as the Δ-resonance. These resonances decay primarily into pions, marking the onset of significant hadronic energy losses:

$$p + \gamma \to \Delta^+ \to \begin{cases} p + \pi^0 & \frac{2}{3} \text{ of the times}, \\ n + \pi^+ & \frac{1}{3} \text{ of the times}, \end{cases} \tag{1-46}$$

As the photon energy increases further, the "multi-pion" production channel opens. The threshold for photopion production occurs at $E_A \gtrsim$ few $\times 10^{19}$ eV. The inelasticity of this process is approximately 0.2, meaning that the outgoing pions get almost 20% of the initial proton energy. As previously discussed, this interaction is responsible for the GZK cutoff in the UHECR spectrum. As an illustration, the photodisintegration and photomeson cross sections for the iron nucleus ($^{56}_{26}$Fe) are shown in Figure 1.14. For the most recent reassessment of these cross sections, refer to (14). The photohadronic interactions outlined in this section will play a central role in our analysis of the ionization states of CRs presented in Chapter 2.

The second significant process to consider is inelastic nucleus-nucleus interactions, which result in the production of both charged and neutral pions.

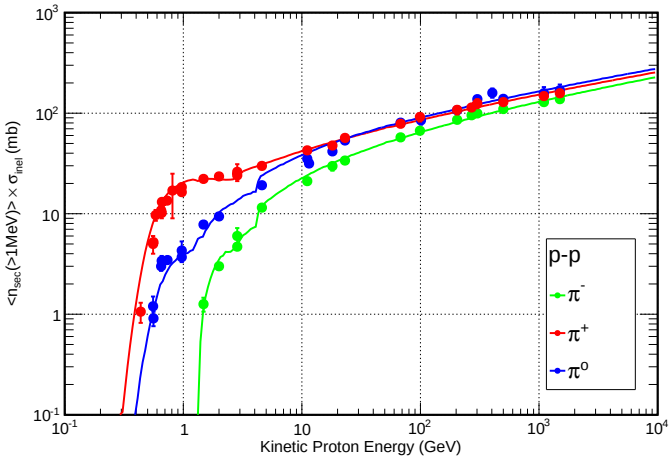

Figure 1.15: Inclusive cross sections for the production of π^0 (blue), π^+ (red) and π^- (green) in pp collision as function of the incoming proton kinetic energy, K_p. Lines from (15). Data points from (16). Figure from (15).

The predominant among the CRs and also the simplest of these is the proton-proton (pp) inelastic interaction:

$$p + p \rightarrow X + \pi^{\pm,0}\,. \tag{1-47}$$

Here, X represents the outgoing hadronic products, which depend on the specific interaction channel. The dominant channels include $X = p + p$ producing π^0, $X = p+n$ or $X = d$ (deutron) producing π^+ and $X = p+p+\pi^+$ producing π^-. The threshold kinetic energy for the projectile proton varies slightly across the channels but is approximately 300 MeV. For instance, in the case of π^0 production

$$s = 2m_p^2 + 2(K_p + m_p)m_p \geq (2m_p + m_{\pi^0})^2 \Rightarrow K_p \gtrsim 290 \text{ MeV}\,, \tag{1-48}$$

where K_p denotes the proton kinetic energy.

Figure 1.15 presents the cross sections for specified channels involved in pp inelastic interactions. At high energies, the production of charged and neutral pions occurs with approximately equal probabilities ($\sim 1/3$) due to isospin symmetry, as reflected in the lines shown in Figure 1.15. The energy-loss rate for a CR nucleus with mass number A, attributed to pion production, can be expressed using the updated parameterizations of pion production cross sections (171, 172) as:

$$-\left(\frac{\mathrm{d}E_A}{\mathrm{d}t}\right) = 3.85\times10^{-16}A^{0.79}\left(\frac{n_{\mathrm{gas}}}{\mathrm{cm}^{-3}}\right)\left(\frac{E_A}{\mathrm{GeV}}\right)^{1.28}\left(\frac{E_A}{\mathrm{GeV}}+200\right)^{-0.2}\ \mathrm{GeV.s}^{-1}\,. \tag{1-49}$$

This formulation encapsulates the dependence of the energy-loss rate on the density of the ambient gas $n_{\rm gas}$ and the CR total energy E_A.

For kinetic energies per nucleon below $K_p \simeq 290$ MeV spallation becomes the dominant inelastic process, leading to the fragmentation of the target and/or projectile nuclei into multiple nucleons or nuclear fragments. As discussed previously, these reactions are the primary origin of light nuclei such as Li, Be, and B. Given the scarce data on nuclear reactions, it is common practice to use semi-empirical methods to obtain the spallation cross sections. These are typically derived by interpolating within the measured region and extrapolating beyond it. The most recent libraries and models for these cross sections are available in CR propagation codes, such as those in (173, 174).

It is important to emphasize that photohadronic processes are the dominant and most relevant energy-loss mechanisms for extragalactic and UHECRs, as their energy thresholds are in the ultra-high-energy regime and their interaction lengths typically exceed galactic scales. In contrast, spallation and pion production (pp) processes are key to understanding galactic CRs.

Another important energy-loss mechanism for CRs is the electrostatic interaction with electrons in the interstellar medium (ISM). The ISM consists of electrons distributed across atomic, molecular, and ionized hydrogen and helium gas, with traces of heavier elements and dust grains. While the electron number density in the ISM is low, about ~ 1 cm^{-3}, the vast propagation distances and long timescales involved make this process non-negligible for CR energy losses. The energy loss can be described by Rutherford scattering, the classical elastic scattering of charged particles via the Coulomb interaction, where the center of potential of charge Z does not recoil.

The stopping power for this interaction is given by (175):

$$-\frac{{\rm d}E}{{\rm d}x} \simeq \frac{4\pi n_e Z^2 \alpha^2}{m_e \beta^2} L\,, \tag{1-50}$$

where Z is the projectile (nucleus) charge, β is the projectile velocity and L is known as the "Coulomb logarithm" given by

$$L = L_0 + \Delta L = \ln\left(\frac{2 m_e \beta^2 \gamma^2}{I}\right) - \beta^2 + \Delta L\,, \tag{1-51}$$

where γ is the Lorentz factor of the CR and I represents the mean excitation potential of the medium. The leading term L_0 in L corresponds to the *Bethe stopping power*, which typically provides a sufficient description of CR energy losses in the ISM. However, higher-order corrections encapsulated in ΔL account for effects related to the medium's structure and the projectile's detailed behavior (176). In Chapter 4, we will further examine the impact of these corrections on CR energy losses.

As discussed in this section, the energy-loss processes of CRs can lead to pion production. However, this is not the end of the process. The produced pions decay into photons, muons, neutrinos, with muons further decaying into neutrinos and electrons as follows:

$$\pi^0 \to 2\gamma\,, \tag{1-52}$$

$$\pi^+ \to \mu^+ + \nu_\mu\,, \tag{1-53}$$

$$\pi^- \to \mu^- + \bar{\nu}_\mu\,, \tag{1-54}$$

$$\mu^+ \to e^+ + \nu_e + \bar{\nu}_\mu\,, \tag{1-55}$$

$$\mu^- \to e^- + \bar{\nu}_e + \nu_\mu\,. \tag{1-56}$$

As a result, diffuse neutrino and gamma ray spectra are expected to emerge from CR propagation. Moreover, as we will discuss further in Chapters 2 and 3, the same processes responsible for neutrino and gamma ray production during CR propagation over cosmological distances can also occur within astrophysical sources, albeit in a different energy range. Consequently, in astroparticle physics, neutrinos produced during CR propagation are commonly referred to as *cosmogenic neutrinos*, while those originating from astrophysical sources are termed *astrophysical neutrinos*. In this dissertation, since the production site is explicitly specified in each case, we do not strictly adhere to this terminology and mostly the observed neutrinos by the neutrino telescopes are called "astrophysical neutrinos".

Neutrinos, being electrically neutral and having extremely small interaction cross sections with other Standard Model particles, travel directly to Earth. The details of the neutrino propagation will be discussed in Section 1.4. On the other hand, gamma ray propagation over cosmological distances is far more intricate, as we mentioned earlier. This subject will be explored in detail in Section 1.5.

Before going further, it is valuable to analyze the energy budget relationship between neutrinos and gamma rays in pion production.

1.3.6.1 $\nu - \gamma$ Connection in Hadronic processes

In charged pion decays, approximately 3/4 of the pion's energy is transferred to the resulting muon, which then shares this energy almost evenly among its decay products. Consequently, each neutrino produced in a charged pion decay carries, on average, one-quarter of the pion's energy: $E_\nu \approx \frac{1}{4} E_{\pi^\pm}$.

For neutral pion decay, the energy is—on average—split equally between two photons, resulting in $E_\gamma = \frac{1}{2}E_{\pi^0}$. Thus, neutrinos from hadronic processes are typically emitted with half the energy of the corresponding photons, assuming similar energies for the parent pions: $E_\nu \approx \frac{1}{2}E_\gamma$. This relationship holds for both pp and $p\gamma$ interactions. Furthermore, charged pions decay into three neutrinos, while neutral pions decay into two photons. This leads to a ratio between the number of emitted neutrinos and photons, given by $3K_\pi/2$, where K_π is the ratio of charged to neutral pions produced in the interaction.

The distribution of energy among pions is shaped by the interaction kinematics and inelasticity. In $p\gamma$ interactions, pions—whether π^0 or $\pi^\pm$—typically capture about 1/2 of the proton's energy, while in pp interactions, each pion receives roughly 1/3 of the proton's energy. Thus, the neutral pion and the charged pion are of similar energy scales in either scenario.

Thus, a roughly estimated connection can be established between the neutrino and gamma ray spectra in hadronic processes:

$$E_\gamma \frac{\mathrm{d}N_\gamma}{\mathrm{d}E_\gamma} \approx \frac{1}{3K_\pi}\left[E_\nu \frac{\mathrm{d}N_\nu}{\mathrm{d}E_\nu}\right]_{E_\nu = E_\gamma/2}, \tag{1-57}$$

where $E\,\mathrm{d}N/\mathrm{d}E$ represents the energy spectrum of the specified species, $K_\pi \approx 1/2$ for $p\gamma$ interactions and $K_\pi \approx 1$ for pp interactions.

It is also important to note that current neutrino telescopes, such as IceCube, cannot distinguish between neutrinos and antineutrinos but can identify neutrino flavors. The flavor composition of neutrinos generated in hadronic processes is approximately $(\nu_e : \nu_\mu : \nu_\tau) = (1 : 2 : 0)$. This flavor composition is different at the detection site, because of the neutrino decoherent oscillation as we will outline in the next section.

1.4 Neutrinos

Neutrinos are among the most abundant particles in the Universe, outnumbering electrons and protons by roughly a billion to one. Within the framework of the Standard Model (SM), neutrinos are massless particles interacting exclusively via weak interactions, mediated either by the exchange of a Z boson (neutral current (NC) interactions) or $W^\pm$ bosons (charged current (CC) interactions). The neutrino states involved in these weak interactions are the *flavor* states, corresponding to the electron, muon, and tau flavors. As previously noted, neutrinos traverse the Universe unimpeded, without interacting with the intergalactic or galactic medium, making their propagation from distant sources to Earth remarkably straightforward compared to other cosmic messengers. This makes them excellent messengers for pinpointing the direction

of astrophysical sources and providing valuable insights into their underlying mechanisms. However, their ability to travel vast cosmological distances also makes their detection on Earth exceptionally challenging. Even cubic kilometer neutrino telescopes, such as IceCube, have rather large uncertainties in reconstructing the direction and energy of neutrino events.

In this section, we outline the astrophysical neutrino propagation and their spectrum detected by IceCube, without delving into the specifics of the detection process, event reconstruction methods, or datasets. These details are beyond the scope of this dissertation and are not essential for most of the discussions herein. Readers interested in these aspects can refer to IceCube collaboration publications, such as (19).

1.4.1 IceCube Observation of Astrophysical Neutrinos

The IceCube Neutrino Observatory has firmly established the existence of high-energy astrophysical neutrinos. Key measurements contributing to this discovery include *through-going muon tracks* from the northern sky (177, 178), *high-energy starting events (HESE)* with interaction vertices contained within the detector's fiducial volume (179, 180, 181, 182), and lower-energy events analyzed using contained cascades (183, 184). Together, these data sets have enabled robust characterization of the astrophysical neutrino flux.

Three fundamental assumptions underpin the analysis of the astrophysical neutrino flux: *(i)* the flux is isotropic at Earth, *(ii)* neutrinos and anti-neutrinos have identical fluxes, and *(iii)* all neutrino flavors contribute equally to the flux. An isotropic distribution is expected if the dominant contributions originate from distant sources (extragalactic sources). Additionally, IceCube's insensitivity to distinguishing neutrinos from anti-neutrinos ensures that any differences in their fluxes minimally affect event detection analysis across most energies. A notable exception occurs near 6.3 PeV, where electron anti-neutrinos can undergo resonant interactions with atomic electrons, known as the Glashow Resonance (GR) (185, 186).

In fact, the observed data also suggest that the arrival directions of astrophysical neutrinos are predominantly (quasi-)isotropic, with a subtle inclination toward the Galactic Center and an approximately equal contribution from all three neutrino flavors (187). Notably, IceCube has recently identified neutrino emission originating from the Galactic plane, achieving a significance level of 4.5σ through the application of advanced machine learning techniques to a decade of observational data (188).

Astrophysical neutrino flux models are often based on power-law spectra,

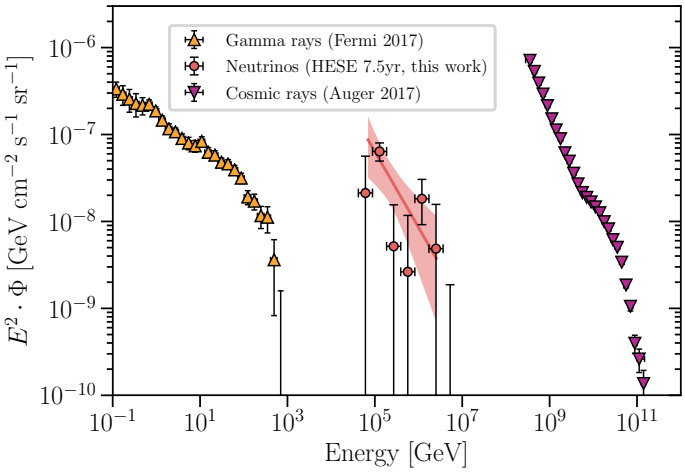

Figure 1.16: High-energy fluxes of gamma rays, neutrinos, and CRs. The high-energy gamma ray measurements by Fermi (17) are shown in orange, while the ultra-high energy cosmic ray measurements by the PAO (18) are shown as purple data points. Figure from (19)

reflecting the potential connection between astrophysical neutrinos and CRs, which themselves exhibit a power-law energy distribution at Earth. The latest IceCube analysis (19) favors the astrophysical neutrino flux with a *single power-law* form:

$$\Phi_\nu = \Phi_{\text{astro}} \left(\frac{E_\nu}{100 \text{ TeV}} \right)^{\gamma_{\text{astro}}} \times 10^{-18} \, [\text{GeV}^{-1} \text{ cm}^{-2} \text{ s}^{-1} \text{ sr}^{-1}] \,, \qquad (1\text{-}58)$$

where $\Phi_{\text{astro}} = 6.45^{+1.46}_{-0.46}$ is the normalization factor, and $\gamma_{\text{astro}} = 2.89^{+0.2}_{-0.19}$ is the spectral index. The high-energy fluxes of astrophysical neutrinos and its best fit, Eq. 1-58, gamma ray and CRs are illustrated together in Figure. 1.16.

In the search for astrophysical neutrino sources, IceCube has so far been able to identify only two point sources: the blazar TXS 0506+056, for which evidence of neutrino emission has been reported (189, 190), and the starburst galaxy NGC 1068, which shows a 4.2σ excess of events (191, 192). However, these two sources together contribute only about 1% of the astrophysical neutrino flux above 200 TeV (191), leaving the vast majority of the observed flux without a confirmed origin (193, 194, 195).

1.4.2 Neutrino Propagation

The only significant effect on neutrinos energy—and by extension, their spectrum— during their propagation to Earth is the cosmological redshift: a neutrino emitted with energy E_ν at a source located at redshift z reaches

Earth with an energy $\varepsilon_\nu = E_\nu/(1+z)$. Considering a source emitting a neutrino spectrum $\frac{\mathrm{d}N_\nu}{\mathrm{d}E_\nu}(E_\nu)$, in units of $[\mathrm{GeV}^{-1}.\mathrm{s}^{-1}]$, the corresponding neutrino flux at the Earth, in units of $[\mathrm{GeV}.\mathrm{cm}^{-2}.\mathrm{s}^{-1}]$, is given by

$$\varepsilon_\nu^2 \Phi(\varepsilon_\nu) = \frac{\left[E_\nu^2 \frac{\mathrm{d}N_\nu}{\mathrm{d}E_\nu}(E_\nu)\right]_{E_\nu=(1+z)\varepsilon_\nu}}{(1+z)^2 4\pi d_c^2}\,, \tag{1-59}$$

where d_c is the comoving distance from the source.

While their energy evolves as discussed, the flavor composition of neutrinos can undergo a "transition" during propagation due to neutrino oscillations. These oscillations, driven by the quantum mechanical mixing of mass eigenstates, become particularly relevant when considering the flavor ratios of neutrinos detected on Earth. In the wave-packet approach, mass eigenstates propagate at slightly different velocities. Over large distances, their wave packets separate, eliminating any interference. This loss of quantum interference—called "decoherence"—occurs once the spatial separation of the mass–eigenstate wave packets exceeds their intrinsic size, so the wave packets no longer overlap. The coherence length, determined by the wave-packet size, neutrino energy, and the neutrino mass differences, is small compared to the cosmological distances that astrophysical neutrinos travel. As a result, they arrive at Earth as an incoherent superposition of mass eigenstates (196).

In the standard theory of neutrino oscillations (197, 198, 199) a neutrino with flavor α and momentum $\vec{p}$, created in a charged-current weak interaction process from a charged lepton ℓ_α^- or together with a charged antilepton ℓ_α^+, is described by the flavor state. While neutrinos interact as flavor eigenstates, ν_α, they propagate as mass eigenstates, ν_i $(i = 1, 2, 3)$. The two representations are related by the Pontecorvo–Maki–Nakagawa–Sakata (PMNS) matrix, expressed as

$$|\nu_\alpha\rangle = \sum_{i=1}^{3} U_{\alpha i}^* |\nu_i\rangle\,, \tag{1-60}$$

where $U_{\alpha i}$ denotes the elements of the PMNS matrix.

The massive neutrino states $|\nu_i\rangle$, being eigenstates of the Hamiltonian, evolve in time as plane waves. Consequently, a pure flavor state $|\nu_\alpha(t)\rangle$, at $t = 0$, becomes a superposition of different flavor states at later times $(t > 0)$, provided that the mixing matrix U is not diagonal, indicating neutrino mixing. The probability of a neutrino transition from an initial flavor ν_α to a different flavor ν_β after traveling a distance L is expressed as:

$$P_{\nu_\alpha \to \nu_\beta}(L,E) = \sum_{i,j}(U^*_{\alpha i}U_{\beta i}U_{\alpha j}U^*_{\beta j}) \exp\left(-i\frac{\Delta m^2_{ij}L}{2E}\right)$$
$$= \sum_i |U_{\alpha i}|^2|U_{\beta i}|^2 + 2\,\mathrm{Re}\sum_{i>j}(U^*_{\alpha i}U_{\beta i}U_{\alpha j}U^*_{\beta j}) \exp\left(-i\frac{\Delta m^2_{ij}L}{2E}\right), \tag{1-61}$$

where $\Delta m^2_{ij} = m^2_i - m^2_j$ is the mass-squared difference between neutrino states, E is the neutrino energy and L is the propagation length. The oscillatory behavior in Eq. 1-61 arises from interference among the components of the massive neutrino states, making the oscillation term highly sensitive to the coherence of these components. When the propagation distance L becomes very large, the oscillatory term averages out to zero due to decoherence. In this case, the transition probability simplifies to:

$$\langle P_{\nu_\alpha \to \nu_\beta}(L,E)\rangle = \sum_i |U_{\alpha i}|^2|U_{\beta i}|^2\,. \tag{1-62}$$

The PMNS matrix is parametrized in terms of three mixing angles, $(\theta_{12}, \theta_{23}, \theta_{13})$, as well as one CP-violating phase δ_{CP}, assuming that neutrinos are Dirac fermions[12]:

$$U = \begin{pmatrix} c_{12}c_{13} & s_{12}c_{13} & s_{13}e^{-i\delta_{\mathrm{CP}}} \\ -s_{12}c_{23} - c_{12}s_{23}s_{13}e^{i\delta_{\mathrm{CP}}} & c_{12}c_{23} - s_{12}s_{23}s_{13}e^{i\delta_{\mathrm{CP}}} & s_{23}c_{13} \\ s_{12}s_{23} - c_{12}c_{23}s_{13}e^{i\delta_{\mathrm{CP}}} & -c_{12}s_{23} - s_{12}c_{23}s_{13}e^{i\delta_{\mathrm{CP}}} & c_{23}c_{13} \end{pmatrix}, \tag{1-63}$$

where $c_{ij}(s_{ij})$ is the shorthand for $\cos\theta_{ij}(\sin\theta_{ij})$. The most recent best-fit values for the PMNS matrix parameters are given in Table. 1.1 [13].

Using these fit parameters to evaluate the elements of the PMNS matrix, we find that, for example, a source flavor ratio of $(\nu_e : \nu_\mu : \nu_\tau)_S = (1,2,0)$ results in a flavor ratio at Earth equal to $(\nu_e : \nu_\mu : \nu_\tau)_\odot = (1,1,1)$. Therefore, the neutrino flux per flavor at Earth is one-third of the total all-flavor neutrino flux typically discussed throughout this dissertation.

Next, we turn to γ-ray propagation, which is considerably more complex than neutrino propagation. However, when carefully studied, it can offer valuable insights into CR propagation both inside and outside astrophysical sources. High-energy photons undergo various interactions on their journey to

[12]If the neutrinos are instead *Majorana* fermions, the mixing matrix contains two additional, so-called Majorana phases. Because these phases appear in the mixing matrix as a mutiplicative diagonal matrix, they do not affect the oscillation probabilities. However, their physical impact is restricted to lepton-number–violating observables such as neutrinoless double-beta decay

[13]http://www.nu-fit.org

Parameter	Best-Fit Value $\pm 1\sigma$
θ_{12} (deg)	$33.68^{+0.73}_{-0.70}$
θ_{13} (deg)	$8.52^{+0.11}_{-0.11}$
θ_{23} (deg)	$48.5^{+0.7}_{-0.9}$
δ_{CP} (deg)	177^{+19}_{-20}

Table 1.1: Best-fit parameter values for the PMNS matrix. The fit assumes normal ordering for the neutrino masses ($m_1 < m_2 < m_3$) and includes data from solar, reactor, accelerator and atmospheric (including Super-Kamiokande) neutrino experiments (32).

Earth, triggering "electromagnetic cascades", a topic we will explore in detail in the next section and a major focus of this thesis.

1.5 Electromagnetic Cascade

High-energy γ-rays, such as those produced by CR propagation and their associated energy-loss mechanisms, are expected to be abundant. Yet, as shown in Figure 1.1, these photons have not been observed directly. This absence becomes less surprising when we consider that γ-rays are known to interact with intergalactic/galactic radiations during their journey to Earth, as illustrated in Figure 1.5. These three pieces of evidence raise a critical question: what mechanism governs the transformation or absorption of these high-energy photons during propagation?

The answer lies in *electromagnetic cascades*, a process triggered by interactions between high-energy photons or electrons and low-energy background photons, such as those from the CMB and EBL. These cascades were first conceptualized shortly after the discovery of the CMB (200) and the GZK cutoff (121, 122). Early hints of this mechanism were presented during the Soviet-Union Cosmic Ray Conference by I.L. Rozental and independently by S. Hayakawa, as later recalled by V. Berezinsky and K. Sato (201). The first comprehensive study of electromagnetic cascades appeared in (202), where they were proposed it as a handle to probe *cosmogenic* neutrinos (neutrinos from the GZK process (203)). Since then, these electromagnetic cascades in the extragalactic space has found numerous applications in the astrophysical studies.

A simple electromagnetic cascade can be described as follows: Starting with a high energy photon propagating in the intergalactic medium, the cascade begins with the high-energy photon interacting with a background

photon via electron pair production (EPP: $\gamma+\gamma_{\rm b} \to e^-+e^+$). Each electron and positron created in this interaction then engages in inverse Compton scattering process with $\gamma_{\rm b}$ (ICS: $e+\gamma_{\rm b} \to e+\gamma$), sending the background photons to high energy levels. At high energies, a large fraction of the incident particle's energy (i.e. the photon in EPP and the electron or positron in ICS) is transferred to one of the resultant particles (either the electron or positron in the EPP and the photon in the ICS). Consequently, after a cycle of EPP and ICS, a photon with energy nearly equal to that of the initial high-energy photon re-emerges. This process can iterate multiple times, resulting in successive cycles of EPP and ICS (EPP+ICS+EPP+...), developing the cascade, until the upscattered photons no longer have enough energy to produce pairs on the background photons. Conversely, starting with a high energy electron/positron, the above scenario remains viable after one step of ICS. As a result, the cascade has transferred the energy of the initial photon into many photons of much lower energy in the X-rays and gamma rays band with energies of $\lesssim$ GeV.

However, the electromagnetic cascade is not always this simple. Depending on the presence of magnetic fields and/or the initial energy of the injected photon or electron, the cascade development can be much more complex. For instance, in the presence of a sufficiently strong magnetic field in the IGM, a portion of the cascade energy may be emitted as synchrotron radiation. Additionally, depending on the energy, there are other possible $\gamma\gamma_{\rm b}$ and $e\gamma_{\rm b}$ interactions, which can alter our simple picture partially or entirely. Of course a close scrutiny of the cascade development needs a comprehensive assessment of all the potential processes, their cross sections and inelasticities together with the knowledge about the intergalactic magnetic fields and the background photon fields which we will partly discuss here, with further details deferred to Chapter 3.

1.5.1 Electron Pair Production (EPP)

The total and differential cross sections of EPP (also dubbed Breit-Wheeler process (204)) are respectively (205)

$$\sigma_{\rm EPP} = \sigma_{\rm T}\,\frac{3}{16}(1-\beta^2)\left[(3-\beta^4)\ln\frac{1+\beta}{1-\beta} - 2\beta(2-\beta^2)\right], \tag{1-64}$$

and

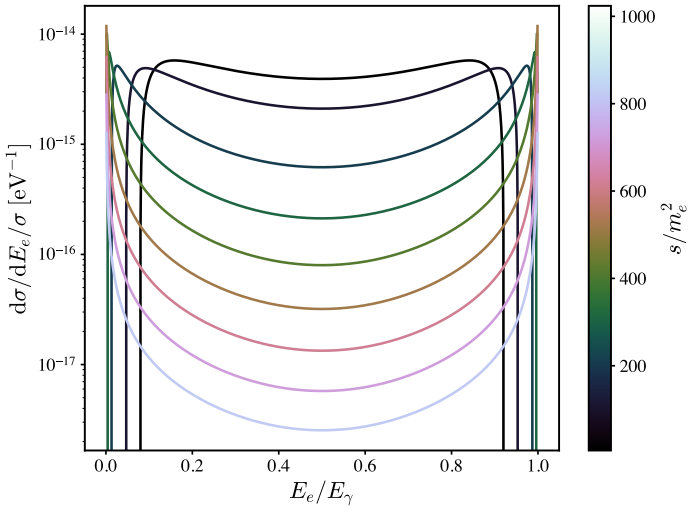

Figure 1.17: Energy distribution of the outgoing $e^{\pm}$ in EPP.

$$\frac{\mathrm{d}\sigma_{\mathrm{EPP}}}{\mathrm{d}E_e} = \sigma_{\mathrm{T}}\frac{3}{4}\frac{m_e^2}{s}\frac{1}{E_\gamma}\left[\frac{E_e}{E_\gamma - E_e} + \frac{E_\gamma - E_e}{E_e} + E_\gamma\left(1-\beta^2\right)\left(\frac{1}{E_e} + \frac{1}{E_\gamma - E_e}\right) - \frac{E_\gamma^2\left(1-\beta^2\right)^2}{4}\left(\frac{1}{E_e} + \frac{1}{E_\gamma - E_e}\right)^2\right], \quad (1\text{-}65)$$

where m_e is the electron mass, $\sigma_T = 8\pi\alpha^2/(3m_e^2) = 0.665$ b is the Thomson cross section, $\beta = \sqrt{1-4m_e^2/s}$ is the velocity of outgoing electron in the CoM frame, $s = 2E_\gamma\epsilon(1-\mu)$ is the CoM energy squared, ϵ and E_γ are respectively the energies of the target and high energy photons, μ is the cosine of the angle between the momenta of the incoming photons, and E_e is the energy of the produced electron (or positron) whose allowed range is $(1-\beta)/2 \leq E_e/E_\gamma \leq (1+\beta)/2$.

The threshold energy for EPP derives from the condition $s = 4m_e^2$, Thus for a monochrome target photon of energy ϵ, we obtain $E_\gamma \gtrsim m_e^2/\epsilon$.

The inelasticity of an interaction is defined in Eq. 1-40. For electron pair production (EPP), the energy range of the outgoing electron/positron are given by $E_{\mathrm{min}} = E_\gamma(1-\beta)/2$ and $E_{\mathrm{max}} = E_\gamma(1+\beta)/2$. It is important to note that, intuitively, Eq. 1-40 represents the average fraction of energy, $E_{\mathrm{out}}^{(i)}/E_{\mathrm{in}}^{(L)}$, carried by the outgoing particle. However, in EPP, the indistinguishability of the electron and positron imposes a symmetry, suggesting $\eta_{\mathrm{EPP}} = 0.5$. Yet, this inelasticity value contradicts the behavior inferred from the differential cross section, $\mathrm{d}\sigma_{\mathrm{EPP}}/\mathrm{d}E_e$: Close to the threshold, $\mathrm{d}\sigma_{\mathrm{EPP}}/\mathrm{d}E_e$ is approximately flat, but at high energies, it develops sharp peaks at $E_e = E_\gamma(1\pm\beta)/2$ (see Figure. 1.17). This indicates that at high energies, one of the particles—the

"leading" particle—takes most of the energy ($E_{\max} = E_\gamma(1+\beta)/2$), while the other carries the remaining energy, $E_\gamma - E_{\max} = E_\gamma(1-\beta)/2$. As a result, the actual inelasticity is expected to exceed 50%. The underlying issue stems from the indistinguishability of the outgoing particles in EPP, which imposes symmetry in the differential cross section (energy distribution). To address this, the integration limits must be adjusted to capture only the leading particle's contribution, resulting in the corrected expression for EPP inelasticity:

$$\eta_{\rm EPP}(s) = 2 \times \frac{1}{\sigma_{\rm EPP}(s)} \int_{E_\gamma/2}^{E_\gamma(1+\beta)/2} {\rm d}E_e \, \frac{E_e}{E_\gamma} \, \frac{{\rm d}\sigma_{\rm EPP}}{{\rm d}E_e}(E_e, s) \ . \tag{1-66}$$

At high energies, $E_\gamma \gg m_e^2/\epsilon$, this inelasticity behaves as

$$\eta_{\rm EPP} \simeq 1 - [\ln(2E_\gamma\epsilon/m_e^2)]^{-1} \, , \tag{1-67}$$

while close to the threshold $\eta_{\rm EPP} \approx 0.5$.

1.5.2 Inverse Compton Scattering (ICS)

The total cross section for ICS is given by the well-known Klein-Nishina formula:

$$\sigma_{\rm ICS} = \sigma_{\rm T} \, \frac{3}{8} \, \frac{m_e^2}{s\beta} \left[\frac{2}{\beta(1+\beta)} (2 + 2\beta - \beta^2 - 2\beta^3) \right. \\ \left. - \frac{1}{\beta^2} (2 - 3\beta^2 - \beta^3) \ln \frac{1+\beta}{1-\beta} \right] \ , \tag{1-68}$$

where $\beta = (s - m_e^2)/(s + m_e^2)$ represents the velocity of the outgoing electron in the CoM frame and $s = m_e^2 + 2\epsilon(E_e - \mu\sqrt{E_e^2 - m_e^2})$.[14]

Furthermore, the differential cross section for an electron with initial energy E_e producing a scattered electron with energy E'_e is given by (206, 207):

$$\frac{{\rm d}\sigma_{\rm ICS}}{{\rm d}E'_e} = \sigma_{\rm T} \, \frac{3}{8} \, \frac{m_e^2}{s} \, \frac{1}{E_e} \, \frac{1+\beta}{\beta} \left[\frac{E'_e}{E_e} + \frac{E_e}{E'_e} \right. \\ \left. + \frac{2(1-\beta)}{\beta} \left(1 - \frac{E_e}{E'_e} \right) + \frac{1-\beta^2}{\beta^2} \left(1 - \frac{E_e}{E'_e} \right)^2 \right] \ , \tag{1-69}$$

[14]Note that s and β vary depending on the specific interaction. For simplicity, the same notation is used throughout this dissertation, with the relevant definitions provided for each interaction.

where the allowed range is $(1-\beta)/(1+\beta) \leq E'_e/E_e \leq 1$. Note that the differential cross section with respect to the energy E'_γ of the outgoing photon can be obtained by replacing $E_e - E'_\gamma$ for E'_e in Eq. 1-69.

The inelasticity of ICS can be directly obtained from Eq. 1-40 and can be approximated as $\eta_{\rm ICS} \sim \frac{4}{3}\frac{E_e\epsilon}{m_e^2}$. While this approximation deviates significantly from the exact ICS inelasticity at very high energies (see Figure 2 in (20)), it provides a useful estimation for the energy transfer in ICS, allowing for an approximate analytical treatment of the electromagnetic cascade, as will be discussed in the next section. However, I should emphasize that throughout this work, particularly in the results presented in Chapter 3, we rely on the exact inelasticity computed numerically using Eq. 1-40.

It is important to note that the cascade development is primarily driven by the high inelasticity of EPP and ICS. In both interactions, the majority of the initial high-energy particle's energy (one of the photons in EPP and the electron or positron in ICS) is transferred to a leading particle—either an e^+ or e^- in EPP, or the photon in ICS. This regeneration of the leading particle at each step of the EPP + ICS slows energy degradation, allowing sufficient time for the cascade to achieve high multiplicity. This remark also plays a crucial role in neutrino production during cascade development, as will be explored in detail in Chapter 3.

Despite its complexity, an analytic solution for the remnant (*cascaded*) photon spectrum can be derived under certain simplified assumptions. Some reviews of this analytical calculation can be found in (208, 209, 210). The following section outlines these assumptions and presents the solution.

1.5.3 Analytical Solution to Electromagnetic Cascade

Under three key assumptions, an approximate analytic solution for the cascaded photon spectrum can be derived:

(i) The photon backgrounds are monochromatic.

(ii) The cascade fully develops, meaning no photon remains with sufficient energy for pair production.

(iii) Energy conservation holds across all cascade particles, with no losses to processes other than EPP and ICS. Specifically, the magnetic field is assumed to be sufficiently weak to prevent energy loss via synchrotron radiation.

Under the stated assumptions, we consider a high-energy photon emitted at a sufficiently large distance to allow the cascade to fully develop. The cascade

evolution can be categorized into three regimes, depending on the energy of the incoming particle at each interaction, E:

1. **Leading Particle Regime** ($E\epsilon/m_e^2 \gg 1$): At very high energies, the cascade follows a sequence dominated by the leading particle: $\gamma \to e \to \gamma \to \ldots$. In this regime, inelasticity is high, meaning the majority of the particle's energy is retained by the leading particle after each interaction, with only a small fraction lost.

2. **Multiplication Regime** ($E\epsilon/m_e^2 \gtrsim 1$): This regime marks a shift where the EPP inelasticity decreases to $\eta \sim 0.5$, resulting in a more balanced energy distribution between outgoing particles. As a result, cascades initiated by both outgoing particles of each EPP or ICS event evolve similarly. The energy distribution becomes more democratic, and within a few interaction steps, photons degrade to energies below the EPP threshold. After this point, they lose energy only through redshifting. Another subtle assumption is that low-energy particles produced during the leading particle regime directly transition into the multiplication regime.

3. **Low-Energy Regime**: In the final stage, photons lack sufficient energy for pair production and primarily lose energy via redshift. Electrons and positrons in this regime, however, can still undergo energy losses through ICS interactions.

Figure 1.18 illustrates a schematic of different regimes in cascade development.

However, even within the scope of these approximations, a more complex setup is required due to the large energy gap between the typical energies of the CMB and the EBL. This necessitates considering a dichromatic photon field with corresponding energies $\epsilon_{\rm CMB} = 6.4 \times 10^{-4}$ eV and $\epsilon_{\rm EBL} = 0.68$ eV. It is also important to note that the CMB number density significantly exceeds that of the EBL, *i.e.*, $\bar{n}_{\rm CMB} \gg \bar{n}_{\rm EBL}$. Due to the inequality in number densities, the cascade development proceeds in two stages. In the first stage, the cascade develops primarily through interactions with CMB photons: $\gamma + \gamma_{\rm CMB} \to e^+e^-$ and $e + \gamma_{\rm CMB} \to e + \gamma$. In the second stage, the high-energy tail of the photon spectrum produced in the first stage is involved. Although these photons now have energies below the pair production threshold on the CMB, they are still capable of pair production on EBL photons, due to the higher energy of the EBL. Meanwhile, the ICS continues on the CMB: $\gamma + \gamma_{\rm EBL} \to e^+e^-$ and $e + \gamma_{\rm CMB} \to e + \gamma$.

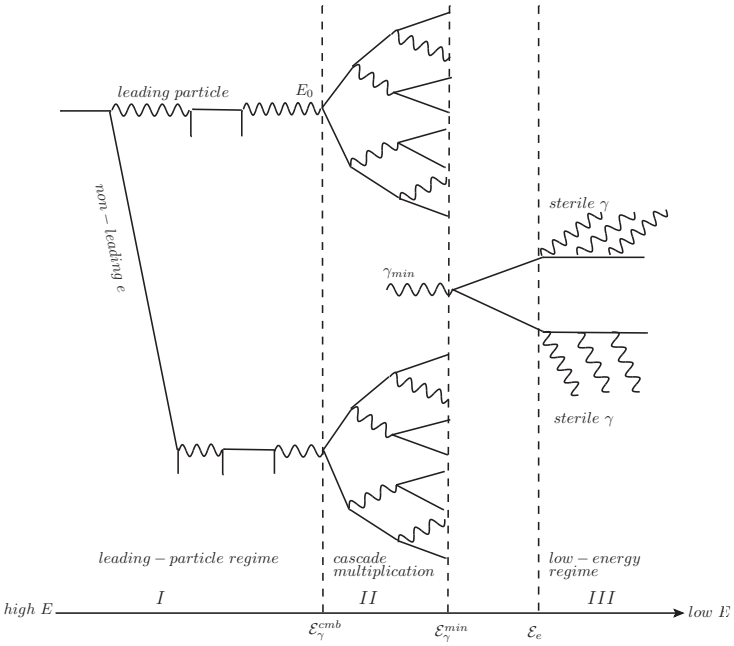

Figure 1.18: Schematic picture of the electromagnetic cascade development in a static Universe with a dichromatic background photon field. See the text for the details. Figure. from (20).

In this setup, we can identify key benchmark energies that govern the cascade dynamics. The minimum energy of a photon that can undergo pair production is $\mathcal{E}_\gamma^{\rm min} = m_e^2/\epsilon_{\rm EBL} = 3.9 \times 10^{11}$ eV. Below this threshold, photons cannot pair produce. This benchmark specifically reflects the photon absorption threshold for interactions with EBL photons since the EBL typical energy is higher that CMB.

Similarly, the minimum energy required for a photon to pair produce on the CMB is $\mathcal{E}_\gamma^{\rm cmb} = m_e^2/\epsilon_{\rm CMB} = 4.1 \times 10^{14}$ eV, clearly satisfying the relation $\mathcal{E}_\gamma^{\rm min} < \mathcal{E}_\gamma^{\rm cmb}$.

In the low-energy regime of the pair production (EPP) process, the inelasticity is approximately $\eta_{\rm EPP} \approx 0.5$, which means the cascade electrons or positrons produced from the last absorbed photon will carry an energy of $\mathcal{E}_e = \eta_{\rm EPP}\mathcal{E}_\gamma^{\rm min} = \mathcal{E}_\gamma^{\rm min}/2$.

To estimate the energy of photons that no longer undergo pair production, we include one additional step of inverse Compton scattering (ICS). The energy of these photons is approximately $\mathcal{E}_X \approx \eta_{\rm ICS}\,\mathcal{E}_e$. Applying the ICS inelasticity approximation, this energy becomes:

$$\mathcal{E}_X = \frac{4}{3}\frac{\mathcal{E}_e^2\epsilon_{\rm CMB}}{m_e^2} = \frac{1}{3}\mathcal{E}_\gamma^{\rm min}\frac{\epsilon_{\rm CMB}}{\epsilon_{\rm EBL}}\,. \tag{1-70}$$

To determine the energy spectrum of photons produced in a cascade, we define $q(E)$ as the number of cascade particles passing through energy E during the entire cascade evolution. The contributions from electrons and photons are

denoted by $q_e(E)$ and $q_\gamma(E)$, respectively, and satisfy the relation:

$$q(E) = q_\gamma(E) + q_e(E)\,. \tag{1-71}$$

Assuming energy conservation throughout the cascade, the energy injected into the cascade relates to $q(E)$ as $E_{\rm inj} = Eq(E)$, where $E_{\rm inj}$ is the energy of the particle initiating the cascade.

During the multiplication regime, each photon produces an electron-positron pair, resulting in approximately $N_e \approx 2N_\gamma$. Conservation of energy in this regime gives $Eq_e(E) \approx 2Eq_\gamma(E)$. Using this and the definition of $q(E)$, we find

$$q_e(E) = \frac{2}{3}\frac{E_{\rm inj}}{E} = 2q_\gamma(E)\,, \tag{1-72}$$

implying $q_e(E) \propto E^{-1}$. (This behavior can be derived alternatively, as shown in [4, 34].)

At lower energies, where pair production ceases, $q_e(E)$ becomes constant. Meanwhile, $q_\gamma(E)$ increases with energy due to the contribution from the low-energy photon tail generated through inverse Compton scattering (ICS) by electrons.

For a set of $q_e(E_e)$ electrons with energy E_e, the energy they radiate, $q_e(E_e)\mathrm{d}E_e$, is distributed among $\mathrm{d}N_\gamma$ photons of energy E_γ. This relationship is expressed as:

$$\mathrm{d}N_\gamma(E_\gamma) = q_e(E_e)\frac{\mathrm{d}E_e}{E_\gamma}\,. \tag{1-73}$$

Since ICS produces photons with $E_\gamma \propto E_e^2$ (See the approximate ICS inelasticity relation), the resulting photon spectrum is determined by the behavior of $q_e(E_e)$. In the multiplication regime, where $q_e(E_e) \propto E_e^{-1}$, we find

$$\frac{\mathrm{d}N_\gamma}{\mathrm{d}E_\gamma} \propto E_\gamma^{-2}\,. \tag{1-74}$$

In the low-energy regime, where $q_e(E_e)$ is constant,

$$\frac{\mathrm{d}N_\gamma}{\mathrm{d}E_\gamma} \propto E_\gamma^{-3/2}\,. \tag{1-75}$$

In the leading particle regime, because all cascade photons are absorbed,

$$\frac{\mathrm{d}N_\gamma}{\mathrm{d}E_\gamma} = 0\,. \tag{1-76}$$

Combining these results, the photon spectrum of a fully developed cascade is given by:

$$\frac{\mathrm{d}N_\gamma}{\mathrm{d}E_\gamma}(E_\gamma) = \begin{cases} \frac{\mathcal{N}}{\mathcal{E}_X}\left(\frac{E_\gamma}{\mathcal{E}_X}\right)^{-3/2}, & \text{for } E_\gamma < \mathcal{E}_X, \\ \frac{\mathcal{N}}{\mathcal{E}_X}\left(\frac{E_\gamma}{\mathcal{E}_X}\right)^{-2}, & \text{for } \mathcal{E}_X \le E_\gamma \le \mathcal{E}_\gamma^{\rm min}, \\ 0, & \text{for } E_\gamma > \mathcal{E}_\gamma^{\rm min}\,, \end{cases} \tag{1-77}$$

where $\mathcal{N}$ is the normalization which can be obtained by the energy conservation condition:

$$E_{\rm inj} = \int E_\gamma \frac{{\rm d}N_\gamma}{{\rm d}E_\gamma} {\rm d}E_\gamma \,, \tag{1-78}$$

thus

$$\mathcal{N} = \frac{E_{\rm inj}}{\mathcal{E}_X (2 + \ln \mathcal{E}_\gamma^{\rm min}/\mathcal{E}_X)} \,. \tag{1-79}$$

The spectrum described in Eq. 1-77 is often called a universal spectrum due to its independence from the injection energy, $E_{\rm inj}$, or the specific shape of the injection spectrum. While $E_{\rm inj}$ determines the overall normalization, $\mathcal{N}$, it does not affect the spectral shape. However, this spectrum does not apply to astrophysical sources located near Earth or sources at high redshift, $z \gtrsim 0.3$. The term "near" depends on the injection energy since a fully developed cascade requires sufficient propagation distance to form. For sources at high redshifts, the overall spectral shape remains intact, but the benchmark energies must be adjusted to account for changes in the energy densities of the EBL and CMB at earlier epochs. At a redshift z, the energy of CMB photons scales as $\epsilon_{\rm CMB}(z) = (1+z)\epsilon_{\rm CMB}(0)$, while the EBL photon energy becomes $\epsilon_{\rm EBL}(z)$. This leads to the characteristic energies of the spectrum at Earth being expressed as:

$$\mathcal{E}_\gamma^{\rm min}(0) = \frac{m_e^2}{\epsilon_{\rm EBL}(z)} \frac{1}{1+z}, \quad \mathcal{E}_X = \frac{m_e^2 \epsilon_{\rm CMB}(0)}{3\epsilon_{\rm EBL}^2(z)} \,. \tag{1-80}$$

Figure 1.19 compares the numerical cascade simulation performed by the code `ELMAG` (21) and the universal spectrum discussed above. The low-energy spectrum, $\propto E_\gamma^{-1.5}$, along with its normalization and the characteristic energies show strong agreement. However, the spectrum in the multiplication regime follows a slope of $E_\gamma^{-1.9}$, differing slightly from the predicted E_γ^{-2}.

To accurately solve the electromagnetic cascade, a numerical approach is essential. Several numerical simulations have been developed for this purpose, employing Monte Carlo or semi-analytical methods to solve the transport equations for photons. Prominent codes in this area include `ELMAG` (21), `EleCa` (211), `GCascade` (212, 210) and `CRPropa` (213). The methods employed by these codes are detailed in their respective publications.

As we will discuss in Chapter 3, electron-positron pair production (EPP) and inverse Compton scattering (ICS) are not the only photon-photon and electron-photon interactions relevant at very-high and ultra-high energies. Codes like `ELMAG`, `ELECA` and `GCascade` consider EPP and ICS as the primary mechanisms driving cascade development, as well as synchrotron losses in the presence of an intergalactic magnetic field (IGMF). On the other hand,

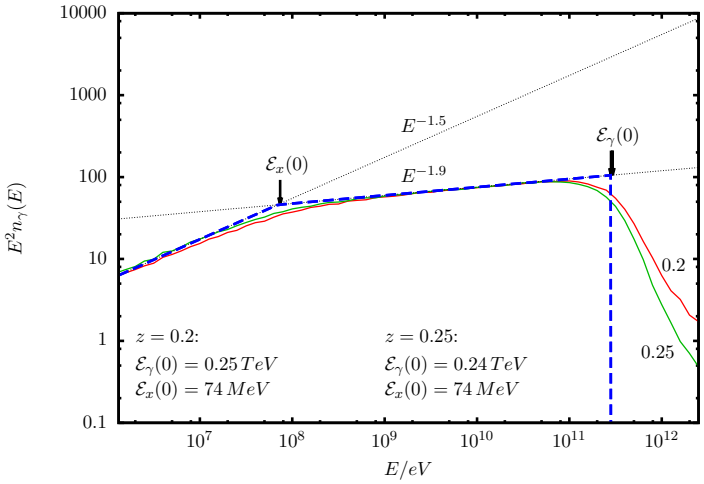

Figure 1.19: Comparison between the numerical cascade result from (21) and the discussed analytical approach of cascade development. Figure from (20).

`CRPropa` account for additional processes, such as double pair production (DPP: $\gamma\gamma \rightarrow e^{\pm}e^{\pm}$) and electron triplet production (ETP: $e\gamma \rightarrow e + e^{\pm}$), the latter often referred to in the literature as triplet pair production (TPP).

In Chapter 3, we will further explore additional processes, such as those leading to muon production and their contribution to a neutrino spectrum emerging from electromagnetic cascades. In this context, we introduce a Monte Carlo simulation named `MUNHECA`, specifically designed to compute the neutrino spectrum from electromagnetic cascades at the ultra-high energy regime.

1.5.4 Applications of the Electromagnetic Cascade

Electromagnetic cascades have significantly shaped our understanding of gamma ray astronomy for discrete sources. A pioneering study by Gould and Schreder (214) demonstrated the absorption of gamma rays with energies above 100 TeV by the CMB in the Universe. By the 1970s, the cascade process was well understood, as previously discussed, and soon afterward, magnetic field effects were incorporated into cascade models. A major breakthrough came with the work of (215), which introduced a critical aspect previously overlooked—the deflection of cascade electrons by magnetic fields.

Earlier studies had primarily considered magnetic fields in terms of energy losses for electrons and photon absorption in extremely strong fields. In contrast, (215) discussed that even weak extragalactic magnetic fields near the source could deflect low-energy cascade electrons ($e^{\pm}$), causing them to produce an isotropic low-energy gamma ray component $E_\gamma \lesssim 1\,\mathrm{TeV}$—commonly referred to as the "halo component." This discovery highlighted the potential

of using halo components to probe the presence of weak seed magnetic fields in the Universe (216).

The angular size of the halo depends on three factors: the initial gamma ray energy, the magnetic field strength along the line of sight and the magnetic field correlation length (See Section. 1.3.1). Higher emission energies result in smaller halo sizes (217, 218). Additionally, a key consequence of the halo component is the *time delay* arising from the difference in the paths traveled by the direct gamma ray signal along the line of sight and the secondary emission generated by the deflected $e^{\pm}$ pairs through ICS (halo component). The magnitude of this delay is sensitive to the magnetic field properties (strength and correlation length), offering another avenue for probing extragalactic magnetic fields (219, 220, 221, 222, 223). In summary, higher values of the IGMF result in stronger deflection of the $e^{\pm}$ pairs, leading to larger pair halos (with lower surface brightness), reduced GeV excess of cascade photons, and longer time delays.

These effects make imaging and timing observations of cascaded gamma rays, particularly in the 1–100 GeV range, an invaluable tool for constraining extragalactic magnetic fields. Instruments like *Fermi*-LAT are well-suited for such analyses. For an in-depth overview of this topic, see (111).

The most recent lower limits on the parameter space (B, λ_B) for the extragalactic magnetic field have been determined through a joint analysis by the *Fermi*-LAT and High Energy Stereoscopic System (H.E.S.S.) collaborations, based on observational data from blazars (22). These results are presented in Figure 1.20. For a detailed account of the analysis, I refer the reader to the original publication (22).

1.6 Multi-messenger Approach in Astroparticles

To close this chapter, it is fitting to introduce the multi-messenger approach in astroparticle physics. The multi-messenger approach goes beyond the mere observation of different messengers—such as neutrinos, CRs and gamma rays—from astrophysical sources. Instead, it focuses on the connections between these messengers, often manifested as relationships between their energy profiles or spectra. Additionally, for point sources, the temporal correlation of messenger detections provides critical insights into the mechanisms powering the source and the propagation of these messengers to Earth. This connection lies in the microphysics of particle interactions; thus, particle physics determines this correlation.

For point sources, the primary particles of interest are neutrinos and

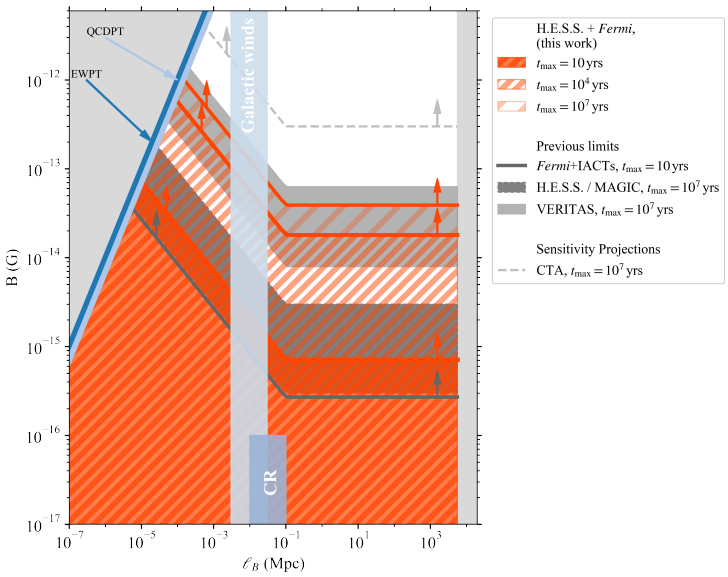

Figure 1.20: The IGMF parameter space probed with gamma ray instruments. The vertical axis shows the magnetic-field strength B, while the horizontal axis depicts the field's coherence length ℓ_B. Lower limits at 95 % confidence level on the IGMF derived from the combined *Fermi*-LAT and H.E.S.S. analysis for different assumed blazar activity times, $t_{\rm max}$ are shown as orange filled and hatched regions. Figure from (22).

photons. Meanwhile, as noted in Section 1.4, most detected astrophysical neutrinos show no correlation with known sources observed across electromagnetic wavebands. Exceptions, such as TXS 0506+056 and NGC 1068, stand out as rare cases of point-source detections across multiple messengers. These observations have motivated extensive modeling efforts to account for the associated neutrino and gamma ray emissions (23, 25, 224). Constraints have also been placed on source classes contributing to the diffuse neutrino flux; for example, Gamma-Ray Bursts (GRBs) likely account for less than one percent of this flux (225). Beyond well-established sources, additional candidates have emerged, such as Tidal Disruption Events (TDEs), which provide intriguing hints of neutrino-source associations (226, 227, 228, 229). It is important to emphasize that the astrophysical sources mentioned are promising candidates for UHECR acceleration and, consequently, for neutrino production, since Neutrinos are often regarded as the *smoking gun* of high-energy CRs.

The multi-messenger approach has taken a significant new step forward with IceCube's observation of neutrino emission from the Galactic plane. Galactic diffuse emission (GDE) arises from either hadronic processes, where CR nuclei interact with the interstellar medium, or leptonic processes, such as inverse Compton scattering by electrons. Recent analyses reveal that the gamma ray flux accompanying the high-energy neutrinos observed by IceCube matches the GDE measured by *Fermi*-LAT and Tibet ASγ at around 1 TeV

and 0.5 PeV, respectively. This agreement strongly points to hadronuclear interactions as the dominant mechanism behind the diffuse gamma ray emission above ∼1 TeV, although a contribution from leptonic processes cannot be entirely excluded. Additionally, comparisons between Galactic and extragalactic diffuse emission fluxes indicate that the Milky Way's neutrino luminosity is one to two orders of magnitude lower than the average of distant galaxies. This finding implies that the Milky Way has not hosted the types of powerful neutrino emitters responsible for the isotropic neutrino background, at least over the past several tens of kiloyears (230).

In the context of the isotropic fluxes observed at Earth—CRs, gamma rays, and neutrinos—the multi-messenger approach reveals valuable connections. Neutrino production, whether through pp or $p\gamma$ interactions as discussed in Section 1.3.6, is intrinsically linked to gamma ray emission. These gamma rays, degraded in energy by electromagnetic cascades, contribute to the diffuse GeV–TeV flux (EGB) measured by *Fermi*-LAT (see Section 1.2.3). Crucially, the cascade gamma rays must remain below the IGRB, which constrains the origin and spectrum of the IceCube neutrino flux, particularly at lower energies. However, the intensity of the neutrino flux at energies below 100 TeV are very high compared to the IGRB flux. This suggests that neutrino sources must be *opaque* to gamma rays. Such opacity implies that gamma rays produced within the source are absorbed via interactions with lower-energy photons, triggering electromagnetic cascades. These cascades redistribute the emission to lower frequencies, ensuring the flux does not exceed the observed IGRB. For more details, for instance, see (231, 232).

In conclusion, the multi-messenger approach offers a powerful framework for placing stringent constraints on astrophysical models by leveraging the complementary information provided by different cosmic messengers.

Within the scope of this dissertation, Chapter 3 delves into a key multi-messenger phenomenon: electromagnetic cascades in the ultra-high-energy regime. At these energies, the cascade challenges the conventional assumption that astrophysical neutrinos are produced exclusively through hadronic processes. As we will demonstrate, leptonic interactions within these cascades contribute a significant neutrino spectrum, broadening our perspective on high-energy neutrino production mechanisms.

2
Pair production with capture by energetic cosmic ray nuclei in a photon background

This chapter is based on the published paper of the same title (33). In this work, we explored an often-overlooked aspect of UHECR propagation through photon fields, including the CMB in extragalactic space and the radiation environment surrounding astrophysical accelerators: the ionization state of nuclei. Specifically, we examine two key processes—pair production with electron capture and photo-ionization.

The first process, hereafter referred to as PPC, involves the interaction of a high-energy photon with a nucleus, leading to the production of an $e^{\pm}$ pair (analogous to the Bethe-Heitler process), followed by the subsequent capture of an electron by the nucleus. This effectively reduces the nuclear charge by one unit. In contrast, photo-ionization occurs when a partially "dressed" nucleus—one with electrons in its atomic shells—loses an electron due to interaction with a photon. As we will discuss in this chapter, these two processes can, in principle, reach equilibrium more rapidly than other UHECR energy loss mechanisms, thereby influencing the effective charge of propagating nuclei.

As outlined in Chapter 1, the electric charge of cosmic-ray nuclei plays a crucial role in both their acceleration and deflection. In this chapter, we examine the conditions under which PPC and photo-ionization become significant, identifying the regions of parameter space where these processes must be considered in UHECR studies. Notably, their effects are most pronounced for UHECRs heavier than iron. Thus, to set the stage for this discussion, I begin by highlighting the growing interest in *heavy* and *ultra-heavy* cosmic-ray nuclei in recent UHECR research.

2.1
Motivation

In addition to what we discussed in Section. 1.3 on the UHECR composition, one of the main motivations for the recent interest in heavy and ultra-heavy UHECRs is that they impose significantly looser conditions on the acceleration to the highest energies. Almost always, a heavy nucleus ${}^{A}_{Z}X$, of mass number A and atomic number $Z \lesssim A/2$, is assumed to be fully ionized with its charge equal to Ze; making abstraction of species-dependent energy-loss mechanisms, a given accelerator capable of an effective potential ΔV allows

for a maximum energy $E_{\rm max} = Ze\Delta V$, proportionally higher for a nucleus than a proton.

However, this picture changes if the heavy nucleus dresses with one or more electrons, effectively reducing its charge. To our knowledge, this possibility has been overlooked in the literature since, at low energies, photo-ionization rates are orders of magnitude faster than any other process. Reassessing the extent to which this conclusion stays true at ultra-high energies for (ultra-)heavy nuclei is our job in this chapter.

The dressing process involves the interaction of ultra-heavy UHECRs with photons. In the course of propagation over cosmological distances, CRs encounter low-energy photon fields permeating the Universe, with the CMB being the most prominent one. Additionally, in the scenarios where CRs are accelerated inside compact astrophysical sources, such as the magnetosphere of a Super Massive Black Hole (SMBH) or GRBs, the acceleration site contains dense background photon fields. In fact, recent multi-messenger searches for the origin of high energy neutrinos observed by IceCube (19, 233), in combination with diffuse gamma ray data (17), strongly point to opaque sources which contain relatively dense photon fields, as discussed in Section 1.6 (231, 232, 234, 235). Then, the observation of neutrinos with energy up to $\sim 10^{16}$ eV by IceCube suggests then sources surrounded by dense photon fields exist that may accelerate protons (nuclei) up to $\sim 10^{17} \div 10^{18}$ eV ($\gtrsim 10^{19}$ eV). Sufficiently energetic photons interacting with such nuclei can produce an $e^{\pm}$ pair (Bethe-Heitler process), with a non-vanishing probability that the electron is captured, thereby reducing the effective charge of the nucleus (or ion) by one unit. The Feynman diagram for this process is shown in Figure. 2.1. Of course, this process is unavoidably accompanied by its inverse, where the same target photons can ionize a dressed nucleus and increase its charge by one unit. Both the PPC and photo-ionization can play important role for ultra-heavy UHECRs due to their scaling $\propto Z^5$. The ion can in principle reach a state of equilibrium for some effective charge, denoted as $Z_{\rm eq}$, lower than the nucleus atomic number, such that the PPC rate at $Z_{\rm eq}$ is equal to photo-ionization rate of the ion with charge $(Z_{\rm eq} - 1)$. Of course, the dressing is relevant for a significant fraction of nuclei at some energy E only if the PPC rate is sufficiently fast, compared to the timescale with which substantial energy loss due to the well-known mechanisms (such as Bethe-Heitler pair production, photo-meson production or photo-disintegration) take place.

The possibility of an equilibrium between PPC and photo-ionization during the cosmological propagation of heavy nuclei has been briefly mentioned (with different motivations) in (236). Due to their approximations, we disagree

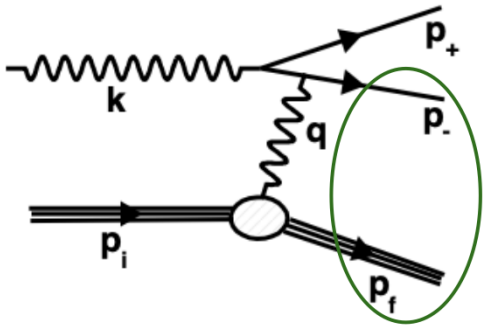

Figure 2.1: Feynman diagram for pair production with capture (PPC). An incoming photon with four-momentum k interacts with an initial proton / nucleus of momentum p_i via exchange of a virtual photon q, producing an $e^{\pm}$ pair. The electron e^- is captured by the Coulomb field of the recoiling final proton / nucleus p_f, as indicated by the enclosing ellipse. This capture lowers the nuclear charge by one unit, $Z \to Z-1$.

with their conclusions, but for the (rather academic) case of protons.

This chapter is structured as follows: in Section 2.2 we introduce the key ingredients used to evaluate the rates of PPC and photo-ionization processes. To determine the time evolution of the ionization state and the possible equilibrium condition, we discuss and solve a set of Saha-like equations, described in Section 2.3. Our main results are presented in Section 2.3. Finally, Section 2.4 includes a discussion, possible directions for future investigations and applications, and our conclusions.

2.2 PPC and Photo-Ionization Rates

The energy spectra of nuclei emitted from astrophysical sources are shaped by the complex interplay between acceleration, cooling, and escape processes (see e.g. (23)). As these nuclei propagate over cosmological distances, their spectra are further modified by energy loss processes, primarily through interactions with background photon fields such as the CMB. By introducing the species ionization state as further dynamical variable, as advocated here, one greatly complexifies the treatment: In principle, by considering nuclei up to a mass number $A_{\rm max}$, instead of dealing with $\sim A_{\rm max}$ different kinetic (or stochastic) differential equations, one should now solve $\sum_i A_i \times Z_i \propto A_{\rm max}^2$ equations, in order to describe abundances, spectra, and ionization states of each species, with an interplay among those variables. In practice, and in particular for a first assessment of the relevance of the effect, *if the PPC and ionization interaction rates exceed the energy-loss rates, we can factorize the problem and separately compute the typical ionization state mixture of nuclei*

having a certain energy, as attained over a length scale set by the energy losses. This approximation fails when this "fast PPC" hypothesis is not met. However, in this regime we expect small effects, so one has limited interest in solving for them.

To evaluate the impact of PPC and photo-ionization processes, the key parameters are the interaction and loss rates or, equivalently, the interaction and loss lengths. For a nucleus with energy E_A and mass m_A interacting with a photon field of spectrum $n(\varepsilon_\gamma)$ in the Lab frame, the interaction rate for a process p is given by (Also remember Eqs. 1-36 and 1-37)

$$\Gamma_p^{\rm int}(E_A) = \int \mathrm{d}\varepsilon_\gamma \int_{-1}^{1} \mathrm{d}\mu \, P(\mu) n(\varepsilon_\gamma) \sigma_p(s) \,, \tag{2-1}$$

where σ_p denotes the total cross section of the process, μ represents the cosine of the collision angle in the photon-nucleus interaction, $s = m_A^2 + 2\varepsilon_\gamma(E_A - \mu\sqrt{E_A^2 - m_A^2})$ is the CoM energy squared, and $P(\mu) = (1 - \beta_A \mu)/2$ is the flux factor, with β_A being the velocity of the nucleus in the Lab frame. The *loss rate* can be defined analogously to the interaction rate, incorporating a measure of energy loss into the formula. Since the inelasticity provides the only dimensionless measure of energy loss, the loss rate of an interaction with inelasticity $\eta(s)$ can be expressed as:

$$\Gamma_p^{\rm loss}(E_N) = \int \mathrm{d}\varepsilon_\gamma \int_{-1}^{1} \mathrm{d}\mu \, P(\mu) n(\varepsilon_\gamma) \sigma_p(s) \eta(s) \,, \tag{2-2}$$

In section 2.2.1 we review the total cross sections of PPC and photo-ionization. Using these established cross sections in Eqs. 2-1 and 2-2, we calculate the corresponding rates in two distinct scenarios: interaction with the CMB during cosmological propagation and inside astrophysical sources where a thermal photon field is present. In Section. 2.2.2 we discuss Bethe-Heitler, photo-disintegration and photo-meson processes as the most relevant energy loss mechanisms for nuclei in our context. We then provide the associated loss and interaction lengths. Note that, quantities in the nucleus rest frame are distinguished by prime ($'$) notation as introduced in the introduction.

2.2.1 Total Cross Sections and Rates of PPC and Photo-Ionization

The capture and ionization processes are most pronounced for the atomic K-shell of the nucleus, so we focus on the relevant formulae specific to the K-shell. The cross section of PPC in the K-shell can be derived from its inverse process, where a positron annihilates with a K-shell electron, resulting in photon emission, as described in (237). In the Born approximation limit ($\alpha Z \ll 1$) this cross section is given by

$$\sigma_{\rm PPC}(E'_+) = \frac{4\pi\alpha^6 Z^5}{m_e\sqrt{E'^2_+ - m_e^2}} \frac{E'^2_+ - \frac{m_e E'_+}{3} + \frac{m_e^2}{3}}{(E'_+ + m_e)^2} \,. \tag{2-3}$$

where, E'_+ denotes the outgoing positron energy. In the nucleus rest frame, the incident photon energy, ε'_γ, the ionization energy, I_K, and the positron energy are related by

$$\varepsilon'_\gamma = E'_+ + m_e - I_K \,, \tag{2-4}$$

where the K-shell ionization energy writes $I_K = m_e(\alpha Z)^2/2$. The K-shell photo-ionization cross section in the relativistic regime, applicable when $\alpha Z \ll 1$, calculated in (238), is given by

$$\begin{aligned} \sigma_{\rm ion} = & \frac{4\pi\alpha^6 Z^5}{m_e \varepsilon'_\gamma} \left(\gamma_e^2 - 1\right)^{3/2} \left[\frac{4}{3} + \right. \\ & \left. \frac{\gamma_e(\gamma_e - 2)}{\gamma_e + 1} \left(1 - \frac{1}{2\gamma_e\sqrt{\gamma_e^2 - 1}} \ln \frac{\gamma_e + \sqrt{\gamma_e^2 - 1}}{\gamma_e - \sqrt{\gamma_e^2 - 1}}\right)\right] , \end{aligned} \tag{2-5}$$

where $\gamma_e = 1 + \varepsilon'_\gamma/m_e$ is the electron Lorentz factor.

Two remarks are in order: First, the PPC and photo-ionization cross sections for higher atomic shells are notably smaller than those of the K-shell. Specifically, the photo-ionization cross sections for the $2s$ and $2p$ sub-shells of the L-shell are suppressed by factors of $2^3(I_L/I_K)^3$ and $2^3(I_L/I_K)^3(I_L/\varepsilon'_\gamma)$, respectively (238). This suppression plays a pivotal role in the PPC-ionization equilibrium stage, which will be further discussed in the next section. Second, while the cross sections provided in Eqs. 2-3 and 2-5 are not viable for high charges ($\alpha Z \sim 1$), the suppression for the largest Z values considered in this work is at most a factor of $\sim$ few compared to the above scaling. Thus, our findings remain robust even in absence of detailed shell-specific cross sections, whose precise calculation is beyond the scope of this exploratory study, and for which we are not aware of well-established fits or numerical tables in the literature.

Using the energy relation in Eq. 2-4 and CoM energy squared in the rest frame of the nuclei, $s = m_A^2 + 2\varepsilon'_\gamma m_A$, these cross sections can be expressed in terms of the Lorentz invariant variable s, which can be used in Eqs. 2-1 and 2-2. Note that while the cross sections in Eqs. 2-3 and 2-5 depend solely on the nuclear charge in the nucleus rest frame, independent of the atomic number or atomic mass number, the same is not true in the Lab frame: Due to the relativistic boost, the cross sections in the Lab frame depend on the atomic mass number of nucleus.

2.2.2 Nuclei Energy Loss Processes

As nuclei propagate through a photon field, they can lose energy through various interactions such as Bethe-Heitler pair production, photo-disintegration and photo-meson production. Additionally, energy loss can occur via synchrotron radiation, due to the presence of magnetic fields in the medium. The competition between synchrotron radiation and other loss processes is influenced by the relative energy density in the magnetic field with respect to the energy density in the background photon field. Since this ratio is rather model-dependent and since the synchrotron radiation is inversely proportional to the nucleus mass, for simplicity we will ignore synchrotron losses in the following.

For sufficiently broad photon spectra, an unavoidable and nuanced competition exists between Bethe-Heitler, photo-disintegration and photo-meson losses. This complexity stems from two facts: On the one hand, the threshold energies for the these processes in the nucleus frame are $\sim 1\,\mathrm{MeV}$ for the Bethe-Heitler, a few MeV (the exact value being nucleus-dependent) for the photo-disintegration and $\sim 100\,\mathrm{MeV/nucleon}$ for the photo-meson interaction. Just based on this trend, one would expect that the Bethe-Heitler matters the most at low-energies, while photo-meson interactions dominate at the highest energies, with a relevant role of the photo-disintegration in between, due to the onset of the Giant Dipole Resonance (GDR). However, the onset energy scale for these processes depend on the nucleus since Bethe-Heitler cross section scales with $\alpha^3 Z^2$, while both the photo-disintegration and photo-meson cross sections scale approximately as $\sim A$. Furthermore, the interplay between these photon-nucleus interactions is further complicated by their inherently stochastic nature. In the context of this study, we adopt a simplified approach by defining a characteristic loss length at each energy and for each nucleus as the smallest among the Bethe-Heitler loss length, photo-meson loss length and the photo-disintegration interaction length (or timescale). Within this timescale, we will solely focus on the competition between PPC and photo-ionization processes. This approximation makes sense only if these processes are fast enough, but this is the only regime where the effects of PPC and photo-ionization cannot be neglected. Technically, we adopt the total cross section and inelasticity of the Bethe-Heitler process from (166). The interaction rate for photo-disintegration is estimated using the single-pole approximation within the Narrow-Width Approximation, as outlined in (239). For the photo-meson cross section we employ the fit in (240), based on GEANT4, along with the inelasticity $\eta_{\mathrm{phmes}} = 0.5$, for estimating the photo-meson loss rate.

For an ion with atomic number Z, mass number A and charge Z_* (where $Z_* \leq Z$, meaning that the nucleus is dressed by $Z - Z_*$ electrons), the PPC and ionization rates are denoted respectively by $\Gamma_{\rm PPC}(Z_*, E_A)$ and $\Gamma_{\rm ion}(Z_*, E_A)$, as functions of the charge Z_* and the ion energy E_A. We start our treatment with a fully stripped nucleus ($Z = Z_*$); which reflects the fact that at low energies where it presumably enters the acceleration process, ionization rates exceed all the other rates of interest. Our goal is then to identify for each species, labeled by its atomic number Z, the energy at which the PPC rate, $\Gamma_{\rm PPC}(Z_* = Z)$, is comparable to the ionization rate when the nucleus is dressed with a single electron, $\Gamma_{\rm ion}(Z'_* = Z-1)$, in a photon background parameterized by either a blackbody [1] temperature T or a monochromatic spectrum of energy ϵ_0, occupying a region of spatial extent R. Only if, simultaneously, these rates surpass those of the relevant loss processes, a significant fraction of dressed nuclei then exists within the specified parameter space.

The characteristic lengths of energy loss processes, as well as the PPC and ionization interaction lengths, are illustrated for both cosmological propagation and propagation within astrophysical sources in Figures 2.2a, 2.2b and 2.2c, respectively for Tungsten, Zirconium and Iron. For the cosmological propagation we consider interactions with the CMB photons at redshift $z = 0$ (upper x-axis), while for the astrophysical case we use a thermal photon field with the temperature 100 eV (lower x-axis), both plotted against the nuclei total energy E_A. It should be noted that the photon field's number density, $\bar{n}_\gamma = \int n_\gamma(\varepsilon_\gamma) {\rm d}\varepsilon_\gamma$, acts as a normalization factor for the interaction/loss lengths and scales them uniformly. As a result, the normalized inverse areas $\bar{n}_\gamma \Gamma^{-1}$ depend only on the energy of the incident ion and the shape of the target photons energy spectrum. Given that both considered photon fields have blackbody spectrum, the normalized lengths are universal at ultra-high energy regime, as shown in Figure 2.2. As a consequence, as long as the PPC and photo-ionization interaction lengths are smaller than or comparable to the source radius R, the number density does not impose any further constraints.

In Figure 2.2 two features are worth noting: *i*) PPC and ionization lengths converge at sufficiently high energies; *ii*) In the energy range where they are comparable, they are sufficiently short with respect to the energy loss lengths only if the atomic number is sufficiently large.

Thus, from Figure 2.2, we expect only a mild dressing of iron nuclei, say, but potentially large deviations from "fully stripped" ultra-heavy nuclei, such as Zirconium (middle panel) or Tungsten (top panel). Note that, due to the typical energy of the CMB photons in the local universe, $\varepsilon_{\rm cmb} \approx 6.3 \times 10^{-4}\,{\rm eV}$,

[1] The results can be trivially generalized to the case where a greybody factor ξ is present.

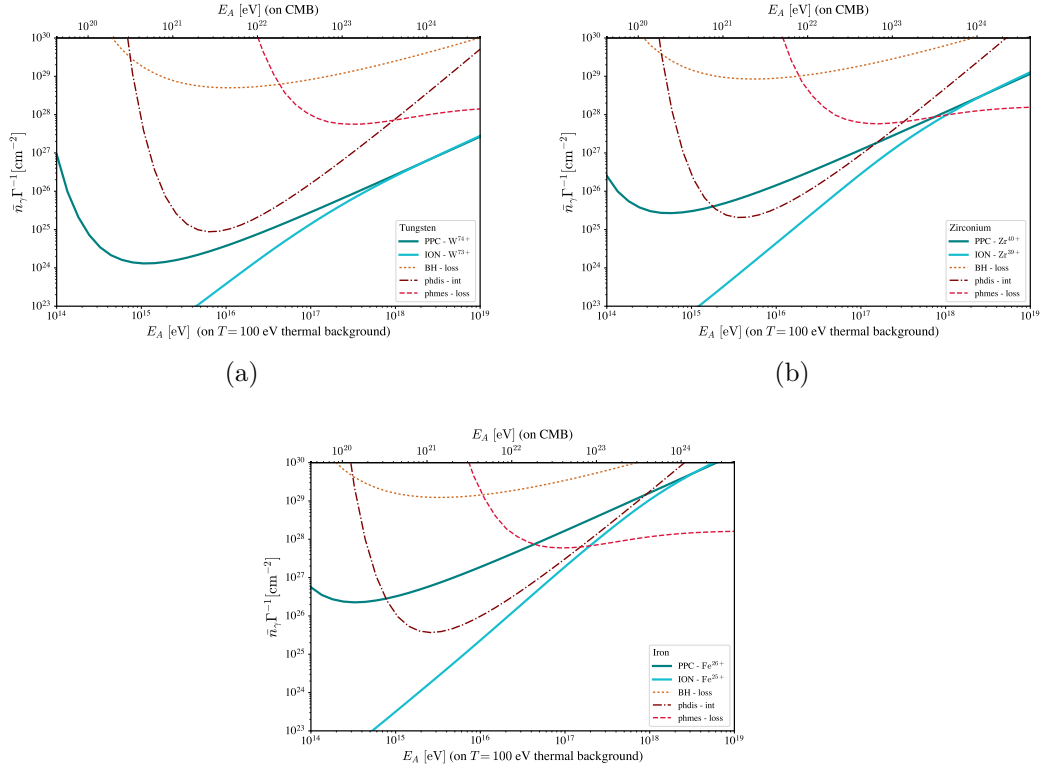

Figure 2.2: Characteristic lengths for (a) Tungsten, (b) Zirconium and (c) Iron. The lower x-axis represents the nuclei's energy for the propagation inside an astrophysical source with a thermal photon field with temperature 100 eV. The upper x-axis corresponds to cosmological propagation in CMB. The y-axis shows interaction rates, normalized by the total number density of the photons, resulting in universal curves at ultra-high energies. The universality holds in the regime where $s \approx 4\varepsilon_\gamma E_A$, where ε_γ is the photon's energy, which is valid at sufficiently high energies.

a comparable PPC and ionization rate is only attained at extremely high energies, $E_A \gtrsim 10^{23}$ eV, as is manifested in Figure 2.2. Thus, *only a tiny fraction of dressed nuclei is expected to be observed in UHECRs propagating over cosmological distances*. Apart from the case of protons, this result is at odds with the conclusion of (236), which predicts, for instance, that Fe in UHECRs should have an equilibrium $Z_* = Z - 1 = 25$. As far as we can infer, this stems from the incorrect scaling of the photo-ionization cross section with Z, implicitly used in (236). Instead, for the propagation inside the astrophysical sources, if the acceleration site is surrounded by a sufficiently extended environment dominated by a (not too broad) photon background, we expect that a significant fraction of partially dressed nuclei will be established.

After this qualitative assessment, in the next section we will tackle the problem more quantitatively by formulating the Saha-like equations to

determine the fraction of dressed nuclei at different energies and for different elements.

2.3 Saha-like Equations and Results

To gauge the influence of PPC and photo-ionization processes on the propagation of ultra-heavy and ultra-high-energy nuclei, we employ a set of "Saha-like" rate equations. These equations allow us to calculate the fraction of nuclei that remain partially dressed after traveling a given distance. The rate of change in the population of nuclei in a particular ionization state is governed by the following time-dependent set of equations:

$$\begin{aligned}\dot{X}_i = &(1-\delta_{i0})\Gamma_{\rm ion}(i-1)X_{i-1} \\ &+ (1-\delta_{iZ})\Gamma_{\rm PPC}(i+1)X_{i+1} \\ &- \left[(1-\delta_{iZ})\Gamma_{\rm ion}(i) + (1-\delta_{i0})\Gamma_{\rm PPC}(i)\right] X_i \ .\end{aligned} \tag{2-6}$$

As before, Z represents the atomic number equal to the charge of the fully stripped nucleus, while X_i refers to the fraction of nuclei with same mass number A in an ionization state corresponding to charge i, where $0 \leq i \leq Z$, and the system must be solved from top (X_Z, fully stripped) to bottom (X_0, fully dressed).

We begin by setting the boundary condition $X_i(0) = \delta_{iZ}$, which means that initially all the nuclei are fully stripped. Additionally, we impose the constraint $\sum_i X_i = 1$, ensuring that the total population of nuclei remains conserved across different ionization states. The system of differential equations is then solved over the time interval $(0, \Gamma_{\rm max}^{-1})$, with $\Gamma_{\rm max}$ being the most efficient loss rate at the considered energy for the specific nucleus. This ensures that the conservation of the number of ions of each species is approximately valid, and also allows us to solve the equations for constant values of energy.

Formally, Eq. 2-6 admits a steady state solution if all the time derivatives vanish after a *relaxation* time scale $\tau_{\rm rel}$, *i.e.* $\dot{X}_i(t \gtrsim \tau_{\rm rel}) = 0$. In the steady state the population of nuclei in each ionization state remains constant over time and the the solution of the system of equations in Eq. 2-6, for $t \gtrsim \tau_{\rm rel}$, takes the following form:

$$X_{Z-n} = \prod_{i=0}^{n-1} \frac{\Gamma_{\rm PPC}(Z-i)}{\Gamma_{\rm ion}(Z-i-1)} \, . \tag{2-7}$$

Clearly, the steady state can be achieved if *all* the PPC and photo-ionization rates exceed the loss rates, allowing the nuclei to reach a stable ionization state. The relaxation time can then be estimated by $\tau_{\rm rel} \sim \left[\sum_{i=0}^{Z-1} \Gamma_{\rm PPC}^{-1}(Z-i) + \Gamma_{\rm ion}^{-1}(Z-i-1)\right]$. It is evident that the set of equations

in Eq. 2-6 may never have enough time to reach the steady state in a physical situation, because of the significantly suppressed PPC and photo-ionization rates in the higher atomic shells, as previously discussed. In the absence of the high-shell suppression, the PPC and ionization rates would be comparable and the system would quickly achieve a steady state with a "democratic" distribution of dressed nuclei, that is $X_i \sim 1/Z$ for all i.

In practice and for the physical conditions we are dealing with in this work, we can safely assume that $X_{i<Z-4} \approx 0$, allowing us to truncate the system of equations in Eq. 2-6 at X_{Z-3} and simplify the last equation to

$$\dot{X}_{Z-3} = -\Gamma_{\rm ion}(Z-3)X_{Z-3} + \Gamma_{\rm PPC}(Z-2)X_{Z-2}\,. \tag{2-8}$$

For the purposes of this study, we rely on the K-shell PPC and photo-ionization cross sections. Additionally, we incorporate a suppression factor of 1/8 for the $(Z-3)$ ionization state with respect to the $(Z-2)$ one.

For our truncated system of equations, the steady state solution is attainable (i.e., can be achieved for ultra-heavy nuclei, such as Tungsten), and takes the form:

$$\begin{aligned} X_{Z-1} &= \frac{\Gamma_{\rm PPC}(Z)}{\Gamma_{\rm ion}(Z-1)}\,, \\ X_{Z-2} &= \frac{\Gamma_{\rm PPC}(Z-1)}{\Gamma_{\rm ion}(Z-2)}\frac{\Gamma_{\rm PPC}(Z)}{\Gamma_{\rm ion}(Z-1)}\,, \\ X_{Z-3} &= \frac{\Gamma_{\rm PPC}(Z-2)}{\Gamma_{\rm ion}(Z-3)}\frac{\Gamma_{\rm PPC}(Z-1)}{\Gamma_{\rm ion}(Z-2)}\frac{\Gamma_{\rm PPC}(Z)}{\Gamma_{\rm ion}(Z-1)}\,. \end{aligned} \tag{2-9}$$

This solution aligns well with the numerical solution of the Saha-like equations shown in Figure 2.3 for the propagation of nuclei in a blackbody photon field of temperature 100 eV. Figure 2.3a shows that for a Tungsten nucleus, $Z = 74$, with the energy $E_A = 10^{17}$ eV and propagating through the blackbody photon field of temperature 100 eV, the fractions of dressed nuclei with one, two or three electrons reach $\{X_{73}, X_{72}, X_{71}\} = \{0.22, 0.09, 0.23\}$ until the smallest energy loss length indicated by the vertical gray solid line, meaning that nearly half of the initially bare nuclei become dressed. By increasing the energy to $E_A = 10^{18}$ eV (10^{19} eV) the fraction of dressed nuclei, $1 - X_{74}$, increases to approximately 89% (79%). For Zirconium in Figure 2.3b, the effect is smaller but is not negligible and $1 - X_{40}$ reaches $\sim 40\%$ at 10^{18} eV. Going to Iron in Figure 2.3c, the effect is less pronounced but still $1 - X_{26} \simeq X_{25} \sim 10\%$. The upper x-axis in the panels of Figure 2.3 shows the required propagation length in the CMB for achieving the same dressing fractions at the energies displayed in the legends. For example, 89% of Tungsten nuclei dress in the propagation through CMB at the energy 1.6×10^{23} eV, which is extremely large by the Hillas criterion. The dressing fractions that can be achieved for nuclei propagating

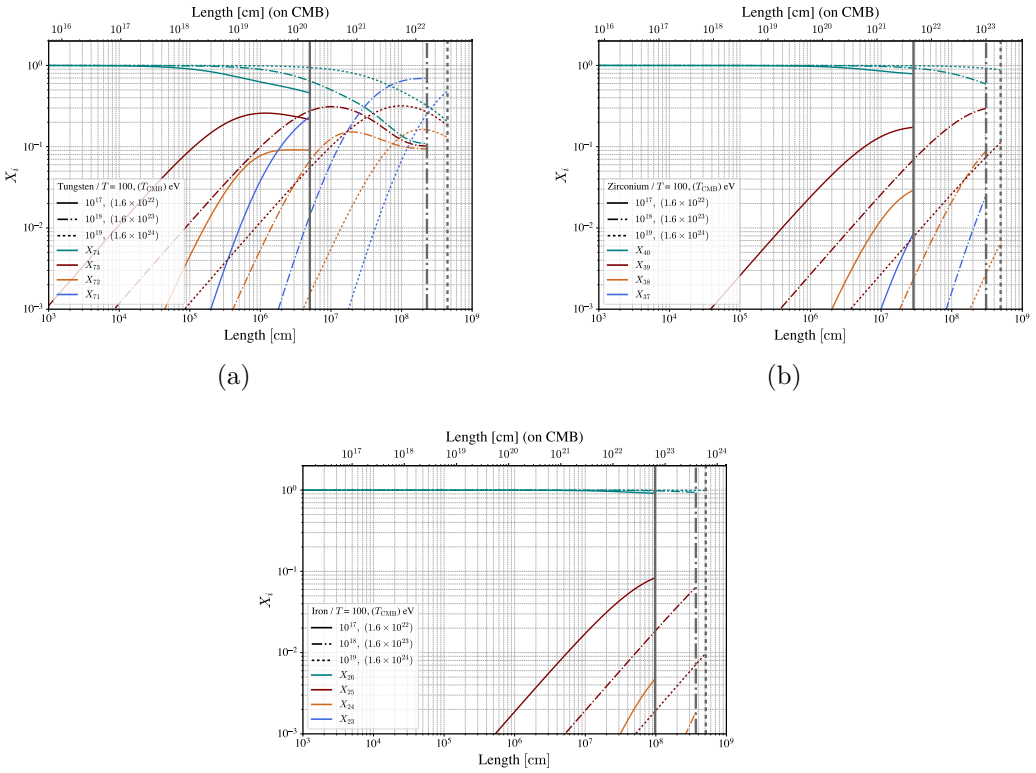

Figure 2.3: Fraction of nuclei dressed with one, two and three electrons, from numerical solution of Eq. 2-6 for (a) Tungsten, (b) Zirconium and (c) Iron, propagating in a thermal photon field of temperature $T = 100$ eV, with energies $E_A = 10^{17}$, 10^{18} and 10^{19} eV. The vertical thick gray lines illustrate the minimum loss length for the corresponding energies. For propagation in CMB the dressing fractions can be achieved for nuclei with energies reported in the legends and over distances in the upper x-axis.

in CMB with highest observed energies are shown in Figure 2.4. For example, from Figure 2.4a, a Tungsten nucleus escaping its source fully stripped and with $E_A = 10^{22}$ eV would arrive at Earth with $\sim 16\%$ probability of being dressed once and $\sim 3\%$ of acquiring two electrons. The Iron is not shown in Figure 2.4 since the dressing probability is negligible; only $\sim 0.3\%$ of Iron nuclei at $E_A = 10^{21}$ eV dress with one electron in the course of propagation in CMB. As anticipated, we estimate that the dressing fraction associated to the extragalactic propagation is thus negligible over the range of UHECR energies observed.

The maximum dressing fraction, $1 - X_Z$, for propagation in a blackbody photon field of temperature T and the energy of nucleus at which it occurs for elements heavier than Iron are reported in Table 2.1. For this case, the CoM energy squared at ultra-high energies is approximately $s \approx E_A T$. Thus, by choosing a temperature, the E_A values can found from the reported value

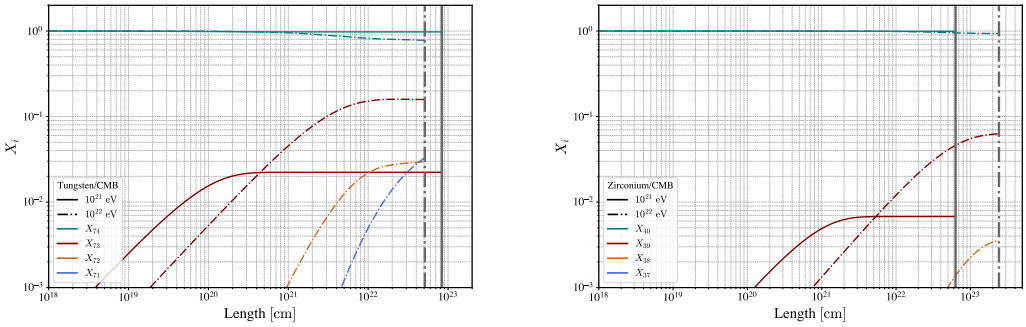

(a) (b)

Figure 2.4: Same as Figure 2.3, for (a) Tungsten and (b) Zirconium nuclei propagating in the CMB and with energies $E_A = 10^{21}$ and 10^{22} eV.

of $E_A T$ in the table.

Can the results obtained assuming a blackbody photon spectrum be considered representative? To answer, we turn to a state-of-the-art Active Galactic Nuclei (AGN) disk-corona scenario (23) and use the spectral energy distribution (SED) with an X-ray luminosity of $L_X = 10^{46}$ erg/s, dubbed SED46. The SED46 has a power-law spectrum for the photon field, marking a significant departure from the blackbody spectrum examined earlier (see (23) for further details on SED46). Figure 2.5 shows the fraction of dressed nuclei, same as Figure 2.3 but for propagation in the SED46 photon field. Comparison between Figures 2.5 and 2.3 shows an almost equal dressing fractions, pointing to the robustness of results with respect to the assumption about the photon field spectrum.

A close inspection reveals that the most important feature that may alter the obtained results is the broadness of the background photon distribution. To illustrate this, in Figure 2.6a we compare the dressing fractions for Tungsten propagating in blackbody of $T = 100$ eV and monochromatic $\varepsilon_\gamma = 100$ eV photon fields. The vertical solid and dot-dashed lines correspond to $E_A = 10^{18}$ eV. An increase of a few percent in the fraction of dressed nuclei can be noticed for propagation in monochromatic photon field. Qualitatively, the reason for this increase is that the photons in the low-energy tail of the blackbody spectrum contribute more to the photo-ionization than the PPC process and therefore suppress the fraction of dressed nuclei. This can be understood by inspecting Figure 2.6b, which shows the dependence of PPC and photo-ionization cross sections for Tungsten on photon energy ε_γ in the lab frame, with the former being penalized by a higher energy threshold and, initially, a milder decrease with energy: Due to the photo-ionization cross section growth at low-energy, even relatively few photons can move the balance

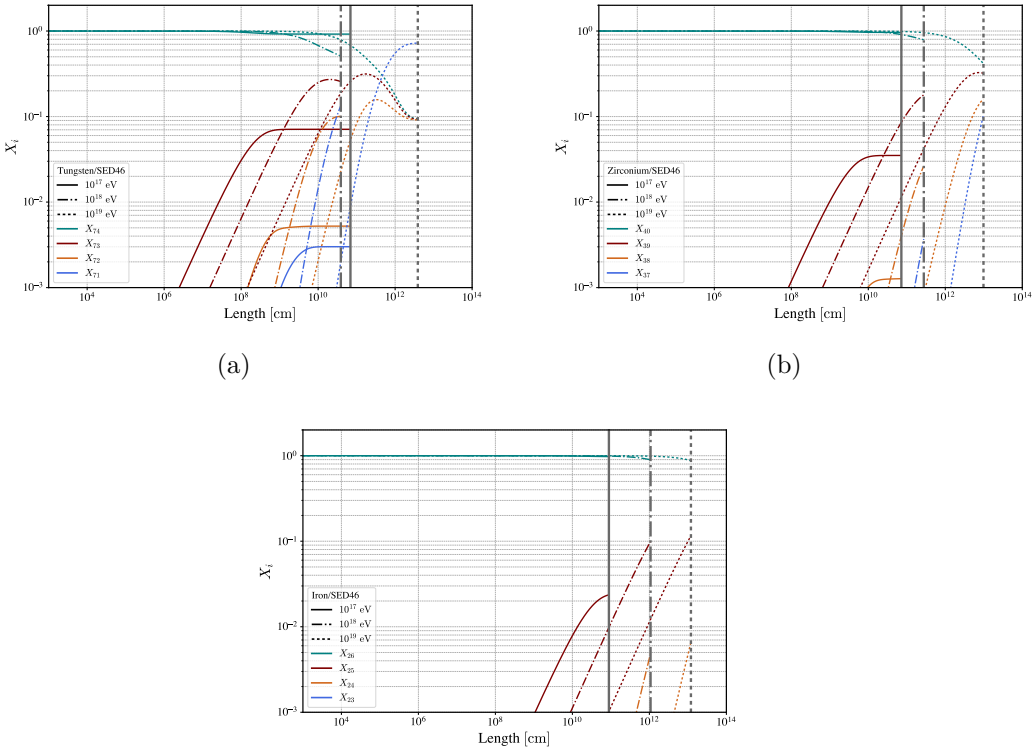

Figure 2.5: Same as Figure 2.3, but for propagation within a source characterized by an SED with X-ray luminosity $L_X = 10^{46}$ erg/s, taken from (23).

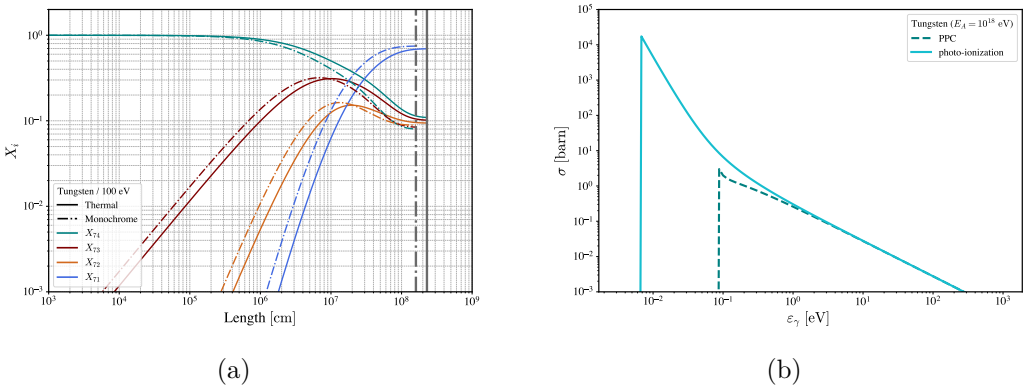

Figure 2.6: Panel (a): The fraction of dressed Tungsten nuclei, comparing the case of propagation in a blackbody spectrum of temperature $T = 100$ eV with a monochromatic photon field of energy 100 eV. The vertical lines correspond to $E_A = 10^{18}$ eV. The number density is fixed. Panel (b): The cross sections of PPC and photo-ionization processes as function of the photon energy in the Lab frame.

in favor of the ionization.

We close this section by a brief discussion about the effect of PPC on the energy loss rate of nuclei. The PPC process adds to the Bethe-Heitler

process, and thus modifies the overall energy loss incurred by heavy nuclei. This modification manifests in two distinct ways, termed here as direct and indirect ways.

The direct modification to energy loss rate can be estimated by assuming a similar inelasticity for both PPC and Bethe-Heitler processes. Then, the loss rate due to PPC can be thought of as a correction to the Bethe-Heitler loss rate given by $\sigma_{\rm PPC}/\sigma_{\rm BH} \sim [9\pi(\alpha Z)^3 m_e/(7\varepsilon'_\gamma \ln(2\varepsilon'_\gamma/m_e))]$. At high energies the photo-disintegration dominates the energy loss rate for heavy nuclei except for a window at $E_A \sim$ few $\times 10^{20}$ eV (see figure 5 in (241)) where Bethe-Heitler energy loss length is marginally smaller, for interaction with CMB. This corresponds to $\varepsilon'_\gamma \sim 10 m_e$, which from our estimate leads to $\sim 2\%$ (0.3%) modification of Bethe-Heitler loss rate for Tungsten (Zirconium).

Indirectly, PPC alters the loss rate of nuclei by modifying the ion's charge state, which the Bethe-Heitler energy loss depends on it quadratically. For the fraction X_{Z-1} of nuclei that acquire one bound electron, the Bethe-Heitler energy loss is reduced by a factor of $(1 - 1/Z)^2$. For ultra-heavy nuclei, this suppression is minimal, of the order of $\lesssim 10^{-3}$, and is therefore negligible in most cases.

2.4 Discussion

In the ongoing efforts to understand the origin and acceleration mechanisms of UHECRs, this study revisits a crucial but often overlooked aspect, the ionization state of nuclei, both during acceleration inside astrophysical sources and during cosmological propagation. We demonstrated that processes such as PPC and photo-ionization, while negligible for light nuclei ($Z \lesssim 26$), have a significant impact on the propagation of heavy and ultra-heavy nuclei at ultra-high energies in the presence of background photon fields. We find that a significant fraction of these nuclei become dressed during their journey through dense photon fields, accumulating electrons in the innermost shells, changing their effective electric charge. A summary of the dressing fractions for different nuclei is reported in Table 2.1.

It is important to note that our analysis does not incorporate the acceleration rates of the nuclei within the UHECR sources. The reduction of a nuclei's net charge by PPC has two consequences for these sources. First, if a site accelerates particles fast enough that the acceleration time is comparable to—or shorter than—the relevant energy-loss timescale, the nuclei will be driven to still higher energies; because both PPC and photo-ionization relevance rise with energy, omitting explicit acceleration in our calculation

makes our estimates conservative: a realistic treatment would increase the fraction of "dressed" nuclei.

Second, PPC lowers the effective charge Z of each nucleus during acceleration, therefore reducing its maximum energy attainable in a given electromagnetic field; to reach a target energy one must therefore start with nuclei of higher atomic number than would be required in the absence of PPC.

Our results further indicate that cosmological propagation of UHECRs through the CMB does not significantly affect the ionization state of these nuclei. For the energy ranges of interest in UHECRs, photo-ionization remains the dominant process and we expect most UHECRs to arrive at Earth in a fully stripped state. Even if nuclei are emitted in a partially dressed state from their source, they will quickly become fully ionized due to the efficiency of photo-ionization in their extragalactic propagation. However, should nuclei be accelerated to extremely high energies, that is $E_A \gtrsim 10^{22}$ eV, the impact of PPC and photo-ionization would become significant even in cosmological propagation, yielding $\mathcal{O}(10\%)$ of the population to be dressed. Additionally, we have shown that the PPC process contributes to a little extent to Bethe-Heitler energy losses for UHECRs. While a secondary effect, it can reach the few percent level for cosmic rays with energies of the order of a few $\times 10^{20}$ eV propagating through the CMB. This motivates the inclusion of PPC losses in precision modeling of UHECR energy loss mechanisms.

Overall, the dominance of photo-ionization in cosmological propagation implies that the PPC can essentially affect the characteristics of UHECRs (energy spectrum and composition) observed at PAO and TA indirectly, via the acceleration at the sources. In particular, recent proposals including ultra-heavy UHECRs in the analysis of data, sometimes leading to improved fits to the observed energy spectrum and composition in comparison to scenarios with only conventional nuclei (p, He, O, Si, Fe) (241), will have to assess the importance of the PPC process on a case-by- case basis, depending on the acceleration environment considered. This may alter expectations and signatures associated to different putative sources, such as the surroundings of merging neutron stars, which have been recently highlighted (242).

Future work will focus on a more precise assessment of the ionization states of heavy nuclei, which requires detailed calculations of PPC and photo-ionization cross sections for different atomic shells and charge states. Having these cross sections, the problem can be addressed using Monte Carlo simulations or semi-analytical methods. One interesting scenario involves nuclei capturing electrons directly into the L-shell without first occupying the K-shell. In such cases, the de-excitation of the captured electron could produce a

gamma ray signal characteristic of heavy UHECRs, which represents another promising direction for future UHECR searches, analogous to what discussed in (243, 244).

Table 2.1: Maximum dressing fractions $1 - X_Z$ and $E_A T$ for nuclei from $^{56}_{26}$Fe to $^{231}_{91}$Pa propagating in a blackbody photon field of temperature T. E_A is the energy of nucleus at which the maximum dressing occurs.

Element	$E_A T$ [eV^2]	max$(1 - X_Z)$	Element	$E_A T$ [eV^2]	max$(1 - X_Z)$
$^{56}_{26}$Fe	1.75×10^{19}	0.123	$^{141}_{59}$Pr	6.97×10^{19}	0.809
$^{59}_{27}$Co	2.06×10^{19}	0.140	$^{144}_{60}$Nd	7.56×10^{19}	0.821
$^{59}_{28}$Ni	2.23×10^{19}	0.157	$^{145}_{61}$Pm	7.56×10^{19}	0.831
$^{64}_{29}$Cu	2.42×10^{19}	0.179	$^{150}_{62}$Sm	8.21×10^{19}	0.841
$^{65}_{30}$Zn	2.63×10^{19}	0.198	$^{152}_{63}$Eu	8.90×10^{19}	0.850
$^{70}_{31}$Ga	2.85×10^{19}	0.223	$^{157}_{64}$Gd	9.66×10^{19}	0.858
$^{73}_{32}$Ge	3.09×10^{19}	0.247	$^{159}_{65}$Tb	1.14×10^{20}	0.870
$^{75}_{33}$As	3.35×10^{19}	0.269	$^{164}_{66}$Dy	1.23×10^{20}	0.881
$^{79}_{34}$Se	3.64×10^{19}	0.291	$^{165}_{67}$Ho	1.34×10^{20}	0.892
$^{80}_{35}$Br	3.64×10^{19}	0.319	$^{167}_{68}$Er	1.45×10^{20}	0.899
$^{84}_{36}$Kr	4.28×10^{19}	0.342	$^{169}_{69}$Tm	1.57×10^{20}	0.902
$^{85}_{37}$Rb	4.28×10^{19}	0.369	$^{173}_{70}$Yb	1.85×10^{20}	0.904
$^{88}_{38}$Sr	4.64×10^{19}	0.392	$^{175}_{71}$Lu	1.85×10^{20}	0.905
$^{89}_{39}$Y	4.64×10^{19}	0.416	$^{178}_{72}$Hf	2.01×10^{20}	0.907
$^{91}_{40}$Zr	4.64×10^{19}	0.441	$^{181}_{73}$Ta	2.36×10^{20}	0.908
$^{93}_{41}$Nb	5.46×10^{19}	0.463	$^{184}_{74}$W	2.36×10^{20}	0.909
$^{98}_{42}$Mo	5.93×10^{19}	0.485	$^{187}_{75}$Re	2.57×10^{20}	0.910
$^{98}_{43}$Tc	5.93×10^{19}	0.505	$^{192}_{76}$Os	2.78×10^{20}	0.912
$^{101}_{44}$Ru	5.93×10^{19}	0.531	$^{193}_{77}$Ir	3.02×10^{20}	0.913
$^{103}_{45}$Rh	5.93×10^{19}	0.551	$^{195}_{78}$Pt	3.27×10^{20}	0.914
$^{106}_{46}$Pd	5.93×10^{19}	0.570	$^{197}_{79}$Au	3.55×10^{20}	0.915
$^{107}_{47}$Ag	5.93×10^{19}	0.594	$^{202}_{80}$Hg	3.85×10^{20}	0.915
$^{114}_{48}$Cd	5.93×10^{19}	0.613	$^{205}_{81}$Tl	3.85×10^{20}	0.916
$^{115}_{49}$In	5.93×10^{19}	0.633	$^{208}_{82}$Pb	4.18×10^{20}	0.916
$^{120}_{50}$Sn	5.93×10^{19}	0.656	$^{209}_{83}$Bi	4.92×10^{20}	0.917
$^{121}_{51}$Sb	6.43×10^{19}	0.675	$^{210}_{84}$Po	4.92×10^{20}	0.917
$^{126}_{52}$Te	6.43×10^{19}	0.693	$^{210}_{85}$At	5.34×10^{20}	0.917
$^{127}_{53}$I	6.97×10^{19}	0.712	$^{222}_{86}$Rn	5.79×10^{20}	0.918
$^{132}_{54}$Xe	7.56×10^{19}	0.733	$^{223}_{87}$Fr	5.79×10^{20}	0.918
$^{133}_{55}$Cs	7.56×10^{19}	0.751	$^{226}_{88}$Ra	6.28×10^{20}	0.918
$^{138}_{56}$Ba	8.21×10^{19}	0.765	$^{227}_{89}$Ac	6.28×10^{20}	0.918
$^{139}_{57}$La	8.90×10^{19}	0.782	$^{232}_{90}$Th	6.28×10^{20}	0.919
$^{140}_{58}$Ce	9.66×10^{19}	0.797	$^{231}_{91}$Pa	6.28×10^{20}	0.919

3
Neutrinos from muon-rich ultra high energy electromagnetic cascade and `MUNHECA` code

This chapter delves into the findings presented in (34, 35), focusing on the development of electromagnetic cascades at ultra-high energies (UHE). In (34), we investigated the influence of specific interactions, namely muon pair production (MPP: $\gamma\gamma \to \mu\mu$) and double pair production (DPP: $\gamma\gamma \to e^{\pm}e^{\pm}$), on cascade developments under conditions where these processes are relevant. Our analysis centered on the propagation of UHE photons and electrons originating from astrophysical sources in the high-redshift Universe ($z \gtrsim 5$), interacting with the CMB. The results highlighted that a considerable fraction of the energy injected into the cascade could, in principle, be carried by the neutrinos.

Building on this work, (35) expanded the scope by including additional $\gamma\gamma$ and $e\gamma$ interactions that are operative at the UHE regime. This study also introduced a publicly available `python3` code, `MUNHECA`, designed to compute the resulting neutrino spectrum. The code accounts for these QED processes as the cascade develops, either during propagation through the CMB in the high-redshift Universe or within a predefined photon background around astrophysical sources. Overall, electromagnetic cascades emerge as a compelling pure leptonic mechanism for the production of astrophysical neutrinos.

3.1
Motivation

Unraveling the origins of ultra-high-energy astrophysical sources requires a multi-messenger approach, leveraging the complementary information carried by charged cosmic rays, photons, and neutrinos. This endeavor demands a deep understanding of the microphysical processes that govern the energy distribution and spectral characteristics of these messengers. However, as we discussed in Chapter. 1, neutrinos are the most promising messengers from the large distance astrophysical sources: UHECRs lose significant energy during propagation and are deflected by extragalactic magnetic fields, obscuring their sources. Photons and electrons, in turn, interact rapidly with the CMB, quickly degrading their energy and contributing mainly to the diffuse extragalactic background at sub-TeV energies. Gravitational waves, while offering intriguing prospects, require next-generation detectors to probe high-redshift events and

remain difficult to connect with high-energy counterparts (245). In this sense, the high-redshift Universe ($z \gtrsim 5$) still remains mysterious.

The astrophysical neutrino flux detection by IceCube (246, 247, 248, 249), extending up to $\sim \mathcal{O}(10)$ PeV (250), has marked a turning point in multi-messenger astrophysics. Future advances in neutrino telescope sensitivity promise to push the frontier further, particularly into the UHE range ($E \gtrsim 10^{17}$ eV). While these neutrinos are guaranteed from interactions of UHECRs with the CMB, they might also reveal unknown astrophysical or exotic phenomena (251, 252, 253). Crucially, the interplay between messengers, especially between photons and neutrinos, offers powerful diagnostic potential. For instance, gamma rays have long provided stringent constraints on UHE neutrino production, as demonstrated in works such as (254, 255, 256).

The fact that the propagation of UHE photons/electrons may be quantitatively different at high-z was studied in (257, 258), where the key process responsible for the drainage into the neutrino channel was thought to be the *electron muon-pair production* (EMPP: $e\gamma \to e\mu\mu$). Soon after, this process was reassessed and found of negligible importance in (24). The same article also suggested that the MPP process may however play a similar role [1]. This process has been studied within some approximations in (260), where it was concluded that at low redshift $0 \leq z < 5$, and due to the interplay with the diffuse CRB [2], only a relatively small fraction of the initial energy of electromagnetic cascades ($\lesssim 10\%$) channels into neutrinos. Similar considerations were also briefly exposed in (261).

The basic idea is that the MPP is non-negligible in the interaction of UHE photons with CMB, where the subsequent decay of muons generates neutrinos. The MPP introduces an important deviation from the course of well-studied electromagnetic cascade of high energy photons/electrons, where it is the chain of EPP and ICS which leads to the degradation of initial photon/electron energy and the production of a lower-energy photon spectrum. The large inelasticity in both EPP and ICS renders the MPP feasible since effectively the energy loss length in electromagnetic cascade is larger than the interaction length of MPP. This picture is further modified by the role of DPP. In DPP, one of the $e^{\pm}$ pairs carries nearly all the energy of the incoming photon, while the energy is almost evenly distributed between the electron and positron in this pair. Consequently, DPP plays a key role in energy drainage but also increases the cascade multiplicity, enhancing the probability of MPP at lower

[1] An early mention of this process can also be found in (259).

[2] Furthermore, the $e^{\pm}$ in the cascade could also quickly lose energy via synchrotron emission in intergalactic magnetic fields, if these are close to the current upper limits at the nG level.

energies.

On the other hand, if the magnetization of the environment is sufficiently low, the same microphysics can play a role in the processing of moderately high energy photons, say of energy $\sim \mathcal{O}(100)$ TeV, within an astrophysical source where they interact with thermal X-ray environmental photons. The neutrino flux emerging from the electromagnetic cascade development inside the source serves at least in principle as a counterexample to the common consensus that neutrino detection is the smoking gun signal for hadronic processes in the source.

Motivated by these remarks, *i.e.* the possibility of neutrino production in a purely leptonic framework, and aware of the complication brought by several relevant processes in the development of the electromagnetic cascade, we developed a public code, `MUNHECA`[3], facilitating the computation of the emergent neutrino spectrum.

In this chapter, first, we recompute the cross sections and inelasticities for the processes of interest to conduct dedicated studies on their impact on cascade development. At the time these studies were published, detailed calculations of the relevant cross sections and inelasticities were either unavailable or rarely found in the literature. For instance, the only relatively recent study on DPP, already over 15 years old, is (262), which builds upon much older, cursory analyses (263, 264) that remain widely cited in the field (e.g., (265)). Next, a qualitative description of electromagnetic cascade development at ultra-high energies, along with the influence of the relevant processes, is presented in section 3.3. The structure and features of the `MUNHECA` are detailed in section 3.4. In section 3.5, we provide the code's output for two case studies: (i) the propagation of monochromatic ultra-high-energy photons injected at high redshift in the cosmological background, and (ii) the cascade development within a source, taking NGC 1068 (191) as a proxy. The latter case is compared to the more simplistic estimate in (25). In section 3.6, we introduce a *quasi-universal* relation for the neutrino spectrum of UHE electromagnetic cascades, similar to what has been obtained for the gamma rays in Section. 1.5. Finally, in section 3.7, we discuss our findings and present conclusions and perspectives for future work.

For convenience, a list of acronyms for the processes discussed in this chapter is provided in Table 3.1.

[3]**MU**ons and **N**eutrinos in **H**igh-energy **E**lectromagnetic **CA**scades. The code can be downloaded from <https://github.com/afesmaeili/MUNHECA.git>

Table 3.1: List of the processes considered in this article and their acronyms.

Process	Name	Acronym
$\gamma\gamma \to e^+e^-$	Electron Pair Production	EPP
$\gamma\gamma \to \mu^+\mu^-$	Muon Pair Production	MPP
$\gamma\gamma \to e^+e^-e^+e^-$	Double Pair Production	DPP
$\gamma\gamma \to \pi^+\pi^-$	Charged Pion Pair Production	CPPP
$e\gamma \to e\gamma$	Inverse Compton Scattering	ICS
$e\gamma \to e\mu^+\mu^-$	Electron Muon-Pair Production	EMPP
$e\gamma \to ee^+e^-$	Electron Triplet Production	ETP

3.2 Cross Sections and Inelasticities

3.2.1 An Alternative Parametrization of Inelasticity

Before delving into the details of each interaction, it is helpful to introduce an alternative parametrization for the inelasticity. This approach, especially, streamlines the computation of inelasticity, leveraging the numerical results for the cross sections to achieve greater efficiency.

Previously, we introduced $\eta^{(i)}$ as the fraction of the leading particle's initial energy ($E_{\rm in}^{(L)}$) transferred to the outgoing particle i ($E_{\rm out}^{(i)}$):

$$\eta^{(i)}(s) = \frac{1}{\sigma}\int_0^{E_{\rm in}^{(L)}(s)} \frac{E_{\rm out}^{(i)}}{E_{\rm in}^{(L)}} \frac{{\rm d}\sigma}{{\rm d}E_{\rm out}^{(i)}}\,{\rm d}E_{\rm out}^{(i)}\,, \tag{3-1}$$

In case where the target particles in the Lab frame are at rest, s and $E_{\rm in}^{(L)}$ can be used equivalently to completely fix the kinematics. If the target particles have a non-trivial momentum distribution, an implicit average over their momentum directions is meant. The total inelasticity is then defined as $\eta \equiv \sum_{i\neq L}\eta^{(i)}$, while in the limit $E_{\rm in}^{(L)} \gg E_{\rm in}^{(i)}$ one obviously has $\sum_i \eta^{(i)} = 1$.

Often, the differential cross section is available in the CoM frame, while $E_{\rm in}$, $E_{\rm out}$ are known in the Lab frame; in this case, a Lorentz transformation should be performed. For the processes in which the final particles are scattered mostly in the forward/backward directions (See Section. 3.2.3 for the discussion on the forward/backward scattering), like the ones of our interest, one can write

$$\frac{{\rm d}\sigma}{{\rm d}E_{\rm out}}\,{\rm d}E_{\rm out} = \frac{{\rm d}\sigma}{{\rm d}E^*_{\rm out}}\,{\rm d}E^*_{\rm out}\ , \tag{3-2}$$

where the CoM quantities are marked by '$*$'. When the scattered particles are strongly collimated in forward/backward directions, the Lorentz transformation can be approximated by $E_{\rm out} = E^*_{\rm out}\gamma_c(1\pm\beta^*_{\rm out})$, where $\beta_{\rm out}$ is the velocity of the outgoing particle, $\gamma_c = E_{\rm out}/\sqrt{s}$ is the boost factor from the CoM to lab frame, and the $+(-)$ sign designates the forward (backward) direction. Thus, in the high energy regime ($\beta_{\rm out} \to 1$) the inelasticity of the forward scattered particles, η_+, can be obtained by using $E_{\rm out} = 2\gamma_c E^*_{\rm out}$,

$$\eta_+(s) = \frac{1}{\sigma}\int_0^{\sqrt{s}/2} \frac{2E^*_{\rm out}}{\sqrt{s}}\frac{{\rm d}\sigma}{{\rm d}E^*_{\rm out}}\,{\rm d}E^*_{\rm out}\ . \tag{3-3}$$

For the backward particles,

$$E_{\rm out} = E^*_{\rm out}\gamma_c(1-\beta^*_{\rm out}) = \frac{E^*_{\rm out}\gamma_c}{(\gamma^*_{\rm out})^2(1+\beta^*_{\rm out})} \simeq \frac{\gamma_c m^2}{2E^*_{\rm out}}\,,$$

where m is the outgoing particle mass. The inelasticity for backward scattered particle, η_-, can be written as

$$\eta_-(s) = \frac{1}{\sigma}\int_{\frac{m^2}{2\sqrt{s}}}^{\sqrt{s}/2} \frac{m^2}{2\sqrt{s}}\frac{1}{E^*_{\rm out}}\frac{{\rm d}\sigma}{{\rm d}E^*_{\rm out}}\,{\rm d}E^*_{\rm out}\ . \tag{3-4}$$

Using the convention of Ref. (262), the differential cross section for the outgoing particle ℓ can be parameterized as

$$\frac{{\rm d}\sigma_\ell}{{\rm d}E^*}(s) = \frac{1}{\sqrt{s}}\,\phi_\ell(r_\ell, s)\sigma_{\rm tot}(s)\ , \tag{3-5}$$

where $r_\ell = 2E^*_{\ell,{\rm out}}/\sqrt{s}$ and $\phi_\ell(r_\ell, s)$ is a function that should satisfy

$$\int_0^1 \phi_\ell(r_\ell, s)\,{\rm d}r_\ell = 2 \quad \text{and} \quad \sum_\ell \int_0^1 r_\ell\phi_\ell(r_\ell, s)\,{\rm d}r_\ell = 4\ ,$$

respectively imposing the conservation of probability and energy. Using the function $\phi_\ell(r_\ell, s)$ one can calculate the inelasticity of particle ℓ, scattered either in forward or backward direction, by rewriting respectively the eqs. (3-3) and (3-4) as

$$\eta_{\ell,+}(s) = \int_0^1 \frac{r_\ell}{2}\,\phi_\ell(r_\ell, s)\,{\rm d}r_\ell\ , \tag{3-6}$$

and

$$\eta_{\ell,-}(s) = \int_{\frac{m^2}{s}}^1 \frac{m^2}{2sr_\ell}\,\phi_\ell(r_\ell, s)\,{\rm d}r_\ell\ . \tag{3-7}$$

3.2.2 Muon Pair Production (MPP)

Muon pair production (MPP) is operative when the CoM energy squared satisfies $s \geq 4m_\mu^2$. As previously discussed, quantifying the role of MPP in cascade development requires accurate calculations of its total and differential cross sections. Given the structural similarity between MPP and EPP, the cross sections for MPP—$\sigma_{\rm MPP}$ (total) and ${\rm d}\sigma_{\rm MPP}/{\rm d}E_\mu$ (differential)—can be derived by substituting $m_e \to m_\mu$ in the well-established formulas for EPP, Eqs. 1-64 and 1-65, including those involving the Thomson cross section $\sigma_{\rm T}$. Thus, the inelasticity for MPP can be determined using the same method discussed in Section 1.5.1. The inelasticity of MPP and EEP is compared in Figure 3.1 for the case of interacting with CMB at redshift $z = 0$. Each muon produced undergoes decay, generating neutrinos and electrons (see Eqs.

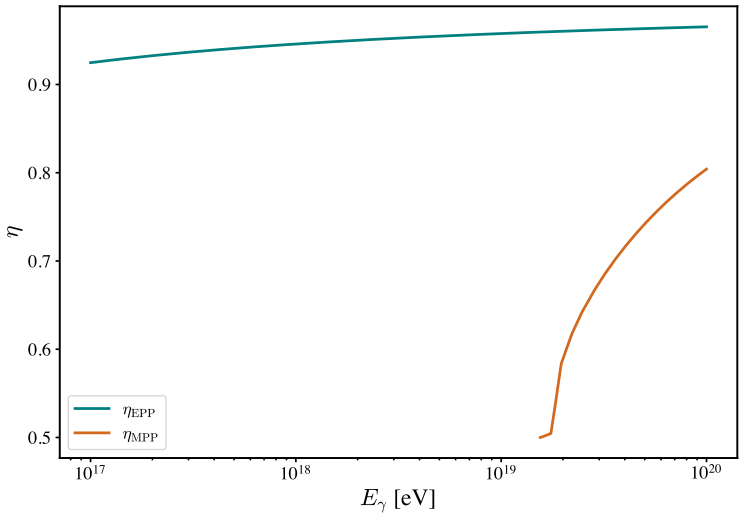

Figure 3.1: Comparison of EPP and MPP inelasticity as a function of incoming photon energy for interaction with CMB at redshift $z = 0$.

1-55 and 1-56). In this process, the electron carries approximately 35% of the muon's energy, while the remaining 65% is distributed between the two neutrinos. The neutrinos escape the cascade, propagating freely through the medium, whereas the electron re-enters the cascade evolution—though with a significantly reduced probability of initiating further muon production.

3.2.3 Double Pair Production (DPP)

Double pair production (DPP) is operative when $s \geq 16m_e^2$. To calculate the energy fraction carried by each of the final particles in DPP we need the differential cross sections and inelasticity of this process, which can be derived at leading order in perturbation theory from the tree level Feynman diagrams shown schematically in Figure 3.2. We use the `calcHEP.3.8.10` [4] code (266) for the numerical computation of Feynman diagrams. `calcHEP` provides an automatic evaluation of the matrix elements and their squares, and performs Monte Carlo phase space integration, via the `VEGAS` algorithm, for elementary particle collisions and decays at the lowest order in perturbation theory (267, 268).

The Feynman diagrams of DPP can be arranged according to either the topology of the diagram, depicted as classes (a), (b) and (c) in Figure 3.2, or the mediator, depicted by the dashed lines, which can be the photon, the Z boson or the Higgs (h). Among the three topologies, at high energy the main contribution to the total cross section of DPP comes from type (c), having

[4] `https://theory.sinp.msu.ru/~pukhov/calchep.html`

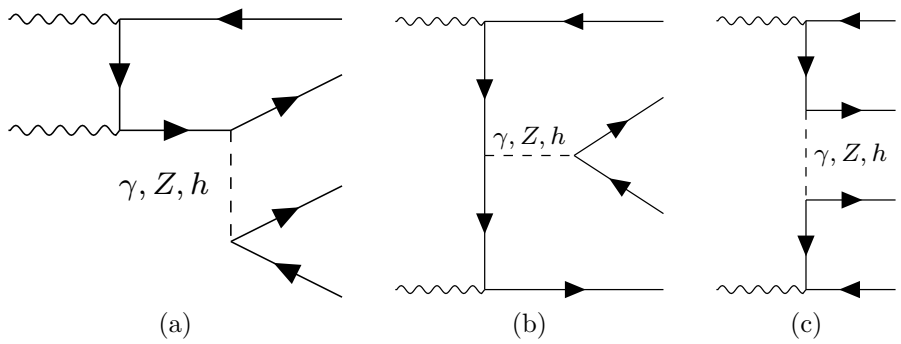

Figure 3.2: DPP Feynman diagrams at tree-level: Wavy lines are photons, solid lines are electrons and dashed lines are mediator propagators (see discussion in the text).

$\frac{\sigma_a+\sigma_b}{\sigma_c}|_{s=100\ \mathrm{GeV}^2} \approx 10^{-5}$, while at energies close to the threshold of DPP the types (a) and (b) diagrams become relevant such that $\frac{\sigma_a+\sigma_b}{\sigma_c}|_{s=10^{-4}\ \mathrm{GeV}^2} \approx 0.17$. Among the three mediators, the contributions of Z and h mediators are negligible, respectively $\mathcal{O}(10^{-12})$ and $\mathcal{O}(10^{-32})$ with respect to photon-mediator diagrams. Thus, for the rest of our discussion, we consider only the diagrams with the photon mediator.

The following approximation of the total cross section of DPP, based on a fit to the numerical integration over the phase space close to the threshold, is reported in the literature (269, 270, 264)

$$\sigma_{\mathrm{DPP}}(s) \simeq \frac{\alpha^4\theta(s-s_{\mathrm{th}})}{\pi m_e^2}\left(\frac{175}{36}\zeta(3)-\frac{19}{18}\right)\left(1-\frac{s_{\mathrm{th}}}{s}\right)^6 , \tag{3-8}$$

where $\zeta(3) = 1.202$ is the Riemann zeta function and the threshold value $s_{\mathrm{th}} = 16m_e^2$ is taken into account by the step function θ. At high energies, eq. (3-8) approaches the asymptotic value $\sigma_{\mathrm{DPP}}(s \to \infty) \approx 6.45\,\mu\mathrm{b}$. To assess the validity of eq. (3-8), in Figure 3.3 we compare it (dashed black curve) with the numerical evaluation of σ_{DPP} (solid blue curve): Deviations are evident below $s \lesssim 10^{-2}$ GeV^2. A better approximation can be obtained by the following expression

$$\sigma_{\mathrm{DPP}}(s) \simeq 6.45\,\mu\mathrm{b}\left[1-\left(\frac{s_{\mathrm{th}}}{s}\right)^{1/3}\right]^{14/5} , \tag{3-9}$$

which is depicted by the dotted red curve in Figure 3.3. Eq. (3-9) approximates the exact DPP cross section better than $\sim 10\%$ at all values of s, while eq. (3-8) deviates from the exact cross section by a factor $\sim$ two.

The angular distribution of the outgoing electrons and positrons in DPP can be inferred from the differential cross section. In the CoM frame, the four outgoing electrons/positrons are typically emitted 'back to back' in pairs, i.e. each electron is closest in angular space to a positron, and the angular separation between e^+ and e^- is small; the two pairs $e^\pm$ are separated by an

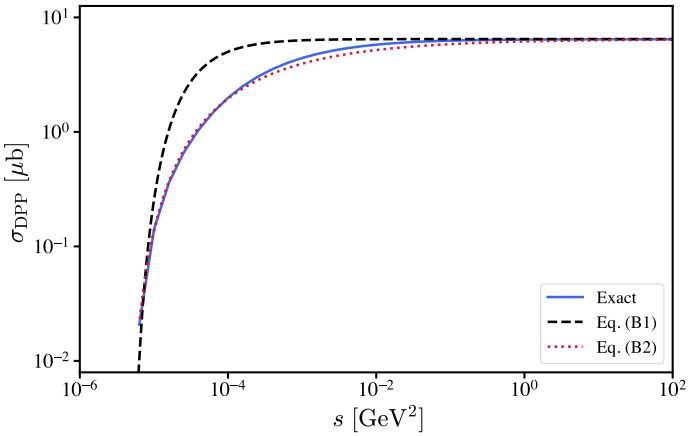

Figure 3.3: Total cross section of DPP as function of s: the result of numerical computation is shown by the blue solid curve, the black dashed and red dotted curves show respectively the approximations in eq. (3-8) and eq. (3-9).

angle π. To assess the degree of accuracy of this statement, the differential cross section $\mathrm{d}\sigma_{\rm DPP}/\mathrm{d}\Omega$ in the CoM frame as a function of $\cos\theta_{e^-e^+}$ is shown in Figure 3.4, where $\theta_{e^-e^+}$ in the angle between the electron and the positron. The sharp peak at $\theta_{e^-e^+} \approx 0$ shows that the members in each pair are collinear with error $\sim 10^{-5}$ (at the chosen value $s = 100$ GeV^2). Close to the threshold of DPP, this statement has to be mitigated; still, only $\sim 10^{-2}$ of the events escape the above-mentioned simplifying classification.

Although the tree level diagrams in Figure 3.2 are straightforward to compute, a technical remark is in order: To distinguish between the two $e^\pm$ pairs in DPP and at the same time to ease the convergence of phase space integrals, it is convenient to differentiate between the two pairs by assigning different names to them (i.e. to treat them as if they were distinguishable, like if they belonged to a different lepton family) while keeping the masses of the new leptons equal to the electron mass. This, of course, would artificially double the yields, an effect which can be compensated for by setting a cut requiring positive rapidity for one of the pairs. With reference to the oriented direction of the high energy photon in the Lab frame, we label the pairs as *forward* and *backward*, respectively containing $e^\pm_{\rm F}$ and $e^\pm_{\rm B}$ electrons/positrons.

The energy distribution between the final particles can be assessed by considering the single and double differential cross sections with respect to one or two electron energy. Here, we show the distributions for the case $s = 100$ GeV^2 in the CoM frame as a benchmark. The differential cross section with respect to the sum of $e^+_{\rm F}$ and $e^-_{\rm F}$ energies has a sharp peak at the corresponding incoming photon energy, half of the total energy (here 5 GeV), as shown in Figure 3.5. For the backward pair, the distribution is of course

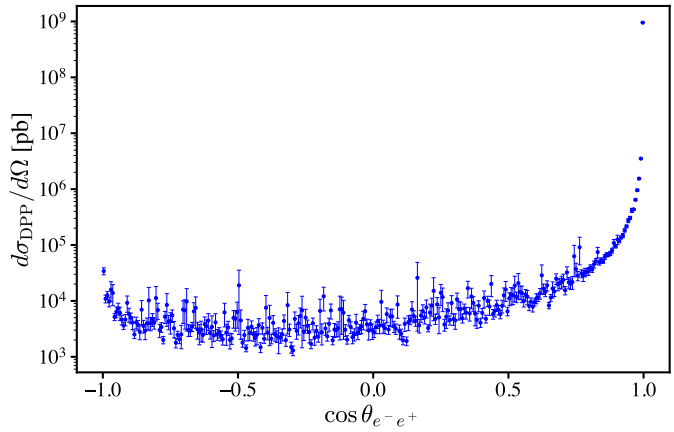

Figure 3.4: The differential cross section $\mathrm{d}\sigma_{\rm DPP}/\mathrm{d}\Omega$ in the CoM frame, as function of the angle between the electron and positron in a pair, $\cos\theta_{e^-e^+}$, for $s = 100$ GeV^2.

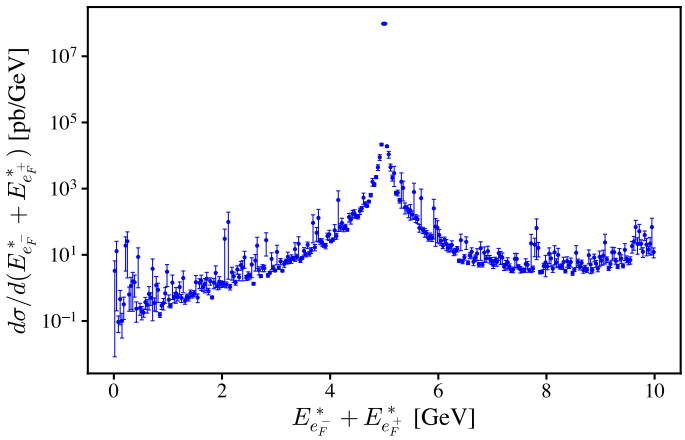

Figure 3.5: Differential cross section as function of the total energy of the forward pair $E^*_{e^-_{\rm F}} + E^*_{e^+_{\rm F}}$ in the CoM frame, assuming $s = 100$ GeV^2, *i.e.* the photons in the initial state have $p_{\gamma,1} = p_{\gamma,2} = 5$ GeV.

the mirror image of Figure 3.5 with respect to the peak. In other words, the energy is shared equally between the forward and backward pairs.

The energy partition within each pair can be understood from the differential cross section with respect to the energy of one of the members in each pair; *i.e.*, the function $\phi_{e,\rm DPP}(r_e, s)$ defined in eq. (3-5), computed by `calcHEP` and depicted in Figure 3.6 for different values of s, where $r_e = 2E^*_e/\sqrt{s}$ is the energy fraction of one electron (E^*_e being the electron energy) in the CoM frame. Close to the threshold of DPP, and in CoM frame, in each pair the electron and positron share the pair energy almost equally (see the peak at $r_e \approx 0.5$ for the darker color scale in Figure 3.6). For $s \gtrsim 0.01$ GeV^2, the energy distribution is wide and can be fitted accurately by $\phi_{\rm fit}(r) = 5/3 + (2r-1)^2$ (262), which means that the relative energy share of the

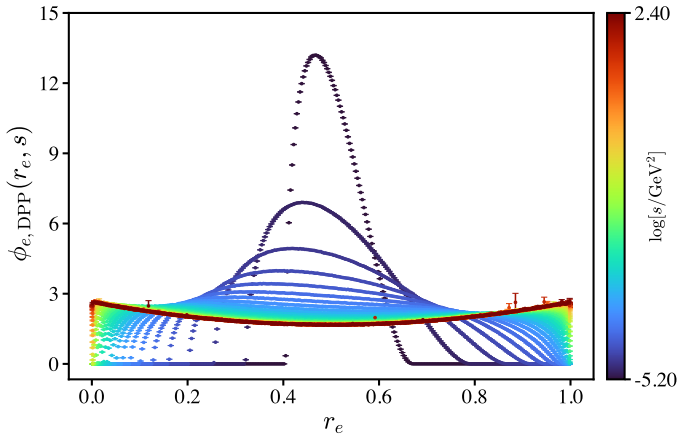

Figure 3.6: $\phi_{e,\mathrm{DPP}}(r_e, s)$ as function of $r_e = 2E_e^*/\sqrt{s}$ and for different values of CoM squared energy s.

members in the pair is almost equally probable for any value from zero to one. The maximum energy shown in Figures. 3.6 and 3.7 ($s \sim 100$ GeV^2) is well beyond the interesting energy range for our purpose. At energies even higher than those covered here one should worry about electroweak processes, but we deem that regime so extreme compared to what are currently considered realistic scenarios that we can safely omit its treatment at this stage. Moreover, the numerical computation with `calcHEP` shows that the fit proposed for $\phi_{e,\mathrm{DPP}}$ can be safely utilized at least up to $s \sim 10^4$ GeV^2.

Using the $\phi_{e,\mathrm{DPP}}$ in eqs. (3-6) and (3-7), the *average* inelasticities of the backward and forward pairs can be computed. Increasing the energy, the average fraction of energy carried by the backward pair in the lab frame decreases such that almost 100% of the leading photon energy is transferred to the forward pair. To compute the partition of energy within the forward pair, we can resort to the particles inelasticities. Because of the symmetric energy sharing in CoM frame, the inelasticities of the members of forward pair can be written as

$$\eta_H(s) = 2 \int_{0.5}^{1} \frac{r_e}{2}\, \phi_{e,\mathrm{DPP}}(r_e, s)\, \mathrm{d}r_e \ , \tag{3-10}$$

and

$$\eta_L(s) = 2 \int_{0}^{0.5} \frac{r_e}{2}\, \phi_{e,\mathrm{DPP}}(r_e, s)\, \mathrm{d}r_e \ , \tag{3-11}$$

where the H and L respectively refer to the higher and lower energy member of the forward pair. The solid blue curve in Figure 3.7 shows η_H as function of s. A fit to this curve can be written as

$$\eta(s) \approx a + b\, \exp\left[-(s_{\mathrm{th}}/s)^c\right] \ , \tag{3-12}$$

with fit parameters $a = 0.32$, $b = 0.45$, and $c = 0.44$, and is depicted by the dashed red curve in Figure 3.7. From this Figure, on the average the maximum energy fraction carried by the high energy member of the forward pair is $\sim 77\%$

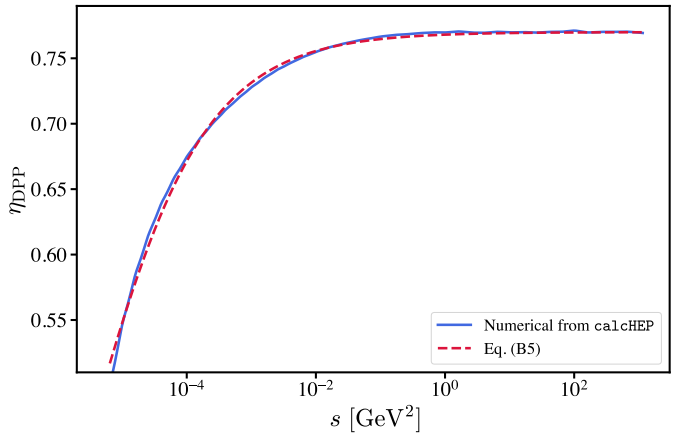

Figure 3.7: The inelasticity of the higher energy member of the forward pair, eq. (3-10), in DPP, as function of s. The solid blue and red dashed curves show the result of numerical calculation and the fit of eq. (3-12), respectively.

at $s \gtrsim 0.1\,\mathrm{GeV}^2$; *i.e.*, an average energy share with the ratio 1 : 3 between the members of the forward pair.

Remembering that Ref. (262) claims that the forward pair takes all the initial energy and shares it equally between the members, we find that at $s \gtrsim 10^{-2}$ GeV^2 a fraction of $\sim 10^{-5}$ of the leading particle energy is carried by the backward pair, thus confirming their first approximation; however, we find that—apart for near threshold—the bulk of the energy is shared between the forward pair members with an average ratio 1 : 3, so the other approximation of Ref. (262) is relatively poor and leads to errors of several tens of percent.

3.2.4 Electron Muon-Pair Production (EMPP)

The four types of EMPP Feynman diagrams are depicted in Figure 3.8. The contribution of the diagrams with Z boson exchange are $\mathcal{O}(10^{-10})$ smaller than the diagrams with photon propagator. Also, the relative contributions of diagrams in Figures 3.8a and 3.8b to the total EMPP cross section are $\mathcal{O}(10^{-3} - 10^{-2})$. The total cross section of EMPP, at high s and in the range $5m_\mu^2 < s < 20m_\mu^2$ has been discussed and computed both numerically (using `compHEP`) and analytically (by equivalent-photon approximation) in (24). For this work, as a cross-check and since the total and differential cross sections are needed in a wider range of energy, we re-computed them by `calcHEP`.

In the equivalent-photon approximation, the EMPP total cross section can be estimated from the MPP cross section by (24)

$$\sigma_{\rm EMPP}(s) \approx \int_{4m_\mu^2/s}^{1} dx\, f_{\gamma/e}(x)\, \sigma_{\rm MPP}(\hat{s} = xs)\ , \tag{3-13}$$

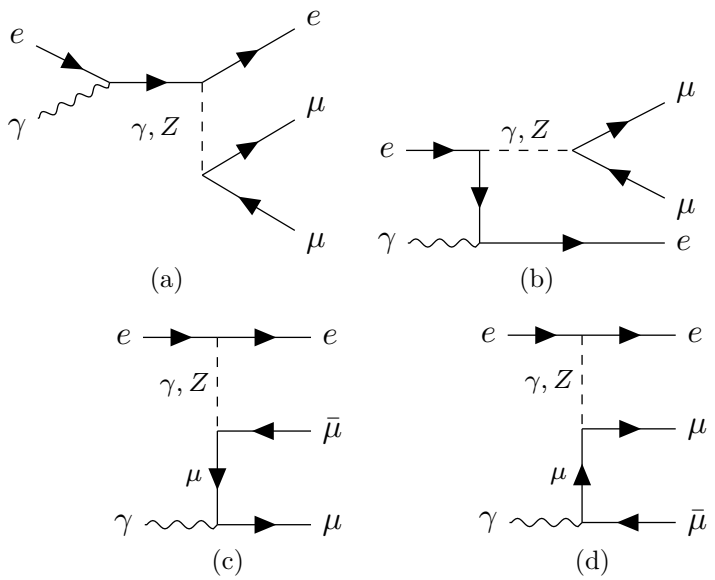

Figure 3.8: EMPP Feynman diagrams at tree-level: Wavy lines are photons, solid lines electrons and dashed lines are mediator propagators (see discussion in the text).

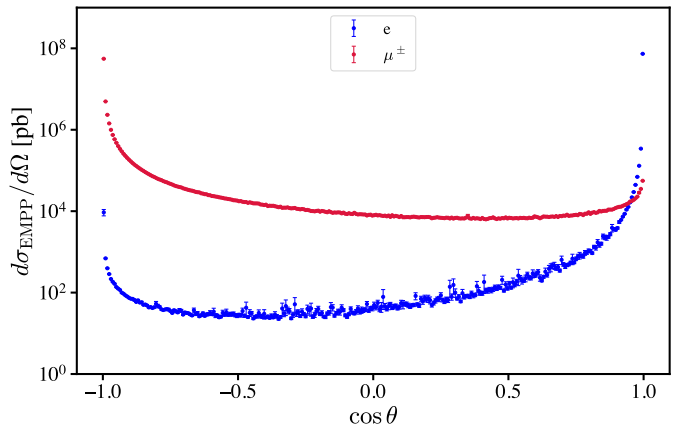

Figure 3.9: The angular distributions of the outgoing electron (blue color) and muons (red color) in EMPP process, at $s = 100$ GeV^2 and in the CoM frame. θ is the angle between the direction of outgoing particle and the collision axis in the CoM frame.

where $f_{\gamma/e}(x) = (\alpha/2\pi)[(1+(1-x)^2)/x]\ln(s/m_e^2)$ is the probability of the emission of a photon with energy E_γ from the incident electron with energy E_e, where $x = E_\gamma/E_e$. The approximation in Eq. 3-13 is shown by the dashed cyan curve in Figure 3.12 and is compared with the `calcHEP` numerical computation depicted by the green data points.

The angular distributions of the outgoing electron and muons, at $s = 100$ GeV^2 and in the CoM frame, are depicted in Figure 3.9 respectively by the red and blue colors, where θ is the angle between the direction of outgoing particle and the collision axis. As can be seen from this plot, with errors $< 10^{-4}$

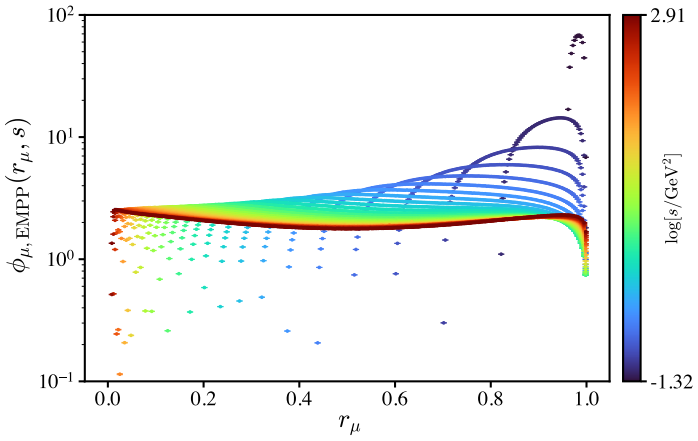

Figure 3.10: The $\phi_\mu(r_\mu, s)$ for EMPP process, as function of $r_\mu = 2E^*_\mu/\sqrt{s}$ and for different values of s, where E^*_μ is the muon energy in the CoM frame.

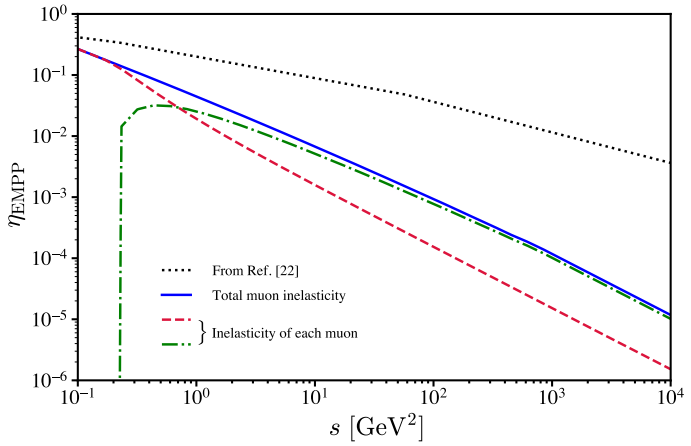

Figure 3.11: The inelasticities of muons in EMPP. The dashed red and dot-dashed green curves show the inelasticities of the two muons and the sum in shown by the solid blue curve. The dotted black curve depicts the approximation taken from (24).

and $< 10^{-3}$ the electron and muons are scattered in the forward and backward directions, respectively. Thus, once more, the forward/backward configuration of the outgoing particles helps us to calculate the inelasticity just from the energy distribution in the interaction, as explained in Section. 3.2.1.

The functions $\phi_\ell(r_\ell, s)$ for each outgoing particle, in the CoM frame, can be computed numerically. Figure 3.10 shows the $\phi_\mu(r_\mu, s)$ as function of r_μ and for different values of s. The energy share of each muon in EMPP can be obtained by changing the integration limit in Eq. 3-7 to $[m^2_\mu/s\,,\,0.5]$ ($[0.5\,,1]$) for the low energy (high energy) muon and multiply it by 2. The inelasticities of the two muons in EMPP and their sum are shown respectively by the dashed red, dot-dashed green and solid blue curves in Figure. 3.11. The solid blue curve, that is the total inelasticity of the muons, can be compared

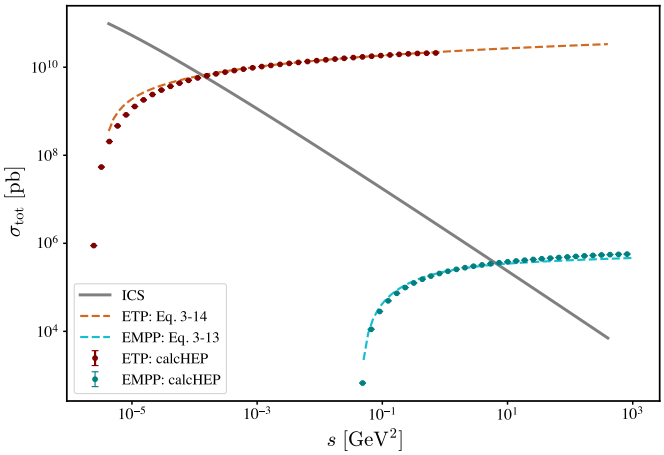

Figure 3.12: The total cross section of $e\gamma$ interactions considered in this study: The ETP cross section is shown as the dashed orange curve (analytical approximation from Eq. 3-14) and maroon data points (`calcHEP` results). The EMPP cross section is represented by the dashed cyan curve (analytical approximation from Eq. 3-13) and green data points (`calcHEP` results). The solid gray line corresponds to ICS.

with the approximation $\eta \approx 3.44 \left(s/m_\mu^2\right)^{-0.5}$, at high s values, from (24) which is depicted by the dotted black curve in Figure 3.11. It turns out that it is acceptable at the $\sim 30\%$ level only at the lowest energies considered here.

3.2.5 Electron Triplet Production (ETP)

Electron triplet production (ETP) is a notable interaction for ultra-high-energy (UHE) electrons. In this section, we will present a new numerical re-assessment of the kinematics of this process. This process has been explored in depth in (271, 272, 273). The Feynman diagrams for ETP are structurally identical to those for EMPP, with the muons (anti-muons) replaced by electrons (positrons). The contributions from Z-boson exchange diagrams are negligible, being suppressed by a factor of $\mathcal{O}(10^{-17})$ relative to photon-mediated diagrams. Similarly, the diagrams analogous to Figures 3.8a and 3.8b contribute only $\mathcal{O}(10^{-5})$ to the total cross section.

In the UHE regime, the ETP total cross section grows asymptotically with s in a logarithmic fashion, and can be approximated by:

$$\sigma_{\rm ETP}(s) = \frac{3\alpha}{8\pi}\sigma_T \left(\frac{28}{9}\ln\left(\frac{s}{m_e^2}\right) - \frac{218}{27}\right). \tag{3-14}$$

Figure 3.12 compares the numerically computed ETP cross section, obtained using `calcHEP`, with the analytical approximation given in Eq. 3-14. For comparison, the cross sections for EMPP and ICS are also displayed.

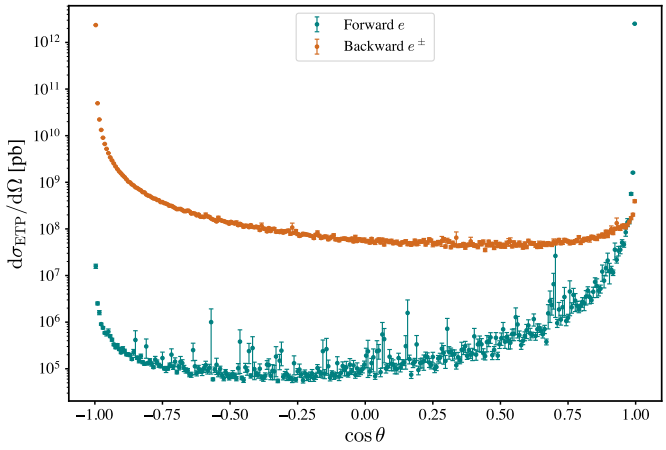

Figure 3.13: The angular distributions of the forward outgoing electron (green color) and the backward $e^{\pm}$ pair (maroon color) in ETP process, at $s = 0.04$ GeV2 and in the CoM frame. θ is the angle between the direction of outgoing particle and the collision axis in the CoM frame

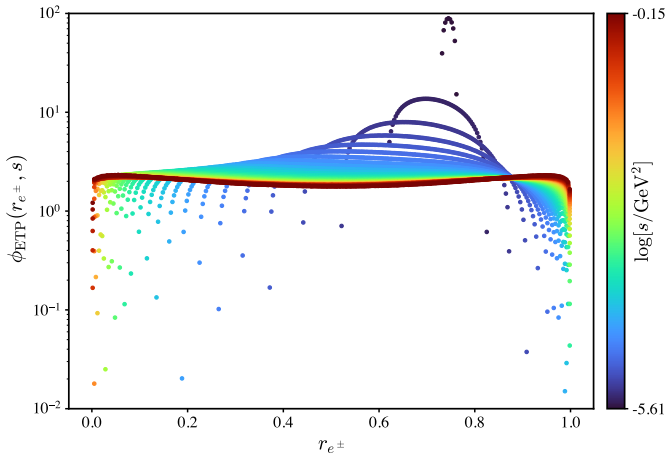

Figure 3.14

Similar to EMPP, the $e^{\pm}$ pair produced in this process is predominantly scattered in the backward direction with respect to the collision axis in the CoM frame. The angular distribution of the final-state particles for ETP is shown in Figure 3.13 at $s = 0.04$ GeV^2. Consequently, the inelasticity of this process can be computed using the same methodology outlined in Sections. 3.2.3 and 3.2.4.

The function $\phi(r_{e^\pm}, s)$ for the ETP, computed numerically using `calcHEP`, is shown in Figure 3.14.

Thus, the ETP inelasticity can be obtained using Eq. 3-7. The energy fraction of the low energy pair produced in the ETP has been estimated in (24) by the approximation:

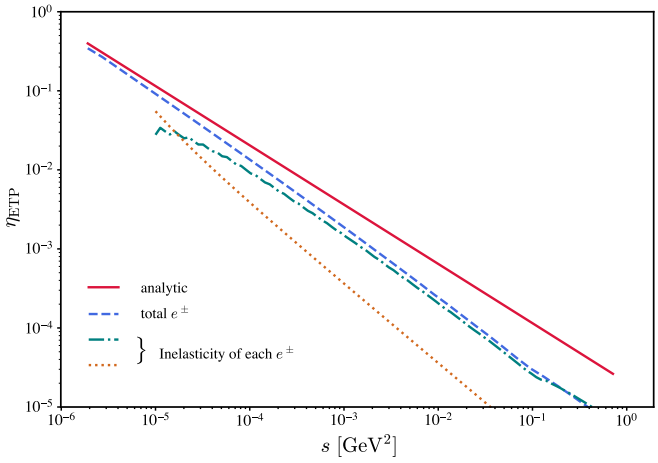

Figure 3.15: The inelasticities of backward scattered $e^{\pm}$ in ETP. The dot-dashed green and dotted orange curves show the inelasticities of the two electron/positron and the sum in shown by the dashed blue curve. The solid red curve depicts the approximation taken from (24)

$$\eta_{\rm ETP} \approx 1.768 \left(\frac{s}{m_e^2}\right)^{-3/4} \tag{3-15}$$

Figure. 3.15 shows our numerical re-assessment and the approximation Eq. 3-15.

3.2.6 Charged Pion Pair Production (CPPP)

Among the various possible hadronic processes for $\gamma\gamma$ interactions, the MUNHECA code currently incorporates only the charged pion pair production (CPPP: $\gamma\gamma \to \pi^+\pi^-$), therefore we will discuss it here. This process can enhance the probability of neutrino production within the cascade whenever it becomes viable ($s \gtrsim 4m_\pi^2$), where $m_\pi = 139.570$ MeV is the charged pion mass. Hadronic $\gamma\gamma$ processes generally require a detailed assessment due to their complex cross sections, influenced by various hadronic resonances. However, for now, we employ the Born approximation as outlined in (274), treating charged pions as point-like scalar particles. Notably, within this approximation, the cross section for neutral pion pairs ($\gamma\gamma \to \pi^0\pi^0$) vanishes. While the Born approximation offers only a rough representation of the underlying process, its application here is justified given the sub-leading contribution of the pion channel ($\approx 5\%$). Within this approximation, the pion is treated as a structureless particle, effectively functioning as a heavier, scalar version of the muon. Consequently, given the relatively small mass difference between the pion and the muon, we adopt the inelasticity for CPPP to be the same as that for MPP.

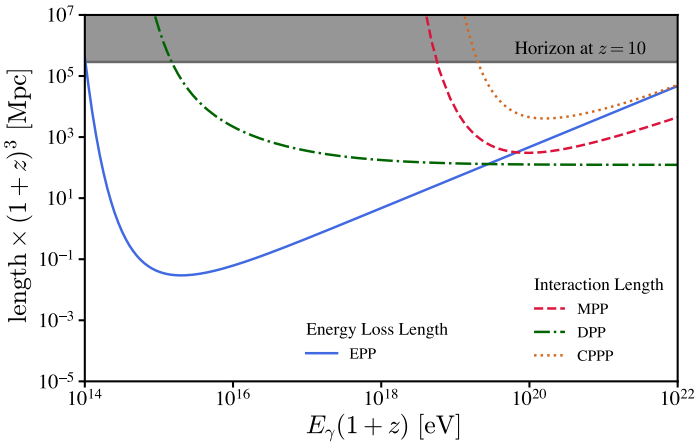

Figure 3.16: Characteristic lengths of photon-photon processes considered in this work, if interacting with CMB target photons. The EPP energy loss length is compared with the MPP, DPP and CPPP interaction lengths. The Hubble horizon at $z = 10$ is shown by the gray line.

The charged pion produced in the CPPP decay to muons and neutrinos, followed by the subsequent decay of muons into neutrinos and electrons. As previously noted, while the neutrinos decouple from the cascade development, electrons remain and continue to drive its development.

3.3 Electromagnetic cascades at ultra high energies

As detailed in Section 1.5, the high-energy cascade above the EPP threshold is dominated by the dynamics of EPP and ICS, both characterized by their significant inelasticities. In each process, the bulk of the initial particle's energy is transferred to a single leading particle. This regeneration of the leading particle in each step in EPP and ICS makes the energy degradation rather slow and quasi-continuous.

However, once raising the energy scale above the appropriate threshold, the feasibility of muon production changes the energy repartition in the cascade development. The muon production, primarily through MPP, is relevant in spite of its cross section being smaller than the EPP one, since the *energy loss length* of electrons is smaller than the interaction length of muon production processes. Note that the energy loss length is simply the inverse of the loss rate defined in Eq. 2-2 from the previous chapter.

For example, for the case of cascade development on the CMB, figure 3.16 shows the interaction length of MPP (dashed red curve) and the energy loss length of electrons via EPP (solid blue curve), where the predominance of muon production at $E_\gamma(1+z) \gtrsim 10^{20}$ eV is evident (z being the injection redshift of the high energy photon with energy E_γ). Notice that in figure 3.16, the vertical

and horizontal axes are scaled by $(1+z)^3$ and $(1+z)$, respectively, ensuring that the curves remain valid for any injection redshift. This scaling reflects the fact that the differential CMB photon density, $n_{\rm CMB}(\epsilon)$, scales as $(1+z)^2$, causing interaction lengths to contract by a factor of $(1+z)$ and energies to increase by the same factor with redshift. Consequently, the interaction length can be expressed as $\lambda(E,z) = (1+z)^{-3}\lambda_0[E(1+z)]$, which λ_0 denotes the interaction length at redshift $z = 0$. An analogous relation holds for the energy loss length (denoted by Λ).

However, whenever the MPP interaction length is smaller that the EPP energy loss length, the DPP interaction length plays the leading role in photon-photon interactions, as illustrated by the dot-dashed green curve in figure 3.16. At high energies, one of the produced pairs of $e^{\pm}$ takes almost all of the initial energy and shares it between the e^+ and e^- roughly in a ratio 1 : 3. As a result, the impact of the DPP on the cascade development is twofold: First, it effectively reduces the energy of the initial photon by a factor ~ 2, contrary to the energy degradation via EPP which is gradual. Second, it doubles the number of $e^{\pm}$ in the cascade, increasing the multiplicity of MPP events and hence the neutrino yield (as long as one is above threshold). The two effects compete against each other, especially at $E_\gamma(1+z) \gtrsim 10^{21}$ eV where the DPP suppresses the muon (and neutrino) production while the increase in multiplicity of MPP occurrence significantly increases the neutrino yield at $E_\gamma(1+z) \simeq 10^{20}$ eV. A minor but still appreciable effect is due to CPPP (whose interaction length is depicted by the dotted orange curve in figure 3.16) which further raises the neutrino yield at $E_\gamma(1+z) \gtrsim 10^{19}$ eV.

The horizontal line in figure 3.16 shows the Hubble horizon of universe at $z = 10$ laying above the curves which justifies our omission of cosmological evolution effects in the cascade development. We used $H_0 = 67.4$ km s^{-1} Mpc^{-1}, $\Omega_M = 0.315$ and $\Omega_\Lambda = 0.685$, according to (275). For all practical purposes of this study ($z \gtrsim 5$), the cascade happens instantaneously at the injection redshift, which only determines the density and energy of the target photons. We estimate the error of this approximation to be $\Delta z \sim \mathcal{O}(10^{-4})$.

The characteristic lengths for electron-photon interaction processes are shown in figure 3.17. At low energies we recover the standard picture where the ICS (whose interaction length is depicted by the solid blue curve) governs the cascade development. However, already at $E_\gamma(1+z) \gtrsim 10^{17}$ eV the ETP becomes the most frequent process. Yet, the peculiar energy share among the three produced electrons/positrons in ETP renders it ineffectual for the cascade development: The pair of $e^{\pm}$ produced in ETP only carries a very small fraction ($\sim 10^{-5}$) of the initial high energy interacting e. Two of the three particles thus

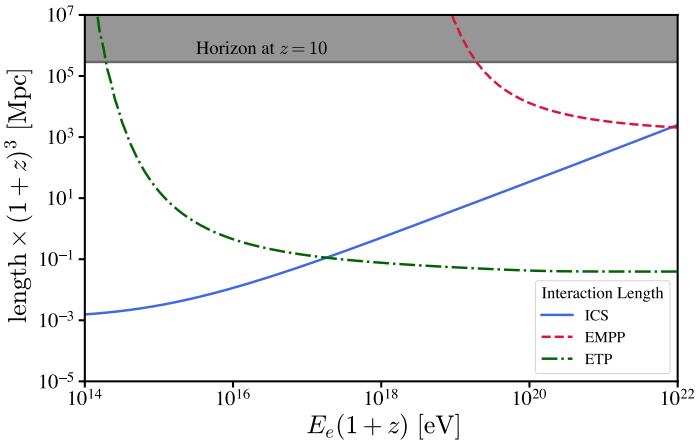

Figure 3.17: Interaction length of the electron-photon processes considered in this work, if interacting with CMB target photons.

drop below the MPP threshold, while the third one is basically unaffected. In summary, the ETP only causes the leading particle to lose a negligible fraction of its energy, and it can be safely ignored in our simulation (as typically done in the specialized literature). Another muon-producing process in the $e\gamma$ interaction is the EMPP, whose interaction length is shown by the dashed red curve in figure 3.17. It only becomes notable at $E_\gamma(1+z) \gtrsim 10^{21}$ eV.

A remark on ICS is in order. The cross section of double Compton scattering (DCS) $e\gamma \to e\gamma\gamma$ logarithmically increases at high energy and, for $\epsilon_\gamma \gtrsim 10^{11}$ eV, it is larger than the conventional ICS cross section (276), where ϵ_γ is the energy of photon in the rest frame of electron. The extra photon emitted in DCS is a soft photon and the cross section is in fact infrared-divergent, *i.e.* in the limit of zero energy of the soft photon. However, two other related QED processes should be considered: the *multiple* Compton scattering $e\gamma \to e + n\gamma$, where $n \geq 3$, and radiative corrections to the conventional (single) Compton scattering. The sum of the amplitudes for these processes not only cures the infrared divergence in cross section but also cancels the apparent increase of DCS cross section at high energy (277), such that the total cross section of these processes only differs at the few percent level from the leading-order cross section of the single Compton scattering at the energy range of our interest. All the emitted extra soft photons in the multiple Compton scattering land in the very low energy range and their impact on the evaluation of cascade evolution at ultra high energy is negligible. Hence, in our simulation we use the conventional ICS cross section, being aware that, apart for a small logarithmic factor, it accounts also for the above-mentioned effects.

The development of an electromagnetic cascade at ultra high energies is intrinsically stochastic. If focusing on the energy drainage to neutrinos, the

diverse processes discussed earlier contribute unequally to the formation of the neutrino spectrum. To capture the multiple occurrences of muon (and occasionally pion) producing processes, realizable due to electron-proliferating DPP process, and to handle the abrupt energy degradation, a Monte Carlo simulation of the cascade evolution is required. This is handled by the `MUNHECA` code, described in the next section.

3.4 `MUNHECA`: structure and features

To compute the full-fledged cascade evolution including all the relevant $\gamma\gamma$ and $e\gamma$ interactions discussed in the previous section, we have developed a Monte Carlo code named `MUNHECA`. The `MUNHECA`, written in `python3`, can be used to compute the neutrino spectrum from electromagnetic cascade at the ultra high energies, either inside an astrophysical source characterized by arbitrary target spectrum, or in the cosmological propagation setting with the CMB as target. `MUNHECA` consists of two parts. The main part, using a Monte Carlo algorithm, tracks the particles' energy along the cascade evolution and produces seven output files recording all the muon, pion, photon and electron energies at the end of cascade evolution, as well as the number of occurrences of neutrino-producing processes (MPP, CPPP and EMPP) for each of the n (to be chosen by the user) monochromatic-energy photons injected into the Monte Carlo realization. The secondary piece of code reads instead the muon and pion outputs of the main part and yields the corresponding neutrino spectra at the Earth.

3.4.1 Installation and Execution

`MUNHECA` uses the `numpy` and `Scipy` packages and does not need any additional installation. To run the code, a `.txt` file should be created which contains the input to the code. A self-explanatory example of the input file, the `test.txt`, is provided in the `/Work` directory. Further description of the format and some clarifications are provided in section. 3.4.2.

To run the Monte Carlo session, the following command can be used

```
python3 [PATH]/run/Main.py [INPUT_PATH]/[InputFileName].txt
```
[5]

[5]The executable `Main.py` is located inside the `run` directory. The execution should be addressed to `/run` as it is indicated in the commands.

After the execution, the results of the session are saved, together with a copy of the input file, into the `/results` directory. The copied input file name, depending on the chosen injection spectrum (`Monochrome` or `PowerLaw`) are named `OM_input.txt` or `OS_input.txt`, respectively.

To obtain the neutrino fluxes at the Earth, the relevant syntax is

```
python3 [PATH]/run/nuSpec.py [PATH]/results/[DESTINATION_DIR]/OM_input.txt
```

or

```
python3 [PATH]/run/nuSpec_Weight.py [PATH]/results/[DESTINATION_DIR]/OS_input.txt
```

for `Monochrome` or `PowerLaw` injection, respectively.

These commands result in the creation of the file `NEUTRINO_EARTH.txt` in the same destination directory, which contains a table of the neutrinos fluxes at the Earth, including all-flavors and each flavor separately.

3.4.2 Inputs and Outputs

As we mentioned above, the input file format is important and discrepancies may cause `ValueErrors`. Therefore, in this section we describe the structure and the input keywords based on the provided template `test.txt`.

Before describing the input structure, let us make a remark. In the input file, the letter capitalization and the place of the colons and the spaces are important. Any parameter inside the input file should be followed by a *colon* (:) and a *space* as is written in this section.

The input file contains four sets of parameters: The choice of processes in the cascade evolution, the background photon field choice, the injection settings and the output file names and directory. Among all the six implemented interactions (5 leptonic + 1 hadronic) the EPP and ICS are activated by default, while the user can turn on or off the MPP, DPP, EMPP and CPPP; for example by selecting `MPP: ON` or `MPP: OFF`; equivalent syntax applies to `DPP`, `EMPP` and `CPPP`.

The background photon field (`Source`) can be chosen among: i) CMB (in case of propagation in a cosmological setting), ii) Black-body, and iii) Power-law (in case of propagation inside a source) distributions by setting `Source: CMB`, `Source: BlackBody` or `Source: PowerLaw`, respectively. Once the background photon field is chosen, its characteristics should be set. For

the CMB the injection redshift, for the black-body its temperature (in eV) and for the power-law the energy index are the parameters that should be written in front of the `Redshift`, `BB_temp` and `PL_index`, respectively. Also, for the `BlackBody` and `PowerLaw` photon fields, the energy range of the spectrum should be set by using the keywords `BB_Emin`, `BB_Emax`, `PL_Emin` and `PL_Emax`.

The photon injection setting can be chosen between `INJ_Spectrum: Monochrome` and `INJ_Spectrum: PowerLaw`. The relevant input parameters for the monochromatic injection, `Monochrome`, are the number of Monte Carlo realizations, `Number_of_photons`, and the injected photon energy, `E_gamma`. For the `PowerLaw` injection there are nine parameters: the `INJ_SPEC_Index` fixes the energy index α; the energy range of injection $[E_{\rm min}, E_{\rm max}]$ is defined by `INJ_Emin` and `INJ_Emax` and characterized by sharp cutoffs. Alternatively, the minimum and maximum energies can be characterized by exponential cutoff scales E_0 and E_0', respectively, controlled by `ExpCut_LowEnergy` and `ExpCut_HighEnergy`. In this case, the injected spectrum takes the form

$$\frac{\mathrm{d}N}{\mathrm{d}E} \propto E^{-\alpha} e^{-E/E_0'} e^{-E_0/E} \ .$$

All the energies should be provided in eV. To implement the low and high energy exponential cutoffs, respectively the `EXP_LOW_CUTOFF` and `EXP_HIGH_CUTOFF` should be set to `ON`. The `NUMBER_OF_BINS` and `PHOTON_PER_BIN` set the number of bins in the energy range and the number of photons injected in each bin, respectively. The `PowerLaw` injection is basically an automatized example of a user-defined arbitrary injection spectrum which will be described in the next section.

There are two other parameters common to both spectra: the `BREAK_Energy` is the energy at which the simulation stops and the `Redshift` which defines the redshift of the source. As we mentioned earlier, only if the `CMB` background photon field is chosen, the redshift will be needed in the simulation. However, for any choice of the background photon field, the source redshift is still needed for the computation of neutrino flux at the Earth. The break point of the Monte Carlo, in principle, can be set to any reasonable value, even below the EPP threshold and of course this will give the complete cascade evolution down to this energy. However, for the purpose of computing the neutrino spectrum generated during the cascade evolution, a break energy just below the MPP threshold saves a considerable computational time. If interested in lower energies, it is more effective to re-inject the outputs of the evolution till the MPP threshold into a new run with just the EPP, DPP and ICS switched `ON`.

At the end of the `test.txt` file, there are eight lines controlling the destination directory and output files names:

- `DESTINATION_DIR`: is the name of the directory in which the outputs will be written. This directory will be created inside the `/results` as soon as the code starts running.
- `Muon_Output` and `Pion_Output`: contain, respectively, all the muon and charged pion energies produced during the cascade evolution.
- `Gamma_Output` and `Electron_Output`: are the histogram list of the photons and electrons below the break energy, each file consisting of three columns. The first column is the center of each bin, the bin widths are written in the second column and the third contains the number of photons/electrons in the bin. To reduce the RAM consumption and the running time, a histogram of the electrons and photons with a fine binning is performed after each realization.
- `MPP_Output`, `EMPP_Output` and `CPPP_Output`: are the occurrences of MPP, EMPP and CPPP interactions, respectively, in each Monte Carlo realization. The size of the lists in these files is equal to the number of injected photons.

3.4.3 Algorithm

`MUNHECA` is organized into six self-contained source files whose names also serve as a guide for the flow of the program. The `Basics` module defines everything that is universal: physical constants, kinematic thresholds, simple analytic forms for the CMB and for generic black-body radiation fields, together with those cosmological parameters that enter the cascade calculations.

`Settings` parses the user's input file, stores all run–time switches, and prepares the output file structure.

All particle–interaction physics is collected in `Interactions`. Wherever closed-form expressions are available (EPP, MPP, CPPP, and inverse-Compton scattering)„ the total cross sections are coded analytically; for DPP, EMPP, and all inelasticities, we precompute grids in the square of the CoM energy and read them from the `/Tables` directory.

Random numbers required for collision angles and background-photon energies are supplied by `RandomGenerator`, which uses rejection sampling: Two routines draw cosines of the scattering angle with the flux factor $(1 - \beta\mu)$ as

weight, while three additional routines sample photons from the CMB, an arbitrary black-body, or a power-law spectrum.

Given a high-energy particle, a sampled angle, and a target-photon energy, `ProcessChoice` evaluates the total cross section of every open channel and selects one according to its relative weight; channels that are below threshold or are deactivated in the input file automatically receive zero probability.

Finally, the `Main` program orchestrates the cascade. It defines one energy-loss routine for each interaction channel, iterates through the temporary photon and electron arrays, updates secondaries, and moves all particles that have dropped below the user-defined break energy into permanent histograms. Two driver functions are provided: `Cascade_Monochrome`, which injects a mono-energetic photon population, and `Cascade_Uniform`, which steps across a user-specified energy range and later re-weights the result to a power-law before the neutrino-spectrum module is called. Throughout, muon and pion decay electrons are treated in approximation with an average energy of $0.35\,E_\mu$, a choice that has negligible impact on the high-energy tail of the cascade, but greatly reduces the computational load.

3.4.4 Neutrino Spectrum

Muon decay generates a neutrino spectrum whose shape depends on the energy distribution of produced μ^+ and μ^-. For each run of the code, this spectrum, $\frac{\mathrm{d}N_{\mu^\pm}}{\mathrm{d}E_{\mu^\pm}}$, can be obtained by creating a histogram from the muon tables generated at the end of the first run (except the normalization factor). The total (all flavors) neutrino spectrum $\mathrm{d}N_\nu/\mathrm{d}E_\nu$ from the decay of $\mu^\pm$ with spectrum $\mathrm{d}N_{\mu^\pm}/\mathrm{d}E_{\mu^\pm}$ can be calculated as described in (278):

$$\frac{\mathrm{d}N_\nu}{\mathrm{d}E_\nu}(E_\nu) = \int_{E_{\mu,\min}}^{E_{\mu,\max}} \mathrm{d}E_\mu \, \frac{\mathrm{d}N_{\mu^\pm}}{\mathrm{d}E_{\mu^\pm}}(E_\mu) \times \left[F_{\mu^\pm \to \overset{(-)}{\nu}_\mu}(E_\mu; E_\nu) + F_{\mu^\pm \to \overset{(-)}{\nu}_e}(E_\mu; E_\nu) \right] , \quad (3\text{-}16)$$

where

$$F_{a\to b}(E_a; E_b) = \frac{1}{E_a} F_{a\to b}\left(\frac{E_b}{E_a}\right) , \quad (3\text{-}17)$$

and for unpolarized muons one has

$$F_{\mu^\pm \to \overset{(-)}{\nu}_\mu}(y) = \frac{5}{3} - 3y^2 + \frac{4}{3}y^3 , \quad (3\text{-}18)$$

and

$$F_{\mu^{\pm}\to\overset{(-)}{\nu}_e}(y) = 2 - 6y^2 + 4y^3 \,. \tag{3-19}$$

From these relations we can estimate the total energy drainage from the initial photon to neutrinos. By a simple inspection of the above formulae, on the average $\sim 65\%$ of the energy of a photon at the time of MPP goes to neutrinos.

The neutrino spectrum from pion decay, given a pion energy distribution $\mathrm{d}N_{\pi^{\pm}}/\mathrm{d}E_{\pi^{\pm}}$, consists of two distinct contributions to the final neutrino flux: (i) the monoenergetic (anti)muon neutrino emitted directly from the pion decay $\pi^{\pm} \to \mu^{\pm}\nu_{\mu}(\bar{\nu}_{\mu})$,

$$\frac{\mathrm{d}N_{\nu}}{\mathrm{d}E_{\nu}}(E_{\nu}) = \int_{E_{\pi,\min}}^{E_{\pi,\max}} \mathrm{d}E_{\pi}\, \frac{\mathrm{d}N_{\pi^{\pm}}}{\mathrm{d}E_{\pi^{\pm}}}\, F_{\pi^{\pm}\to\overset{(-)}{\nu}_{\mu}}(E_{\pi}; E_{\nu}) \,, \tag{3-20}$$

where

$$F_{\pi^{\pm}\to\overset{(-)}{\nu}_{\mu}}(x) = \frac{1}{1-r_{\pi}}[1 - \theta(x - 1 + r_{\pi})] \,, \tag{3-21}$$

obeys the scaling in Eq. 3-17 and $r_{\pi} = (m_{\mu}/m_{\pi})^2$, and (ii) the neutrinos emitted in the subsequent muon decay. The latter can be obtained by convoluting

$$\frac{\mathrm{d}N_{\mu^{\pm}}}{\mathrm{d}E_{\mu^{\pm}}}(E_{\mu}) = \int_{E_{\pi,\min}}^{E_{\pi,\max}} \mathrm{d}E_{\pi}\, \frac{\mathrm{d}N_{\pi^{\pm}}}{\mathrm{d}E_{\pi^{\pm}}}\, F_{\pi^{\pm}\to\mu^{\pm}}(E_{\pi}; E_{\mu}) \,, \tag{3-22}$$

in Eq. 3-16, where

$$F_{\pi^{\pm}\to\mu^{\pm}}(x) = \frac{1}{1-r_{\pi}}\theta(x - r_{\pi}) \,. \tag{3-23}$$

The output files of the simulation together with a copy of the input file are written in the `/results/[DESTINATION_DIR]` directory, as we mentioned in section 3.4.1. After executing the neutrino flux computation command, the `nuSpec` and `nuSpec_Weight` will be fed by the copied input files and the muons and pions tables. The neutrino fluxes (all-flavor and the ν_e, ν_{μ} and ν_{τ} flavors separately) at the Earth are computed by using the neutrino spectra from muon and pion decays (Eqs. 3-16 and 3-20) and taking into account neutrino decoherent oscillation with mixing parameters fixed to the best fit parameters from (279) and (280).

The neutrino spectra files provide the sum of the neutrino and anti-neutrino fluxes produced in the course of cascade evolution. Due to the matter-antimatter symmetry of the processes, the individual neutrino or anti-neutrino flux is simply half of the total flux.

The module `nuSpec_Weight` performs the weighting of the neutrino flux according to the injected high energy photon spectrum. The weights, normalizing the neutrinos spectrum in accordance with the number of photons injected in each bin of injected photon spectrum, are defined by

$$w_i = \frac{\int_{E_{i-1}}^{E_i} f(E)\mathrm{d}E}{\int_{E_{\min}}^{E_{\max}} f(E)\mathrm{d}E}\,, \tag{3-24}$$

where $f(E)$ is the injected photon spectrum, E_i and E_{i-1} are the bin edges of the i-th bin, $E_{\min}$ = `INJ_Emin` and $E_{\max}$ = `INJ_Emax`. For the power-law spectrum

$$f(E) = E^{-\alpha}\exp(-k_{\rm hc}E/E_{\rm hc})\exp(-k_{\rm lc}E_{\rm lc}/E)\ ,$$

where α = `INJ_SPEC_Index`, $E_{\rm hc}$ = `ExpCut_HighEnergy`, $E_{\rm lc}$ = `ExpCut_LowEnergy` and $k_{\rm hc/lc} = 1$ (0) if `EXP_HIGH_CUTOFF`/`EXP_LOW_CUTOFF` are set to `ON` (`OFF`). The power-law spectrum, with or without cutoff, is taken care of by the module automatically; instead, for a general injected spectrum $f(E)$, the user can perform the weighting by a separate script. An example of $f(E)$ different than the power-law is given in section 3.5.2.

It is important to note that the current version of `MUNHECA` neither tracks particle trajectories nor accounts for their propagation length. The only parameter that halts cascade development within `MUNHECA` is `BREAK_Energy`. Therefore, when modeling electromagnetic cascades in astrophysical environments where photons may escape before degrading to the MPP energy threshold, it is crucial to estimate an appropriate `BREAK_Energy` to obtain a realistic neutrino spectrum. Addressing this limitation, as well as incorporating the effects of magnetic fields and other refinements, is planned for future versions of the code.

3.5 Case Studies

In this section we illustrate the capabilities of `MUNHECA` by applying it to two cases of astrophysical interest. In section 3.5.1, we compute the neutrino spectrum from the electromagnetic cascade for the propagation of ultra high energy monochromatic photons over cosmological distances at high redshift and discuss the consequences of the included processes. Section 3.5.2 is devoted to the cascade development inside an astrophysical source, re-evaluating the neutrino yields for the model proposed by (25) for the neutrino source NGC1068 with the more complete physics incorporated in `MUNHECA`.

3.5.1 Monochromatic Photon Injection

To explore the role of discussed interaction channels during cascade development, we calculate the neutrino spectrum produced by ultra-high-energy monochromatic photons propagating over cosmological distances interacting

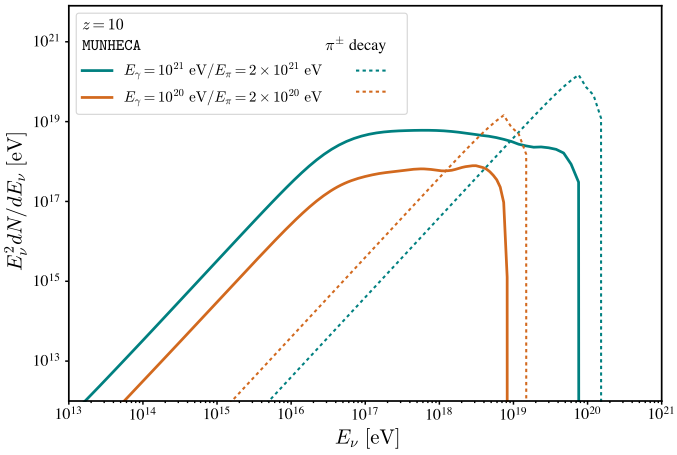

Figure 3.18

with CMB. This simulation incorporates MPP, DPP, EMPP, and CPPP, alongside the conventional cascade interactions (EPP and ICS).

The input parameters for the simulation are as follows:

```
MPP: ON
DPP: ON
EMPP: ON
CPPP: ON
Source: CMB
Redshift: 10
INJ_Spectrum: Monochrome
E_gamma: 1e+21
Number_of_photons: 5000
BREAK_Energy: 1.1e+17
```

We initialize the cascade with 5000 photons, each with an energy of $E_\gamma = 10^{21}$ eV, injected at $z = 10$. Running this configuration on a single core of an Intel(R) 12th Gen i7-12700K processor requires approximately 5 hours.

The solid green curve in Figure. 3.18 illustrates the neutrino spectrum produced in this scenario at Earth. For comparison, the neutrino spectrum resulting from the conventional hadronic process of charged pion decay is depicted by the dotted green curve. To explore the dependence on injection energy, Figure. 3.18 also includes the spectra for UHE photons of energy $E_\gamma = 10^{20}$ eV injected at $z = 10$.

The important feature of neutrino spectrum from the electromagnetic cascade is their dominance over the hadronic neutrino spectrum at lower

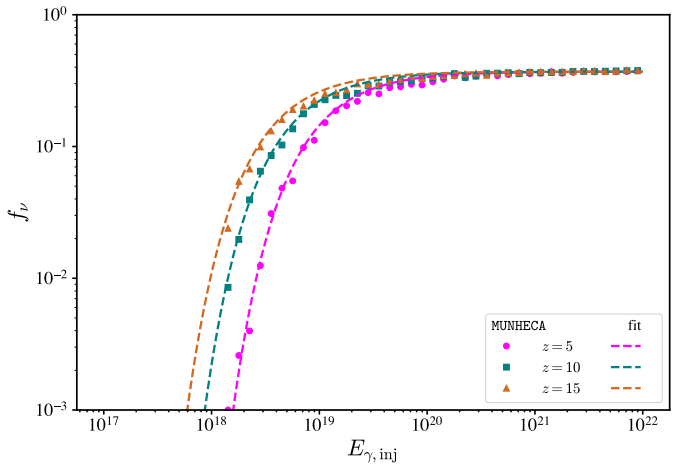

Figure 3.19: Energy fraction f_ν as a function of the injection energy $E_{\gamma,\mathrm{inj}}$ for monoenergetic photons cascading down to the MPP threshold at different redshifts. Each data point represents a simulation with 5000 injected photons at the specified energy and redshift. The dashed lines correspond to the fitting function described in Eq. 3-26.

energies by one to two orders of magnitude as it is evidence from Figure. 3.18.

Another quantity of main interest for phenomenology is the fraction of the initial photon energy channeled into neutrinos, f_ν. This quantity can be obtained by

$$f_\nu = \frac{1}{E_{\gamma,\mathrm{inj}}} \int E_\nu \frac{\mathrm{d}N}{\mathrm{d}E_\nu} \mathrm{d}E_\nu \,. \tag{3-25}$$

The energy fraction f_ν for monoenergetic photons injected into MUNHECA at various redshifts is presented in Figure 3.19 as a function of the injection energy. Each data point corresponds to a simulation run with 5000 photons injected at the specified energy and redshift, cascading down to the MPP threshold energy. The dashed lines in the figure represent a fitting function for f_ν, given by:

$$f_\nu(E_{\gamma,\mathrm{inj}}, z) = f_{\max} \exp\left[-\frac{0.8\, E_{\mathrm{cut}}}{E_{\gamma,\mathrm{inj}}}\right] , \tag{3-26}$$

where $f_{\max} \approx 0.37$ is the maximum fraction of energy channels to neutrinos and $E_{\mathrm{cut}} = 4m_\mu^2/\epsilon_b = 4m_\mu^2/\langle\epsilon_{\mathrm{CMB}}\rangle$ with ϵ_b being the typical energy of the background photon field. The simplicity of expressing the neutrino energy fraction as a fit dependent only on two parameters, $(E_\gamma, \epsilon_\gamma)$, stems from the fact that the "cascade development stage" is governed entirely by the CoM energy squared. At these energies, s scales with the product of the incident and target particle energies—for instance, in the case of EPP, $s \propto E_\gamma \epsilon_b$. What this implies is that if we maintain a constant CoM energy, s = const., but

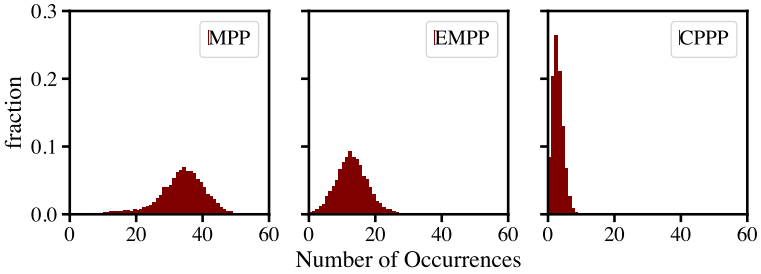

Figure 3.20: The distribution of the occurrences of MPP, EMPP and CPPP in 5000 realization of photon injection at $z = 10$ with energy $E_\gamma = 10^{21}$ eV.

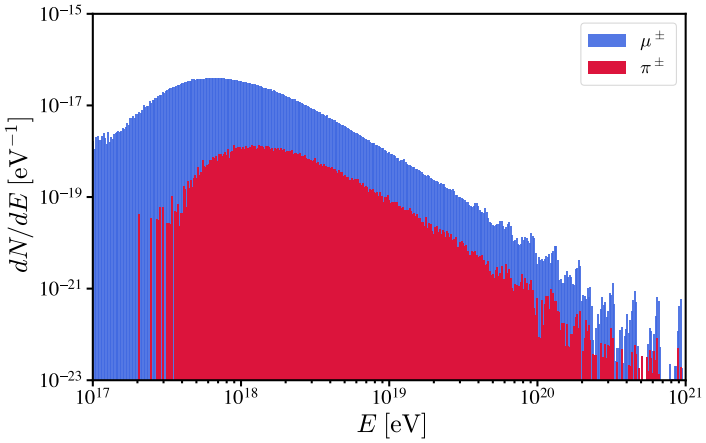

Figure 3.21: The spectra of muons and pions generated in the evolution of a cascade initiated by the injection of monochromatic photons with energy $E_\gamma = 10^{21}$ eV at redshift $z = 10$.

transition to a system with higher target photon energies and correspondingly lower incident photon energies, the cascade development will proceed in the same manner and the fitting relation in Eq. 3-26 remains applicable under such conditions.

The occurrences of muon and pion producing processes (that is, MPP, EMPP and CPPP) as well as their spectra can be obtained from the corresponding output files. For a photon of energy $E_\gamma = 10^{21}$ eV injected at $z = 10$, the occurrences and spectra of muons and pions are shown respectively in Figures 3.20 and 3.21. The multiple muon production in the cascade evolution can be inferred from Figure 3.20 with the dominant process being MPP, while the EMPP and CPPP have subleading contributions, respectively $\sim$ 37% and $\sim$ 8% with respect to MPP. The resemblance between muons and pions spectra in Figure 3.21 is a consequence of treating the CPPP within the Born approximation.

The spectra of electrons and photons generated below the chosen break energy 1.1×10^{17} eV are shown respectively by the blue and red histograms in Figure 3.22. These spectra can be obtained from `Electron_Output` and

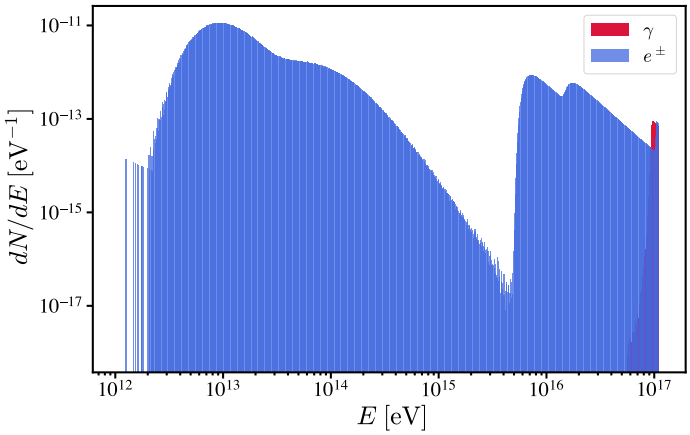

Figure 3.22: The electrons/positrons and photons spectra below the break energy 1.1×10^{17} eV for monochromatic photons injected at redshift $z = 10$ with energy $E_\gamma = 10^{21}$ eV (the case for the solid blue curve in Figure 3.18).

`Gamma_Output` files, that contain the number of electrons and photons per bin, by normalizing to the number of injected photons and dividing by the bin size. The extension of the electron spectrum to lower energies, in comparison with photon one, is mainly a consequence of DPP process and its large inelasticity while the electrons from muon decay and EMPP also contribute. Let us emphasize that the inclusion of the ETP process, while leaving almost unchanged the neutrino yield from the cascade evolution, does have an effect on the spectrum of $e^\pm$ at low energies, $E \lesssim \text{few} \times 10^{15}$ eV, since the $e^\pm$ produced via ETP land in this range.

Another implication worth commenting upon is that the process discussed here alters the multi-messenger γ-ν correlation. As we discussed in Section. 1.3.6, the conventional production scenarios arising from pp or $p\gamma$ interactions in an UHE astrophysical source predict that the neutrino and gamma ray emission spectra are related by

$$\varepsilon_\gamma \frac{\mathrm{d}N_\gamma}{\mathrm{d}\varepsilon_\gamma} = \frac{1}{3K_\pi} \left[\varepsilon_\nu \frac{\mathrm{d}N_\nu}{\mathrm{d}\varepsilon_\nu} \right]_{\varepsilon_\nu = \varepsilon_\gamma/2} , \tag{3-27}$$

where $K_\pi \approx 1\,(1/2)$ is the charged to neutral pion ratio in the $pp\,(p\gamma)$ process. Integrating both sides of Eq. 3-27 over energy implies that, at the source, the ratio of total energies in γ's and ν's obeys $\mathcal{E}_\gamma \simeq 2/3\,(4/3)\,\mathcal{E}_\nu$. The net effect of MPP is to alter this ratio towards the neutrino sector: For example, from Figure 3.19 we read that for a source emitting 10^{21} eV gammas/neutrinos at $z = 5$, approximately 37% of the initial photon energy is transferred to neutrinos during the cascade above MPP threshold; naively, the new balance would be $\mathcal{E}'_\gamma \to 0.63\mathcal{E}_\gamma$, $\mathcal{E}'_\nu \to (1 + 0.37 \times 2/3\,(4/3))\,\mathcal{E}_\nu$, hence $\mathcal{E}'_\gamma/\mathcal{E}'_\nu \simeq 0.34\,(0.56)$, i.e. a ratio changed by a factor of ~ 2. The actual energy budget ending up in

the low energy diffuse photon flux is more complicated to compute, since one must account for the contribution seeded by $e^{\pm}$ from charged pion decays, as well as the fraction of the electromagnetic cascade channelled away by $e^{\pm}$. However, this simple calculation shows that the role of MPP is to make UHE sources at high redshift *darker* than their low-z counterparts even in indirect electromagnetic signals, while making them correspondingly *brighter* in the UHE neutrino signal.

3.5.2 Cascade inside the source: NGC 1068

As an example of cascade development inside an astrophysical source, here we consider the recent proposal of neutrino production in the leptonic model of NGC1068 (25). The high energy photons, which initiate the cascade, are assumed to have a power-law spectrum with a high energy cut-off dictated by the production mechanism of these photons. For the scenario where high energy photons are produced via synchrotron radiation of high energy electrons, as is shown in (25), the spectrum takes the form $P(E_\gamma) = E_\gamma^{-1.5} \exp\left[\sqrt{2\pi m_e^3 E_\gamma / eB}/(300\,\mathrm{TeV})\right]$, where m_e and e are respectively the electron's mass and charge, and $B = 5$ kG is the magnetic field intensity at the production site. The target photons are the X-rays in the hot corona with a thermal (black-body) distribution with the temperature $T_X = 1$ keV. For this temperature, the MPP can happen for $E_\gamma \gtrsim 10$ TeV and hence we choose a sharp low energy cutoff on $P(E_\gamma)$ equal to 1 TeV. The form of $P(E_\gamma)$ does not match to any of the predefined spectra described in section 3.4.2 and the method explained in section 3.4.4 should be applied. In this line, the energy range of $(1-300)$ TeV is divided into 40 bins (logarithmically spaced) and $2,000$ photons are injected in each bin. The resulting neutrino spectrum can be calculated according to Eq. 3-24 and is shown by the solid red curve in Figure 3.23. For comparison, the computed neutrino spectrum in (25) is depicted by dashed black curve. As in (25) the curves of Figure 3.23 are normalized such that the total power injected above 1 TeV is 1.2×10^{43} erg/s. Although the overall shapes of the neutrino spectra from (25) and MUNHECA are grossly in agreement near the peak of the flux, a few remarks on their differences are in order. The computation of neutrino spectrum in (25) is based on a few approximations: the DPP, CPPP and EMTP are not taken into account, the inelasticity in MPP is taken to be equal to 50%, multiple muon production is neglected and the neutrino spectrum in muon decay is approximated as monochromatic. To roughly mimic this setup by MUNHECA, we turn off all the processes except MPP and modify the MPP's inelasticity and the produced

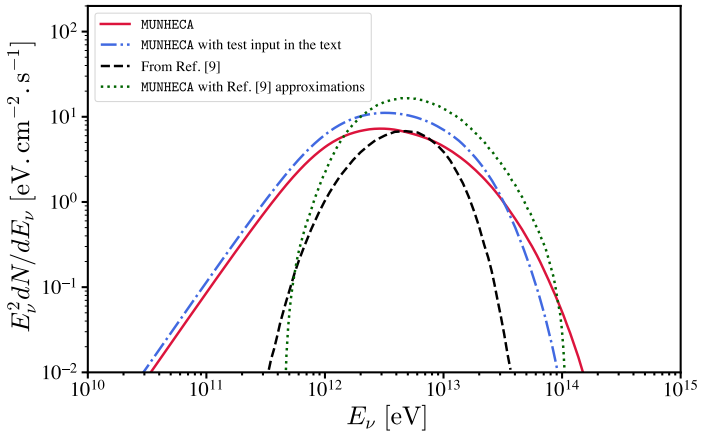

Figure 3.23: Neutrino yield in the interaction of a spectrum of high energy photons with target photons of black-body distribution. The result of MUNHECA is shown by the solid red curve and compared with the dashed black curve taken from (25). The dotted green curve shows an attempt to reproduce the dashed black curve by modifying MUNHECA to incorporate the adopted approximations of (25) (see the text for details). The dot-dashed blue curve depicts the neutrino spectrum for the input file discussed in the text.

neutrino spectrum in muon decay. In this way, all the approximations of (25) are imitated except the muon production multiplicity and the result is shown by the dotted green curve in Figure 3.23 which resembles indeed more closely the dashed black curve. We conclude that, while simplified calculations might lead to correct order of magnitude results near the peak of the spectrum, especially in the low- and high-energy tails a more precise treatment, such as allowed by MUNHECA, is essential for reliable predictions.

To provide an example of the input file for cascade evolution inside an astrophysical source, let us consider the power-law spectrum with exponential cutoff $E_\gamma^{-1.5} \exp[-E_\gamma/(20\,\mathrm{TeV})]$ which closely approximates the $P(E_\gamma)$ of (25). The input file of MUNHECA for this spectrum is:

```
Source: BlackBody
Temperature: 1e+3
BB_E_min: 1.0
BB_E_max: 4.e+4
Redshift: 0.003
INJ_Spectrum: PowerLaw
BREAK_Energy: 1.e+11
INJ_Emin: 1e+12
INJ_Emax: 3e+14
INJ_SPEC_Index: 1.5
EXP_HIGH_CUTOFF: ON
```

```
EXP_LOW_CUTOFF: OFF
ExpCut_HighEnergy: 2.e+13
PHOTON_PER_BIN: 2000
NUMBER_OF_BINS: 40
```

where the range $(1\,\mathrm{eV} - 40\,\mathrm{keV})$ for black-body distribution of target photons is considered and the break energy is set to 0.1 TeV. For this input the runtime on Intel i7 processor is $\sim$ 26 hours. The output of MUNHECA from the above input is shown by the dot-dashed blue curve in Figure 3.23.

Before closing this section, let us briefly comment on the scenario proposed in (25). If intended as a "one zone model", in the case of high energy photon production via synchrotron radiation, the required large magnetic field $\sim$ kG will dramatically change the cascade evolution and hence the neutrino yield. All the $e^{\pm}$ during the cascade evolution suffer energy loss through synchrotron radiation before making ICS or EMPP, which effectively shortens the energy loss length of leading particles and consequently suppress the muon and neutrino production. Thus, for a consistent treatment, the effect of magnetic field on cascade development should be taken into account; we are considering elaborating on it in a future update of MUNHECA. For our current purpose, the neutrino spectrum depicted in Figure 3.23 is valid for scenarios where the spectrum $P(E_\gamma)$ of high energy photons is generated by a mechanism different than synchrotron radiation, such as the ICS of high energy electrons on low energy target photons (25); or, it can be thought of as resulting from an effective multi-zone model, where the magnetic field threading the target photon environment is negligibly low compared to the photon source one.

3.6 The Universal Form of the Neutrino Spectrum

Among the three assumptions discussed in Section 1.5.3, the condition of complete cascade development is the cornerstone for obtaining a universal function, as a fully developed cascade achieves a saturated state. The first assumption in Section 1.5.3 helps identify the breakpoints of the power-law spectrum, while the third assumption together with the second one —complete development— enable the normalization of the spectrum, which reflects the cascade's total energy budget.

Extending this reasoning, a universal neutrino spectrum can also be established for electromagnetic cascades under a similar key assumption: *The cascade develops fully down to the MPP threshold; meaning no further neutrino production.* While the number of contributing processes in this scenario is significantly larger than those addressed in Chapter 1, focusing on

the most dominant interactions—EPP, DPP, and MPP—provides a reasonable expectation for the behavior of the neutrino spectrum. Subsequently, the spectrum's turning points and indices can be fit.

As shown in Figure 3.16, the EPP process dominates at low energies, while at the highest energies, the DPP becomes the leading $\gamma\gamma$ interaction. Between these extremes lies an intermediate energy range where the MPP has its maximum impact. Consequently, we expect two breakpoints in the neutrino spectrum's index, denoted as $E_{\rm br,1}$ and $E_{\rm br,2}$. Below $E_{\rm br,1}$, neutrino production is negligible, and the spectral index should approximately match that of neutrinos from muon decay. Above $E_{\rm br,2}$, neutrino production declines due to the dominance of the DPP process; however, the spectral index in this regime cannot be straightforwardly predicted. The spectrum can therefore be expressed as:

$$\mathcal{G}_\nu = \begin{cases} (E_\nu/E_{\rm br,1})^{-\alpha_l} & (E < E_{\rm br,1}) \\ (E_\nu/E_{\rm br,1})^{-\alpha_m} & (E_{\rm br,1} < E < E_{\rm br,2}) \\ (E_{\rm br,2}/E_{\rm br,1})^{-\alpha_m}(E_\nu/E_{\rm br,2})^{-\alpha_h} & (E_{\rm br,2} < E < E_{\rm inj}) \end{cases} . \tag{3-28}$$

It should be noted that the above expression assumes the injected photon energy satisfies $E_{\rm inj} > E_{\rm br,2}$. For cases where $E_{\rm inj} < E_{\rm br,2}$, the spectrum is given by:

$$\mathcal{G}_\nu = \begin{cases} (E_\nu/E_{\rm br,1})^{-\alpha_l} & (E_\nu < E_{\rm br,1}) \\ (E_\nu/E_{\rm br,1})^{-\alpha_m} & (E_{\rm br,1} < E_\nu < E_{\rm inj}) \end{cases} . \tag{3-29}$$

From the numerical results obtained using `MUNHECA`, the breaking points are determined to be $E_{\rm br,1} = m_\mu^2/(3\epsilon_b)$ and $E_{\rm br,2} \approx 2 \times 10^{17}$ eV$^2/\epsilon_b$, where ϵ_b represents the typical energy of the target photons. The spectral indices corresponding to different energy ranges are $\alpha_l = 0.05$, $\alpha_m = 2.0$, and $\alpha_h = 2.5$. Note that the fit obtained here is specifically for interactions with a blackbody target photon field and Eqs. 3-28 and 3-29 are not applicable to other types of low-energy photon spectra.

The normalization factor, $\mathcal{N}$, similar to what discussed in Section 1.5.3, is determined by the energy budget of the sector under consideration—in this case, neutrinos. This energy budget has already been obtained in Eq. 3-26. Thus, the normalization can be given by:

$$\mathcal{N} = f_\nu(E_{\gamma,\rm inj}, z)E_{\gamma,\rm inj}/\mathcal{I} , \tag{3-30}$$

where $\mathcal{I}$ is given by

$$\mathcal{I} = \int E_\nu \mathcal{G}_\nu \, \mathrm{d}E_\nu = \left[\frac{E_{\mathrm{br},1}^2}{2-\alpha_l} + E_{\mathrm{br},1}^2 \ln\left(\frac{E_{\mathrm{br},2}}{E_{\mathrm{br},1}}\right) - \frac{1}{2-\alpha_h}\left(\frac{E_{\mathrm{br},2}}{E_{\mathrm{br},1}}\right)^{-\alpha_m}\left[E_{\mathrm{br},2}^2 - E_{\mathrm{inj}}^2\left(\frac{E_{\mathrm{inj}}}{E_{\mathrm{br},2}}\right)^{-\alpha_h}\right]\right] , \tag{3-31}$$

for the case $E_{\mathrm{br},2} < E_{\mathrm{inj}}$, and

$$\mathcal{I} = \left[\frac{E_{\mathrm{br},1}^2}{2-\alpha_l} + E_{\mathrm{br},1}^2 \ln\left(\frac{E_{\mathrm{inj}}}{E_{\mathrm{br},1}}\right)\right] , \tag{3-32}$$

for the case $E_{\mathrm{br},2} > E_{\mathrm{inj}}$.

Note that the "energy conservation" condition in the conventional electromagnetic cascade analysis, is a manifestation of Eq. 3-30. In the case of a conventional electromagnetic cascade, the "complete development" implies that, in the low-energy regime, electron/positron production ceases. Furthermore, in this regime, the energy carried by electrons/positrons is transferred to photons via ICS. Consequently, assuming no energy leakage within the cascade, the energy fraction of the photon sector becomes $f_\gamma \approx 1$. Thus, the energy conservation condition essentially determines the energy budget of the cascaded photon spectrum. In contrast, here we computed the energy fraction for neutrinos numerically and derived a corresponding fit.

The merit of the proposed fit, is illustrated in Figure. 3.24 in the cosmological distance propagation in various redshifts and injected energies.

While the neutrino spectrum from cascades can be numerically computed using `MUNHECA`, the universal spectrum proposed here offers significant advantages. It provides not only an analytic understanding of the spectrum but also a practical tool for estimating expected results across various problems. In many cases, instead of running time-intensive Monte Carlo simulations, the universal function can deliver sufficient and efficient estimations.

3.7 Discussion and Summary

In the course of the evolution of ultra high energy electromagnetic cascades, a fraction of energy drains into the neutrino channels, providing a new opportunity in probing the high-redshift and high energy universe via a multimessenger approach. The cascade can occur either inside an astrophysical source, where the high energy photons/electrons interact with the radiation in the source, or along the cosmological propagation of ultra high energy photons/electrons interacting with the CMB photons. The former offers a

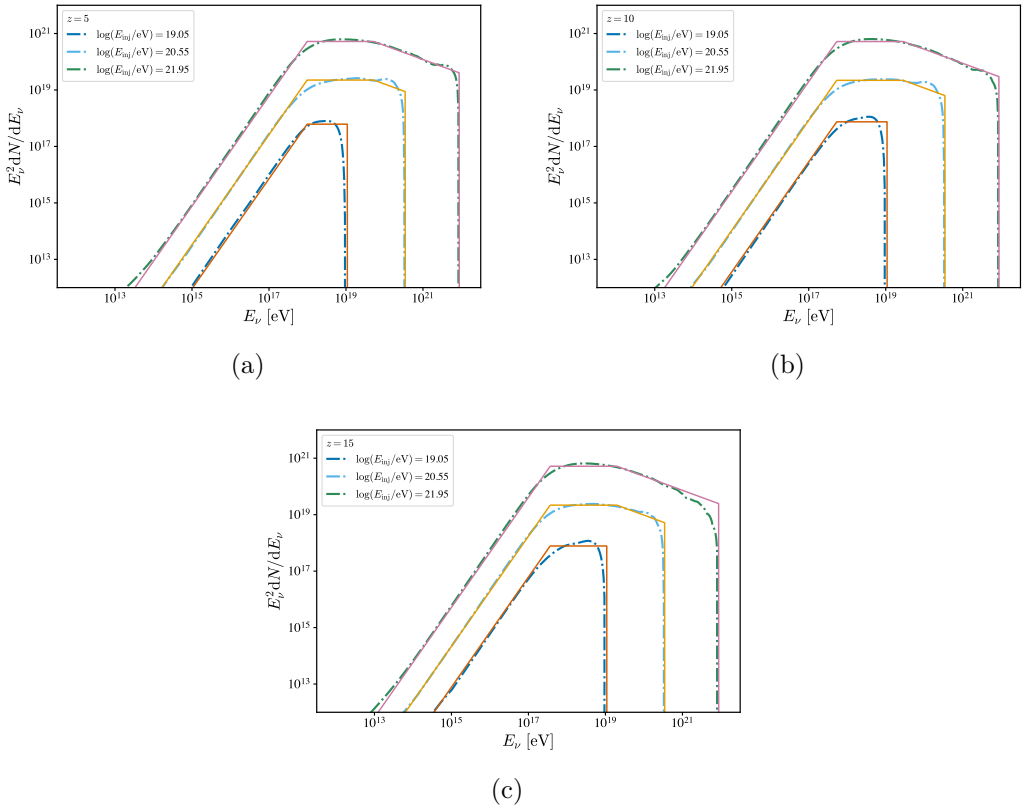

Figure 3.24: Neutrino spectra from electromagnetic cascade development over cosmological distances, computed using `MUNHECA` (dot-dashed lines), compared with the universal function proposed in Section 3.6 (solid lines) for different redshifts and initial photon energies. See text for details.

purely leptonic model for neutrino production inside the sources, while the latter is an alternative source of the ultra high energy diffuse neutrinos beside the conventional hadronic processes leading to cosmogenic neutrinos. In both cases, the generated neutrino flux, either from a population of sources or a single source, can be within the reach of present or near future neutrino observatories such as IceCube-Gen2 (281) and GRAND (282). Thus, it is timely to assess the cascade evolution more thoroughly by including the important micro-physics of muon and pion producing processes.

We introduced `MUNHECA`, a public code in `python3`, which facilitates the computation of neutrino yield in the cascade evolution, accounting for the EPP, ICS, MPP, CPPP, DPP and EMPP processes. In addition, the last two processes have been re-evaluated more accurately. The code structure and options, which include the control over the injection spectra, the choice of background photon field and the processes accounted for, are described in detail in this chapter. These options make `MUNHECA` a cascade simulator that can be applied to a variety of standard or exotic scenarios. As a concrete example of an astrophysical scenario worth exploring, we can mention the (still

largely uncertain) birth and assembly processes of Super Massive Black Holes (SMBHs) at high redshift (283, 284). These objects are notoriously difficult to study, but a peculiar ultra-high energy neutrino flux may offer another handle to constrain or detect them. As an example of exotic processes, we can think of the neutrino and gamma ray fluxes associated to the decay of Super Heavy Dark Matter (SHDM) particles, notably its extragalactic flux component. In these scenarios the unstable dark matter particles can have masses exceeding $m_\chi \gtrsim 10^{18}$ eV and the processes considered here may be relevant, in particular when the dark matter is mostly or exclusively coupled to leptons, but have not been considered in the literature so far.

Compared with earlier and more simplified computations of the neutrino yield, the neutrino flux from `MUNHECA` is markedly different especially in the low-energy tail of the spectrum, which is however of utmost importance since typically easier to explore experimentally. We believe that the current version of the code is enriched enough for it to be realistic at least in applications to high-z diffuse fluxes in the baseline cosmological scenarios, as discussed in ref. (34). Further improvements in the `MUNHECA` may be envisaged. One direction is to include a better treatment of the pion production mechanisms, going beyond Born approximation and including for instance hadronic resonances. Another avenue is to extend the cosmological cascade treatment to cases where an exotic magnetic field of cosmological origin is present: We anticipate diminishing the importance of muon-rich cascades in this case, but it would be interesting to establish the parameter space. Further, one may think of treating the cascade development in 3D: This is not particularly important for the currently considered unmagnetized cosmological application or single zone astrophysical modeling, but would be crucial if including a magnetic field, notably for multi-zone astrophysical scenarios, where the charged particle acceleration region and the secondary production one are spatially distinct and the high-energy particle flux is anisotropic. These extensions would further benefit of cross-validation with other existing codes accounting for cascade processes in the presence of a magnetic field, such as `PRESHOWER` (285).

4
A Closer scrutiny of cosmic ray proton energy losses

This chapter focuses on analyzing processes that impact the propagation of low-energy cosmic rays (CRs) within the percent-level precision, based on (36). Specifically, we examine energy-loss mechanisms affecting low-energy CR protons in the range of $\sim 0.1 - 5$ GeV, where experimental uncertainties are minimal, and collisional effects become comparatively more significant than collisionless transport mechanisms. This study addresses three main aspects:

i) A quantitative evaluation of the nuclear elastic cross section, providing, for the first time, analytical expressions for the stopping power and inelasticity. ii) An assessment of the errors introduced by approximating both elastic and pion-production inelastic interactions as continuous energy loss processes, rather than treating them as catastrophic events—an assumption commonly employed in modern numerical models. iii) An exploration of sub-leading effects, including relativistic corrections, radiative contributions, and medium effects in ionization energy losses.

4.1
Motivation

Over the past decade, a wealth of balloon-borne and space-borne detectors has ushered the study of Galactic cosmic rays (CR) into a precision era, stimulating numerous new questions on the underlying physics (for reviews, see e.g. (286, 287, 288, 289)). This also allows one to tackle some important applications in astroparticle physics with a sharpened diagnostic tool: A notable example is provided by the impact that a refined understanding and error budget of antiproton CR (290, 291, 292, 293) has on constraints on weakly interacting dark matter particles (294, 295, 296, 297).

In particular, we have recently witnessed both a remarkable reduction of errors and an extension of the dynamical range covered by the data: In these respects, AMS-02 [1] measured proton fluxes have a statistical precision often below the permille level, and the overall systematic errors are typically estimated at the 1% level (298). Additionally, the Voyager mission has provided a notable advance by acquiring sub-GeV CR data beyond the heliosphere for the first time, free of solar modulation effects (299). To get the most out of the newly acquired diagnostic power, this reduction in the size of experimental errors must be accompanied by a refinement in theoretical errors.

[1] https://ams02.space

One important ingredient in that direction consists in nuclear, hadronic and particle physics cross sections (for the context of collisional vs. collisionless effects shaping the CR dynamics, see e.g. the lecture notes (300)). The limitations of current libraries, ultimately due to scarce and sparse data, are well-known, and extensively studied for spallation cross sections (301, 302, 303). This has stimulated meetings between collider physicists, CR experimentalists, and theorists to advance knowledge in this direction, such as the `Cross sections for Cosmic Rays` series at CERN [2]. In this context, a more overlooked direction consists in assessing how much of *known* physics is actually included in current CR treatments. In the past decade, some efforts have been made towards a better modeling of yields of secondary particles in CR collisions, see e.g. (27, 304, 305). Here we tackle a somewhat complementary avenue towards this precision goal, focusing on the description of *energy-losses*, along three directions:

i) We revisit the processes affecting protons in the low-energy regime in particular below 5 GeV, which is where losses are most relevant compared to diffusive transport phenomena, and CR data have the best precision. We provide for the first time a realistic assessment of proton-proton nuclear elastic energy losses, only qualitatively gauged as unimportant in the past (see e.g. the comments in (306) or on the `USINE` propagation code webpage). We provide our results in rather compact analytical formulae, which should be included in propagation-loss treatments aiming at reaching percent-level predictions around 1 GeV.

ii) Additionally, we notice that all current popular CR codes (such as `GALPROP` [3](307), `DRAGON` [4], `USINE` [5](308), and `PICARD` [6](309)) deal with *pp* inelastic cross sections as a continuous energy loss channel, typically relying on the analytical formulation for the stopping power reported in (310). We gauge the accuracy of this approximation, both for the inelastic and elastic channels, and find it insufficient for current precision, leading to $\sim 3\%$ errors. An iterative scheme for more correctly incorporating catastrophic losses is presented.

iii) As an ancillary task, we also assess the level of error committed when neglecting sub-leading effects in ionization losses which, contrary to the above-mentioned processes, are electromagnetic in nature. These corrections to the leading effects (typically included by relying on the formulae presented

[2]The website of the latest in the series is at https://indico.cern.ch/event/1377509/
[3]https://galprop.stanford.edu
[4]https://github.com/cosmicrays
[5]https://lpsc.in2p3.fr/usine
[6]https://astro-staff.uibk.ac.at/~kissmrbu/Picard.html

in (311)) are often small, at the 0.1% level for protons, and may still be neglected. We note, however, that they are expected to be one order of magnitude bigger for iron, and neglecting them becomes then more questionable, especially for the precision expected in future measurements.

Through this chapter, in Section. 4.2 presents the main analytical results, focusing on the treatment of elastic *pp* energy losses. Section .4.3 details the semi-analytical model used to evaluate the effects on CR energy fluxes, including the adopted approximations and iterative schemes. The primary results are discussed in Sec.4.4, while Section 4.5 offers a brief overview of subleading effects in ionization energy losses for both protons and Fe nuclei. Finally, in Sextion 4.6 we outline our conclusions and provides perspectives for future research.

4.2
Proton-Proton Elastic Cross Section and Cosmic Ray Energy Losses

The essential ingredients required to leverage a two-body scattering process, $1 + 2 \rightarrow 3 + 4$, within the transport equation are the total and differential cross sections associated with the process. In Section. 4.2.1, we report the expressions for such cross sections for the *pp*-elastic process. In Section. 4.2.2, based on these results, we derive analytical relations for its *Mass Stopping Power* and Inelasticity, crucial derived quantities to incorporate into the transport equation, and compare the magnitude of the stopping power for elastic process to the other processes already accounted for.

4.2.1
The differential elastic *pp* cross section.

As a preliminary step, we review the expressions of the Mandelstam variables, s, u and t, in terms of the incident particle's momentum $p_{\rm lab}$, the i-th body kinetic energy K_i and the transferred energy $W \equiv E_1 - E_3 = K_1 - K_3$. In the Lab frame, where the body 2 is at rest, for the $p + p \rightarrow p + p$ reaction energy conservation implies

$$E_1 + m_p = E_3 + E_4\,, \tag{4-1}$$

and one has additionally

$$t = (p_1 - p_3)^2 = (p_2 - p_4)^2 = 2m_p^2 - 2m_p E_4 = -2m_p(E_4 - m_p) = -2m_p K_4\,, \tag{4-2}$$

where $E_i = K_i + m_p$ is the i-th proton's total energy. The other variables of interest write $W = -t/2m_p$, $s = 2m_p\left(m_p + \sqrt{m_p^2 + p_{\rm lab}^2}\right) = 2m_p(2m_p + K)$,

and $u = -2m_pK_3$. Henceforth, we denote the kinetic energy of the projectile in the Lab frame simply as K.

The *pp*-elastic differential cross section can be parameterized in terms of the Mandelstam variables as (26) [7]

$$\frac{\mathrm{d}\sigma}{\mathrm{d}t} = \mathcal{A}(s)\left[e^{B_{pp}(s)\,t} + e^{B_{pp}(s)\,u}\right], \tag{4-3}$$

where we adopt the parameterization given in Eq. (8) of ref. (26), in units $[(\mathrm{GeV/c})^{-2}]$:

$$B_{\mathrm{pp}} = \begin{cases} \frac{5.5p_{\mathrm{lab}}^8}{7.7+p_{\mathrm{lab}}^8} & (p_{\mathrm{lab}} < 2\ \mathrm{GeV/c^2}) \\ 5.334 + 0.67(p_{\mathrm{lab}} - 2) & (p_{\mathrm{lab}} > 2\ \mathrm{GeV/c^2}) \end{cases}. \tag{4-4}$$

The normalization factor $\mathcal{A}(s)$ in Eq. 4-3 can be determined by integrating the differential cross section over t to match the total elastic cross section σ_{el}, in turn parameterized in the following according to (26)

$$\sigma_{\mathrm{el}} = \begin{cases} 23.5 + 1000(p_{\mathrm{lab}} - 0.7)^4 & p_{\mathrm{lab}} < 0.8 \\ \frac{1250}{p_{\mathrm{lab}}+50} - 4(p_{\mathrm{lab}} - 1.3)^2 & 0.8 < p_{\mathrm{lab}} < 2 \\ \frac{77}{p_{\mathrm{lab}}+1.5} & p_{\mathrm{lab}} > 2 \end{cases}. \tag{4-5}$$

From the relation $t = -2m_pW$, we can write

$$\frac{\mathrm{d}\sigma}{\mathrm{d}W} = \frac{\mathrm{d}\sigma}{\mathrm{d}t}\frac{\mathrm{d}t}{\mathrm{d}W} = -2m_p\frac{\mathrm{d}\sigma}{\mathrm{d}t}. \tag{4-6}$$

Note that the Eq. 4-3 exhibits symmetry under the exchange of particles $3 \leftrightarrow 4$. This symmetry is expected, reflecting the indistinguishability of the final state protons. Thus, to obtain the energy loss rate and the average kinetic energy fraction carried by the leading outgoing proton, we need to restrict the transferred energy range to [0,$K/2$]. Hence

$$\begin{aligned} \sigma_{\mathrm{el}} = \int_0^{K/2} \mathrm{d}W\,\frac{\mathrm{d}\sigma}{\mathrm{d}W} = -2m_p\mathcal{A}\int_0^{K/2}\mathrm{d}W\,\left\{e^{-2m_pB_{\mathrm{pp}}W} + e^{-2m_pB_{\mathrm{pp}}(K-W)}\right\} \\ = -\frac{\mathcal{A}}{B_{pp}}\left(1 - e^{-2m_pB_{pp}K}\right), \end{aligned} \tag{4-7}$$

so that

$$\frac{\mathrm{d}\sigma}{\mathrm{d}W} = 2\sigma_{\mathrm{el}}\,B_{pp}m_p\frac{e^{-2m_pB_{\mathrm{pp}}W} + e^{-2m_pB_{\mathrm{pp}}(K-W)}}{1 - e^{-2m_pB_{pp}K}}\Theta\left(\frac{K}{2} - W\right). \tag{4-8}$$

This cross section, whose trend is illustrated in Figure. 4.1, is almost flat for non-relativistic proton energies, while more and more forward-peaked in the

[7] Here we are taking into account the symmetrized form, which is stated to be the correct one but not actually reported in (26). Also, we are neglecting the Coulomb term, which is negligible for measured CR energies $\gtrsim$0.1 GeV.

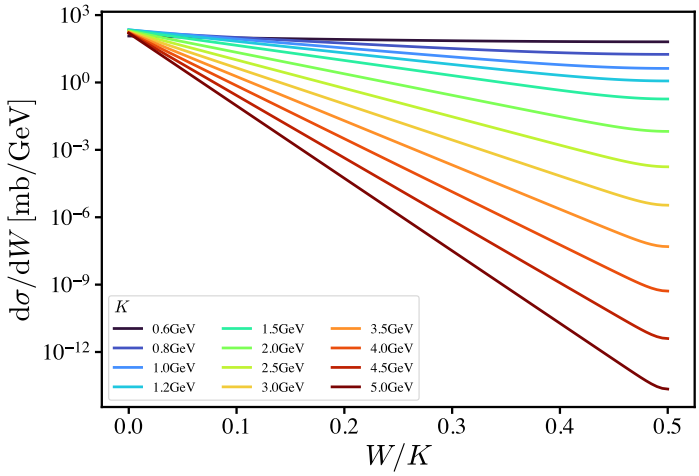

Figure 4.1: Differential energy-transfer cross section, Eq. 4-8, as a function of W/K.

relativistic limit, without however being accompanied by a significant growth of its normalization: We expect thus that the most prominent effect for energy losses is obtained at low-energies, as we confirm in the next section.

4.2.2 Stopping power and inelasticity

The primary input to assess the impact of any process onto CR energy losses is the Stopping power, which is defined for the process i as (See also Eq. 1-39 and its discussion)

$$\left(-\frac{\mathrm{d}E}{\mathrm{d}x}\right)_i = n\int_0^{K_{\max}} \mathrm{d}W W \frac{\mathrm{d}\sigma_i}{\mathrm{d}W}\,, \tag{4-9}$$

where n is the interstellar medium target density. Since nuclear effects are beyond our interest here, in the following a pure hydrogen composition is assumed.

Based on Eq. 4-8, we can compute:

$$\begin{aligned}\left(-\frac{\mathrm{d}E}{\mathrm{d}x}\right)_{\mathrm{el}} &= -2m_p n\mathcal{A}\int_0^{K/2}\mathrm{d}W\,W\,\left\{e^{-2m_pB_{\mathrm{pp}}W}+e^{-2m_pB_{\mathrm{pp}}(K-W)}\right\}\\ &= -\frac{n\mathcal{A}}{2B_{\mathrm{pp}}^2m_p}e^{-2m_pB_{\mathrm{pp}}K}\left(e^{m_pB_{\mathrm{pp}}K}-1\right)^2\,,\end{aligned} \tag{4-10}$$

and using Eq. 4-7, we obtain

$$\left(-\frac{\mathrm{d}E}{\mathrm{d}x}\right)_{\mathrm{el}} = \frac{n\,\sigma_{\mathrm{el}}}{2B_{pp}m_p}\tanh\left(\frac{B_{pp}m_pK}{2}\right)\,, \tag{4-11}$$

as well as

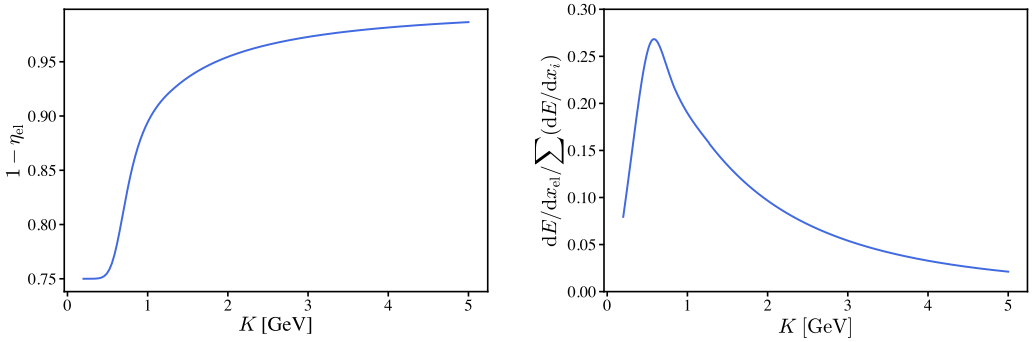

(a) (b)

Figure 4.2: (a) The average energy fraction retained in the collision, $1-\eta_{\rm el}$, from Eq. 4-12. (b) Relative weight of the elastic stopping power with respect to the total stopping power.

$$\eta_{\rm el} \equiv \frac{\langle W\rangle_{\rm el}}{K} = \frac{\int_0^{K/2} \mathrm{d}W\, W \frac{\mathrm{d}\sigma}{\mathrm{d}W}}{K\int_0^{K/2} \mathrm{d}W \frac{\mathrm{d}\sigma}{\mathrm{d}W}} = \frac{\tanh\left(\frac{B_{pp} m_p K}{2}\right)}{2B_{pp} m_p\, K}\,, \tag{4-12}$$

where we introduced the inelasticity η, such that $1-\eta$ is the average fraction of initial kinetic energy retained by the projectile after the collision. In Figure. 4.2a, we show this function vs. K for the elastic channel, computed according to Eq. 4-12: $\eta_{\rm el}$ is exceeding $\sim 10\%$ at $K \lesssim 1\,$GeV and is still of a few percent up to $\sim 5\,$GeV. In the following, we will focus on this energy range.

It is instructive to compare the above quantities with the analogue ones for competing processes. At low energies, the dominant CR proton loss channel is associated to ionization (and, to a less extent, Coulomb losses).

For the ionization stopping power, $(-\mathrm{d}E/\mathrm{d}x)_{\rm ion}$, we use the results from the code `Crange` [8], associated to the publication (312). See Section 4.5 for further details.

Above its kinematical threshold at $K \simeq 290\,$MeV (300), a key inelastic process affecting protons at low energies is (mostly single) pion production; its main effect is to drain on average $\kappa_\pi \simeq 17\%$ of the impinging proton kinetic energy into the produced pion, see (313, 314), so that the resulting downscattered nucleon retains a kinetic energy fraction $\eta_{\rm in} \equiv 1-\kappa_\pi$. The inelastic cross section is obtained from Ref. (26), subtracting from the total cross section in Eq. (1) the total elastic one in Eq. (5). Within this approximation, one has

$$\left(-\frac{\mathrm{d}E}{\mathrm{d}x}\right)_{\rm in} = n\,\sigma_{\rm in}\kappa_\pi K\,. \tag{4-13}$$

In Figure. 5.3, we see that the elastic interaction channel can exceed 20% of the total energy-loss term, hence it makes sense to assess its impact on observable

[8] https://www.thedreamweaver.org/crange/index.html

quantities.

However, loss processes are not the dominant transport for protons, as non-collisional processes, notably diffusion, prevail. To assess the importance of the elastic interactions on the observable, i.e. the CR fluxes, we must introduce the transport equation and elucidate our approach to its solution. This is the goal of the following section.

4.3 Assessing the relative effect on cosmic-ray proton fluxes

A consistent description of CRs as charged test particles moving in stochastic magnetic fields begins with the Liouville equation for the particle distribution function in momentum space, as discussed in Section. 1.3.4. The interaction of magnetic fields with scales smaller than the particle gyroradius leads to the isotropization of the distribution function. The isotropic component, $f(t, r, p)$, normalized as $N = 4\pi \int \mathrm{d}p\, p^2 f$, where N denotes the CR number density, satisfies the diffusion equation. Including nuclear fragmentation effects introduces a set of coupled transport equations that govern both diffusion and fragmentation. The resulting transport equation for nuclei of type α takes the following form:

$$-\frac{\partial}{\partial z}\left[D_\alpha(p)\frac{\partial f_\alpha}{\partial z}\right] + v_A\frac{\partial f_\alpha}{\partial z} - \frac{dv_A}{dz}\frac{p}{3}\frac{\partial f_\alpha}{\partial p} + \frac{f_\alpha}{\tau_{sp,\alpha}} + \frac{1}{p^2}\frac{\partial}{\partial p}\left[p^2\left(\frac{dp}{dt}\right)_{\alpha,ion} f_\alpha\right] = q_\alpha(p,z) + \sum_{\alpha'>\alpha}\frac{f_{\alpha'}}{\tau_{sp,\alpha'}}, \tag{4-14}$$

where, $\tau_{\alpha,sp}$ represents the spallation timescale for nuclei of type α, $q_\alpha(p,z)$ denotes the injection rate per unit volume for nuclei of type α, and $\left(\frac{dp}{dt}\right)_{\alpha,ion}$ corresponds to the ionization energy-loss rate.

One approach to solve this equation, which is also employed in this chapter for our analysis, is the Weighted Slab Approximation. This method separates the problem into two components: an astrophysical part and a nuclear part. The nuclear fragmentation problem is addressed within the Slab Model, where cosmic rays are assumed to traverse a column density X [g.cm^{-2}] of interstellar material. The solutions obtained from the Slab Model are then integrated over all values of X, weighted by a *path length* distribution function $P(X)$. This distribution function is derived from astrophysical propagation models, such as the *empirical leaky box model* or diffusion models.

The weighted slab technique has been extensively used to study the

propagation of cosmic rays in the galaxy, tracing their journey from their sources to observation points near Earth (315). However, as the detailed discussion of this method and the merits of its approximation lie beyond the scope of this dissertation, the reader is referred to (316, 317, 318, 319) for further details.

In a "modified weighted slab" propagation model (see e.g. (316), henceforth reported in the notation of (319)), the proton flux at kinetic energy K, denoted by $I(K)$, can be obtained by solving the transport equation

$$\frac{I(K)}{X(K)}+\frac{\mathrm{d}}{\mathrm{d}K}\left[-\left(\frac{\mathrm{d}E}{\mathrm{d}X}\right)I(K)\right]=2h_d\frac{Ap^2q_0(p)}{\mu v}-\frac{\sigma_p I(K)}{m_p}+\sum_{\alpha'}\int \mathrm{d}K_{\alpha'}\frac{I_{\alpha'}(K_{\alpha'})}{m}\frac{\mathrm{d}\sigma_{\alpha'\to p}(K_{\alpha'},K)}{\mathrm{d}K_{\alpha'}}\,, \tag{4-15}$$

where p is the momentum ($p(K)=\sqrt{K^2+2K\,m_p}$), σ_p is the total proton cross section, $\mathrm{d}\sigma_{\alpha'\to p}/\mathrm{d}K_{\alpha'}$ is the differential cross section for a nucleus α' of kinetic energy $K_{\alpha'}$ to yield a proton of kinetic energy K, $q_0(p)$ is the rate of injection per unit volume in the disc of the Galaxy, v is the velocity of the nuclei type α (in units of $c=1$), $\mu=2h_dn_dm$ is the surface gas density in the disc with h_d being the half-thickness of the Galactic disc, n_d is the gas number density in the disc, and

$$X(K)=\frac{\mu v}{2v_A}\left[1-\exp\left(-\frac{v_A}{D}H\right)\right]\,, \tag{4-16}$$

is the grammage experienced by protons. Here v_A is advection velocity (in units of $c=1$), expected to be of the order of the Alfvén velocity, and D is the diffusion coefficient for protons. For our illustrative purposes, we adopt $n_d=1$ cm^{-3} and $\mu=2.4$ mg/cm^2 (319). The diffusion coefficient D is a universal function (i.e. applies to all CR species) if expressed in terms of the rigidity R, i.e. momentum over charge, simply reducing to momentum for protons. In particular, we use the fits of the `BIG` and `SLIM` models discussed in (320, 321), with the parameterisation

$$D(R)=\beta^\eta D_0\left\{1+\left(\frac{R}{R_l}\right)^{\frac{\delta_l-\delta}{s_l}}\right\}^{s_l}\left(\frac{R}{1\,\mathrm{GV}}\right)^{\delta}\left\{1+\left(\frac{R}{R_h}\right)^{\frac{\delta-\delta_h}{s_h}}\right\}^{-s_h}\,. \tag{4-17}$$

We address the reader to (321) for the meaning and values of the parameters. Also, in this parametrization a halo size of $L=5$ kpc is adopted.

The bracket in eq. (4-15) contains all approximately continuous energy-loss terms, expressed in terms of grammage, $\mathrm{d}X=\rho\mathrm{d}x$, with $\rho=m_p\,n_d$ the ISM medium mass density.

In the baseline model, we include

$$\left(\frac{\mathrm{d}E}{\mathrm{d}X}\right)=\left(\frac{\mathrm{d}E}{\mathrm{d}X}\right)_{\mathrm{ad}}+\left(\frac{\mathrm{d}E}{\mathrm{d}X}\right)_{\mathrm{ion}}\equiv-\mathcal{S}(K)\,, \tag{4-18}$$

for the advection and ionization loss terms, respectively. The advection stopping power is given by

$$\left(\frac{\mathrm{d}E}{\mathrm{d}X}\right)_{\mathrm{ad}} = -\frac{2v_A}{3\mu}\sqrt{K(K+m_{\mathrm{p}}c^2)}\ . \tag{4-19}$$

To solve the propagation equation, we proceed as follows. First, we ignore all but continuous energy losses, which reduces the equation to

$$\frac{I(K)}{X(K)} + \frac{\mathrm{d}}{\mathrm{d}K}\left[-\left(\frac{\mathrm{d}E}{\mathrm{d}X}\right)I(K)\right] = 2h_d\frac{Ap^2q_0(p)}{\mu v}\,. \tag{4-20}$$

Eq. (4-15) can be re-written as

$$\Lambda_1(K)I + \Lambda_2(K)\frac{\mathrm{d}I}{\mathrm{d}K} = Q(K)\ , \tag{4-21}$$

where we assume

$$Q(K) = \kappa\left(\frac{p(K)}{m_p}\right)^{-\gamma}\ , \tag{4-22}$$

with $\gamma \simeq 2.2 - 2.4$, while the normalization factor κ holds no significance for our purposes, as will be clear from the subsequent discussions. The coefficients in the eq. (4-21) can be explicitly written as

$$\Lambda_1 = \frac{1}{X(K)} + \frac{\mathrm{d}\mathcal{S}}{\mathrm{d}K} \tag{4-23}$$

and

$$\Lambda_2(K) = \mathcal{S}(K)\,. \tag{4-24}$$

Hence, the solution to eq. (4-22), vanishing at $K \to \infty$, writes

$$I(K) = \int_K^\infty \mathrm{d}K'\frac{Q(K')}{\Lambda_2(K')}\exp\left[-\int_K^{K'}\mathrm{d}K''\frac{\Lambda_1(K'')}{\Lambda_2(K'')}\right]\ . \tag{4-25}$$

In practice, since the integrand in the exponential is rather large, the following approximation is pretty accurate (typically at 0.1% level or better):

$$I(K) \simeq \int_K^\infty \mathrm{d}K'\frac{Q(K')}{\Lambda_2(K')}\exp\left[-(K'-K)\frac{\Lambda_1((K+K')/2)}{\Lambda_2((K+K')/2))}\right]\ . \tag{4-26}$$

For rough expectations, a more radical approximation valid in the limit $K\Lambda_1 \gg \Lambda_2$ is

$$I(K) \simeq \frac{Q(K)}{\Lambda_1}\,. \tag{4-27}$$

In Fig. 5.5, we illustrate the grammage of eq. (4-16) as well as the traditionally used proxies $K/\mathcal{S}_i$ for the loss terms entering the expression of Λ_1. Based on the rough expectation of eq. (4-27), we anticipate that losses contribute only at the $\mathcal{O}(10\%)$ level in shaping the spectrum. Hence, the effects on the CR

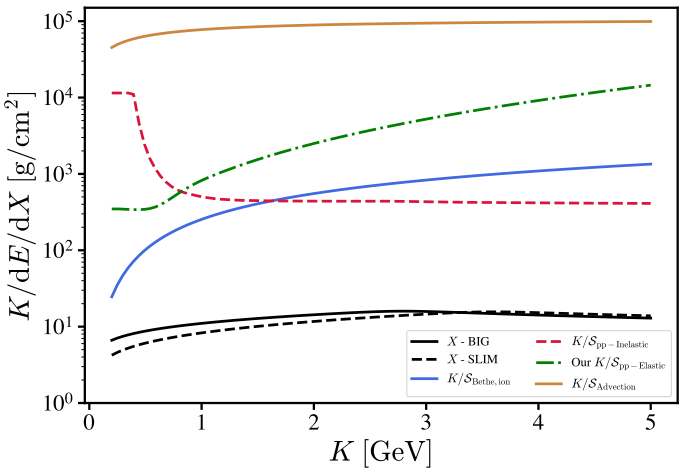

Figure 4.3: Stopping range scale (in terms of grammage) associated to different energy loss channels, compared with the diffusive transport grammage for the `BIG` model.

flux observable should be one order of magnitude smaller than those gauged by merely comparing energy losses.

Once the simplified solution of Eq. 4-26, henceforth denoted with I_0, has been obtained, an iterative approach is adopted to account for catastrophic energy-loss terms, neglected till now.

Within the approximation described in Sec. 4.2.2, the loss and gain terms associated to inelastic, pion production channel can be described by changing the RHS of eq. (4-21) into

$$Q_i(K) = Q(K) - \left[\frac{\sigma_{\rm in}(K)}{m_p} I_{i-1}(K) - \frac{\sigma_{\rm in}\left(\frac{K}{\eta_{\rm in}}\right)}{\eta_{\rm in} m_p} I_{i-1}\left(\frac{K}{\eta_{\rm in}}\right) \right] , \tag{4-28}$$

at iteration stage $i = 1, 2, 3, \ldots$ Usually three iterations are sufficient to obtain convergence at the $\sim 0.1\%$ level.

In order to account for the elastic cross section process, we follow a similar approach, just now

$$\begin{aligned} Q_i(K) = Q(K) &- \left[\frac{\sigma_{\rm in}(K)}{m_p} I_{i-1}(K) - \frac{\sigma_{\rm in}\left(\frac{K}{\eta_{\rm in}}\right)}{\eta_{\rm in} m_p} I_{i-1}\left(\frac{K}{\eta_{\rm in}}\right) \right] \\ &- \left[\frac{\sigma_{\rm el}(K)}{m_p} I_{i-1}(K) - \frac{\sigma_{\rm el}\left(\frac{K}{\eta_{\rm el}}\right)}{\eta_{\rm el} m_p} I_{i-1}\left(\frac{K}{\eta_{\rm el}}\right) \right] . \end{aligned} \tag{4-29}$$

The rapid convergence of this method is illustrated in Fig. 4.4, for the case $\gamma = 2.2$ and the `BIG` model.

In this treatment, the main approximation consists in neglecting *secondary* protons coming from spallations of heavier CR nuclei, such as He,

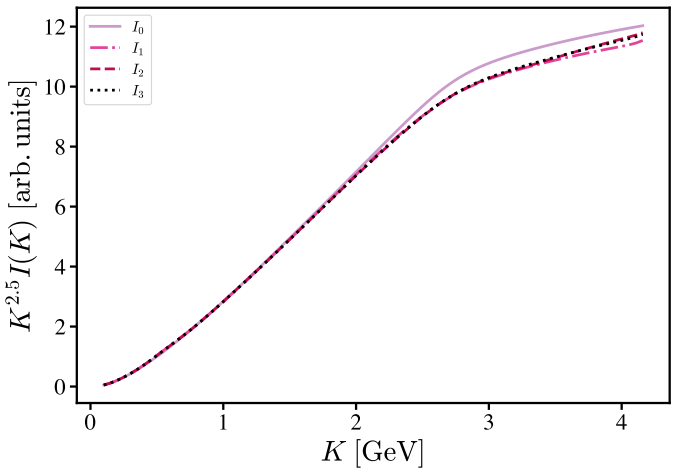

Figure 4.4: Illustration of the iterative solution using Eqs. 4-29 and 4-26. A rapid convergence is manifest. See the text for the details.

C, O... Fe, allowing us to reduce the problem to the integration of a single differential equation, instead of a coupled system. Since we are only interested in the relative effect of including the elastic process, and both primaries and secondary protons undergo losses, accounting for secondaries from nuclear spallations is largely degenerate with the injection spectrum (or index) effect, which we briefly discuss in the next section.

4.4 Results

In Fig. 4.5, we illustrate the relative effect of the inclusion of the elastic loss process with respect to neglecting it, for two propagation models and two injection spectra. The shape of the curves is easy to explain: The process takes protons at higher energies and re-injects them at lower ones, hence the peak-dip structure. Its magnitude is of the order of 0.8% slightly below or slightly above 1 GeV, and should therefore be included whenever the ambition is stated to control the theoretical error to below such a level. The effect is similar in the two propagation models considered: A bit smaller in the `SLIM` model because the relative weight of the diffusion coefficient is more pronounced at low energies. Also note that steeper power-laws reduce the relative re-population effect and enhance the depletion one, as intuitively expected. The effect of including secondary protons should be similar, as discussed in the previous section.

In the limit where $\eta \to 0$, we expect that the "catastrophic" energy losses described via the brackets in eq. (4-29) admit a simpler description in terms of a *continuous* energy loss mechanism. We can easily switch to such a treatment for the elastic channel, for instance, by setting the elastic channel bracket in

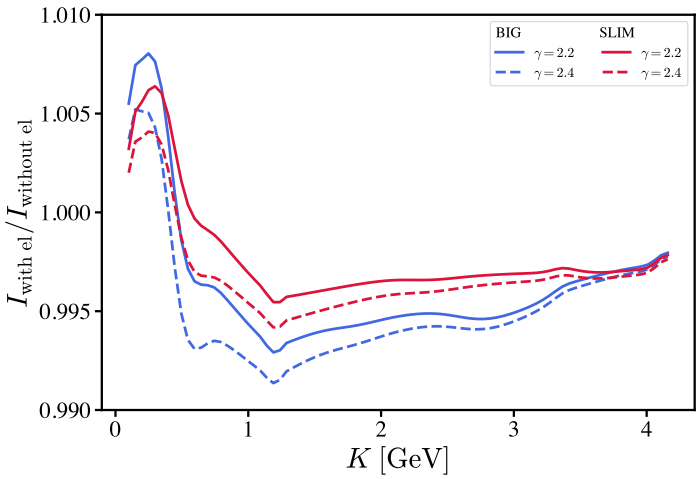

Figure 4.5: Relative effect of including vs. neglecting the *pp*-elastic process, for the `BIG` (blue) and `SLIM` (red) models, and for two injection spectral indices, 2.2 (solid) and 2.4 (dashed).

eq. (4-29) to zero while modifying

$$\mathcal{S}(K) \to \mathcal{S}(K) = -\left(\frac{\mathrm{d}E}{\mathrm{d}X}\right)_{\mathrm{ad}} - \left(\frac{\mathrm{d}E}{\mathrm{d}X}\right)_{\mathrm{ion}} - \left(\frac{\mathrm{d}E}{\mathrm{d}X}\right)_{\mathrm{el}} . \tag{4-30}$$

This change applies to the functions Λ_1 and Λ_2, as a consequence of the new function $\mathcal{S}(K)$ entering them. Of course, we can apply a similar treatment to the inelastic channel (together with or alternatively to the elastic one). In fact, current studies via popular CR propagation codes do adopt this approximation for pion production losses. In Fig. 4.6 we see the effect of this continuous approximation. We see that it is definitely inappropriate for current accuracy goals, with errors reaching 3%. It is easy to explain the different energy behaviour for the elastic and inelastic cases: For the elastic case, the biggest effect is when the elastic process matters the most, basically, just below 1 GeV, reflecting the drop of the inelasticity well above that value. For the pion production, the inelasticity is constant (within our approximation): The impact is higher at higher energies just because the pion-production process becomes the dominant loss channel there (see Fig. 4.3).

4.5 Sub-leading effects in the ionization losses

In each electromagnetic interaction with an electron of the medium, a proton loses a tiny fraction of its energy, as we discussed in Section. 1.3.6, hence a continuous energy-loss approximation is justified. The stopping power for ionization for a CR nucleus of charge Ze takes the well-known form

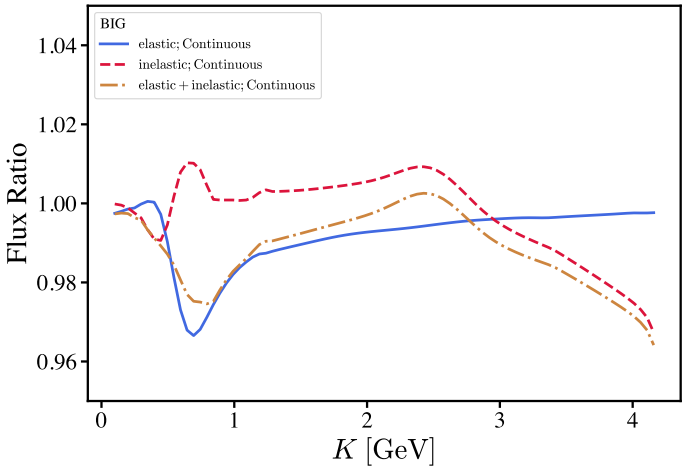

Figure 4.6: CR proton flux ratio between the solution obtained with the continuous approximation for the elastic channel (blue, solid), the inelastic channel (dashed, red) or both (dot-dashed) over the solution obtained with the catastrophic treatment for both channels.

$$\left(-\frac{\mathrm{d}E}{\mathrm{d}x}\right)_{\mathrm{ion}} = \frac{4\pi n_e Z^2 \alpha^2}{m_e \beta^2} L\,, \quad L \simeq L_{\mathrm{Bethe}} \left[\ln\left(\frac{2m_e\beta^2\gamma^2}{\mathcal{I}}\right) - \beta^2\right]\,, \qquad (4\text{-}31)$$

where the expression given for L corresponds to the result obtained by Bethe ($\mathcal{I}$ being the effective ionization potential of the target). Although current treatments in CR astrophysics limit themselves to this approximation, see e.g. appendix C.10.4 in (322), more refined calculations for the dimensionless function L are available. Some of these corrections are discussed in (311), but typically neglected without quantitative assessment of their magnitude. Here, we tackle this task, following the treatment given in (312), associated to the code `CRange` [9] which we use for numerical evaluation accounting for the following additional effects (with two-letters code to label them in parentheses):

- Density effect (New Delta, ND)
- Lindhard-Sørensen correction (LS)
- Radiative correction (RA)
- Finite Nuclear Size (NS)
- Barkas Effect (BA)
- Shell Effect (SH)
- Leung Effect (LE)
- Modern Electron Capture Effect (EC)
- Kinematic Correction (KI)

[9] https://www.thedreamweaver.org/crange/recalc.html

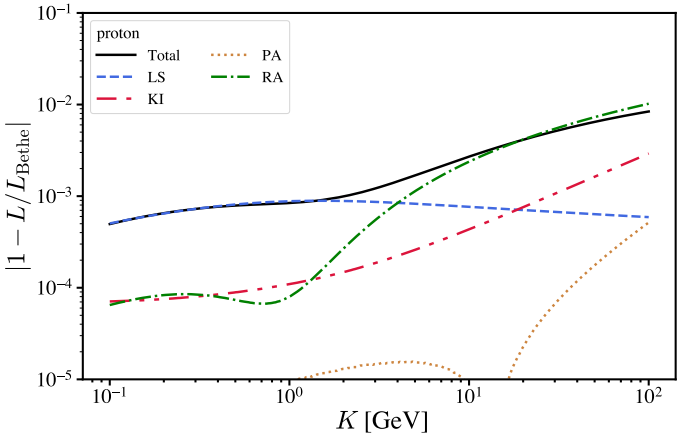

Figure 4.7: Fractional corrections to the Bethe ionization stopping power for CR protons. See text for the labels of the different effects.

– Pair Production (PA)

– Bremsstrahlung (BR)

We refrain here from a theoretical description of these effects, which goes well beyond the goals of our study. A modern exposition can be found for instance in (323). However, as a warning to the reader, we point out that, while `CRange` does nominally include a density effect correction for interstellar medium and Galactic Halo conditions, its implementation is flawed and should not be used [10]. Following the results reported in (324), Sec. 13.3, we checked that contrarily to what an uncritical use of the code would indicate, this effect is completely negligible for CR propagation conditions (i.e. in a very rarefied medium) and can be safely neglected.

In Fig. 4.7 we show the relative correction to the eq. (4-31) due to different effects. The only one worth mentioning is the Lindhard-Sørensen correction (325), since the radiative correction dominating above 4 GeV (but still sub-percent!) intervenes at a point where ionization losses are already subleading (see Fig. 4.3). The LS-correction accounts for the solution of the relativistic Dirac-Coulomb equation, as opposed to the non-relativistic quantum-mechanical treatment of Bethe's results. Anyway, since the corrections are at the level of 0.1%, we conclude that they can be safely ignored at the present accuracy goal.

Although in this study we have focused on CR protons, the electromagnetic corrections dealt with in this appendix are common to all nuclei, with a known parametric dependence on the charge, mass, and size of the nucleus. We have thus explored how the above conclusions are altered in the case of Fe,

[10] We would like to thank Cypris Plantier for pointing out some anomalous output associated to these choices, that triggered our investigation.

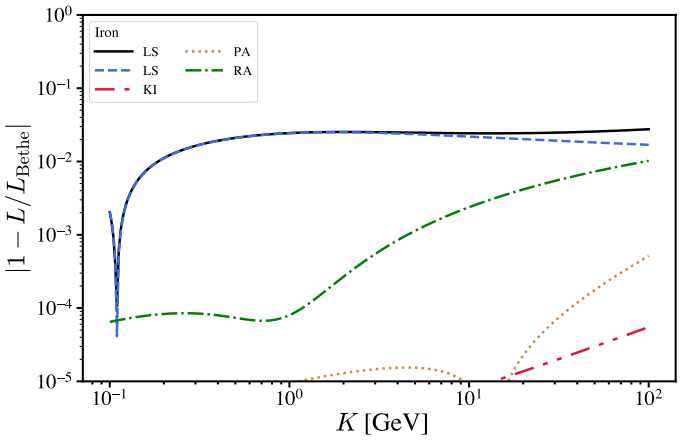

Figure 4.8: Fractional corrections to the Bethe ionization stopping power for CR Fe.

which is the heaviest nucleus with a sizable abundance among CRs. As far as energy losses are concerned, we present our results in Fig. 4.8: we see that the LS correction reaches about 2%.

To gauge the impact on fluxes, we also solve the propagation equation for Fe. Technically, in this case we do not adopt an iterative approach to solve the propagation equation, since the catastrophic loss channel is dominated by spallations onto the interstellar medium protons, but these are not associated to a sizable injection term counterpart, since iron is the heaviest nucleus with appreciable CR flux. Hence, we simply integrate eq. (4-26) taking

$$\Lambda_{1,\rm Fe} = \frac{1}{X_{\rm Fe}(K)} + \frac{{\rm d}\mathcal{S}_{\rm Fe}}{{\rm d}K} + \frac{\sigma_{\rm in}^{\rm Fe}(K)}{m_{\rm Fe}}\,, \tag{4-32}$$

where Fe cross section with H target ($\sigma_{\rm in}^{\rm Fe}$) is taken from Table II of (326). The results are summarised in Fig. 4.9. We see that the LS correction reaches 1.5% just below 1 GeV, larger for instance than the statistical errors (albeit not systematic ones) on Fe data taken by AMS-02 (327).

4.6 Summary and Discussion

In the ongoing effort towards refining theoretical predictions for CR studies, we have focused on the energy loss processes affecting protons, particularly relevant at low energies. Our main driver has been to raise awareness of the insufficient accuracy with which known physics is currently treated. We have scrutinized the currently used approximation in the field, notably the Bethe limit of the ionization energy loss, the neglecting of the elastic energy losses, and the continuous approximation to treat what are more exactly described as catastrophic losses. While we confirm that, at least

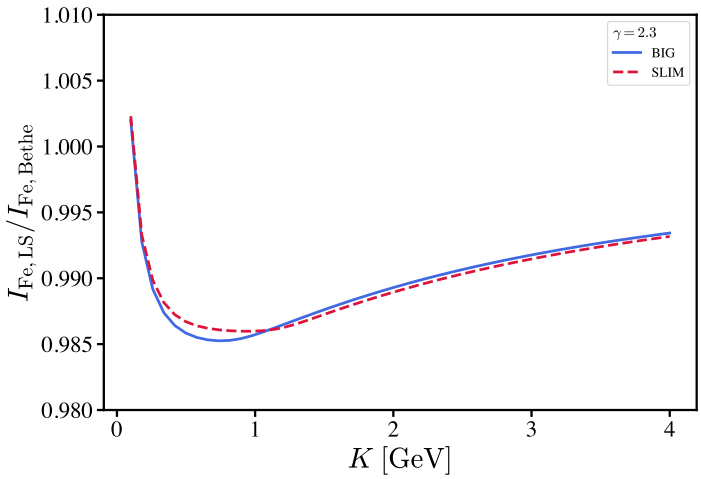

Figure 4.9: Iron flux ratio: The effect of the LS correction to the Bethe ionization expression in the `BIG` and `SLIM` model with $\gamma = 2.3$.

for protons, the former is sufficient, the latter two effects (and definitely the latter one, reaching 3%) should be accounted for precision studies: Note that these are all leading to energy-dependent effects, not reducible to a normalization uncertainty. We have also provided the reader with compact analytical formulae for the quantities of interest for the elastic collision process, and shown that an iterative approach can successfully be used to tackle the last issue.

This is but a step in a more extended effort, of course. A natural follow-up would be to incorporate these inputs in existing codes, and performing data analyses with/without the processes included to directly assess the systematics on astrophysical parameters of interest. This would also naturally account for secondary proton sources. Extending the treatment of these collisional losses to nuclei is another natural direction.

A further avenue consists in improving over existing parameterizations and fits of cross section data, notably if new laboratory data should be available, and assess the errors affecting any parameterization used. As a preliminary step, we have compared the cross section for the inelastic channel used here to the `FLUKA` [11]-based cross section (328) used e.g. in (27), reported in Fig. 4.10. The corresponding effect on fluxes is displayed in Fig. 4.11. We see that, despite the differences in fluxes being typically at around the 0.1% level, differences up to 1% can arise just above the threshold, and should be further examined. In particular, a trade-off may be at play between fits applicable over wide energy ranges and locally optimal fits. For instance, the single-pion production and the assumption of a fixed energy transfer κ_π into the produced

[11] `http://www.fluka.org`

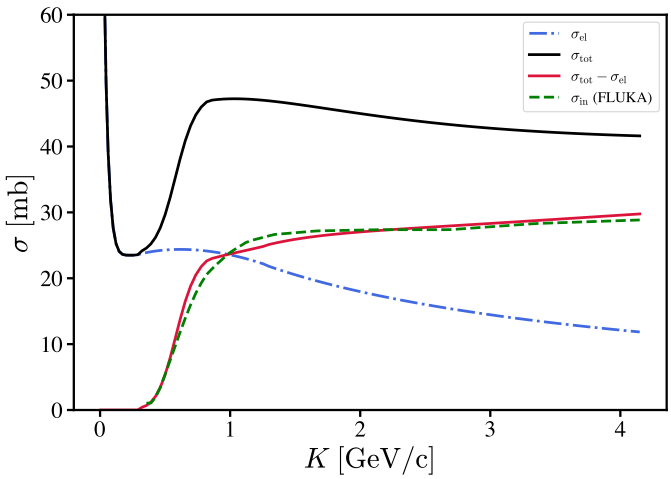

Figure 4.10: total (black) and *pp*-elastic (blue) cross section from (26) and their difference, i.e. the *pp*-inelastic (red). Comparison with the *pp*-inelastic from `FLUKA` as reported in (27) (green dashed).

pion become inadequate at high-energies. Additionally, since these processes are stochastic, one may explore the role of fluctuations in collision via a Monte Carlo study.

There are also other processes that we have not included. In particular, we have neglected the spallations that protons induce on interstellar medium nuclei. Accounting for these would not change qualitatively the above approach nor quantitatively the assessment for the effects we have considered. Our expectations is that, despite the fact that the cross sections for the process p-^{4}He, say, reach $\sim 300\,\mathrm{mb}$, only a very small fraction of the projectile proton ends up in the scattered products, i.e. the inelasticity is very small (see e.g. Figs. 4 and 6 in (27)). Yet, while these processes are taken into account as secondary nuclei sources, it is fair to say that neither the energy-loss effect on the projectile nor the proton source from target spallation are taken into account. These are all issues that we plan to tackle in future works.

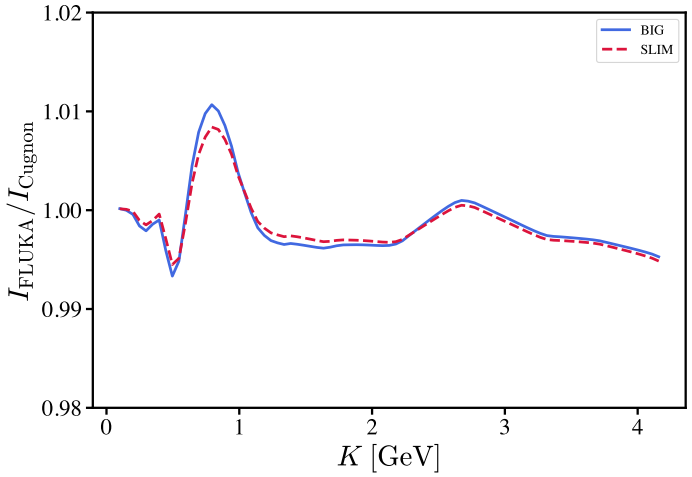

Figure 4.11: Ratio of CR proton fluxes obtained by using the `FLUKA` *pp*-inelastic cross section used in (27) to the one from (26) which is used in this article, i.e. the green-dashed curve with respect to the solid red curve in Fig. 4.10.

5
Evaporating Primordial Black Holes in Gamma Ray and Neutrino Telescopes

Departing from the core topics of this dissertation, this chapter explores the phenomenon of evaporating primordial black holes (PBHs) and their potential detectability through gamma-ray and neutrino telescopes. The analysis presented here builds on the findings published in (37).

Primordial black holes nearing the end of their evaporation process, particularly those situated within the local cosmic neighborhood, are expected to produce detectable transient signals. This work revisits the predicted gamma-ray and neutrino fluxes from such events and evaluates their implications for current observational limits.

5.1
Introduction

One of the prominent predictions of General Relativity (GR) is the existence of black hole (BH), a deformed spacetime around a sufficiently concentrated mass where all geodesics terminate at a singularity point (or region of zero volume). As far as GR is concerned, there is no restriction on the BH's mass; any mass M distributed inside the Schwarzschild radius $r_s = 2M$ will form a BH. However, the formation mechanism of a BH strongly restricts its possible masses. The gravitational collapse of astrophysical objects (stars) can lead to BHs with masses only between $\sim 2M_\odot$ (329) and $\sim 50M_\odot$ (330), which has been observed in X-ray binaries (331, 332). Merger events can create heavier BHs, potentially up to a few hundreds of solar masses, and the existence of such massive BHs has now been confirmed observationally via gravitational waves (333). Extremely heavier BHs of up to $\sim 10^9 M_\odot$ have been detected ubiquitously at the centers of galaxies (including ours), although their formation mechanism is still not well understood.

Meanwhile, on the $\lesssim M_\odot$ part of the mass spectrum, both the formation and the detection of BHs are challenging. In a seminal paper (334), Zel'dovich and Novikov suggested the formation of such BHs via the gravitational collapse of overdense regions in the early universe, which have been fittingly named primordial black holes (PBHs). The formation rate of PBHs depends on the details of the initial power spectrum of the early universe, and the required conditions for having a relevant population of PBHs are still under debate (see (335)). Inspection of the early universe density fluctuations reveals that PBHs

with masses $\sim 5M_{\odot}(t/10^{-4}$ s) indeed can be formed at a time t after the Big Bang (336). Note that, following the literature in astroparticle physics, it is common to express PBH masses in grams, and we henceforth follow this convention. The thermodynamics of BHs plays an important role over cosmological timescales for light PBHs. Hawking showed in (337, 338) that a BH of mass M loses its mass in the form of radiated particles with a quasi-black-body spectrum at temperature $T = (8\pi M)^{-1}$. This so-called Hawking radiation is only appreciable for light BHs (it is extremely small for stellar-mass BHs), and its very existence leads to a complete evaporation of PBHs with masses $\lesssim$ few $\times 10^{14}$ g within the age of the Universe[1]. PBHs with mass $\sim 10^{15}$ g, which (if they exist) have been produced at $t \sim 10^{-23}$ s, are expected to be breathing their last breaths at the present time and are the subject of this study[2].

Hawking radiation leads to a runaway mass loss process: as the BH's mass decreases, the rate of energy loss increases dramatically ($\dot{E} \sim M^{-2}$ (350)) until the BH practically vanishes after emitting all particles in the Standard Model (and any other hypothetical beyond the Standard Model particle) up to Planck scale energies. In the last few hundreds of seconds of the BH's life, when its temperature exceeds the quarks' and gauge bosons' masses, the spectrum of radiated particles significantly deviates from a greybody spectrum due to secondary emission from hadronization and electroweak corrections. Among the stable final products of PBH evaporation, gamma rays have been most extensively used by the H.E.S.S. (351, 352), HAWC (29), Milagro (353), VERITAS (354) and Fermi-LAT (355) experiments in the search for local (within $\sim$ a parsec) PBHs, of course, all with null results. These searches provide independent and complementary bounds to gamma ray observations at larger distance scales, e.g. Galactic scales using EGRET data (356, 357) (refined in (339, 358)) and cosmological scales using the extragalactic gamma ray background (EGB) (359, 339). Besides gamma rays, other particles such as antiprotons (360), electrons/positrons (361, 362, 363) and neutrinos (363) have also been used to constrain the density of $(10^{15} - 10^{17})$ g PBHs and their fractional contribution to dark matter, $f_{\rm PBH}$. Strong upper limits on $f_{\rm PBH}$ for low-mass PBHs have also been obtained from EGB (364), cosmic microwave background anisotropy (365), Galactic gamma ray (366, 367), and 21-cm (368) measurements, the latter yielding the strongest bounds to date:

[1]Strong limits on the abundance of PBHs with masses $\lesssim 10^{14}$ g can be derived from BBN considerations (339), early neutrino and photon production (340, 341), reionization (342, 343), and even contribution to the dark matter if stable Planck-mass remnants are left behind from their evaporation (344, 345, 346).

[2]PBHs with masses $\gtrsim 10^{15}$ g would still be alive and may account for a considerable fraction of the dark matter (347) (see (335, 348, 349) for reviews).

$f_{\rm PBH} \lesssim 10^{-9.7}$ at 95% C.L. for PBHs with mass $\sim 10^{15}$ g. Future X- and gamma ray experiments are expected to tighten these bounds even further, especially for rotating PBHs (369, 370). One may ask whether, in light of these strong bounds, searches for PBHs in the local neighborhood is viable. Considering the local dark matter density $\rho_{\rm DM} \approx 0.0133\ M_\odot\ {\rm pc}^{-3}$ (371), and assuming a uniform PBH distribution throughout the universe, the bound on $f_{\rm PBH}$ leads to the maximum number density of these PBHs:

$$n_{\rm max} = \frac{f_{\rm PBH}\,\rho_{\rm DM}}{M_{\rm PBH}} \approx \frac{10^{-9.7} \times 0.0133\ M_\odot\ {\rm pc}^{-3}}{10^{15}{\rm g}} \approx 5.3 \times 10^6\ {\rm pc}^{-3}. \qquad (5\text{-}1)$$

The corresponding mean separation between bursting PBHs is therefore $d_{\rm min} \approx n_{\rm max}^{-1/3} \approx 6 \times 10^{-3}$ pc. Any smaller spacing would imply a larger PBH number density—and hence a higher local PBH mass density—than is allowed by the 21-cm bound, rendering such a scenario inconsistent with current constraints.

Also, this distance scale can be significantly shorter in case of any (expected) clustering in the PBH's distribution. Since these distance scales are within the reach of gamma ray and neutrino observatories, direct observation of local PBH bursts keeps being motivated.

The idea of using neutrinos in the search for evaporating PBHs has been introduced in (30) (see (372) for the early idea of using stable particles is the search for PBHs), by taking into account the emission of secondary neutrinos and in view of upcoming neutrino telescopes, which are now a reality. In this study we elaborate on this possibility and explore the extent of its feasibility in the current and future neutrino telescopes, as well as its synergy with gamma ray experiments in a multi-messenger approach. As for the expected neutrino production by an evaporating PBH, with respect to previous works (30, 31), we improve on the calculation by using the `BlackHawk` code (373) for the primary particle emission and incorporate the `HDMSpectra` code (374), which is the state-of-the-art code for secondary computation. Applying these improvements to the PBH gamma ray production shows qualitative and quantitative differences to previous works which enables us to improve the existing limits from gamma ray experiments. We also discuss the three-fold advantage of using neutrinos in the search for evaporating PBHs: a) Neutrinos would be able to reach the earth independent of the existence of a speculated optically thick photosphere (375, 376, 377) around PBHs which absorbs the gamma rays. The same applies for PBHs embedded in high density and/or magnetic field regions, where the outgoing flux of all the particles except for neutrinos will be suppressed. b) Extensive air shower experiments for gamma ray detection have a limited field of view – ~ 2 sr ($\sim 16\%$ of the sky) for

HAWC (378) and ~ 1 sr for LHAASO (379) – while neutrino telescopes cover at least 2π sr of the sky with almost zero dead time of the detector. c) In case we observe a flare of neutrinos or gamma rays, pinpointing its origin is crucial. An orphan gamma ray flare can be attributed to a conventional leptonic process. An orphan neutrino flare matches the expectation for a gamma-ray-opaque source, as is favored by multi-messenger analyses (232, 380). The simultaneous observation of neutrino and gamma ray flares, with the peculiar energy and time profile correlations of an evaporating PBH, can easily exclude the former alternatives.

Through this chapter, in section 5.2, we lay out the computational framework of the neutrino and gamma ray radiation from an evaporating PBH, comparing our updated emission spectra from `BlackHawk` and `HDMSpectra` to previous results in the literature. In section 5.3, we estimate IceCube's sensitivity to PBH bursts and set the corresponding upper limit on their local rate density from the 10-years neutrino data set. Section 5.4 is devoted to the multi-messenger γ/ν approach in identifying a PBH event. Discussions and conclusions are summarized in section 5.5.

5.2 Neutrinos and gamma rays from Hawking radiation

The no-hair theorem (381, 382, 383, 384, 385, 386) states that a BH, for an external observer, can be fully characterised by specifying its mass, electric charge and angular momentum. However, BH evaporation causes it to discharge (387, 388, 389) and lose angular momentum (390) at a much faster rate than it loses mass, once the BH approaches the end of its life. This allows us to safely assume that PBHs which are currently on their final hours are simply Schwarzschild BHs and parameterized only by their mass M. Nevertheless, at the end of this section we briefly comment on the rotating PBHs.

In terms of M, the temperature of a BH is $T = (8\pi M)^{-1}$ (337, 338) and its mass loss rate due to Hawking radiation can be obtained by solving the following equation of energy conservation (350)

$$\frac{\mathrm{d}M}{\mathrm{d}t} = -\frac{\alpha(M)}{M^2} \,, \tag{5-2}$$

where $\alpha(M)$ takes into account the total energy carried away by the Hawking radiation and can be calculated by summing over all particle species i of the Standard Model (quarks, charged leptons, neutrinos, gauge bosons and the Higgs)[3]

[3]To a very good approximation, the emission of particle i becomes non-negligible once the BH temperature approaches its rest mass (391).

$$\alpha(M) = M^2 \sum_i \int_0^\infty \mathrm{d}E\, E\, \frac{\mathrm{d}^2 N_{\mathrm{p}}^i}{\mathrm{d}t\mathrm{d}E}(M, E)\ . \tag{5-3}$$

The graph of $\alpha(M)$ as function of M can be found in Fig. 2 of (28). In Eq. (5-3), $\mathrm{d}^2 N_{\mathrm{p}}^i/\mathrm{d}t\mathrm{d}E$ is the emission spectrum rate of particle i arising directly from Hawking radiation – the so-called primary particles (hence the subscript p) – and is given by (337, 338)

$$\frac{\mathrm{d}^2 N_{\mathrm{p}}^i}{\mathrm{d}t\mathrm{d}E}(E, M) = \frac{n_{\mathrm{dof}}^i\, \Gamma^i(M, E)}{2\pi(e^{E/T} \pm 1)}\ , \tag{5-4}$$

where n_{dof}^i is the number of degrees of freedom of particle i (spin/helicity and color; see Table 3 in Appendix C of (373)), $\Gamma^i(M, E)$ is the greybody factor/absorption coefficient of a wave packet scattering in the BH spacetime geometry off into infinity (where an observer would be located) and the $+(-)$ sign corresponds to fermions (bosons). Calculating the greybody factor Γ^i is the nontrivial part of Eq. (5-4), as it depends not only on M and E, but also implicitly on the radiated particle's mass, spin and any other internal degree of freedom it may possess. Although these greybody factors can be approximated analytically (391, 392), we use the exact numerical calculation from the `BlackHawk` code (373). For a given BH mass, `BlackHawk` calculates the instantaneous primary emissions $\mathrm{d}^2 N_{\mathrm{p}}^i/\mathrm{d}t\mathrm{d}E$ for every particle species of interest.

The observable fluxes of stable particles from an evaporating PBH are different from Eq. (5-4) because of hadronization, fragmentation and electroweak corrections, which lead to the emission of secondary particles. For example, the production of pions from hadronization of primary emitted quarks, and their subsequent decay, produces additional spectra of neutrinos and photons. Also, the electroweak corrections on any primary emission of species i lead to secondary neutrino and photon spectra which become increasingly important at energies $\gtrsim 1$ TeV (corresponding to the last ~ 400 s of the evaporating PBH). Typically, the secondary emissions have been either approximated semi-analytically, for example in (359, 393, 394) for gamma ray yield and in (30) for neutrino yield, or calculated numerically by the `PYTHIA` code (395), see for example (28) for gamma ray yield. Both methods have some degree of imprecision: in addition to approximated hadronization/fragmentation calculations, the electroweak corrections are usually absent in the semi-analytical method; in the `PYTHIA` code the electroweak corrections are not included completely (for example, triple gauge couplings are missing), which renders its range of reliability below tens of TeV. In order to improve on the secondary emission calculation, we use the `HDMSpectra` code (374) which is valid up to Planck scale. Although `HDMSpectra` aims at computing the secondary emission from

heavy dark matter annihilation/decay, it can be equally applied to evaporating PBHs; as soon as particle species i is produced either from dark matter or PBH evaporation, the rest (secondary calculation) is the same in both cases. The secondary spectrum of particle j can be obtained by the energy convolution of the primary spectrum of particle i, Eq. (5-4), with the spectrum of particle j from a fixed energy of primary species i (and summing over all species i):

$$\frac{\mathrm{d}^2 N^j_{\mathrm{s}}}{\mathrm{d}t\mathrm{d}E}(E,M) = \sum_i \int_0^\infty \mathrm{d}E_{\mathrm{p}}\, \frac{\mathrm{d}^2 N^i_{\mathrm{p}}}{\mathrm{d}t\mathrm{d}E_{\mathrm{p}}}(E_{\mathrm{p}},M) \frac{\mathrm{d}N^{i\to j}}{\mathrm{d}E}(E,E_{\mathrm{p}})\ . \tag{5-5}$$

In this relation, the $\mathrm{d}N^{i\to j}/\mathrm{d}E$ term has been computed by using `HDMSpectra`. Some remarks about Eq. (5-5) are in order: the summation index i runs over particle and anti-particle of each species and the $\mathrm{d}N^{i\to j}/\mathrm{d}E$ should be computed for each one separately (for u, $\bar{u}$, b, $\bar{b}$, etc), which are provided via explicit fragmentation functions in `HDMSpectra` (using the `HDMSpectra.FF` syntax). In this case the n^i_{dof} in Eq. (5-4) includes the spin/helicity and color degrees of freedom. However, the rates of particle and anti-particle production by a PBH are equal. Thus, by doubling the n^i_{dof}, Eq. (5-4) provides the production rate spectrum of particle plus anti-particle (for particles that are not identical to their anti-particle). By using this convention, one can use the `HDMSpectra.spec` syntax in `HDMSpectra` code which provides the secondary emission from $X\bar{X}$ (X being the particle species). In this convention, the particle species $Y = \gamma, Z^0$, gluons and Higgs need a special treatment since the `HDMSpectra.spec` syntax provides the secondary emission from YY: we should divide their secondary spectra $\mathrm{d}N^{i\to j}/\mathrm{d}E$ by two.

Considering both primary and secondary contributions, the *total* emission rate spectrum of ν_α ($\alpha = e, \mu, \tau$) and γ from a PBH can be written as

$$\frac{\mathrm{d}^2 N^{\nu_\alpha}_{\mathrm{tot}}}{\mathrm{d}t\mathrm{d}E} = \frac{\mathrm{d}^2 N^{\nu_\alpha}_{\mathrm{s}}}{\mathrm{d}t\mathrm{d}E} + \mathcal{A}^{\nu_\alpha\to\nu_\alpha}(E) \frac{\mathrm{d}^2 N^{\nu_\alpha}_{\mathrm{p}}}{\mathrm{d}t\mathrm{d}E}\ , \tag{5-6}$$

and

$$\frac{\mathrm{d}^2 N^{\gamma}_{\mathrm{tot}}}{\mathrm{d}t\mathrm{d}E} = \frac{\mathrm{d}^2 N^{\gamma}_{\mathrm{s}}}{\mathrm{d}t\mathrm{d}E} + \mathcal{A}^{\gamma\to\gamma}(E) \frac{\mathrm{d}^2 N^{\gamma}_{\mathrm{p}}}{\mathrm{d}t\mathrm{d}E} + \mathcal{A}^{Z^0\to\gamma}(E) \frac{\mathrm{d}^2 N^{Z^0}_{\mathrm{p}}}{\mathrm{d}t\mathrm{d}E}\ , \tag{5-7}$$

where $\mathcal{A}^{k\to j}(E)$ is the coefficient of $\delta(1 - E/E_{\mathrm{p}})$ in the $k \to j$ secondary spectrum which takes into account the probability of no corrections for $\nu_\alpha \to \nu_\alpha$ and $\gamma \to \gamma$, and the probability of γ production for $Z^0 \to \gamma$. The $\mathcal{A}$ coefficients are provided by `HDMSpectra`.

A remark on Eq. (5-6) is in order: as can be inferred from this equation, we are assuming emission of neutrinos in flavor eigenstates via Hawking radiation and we suppose Majorana nature for neutrinos by setting $n^{(\nu_\alpha+\bar{\nu}_\alpha)}_{\mathrm{dof}} = 2$. However, although it is undeniably more natural to suppose neutrino emission in mass eigenstates (396), since the majority of neutrino yield originates from secondary production (*i.e.*, small $\mathcal{A}^{\nu_\alpha\to\nu_\alpha}$), this assumption does not modify

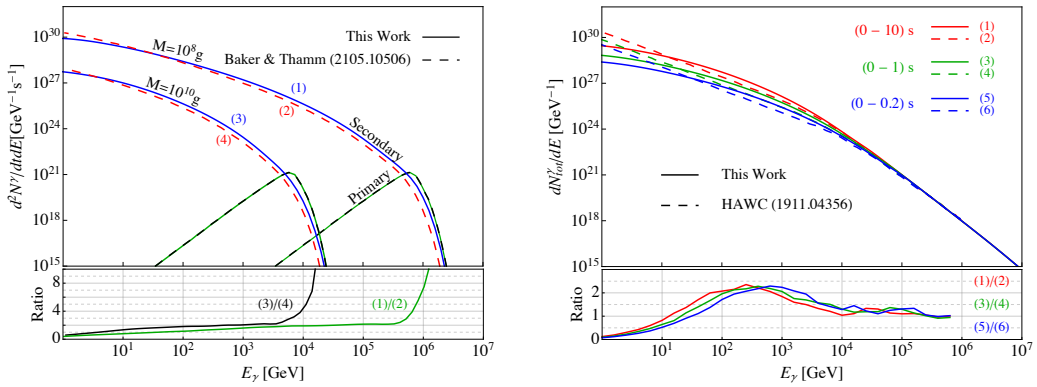

(a) (b)

Figure 5.1: (a) The instantaneous primary and secondary gamma ray spectra from an evaporating PBH. The solid curves show our results and the dashed curves are taken from (28). The lower part shows the ratio of solid to dashed secondary emissions curves. (b) The time-integrated *total* gamma ray spectra for three different time intervals in solid curves. The dashed curves show the spectra used by HAWC (29). The ratio of solid to dashed curves are depicted in the lower part.

our conclusions by more than $\sim$ few percents. In the case of Dirac neutrinos, the number of degrees of freedom will be four (396), instead of two, which enhances the neutrino emission and facilitates the detection of PBHs (to be conservative, we continue with the Majorana neutrino assumption.) Finally, the nonzero neutrino masses (though $\lesssim 0.01$ eV) would not affect the assumed massless-neutrino emission in `BlackHawk` code, for PBHs with $M \sim 10^{15}$ g (396).

Figure 5.1 shows the gamma ray emission spectra. In the left panel the instantaneous spectra (both primary and secondary) are shown for two PBH masses $M = 10^{10}$ g and 10^8 g, corresponding respectively to $\sim$ 400 s and $\sim 4 \times 10^{-4}$ s before the death. In order to compare with previous works, the primary and secondary gamma ray emission spectra from (28) are also shown by dashed curves; the ratios of our secondary emissions to the ones from (28) are depicted in the lower part of Figure 5.1a. While the primary emissions are identical (both in this work and in (28), they are taken from the `BlackHawk` code), the ratio plot manifests a factor of ~ 2 larger secondary gamma ray emission at $E_\gamma \gtrsim 100$ GeV in our computation. The ratio increases at higher energies for both PBH masses. The time-integrated *total* spectra from Eq. (5-7) for three different time intervals are shown in Figure 5.1b, in solid curves, with the corresponding time-integrated spectra used by the HAWC collaboration (29) represented by dashed curves. The ratio plot at the bottom shows a factor ~ 2 larger total spectra from our computation at $E_\gamma \sim$ TeV in all three time intervals.

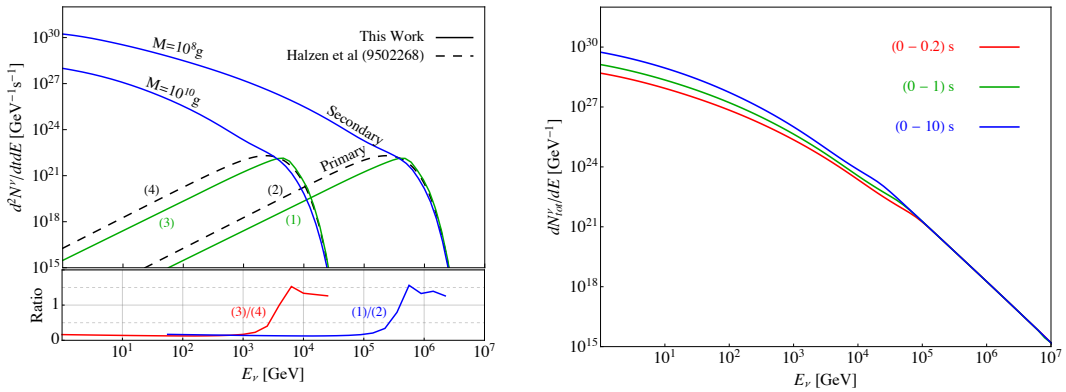

(a) (b)

Figure 5.2: The same as Figure 5.1, but for neutrinos (sum of the three flavors of neutrinos and antineutrinos). The dashed curves in panel (a) show the primary neutrino emission of (30) which has been used by IceCube collaboration in (31). The ratio of solid to dashed curves of primary spectra are shown in the lower part of panel (a). Panel (b) shows the time-integrated total neutrino spectra for three different time intervals before the complete evaporation of PBH.

The expected neutrino spectra from evaporating PBHs are shown in Figure 5.2, where in both panels we plot the sum of all three flavors of neutrinos and antineutrinos. In the left panel, the primary and secondary instantaneous neutrino emissions for two PBH masses are depicted with solid curves and are compared with the primary neutrino emission of (30), which has been used by IceCube collaboration in (31), in dashed curves. The lower ratio plot of Figure 5.2a illustrates a factor ~ 8 smaller primary neutrino emission from `BlackHawk` with respect to the analytical calculation of (30) at energies below the peak of Hawking radiation. Figure 5.2b shows the time-integrated *total* neutrino spectra from Eq. (5-6), for three different time intervals, which we could not find any work in the literature to compare with.

The spectrum of ν_α at the Earth, where by ν_α we mean the sum of neutrinos and antineutrinos of flavor α, can be obtained by taking into account the decoherent flavor oscillations en route from PBH to Earth:

$$\left.\frac{\mathrm{d}^2 N^{\nu_\alpha}_{\mathrm{tot}}}{\mathrm{d}t\mathrm{d}E}\right|_{\oplus} = \sum_{\beta=e}^{\tau}\sum_{i=1}^{3} |U_{\alpha i}|^2 |U_{\beta i}|^2 \left.\frac{\mathrm{d}^2 N^{\nu_\beta}_{\mathrm{tot}}}{\mathrm{d}t\mathrm{d}E}\right|_{\mathrm{PBH}}, \tag{5-8}$$

where $U_{\alpha i}$ are the elements of the PMNS mixing matrix fixed to their best-fit values from the NuFit global analysis (397). The effect of oscillation can be visualized in Figure 5.3a, which shows the prompt (at production) spectra of each neutrino flavor and the ν_μ spectrum after oscillations. The time-integrated flux (fluence) of ν_α from an evaporating PBH located at luminosity distance d_L ($\approx d_c$ for small redshifts, where d_c is the comoving distance) is given by

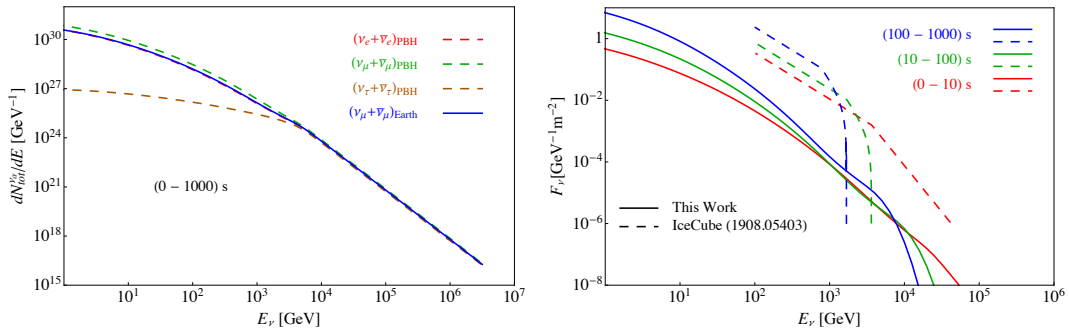

Figure 5.3: (a) The total spectra of each neutrino flavor at the production site (PBH), in dashed curves, and the muon-flavor spectrum (neutrino and antineutrino) at the Earth in the solid curve, after taking into account the flavor oscillation in Eq. (5-8). (b) Solid curves: the time-integrated flux (fluence) of all neutrino flavors at the Earth for three different time intervals. Dashed curves: the fluences used in (31), which are based on the calculation of (30). The distance to the PBH is $d_L = 10^{-2}$ pc.

$$F_{\nu_\alpha}(E; t_i \to t_f) = \frac{1}{4\pi d_L^2} \int_{t_i}^{t_f} \mathrm{d}t \left. \frac{\mathrm{d}^2 N^{\nu_\alpha}_{\rm tot}}{\mathrm{d}t \mathrm{d}E} \right|_{\oplus} . \tag{5-9}$$

The same Eq. (5-9) applies to the fluence of gamma rays, albeit without any flavor oscillation. The solid curves in Figure 5.3b show the fluence of all-flavor neutrinos at the Earth from a PBH at the distance 0.01 pc for three different time intervals. For comparison, the fluences (all neutrino flavors) used in (31) which are based on the calculation of (30) are displayed by dashed curves in Figure 5.3b. A clear mismatch, both qualitatively and quantitatively, can be seen in this figure.

In the case of rotating PBHs, it is well-known that the neutrino and gamma ray (and all other particles) emissions will be amplified by the increase of angular momentum (390). As a consequence, the lifetime of PBHs shortens and effectively the rotating PBHs experience a faster runaway mass loss in the last stage of their life. Whether the nonzero angular momentum of a PBH helps its observation or not depends on the competition between the increase in emission spectra and decrease in the domain of time integration of spectra, or equivalently of the fluence in Eq. (5-9), remembering that for rotating BHs a part of the energy budget is dedicated to rotation and this competition does not necessarily end in a draw. To illustrate the result, we choose the extreme case of a PBH with maximal spin $a^* = J/M^2 = 0.99$, where J is the angular momentum, and assume that it keeps its angular momentum until the complete evaporation. The left and right panels of Figure 5.4 show, respectively, the time-integrated gamma ray spectra and fluence of neutrinos

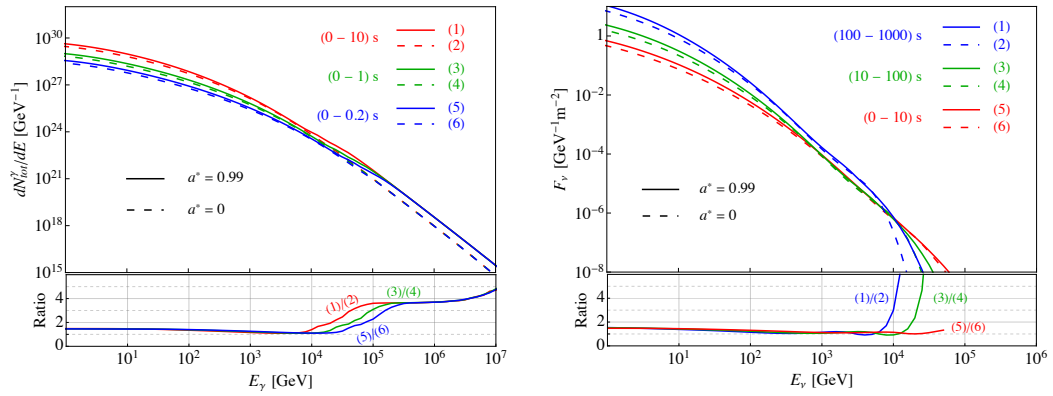

(a) (b)

Figure 5.4: The time-integrated gamma ray spectra (left panel) and fluence of neutrinos (right panel, assuming $d_L = 10^{-2}$ pc) for Schwarzschild PBH ($a^* = J/M^2 = 0$) in dashed curves and maximally rotating PBH ($a^* = 0.99$) in solid curves. The lower plots show the ratio of $a^* = 0.99$ to $a^* = 0$.

(assuming $d_L = 10^{-2}$ pc) for $a^* = 0\,(0.99)$ by dashed (solid) curves. The lower parts of panels depict the ratio of $a^* = 0.99$ to $a^* = 0$, which clearly show an increase in the time-integrated spectra of gamma rays and neutrinos for rotating PBHs. For neutrinos, especially in longer time intervals, the fluence is bigger at high energies for $a^* = 0.99$, while at lower energies a rotating PBH produces marginally more neutrinos than a Schwarzschild PBH. Let us emphasize that the modifications in emission spectra depicted in Figure 5.4 are for PBHs which maximally rotate until the last moments of their life, a scenario that should be considered quite exotic since the evaporating PBHs are expected to be Schwarzschild BHs in the last stages of their life even if they had a large angular momentum at the early stages (390, 398). Therefore, although we do not consider further the rotating PBHs, it can be concluded from Figure 5.4 that possible residual tiny angular momenta of PBHs do not change the bounds that will be derived in the next sections for non-rotating PBHs; *i.e.*, these bounds are robust against possible small a^* since even for maximal a^* they tighten by a factor $\mathcal{O}(1)$ and not more. The limits on rotating PBHs will be provided in the next section.

5.3 PBH detection prospects at IceCube

To quantify the observability of evaporating PBHs as transient point sources in neutrino telescopes, let us calculate the expected number of events at IceCube from the fluence of Eq. (5-9). We consider IceCube's μ-track data set which benefits from a good angular resolution in the reconstruction of the incoming neutrino's direction ($\lesssim 1^\circ$ above $\sim$ TeV energies). The good angular

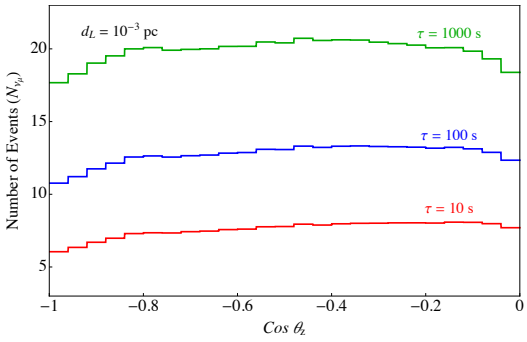

(a) (b)

Figure 5.5: (a) The expected number of μ-track events in IceCube from an evaporating PBH, located at the distance $d_L = 10^{-3}$ pc and different zenith angles, in the last τ seconds before its death. (b) The maximum distance, $r_{\rm max}$, that can be probed by IceCube at 90% C.L., for three time intervals τ.

resolution assists in efficient rejection of background events from atmospheric neutrinos. The atmospheric muon background can be suppressed entirely by restricting to up-going μ-track events in the detector, corresponding to the northern hemisphere.

The expected number of μ-track events from an evaporating PBH located at zenith angle θ_z and with fluence F_{ν_μ} in the time interval $t_i \to t_f$ is given by

$$N_{\nu_\mu}(\theta_z, t_i \to t_f) = \int_{E_{\rm min}}^{E_{\rm max}} {\rm d}E\, F_{\nu_\mu}(E; t_i \to t_f)\, A_{\rm eff}(E, \theta_z)\ , \qquad (5\text{-}10)$$

where $A_{\rm eff}(E, \theta_z)$ is IceCube's effective area (399)[4]. $E_{\rm min}$ is set by the energy threshold of μ-track observation at IceCube, ~ 100 GeV, and $E_{\rm max}$ is governed by the maximum energy of the fluence, which depends on the time interval $t_i \to t_f$. During the last $\sim 10^3$ s of the life of a PBH at distance $\gtrsim 10^{-3}$ pc from us, the proper motion due to PBH's motion is $\lesssim 2^\circ$ (even for ultra-relativistic PBH velocities). The Earth's rotation also leads to $\lesssim 0.5^\circ$ change in the position of PBH. Since the effective area of IceCube changes smoothly as a function of zenith angle, we can assume a fixed angular position for the PBH. Figure 5.5a shows the expected number of μ-track events from an evaporating PBH located at distance $d_L = 10^{-3}$ pc and at different zenith angles of the northern hemisphere, in the last τ seconds of its life. Clearly, as can be evidenced from Figure 5.3b, a larger time interval leads to a larger number of events at IceCube. However, any further increase of the time interval beyond $\sim 10^3$ s results in a marginal gain since the lower temperature of the PBH implies a lower energy neutrino emission, which eventually falls below IceCube's threshold.

The sensitivity of IceCube to a PBH depends on the number of atmo-

[4]In both neutrino telescopes and extensive air shower experiments, the azimuth-dependence of the effective area is very small and can be neglected.

spheric neutrino background events. Assuming a fixed-position PBH and considering 1° uncertainty in the direction reconstruction, the expected number of atmospheric neutrino events in the time interval of $\tau = 10$ s is $\lesssim 10^{-5}$ (we used the HKKM atmospheric neutrino flux (400)). Since the atmospheric neutrino flux is practically constant in time, the expected number of background events scales with τ. Thus, as a consequence of the short transient nature of a PBH signal, the observation is background free[5]. To estimate the constraint on the local density of PBHs, we use the Bayesian upper limit $N_{\nu_\mu} < N_{\rm max} = 2.3$ at 90% C.L. from the Poisson distribution, for our zero background expectation (see (401) for the details). From Eqs. (5-9) and (5-10), this condition corresponds to the maximum distance

$$r_{\rm max}(\theta_z;\tau) = \sqrt{\frac{1}{4\pi N_{\rm max}} \int_{E_{\rm min}}^{E_{\rm max}} {\rm d}E\, A_{\rm eff}(E,\theta_z) \int_0^\tau {\rm d}t\, \frac{{\rm d}^2 N_{\rm tot}^{\nu_\mu}}{{\rm d}t{\rm d}E}\bigg|_\oplus} \ , \tag{5-11}$$

beyond which PBH signal events are compatible with the background. Summing over all the zenith bins in the northern hemisphere (the ith bin is defined by $\theta^i_{z,{\rm min}} \leq \theta^i_z \leq \theta^i_{z,{\rm max}}$), the volume that can be probed by IceCube is

$$V_{\rm max}(\tau) = \frac{1}{3} \sum_i \Omega_i r^3_{\rm max}(\theta^i_z;\tau) \ , \tag{5-12}$$

where $\Omega_i = 2\pi(\cos\theta^i_{z,{\rm min}} - \cos\theta^i_{z,{\rm max}})$. Figure 5.5b shows $r_{\rm max}$ as a function of zenith angle for time interval searches $\tau = 10, 10^2$ and 10^3 s before the PBH's death. The upper limit on local rate density of PBH bursts $\dot\rho_{\rm max}$ (in $[{\rm pc}^{-3}{\rm yr}^{-1}]$) can be obtained via

$$\dot\rho_{\rm max}(\tau) = \frac{N_{\rm max}}{V_{\rm max}(\tau) T} \ , \tag{5-13}$$

where T is the total observation time ($\sim$ 10 years for IceCube). Table 5.1 reports the limits on $\dot\rho_{\rm max}$ found in this work for three different time intervals. Of course, these limits are not competitive with the current best constraints from HAWC, 3400 pc^{-3} yr^{-1} at 99% C.L. (29), yet they show the capability of current neutrino telescopes in the search for PBHs. The factor of $\gtrsim 10^3$ difference is mostly due to $\sim$ 2 – 4 orders of magnitude smaller effective area of IceCube with respect to HAWC's (402). For rotating PBHs with maximal angular momentum ($a^* = 0.99$), the limits reported in Table 5.1 are tighter by $\sim (15 - 30)$% due to their slightly larger fluences in Figure 5.4b (in combination with the energy-dependence of IceCube's effective area which peaks at $\sim$ 100 TeV.) The advantages of using neutrino telescopes in

[5]Strictly speaking, one has to search for clustering of events in a fixed time interval sliding over the data-taking time and properly incorporate the expected number of background events over the whole observation time. However, since performing this search requires detailed information of the detector which is not available, we opt for the simpler approach explained in the text.

Table 5.1: Limits, at 90% C.L., on the local rate density of PBH bursts, $\dot{\rho}_{\max}$, from the ten-years IceCube μ-track data set, for three different time intervals before the PBH's death, for both non-rotating and rotating PBHs.

τ [s]	$\dot{\rho}_{\max}(a^* = 0)$ [pc^{-3} yr^{-1}]	$\dot{\rho}_{\max}(a^* = 0.99)$ [pc^{-3} yr^{-1}]
10	1.7×10^7	1.5×10^7
10^2	8.2×10^6	6.2×10^6
10^3	4.1×10^6	3.3×10^6

the search for PBHs include the larger field of view with respect to gamma ray experiments (in case of one rare event that can be located outside the directional acceptance of these experiments), situations in which gamma rays will be absorbed before reaching the Earth, and simultaneous observation of PBHs in neutrino and gamma ray experiments which eases its identification (the latter will be discussed in the next section). Finally, it should be mentioned that the limit on $\dot{\rho}_{\max}$ does not improve significantly for searches in timescales longer than $\sim 10^3$ s.

5.4 PBH in gamma ray experiments and multi-messenger correlations

Before discussing the multi-messenger observation of an evaporating PBH, let us comment on the HAWC limit on $\dot{\rho}_{\max}$. The number of gamma ray events at HAWC can be calculated analogously to N_{ν_μ} in Eq. (5-10) by substituting the effective area $A_{\rm eff}$ and the fluence accordingly. Our re-evaluation of the gamma ray emission and its ratio to the emission spectra used by HAWC collaboration, shown in Figure 5.1b, reveals quantitative differences. Since the majority of event counts in HAWC are in the energy range $\lesssim 10$ TeV, where the ratio plot of Figure 5.1b points to a factor ~ 2 larger number of events in our evaluation, it corresponds to a factor ~ 1.4 larger $r_{\max}$ that can be probed by HAWC. By taking into account this raise, the current HAWC limit on the local PBH rate density (3400 pc^{-3} yr^{-1}) can be improved to roughly $\dot{\rho}_{\max} \lesssim 1200$ pc^{-3} yr^{-1} at 99% C.L.

Observing any astrophysical event with more than one messenger is always beneficial. While the gamma ray experiments offer the best chance to detect a burst from an evaporating PBH, it might be hard to distinguish the observed signal from other transient gamma ray sources, or pinpointing it unambiguously to a PBH. Unlike the conventional pp and $p\gamma$ scenarios for steady-state emitting sources, the relation between gamma ray and neutrino emission spectra for transient (explosive) sources can be nontrivial and changes depending on the source conditions. However, the exact ratio between the

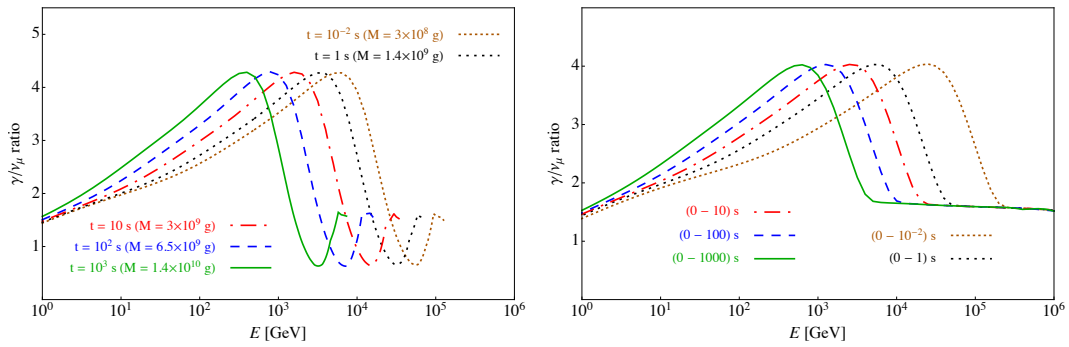

(a) (b)

Figure 5.6: (a) Ratio of the instantaneous γ/ν_μ spectra at various time instants. (b) Ratio of time-integrated spectra of gamma rays and neutrinos for several time intervals.

photon and neutrino spectra (at different times and energies) contains a unique signature of an evaporating PBH. Figure 5.6a shows the energy-dependence of $(\mathrm{d}^2N^{\gamma}_{\rm tot}/\mathrm{d}t\mathrm{d}E)/(\mathrm{d}^2N^{\nu_\mu}_{\rm tot}/\mathrm{d}t\mathrm{d}E|_{\oplus})$ at $t = 10^{-2}, 1, 10, 10^2$ and 10^3 s before the death of PBH. The peculiar, and almost t-independent, features of the curves in Figure 5.6a are the consequence of both the thermal Hawking radiation and the secondary production through hadronization and electroweak corrections in Standard Model. At the highest energies (close to the corresponding energy for each t) the ~ 1.5 gamma to neutrino ratio results from the greybody factors in Eq. (5-4) and the $\mathcal{A}$ coefficients of Eqs. (5-6) and (5-7). The drop in the ratio just below the highest energy, to ~ 0.5, and the rise in lower energies, to ~ 4, are the consequence of the secondary production mechanisms: while both the hadronization and electroweak corrections participate in photon and neutrino secondary productions, the former is more efficient in photon production at lower energies and the latter predominantly creates neutrinos with slightly lower energies than the primary energy. This energy separation in photon and neutrino secondary productions is an outcome of the well-established Standard Model physics, and in harmony with the quasi-black-body radiation from PBHs, shapes the drop and rise of the curves in Figure 5.6a, carrying the signature of PBHs.

Although the features of the curves in Figure 5.6a seem quite compelling, from an observational point of view, which requires some integration over energy and/or time, these features would change. Figure 5.6b shows the ratio of time-integrated spectra,

$$\int_0^{\tau}(\mathrm{d}^2N^{\gamma}_{\rm tot}/\mathrm{d}t\mathrm{d}E)\mathrm{d}t \Big/ \int_0^{\tau}(\mathrm{d}^2N^{\nu_\mu}_{\rm tot}/\mathrm{d}t\mathrm{d}E|_{\oplus})\mathrm{d}t \quad ,$$

as function of energy and for the time intervals $\tau = 10^{-2}, 1, 10, 10^2$ and 10^3 s.

Time integration leads to the disappearance of the dips in Figure 5.6a, while the energy-dependent rise of the gamma ray spectrum with respect to the neutrino's is still evident in Figure 5.6b. For larger τ, the peak of γ/ν_μ ratio moves to lower energies due to the lower PBH temperature. The energy-integrated spectra of gamma rays and neutrinos are in fact more important since both the extensive air shower experiments and neutrino telescopes have limited energy resolutions, while the time resolution is favorable (at the $\sim$ nanosecond level). Figure 5.7a shows the ratio of the energy-integrated spectra (over the energy bins indicated in the figure) of gamma rays to neutrinos as function of the remaining time to the complete evaporation of PBH. In lower (higher) energy bins, the peak of γ/ν_μ ratio is located at larger (smaller) times, although the gamma ray spectrum keeps dominating at t values below the peak. These features are the direct consequence of the dips in Figure 5.6a.

All the features and the correlations between gamma ray and neutrino spectra illustrated in Figures 5.6 and 5.7a can be verified and be used to infer the PBH nature of the observed event in both the extensive air shower and neutrino detectors. At the level of number of gamma ray and neutrino events, and the correlation among them, detector characteristics such as respective effective areas, the location of PBH and experimental cuts should be taken into account. To illustrate how the ratio of gamma ray to neutrino events looks like, in Figure 5.7b we show this ratio as function of time and integrated over energy bins for two different locations of PBH: the solid (dashed) curves correspond to a PBH locating at declination $\delta = 20°(70°)$, where the HAWC has its maximum (minimum) sensitivity, while for both cases IceCube's sensitivity remains almost the same. The drops and rises of the curves in Figure 5.7a are somehow visible also in Figure 5.6b, though modified by the effective areas (compare, for example, the red and blue curves in both panels). We have to emphasize that both the gamma ray and neutrino experiments can infer the observed flux from their number of events distributions and therefore verify the features in Figures 5.6 and 5.7a; of course when the PBH is located close enough to produce statistically adequate number of events, that is $d_L \lesssim 10^{-4}$ pc, and within the field of view of both experiments.

5.5 Discussions and conclusions

While the existence of PBHs has not yet been confirmed experimentally, the search for these remnants of primordial density fluctuations continues as a powerful diagnostic in probing early universe physics and probably the nature of dark matter. In this chapter, we have focused on PBHs with initial

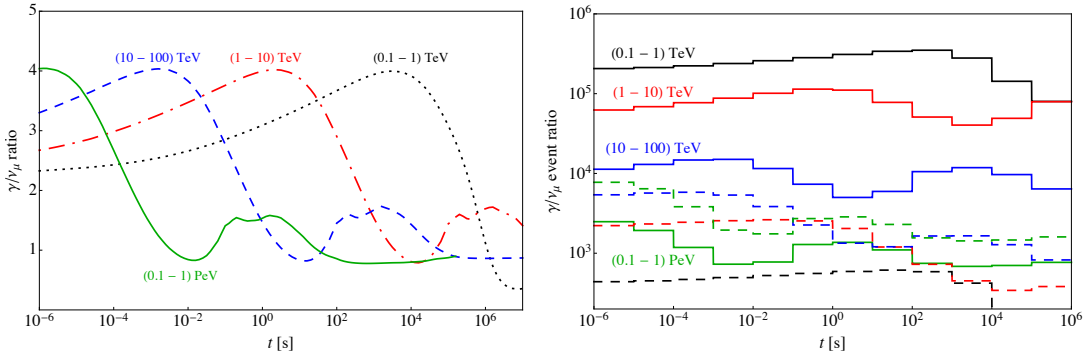

(a) (b)

Figure 5.7: (a) Ratio of the energy-integrated spectra of gamma rays to neutrinos in the stated bins of energy. (b) Ratio of the number of gamma ray to neutrino events, respectively at HAWC and IceCube experiments, for a PBH located at declination $\delta = 20°(70°)$ in solid (dashed) curves.

mass $M \sim 10^{15}$ g, which are expected to be currently in their last stages of evaporation due to Hawking radiation and hence producing detectable bursts of stable high-energy particles, including gamma rays and neutrinos, appearing as transient point sources in observatories. By employing the state-of-the-art `BlackHawk` and `HDMSpectra` codes, we have re-evaluated the primary and secondary gamma ray and neutrino emissions, pointing out important quantitative and qualitative differences from the existing literature. For the gamma rays, the new expected flux leads to a factor ~ 3 improvement on the local PBH burst rate density limit reported by HAWC collaboration, setting it to $\dot{\rho}_{\rm max} \lesssim 1200$ pc^{-3} yr^{-1} at 99% C.L.

For the neutrinos, by using the new flux evaluation which is significantly different from the few existing approximate calculations, we have estimated the IceCube's limit on PBH rate density from the 10-years μ-track data set to $\dot{\rho}_{\rm max} \lesssim 4 \times 10^6$ pc^{-3} yr^{-1} at 90% C.L. Although, as was expected, neutrino detectors cannot compete with gamma rays experiments in constraining PBH rate density, the larger field of view of neutrino telescopes (compared to the limited field of view of gamma ray experiments) renders them useful in PBH searches, especially with the upcoming KM3Net (403) which guarantees 4π sr coverage of the sky. Unfortunately, future extensions of IceCube detector both in the high-energy, IceCube-Gen2 (404), and low energy, IceCube Upgrade (405), does not boost the PBH search. Even though IceCube-Gen2's effective area at $\gtrsim$ PeV energies is expected to increase by a factor of ~ 10, the PBH's neutrino fluence at $\gtrsim$ PeV is several orders of magnitude lower than that around $\sim$ TeV energies, and no gain can be envisaged. In the low energy side ($\lesssim 100$ GeV) the increase in the neutrino emission from PBH is not as stiff

as the atmospheric neutrino flux which is the main target of IceCube Upgrade.

Finally, we have shown how a multi-messenger approach, taking into account the correlation between gamma ray and neutrino spectra, can provide a rapid identification of a PBH with distance $\lesssim 10^{-4}$ pc, in the case of a simultaneous observation in gamma ray and neutrino experiments. The primary thermal radiation of PBHs and the well-established secondary emission due to hadronization and electroweak corrections predict peculiar time and energy profiles of gamma-to-neutrino ratio which can be used in distinguishing PBHs from other astrophysical transients and has been discussed thoroughly. The last argument, one more time, brings forward the importance of multi-messenger approach in the era of precision measurements in astrophysics, that we are entering, and the crucial role of neutrinos in this field.

6
Final Considerations

In the ongoing effort to expand our understanding of astrophysical phenomena, this thesis has explored several key aspects of ultra-high- and high-energy astroparticles by investigating the microphysics governing these processes, primarily in a multi-messenger framework. From the ionization state of heavy nuclei during their acceleration in astrophysical sources to the probability of neutrino production via electromagnetic cascades, from the precision refinement of cosmic ray propagation theories through the Galaxy to the potential detectability of primordial black holes through simultaneous gamma-ray and neutrino observations, this work addresses some previously overlooked or neglected aspects that, with the advent of precision measurements, have become increasingly significant and inevitable.

In Chapter 2 we investigated pair production with capture (PPC)—an often-neglected channel in which a Bethe–Heitler pair-production event leaves the electron bound to the parent nucleus. By assessment of the PPC rate across energy and atomic-number space, we identified a regime—mostly achievable inside UHECR acceleration sites—where PPC outpaces all competing loss processes. In that regime nuclei becomes partially dressed, carrying one or more bound electrons and therefore an effective charge smaller than the atomic number ($Z < Z^*$); this lowers the efficiency of the acceleration mechanisms, particularly for heavy and ultra-heavy species.

For intergalactic propagation, however, the situation differs. Throughout the observed UHECR energy range, photo-ionization in the cosmic radiation fields strips any residual electrons on timescales far shorter than the travel time. Consequently, even if nuclei leave their sources in a partially ionized state, they arrive at Earth fully stripped. The recent composition fits to PAO data that invoke ultra-heavy primaries—e.g. (241)—should therefore consider still heavier elements to compensate for the PPC-induced charge reduction that operates during acceleration but not during propagation.

In Chapter 3 we extended our study of ultra-high-energy cosmic messengers to the development of electromagnetic cascades of the photons and electrons at energies above the muon pair production threshold. Above this threshold, additional photon–photon and electron–photon channels open. These channels divert a sizable fraction of the cascade energy into neutrinos. This "energy leakage" can, in principle, operate both during intergalactic propagation and within astrophysical sources whenever the CoM energy of the interacting

photon fields is sufficiently large.

To quantify the resulting neutrino output we developed `MUNHECA`, a dedicated Monte-Carlo code that follows all relevant particle interactions and decays. Simulations show that up to 37 % of the energy injected into an electromagnetic cascade can escape in the form of neutrinos, a figure that has important implications for multi-messenger modelling. Chapter 3 also analyses the shape of the emergent neutrino spectrum, linking its key features to the underlying reaction channels and to source or propagation conditions.

The astrophysical neutrinos are often known as the definitive signature of hadronic interactions in astrophysical sources; yet our cascade study shows that leptonic channels can produce a comparable—and at low energies, even dominant—neutrino flux. Specifically, while the hadronic component prevails at the highest energies, the neutrinos generated by electromagnetic cascades exceed the hadronic contribution by one to two orders of magnitude below the spectral peak. Consequently, the neutrino spectrum emerging from UHECR accelerators can differ substantially from that predicted by purely hadronic models. Its exact shape is highly model-dependent, reflecting the assumed properties of the source environment. Analogous spectra appear for cosmogenic neutrinos, although in a different energy range because the relevant high- and low-energy photon fields have different characteristic energies.

Cosmogenic neutrinos produced in electromagnetic cascades offer a unique window on the high-redshift Universe and are expected to lie within the discovery reach of forthcoming detectors such as IceCube-Gen2 and the GRAND.

In Chapter 4 we turned to the GeV-energy domain, analyzing the energy-loss mechanisms that govern cosmic-ray protons inside the Milky Way. The impetus was a growing mismatch between the percent-level precision of modern low-energy flux measurements and the comparatively coarse approximations still common in propagation codes. We revisited three such approximations: (i) applying the Bethe ionization formula down to all energies, (ii) neglecting elastic scattering losses, and (iii) treating intrinsically catastrophic energy losses (*i.e.* discrete, high-inelasticity interactions in which a particle surrenders a sizeable fraction of its energy in a single event, so the continuous-loss approximation no longer applies) as continuous. Our assessments confirm that, for protons, the Bethe expression remains adequate; however, elastic losses and, especially, the proper stochastic treatment of catastrophic interactions introduce corrections of up to 3%. These effects must therefore be included in any analysis that aims for percent-level accuracy in the Galactic cosmic-ray spectrum.

Finally, in Chapter 5 we turned to the final moments of $\sim 10^{15}$ g PBHs and analyzed their detectability through a multi-messenger $\gamma - \nu$ approach. Although PBHs have yet to be observed experimentally, they remain a sensitive probe of early-Universe physics and a potential dark-matter component. Our work proceeded on two fronts.

First, we carried out a high-precision re-evaluation of the Hawking-radiation spectra. The resulting gamma ray and neutrino fluxes exhibit important quantitative and qualitative differences from earlier estimates, tightening existing limits from HAWC and yielding revised neutrino expectations for IceCube.

Second, we showed that correlating the characteristic time- and energy-dependent γ/ν ratio predicted by Hawking evaporation allows a rapid, distance-limited identification of PBH bursts: a simultaneous detection in gamma rays and neutrinos would uniquely tag a PBH within $\lesssim 10^{-4}$ pc of Earth.

All in all, these studies again underscores the value of a multi-messenger approach in today's era of precision astrophysics and highlights the pivotal role neutrinos play within it.

Furthermore, next-generation observatories—IceCube-Gen2 and GRAND for neutrinos, CTA and SWGO for very-high-energy γ rays, and the expanding KM3NeT array, alongside continuing facilities such as HAWC, IceCube and many others—will extend both the energy reach and the statistical precision of every cosmic-messenger channel. As statistical and systematic errors shrink, theoretical models must follow suit: fluxes measured at the percent level can only be interpreted if cross-sections, energy-loss rates, and source-population models are treated with comparable accuracy. Meeting this standard will let us exploit the full predictive power of the Standard Model and isolate, unambiguously, those regions where data begin to diverge.

Astrophysical accelerators—relativistic jets, supernova shocks, compact-object magnetospheres—probe magnetic fields, densities, and Lorentz factors far beyond terrestrial capabilities. Studied with multi-messenger data sets, these sources can tighten constraints on physics beyond the Standard Model—for example, on dark-matter annihilation—and reveal otherwise inaccessible regions of the cosmos, such as the high-redshift Universe traced by cosmogenic neutrinos. With accurate microphysics in place, upcoming measurements will do more than refine the existing models; they will map the parameter space where observations depart from Standard Model expectations. The phenomenological tools developed in this thesis are intended to meet that precision era head-on.

With these reflections I draw this thesis to a close. I hope the ideas developed here prove useful to those who share a fascination with the high-energy Universe, and I am grateful to every reader who has accompanied me along this path.

7
Bibliography

1 DRIVER, S. P. Measuring energy production in the Universe over all wavelengths and all time. In: **IAU Symposium 355: The Realm of the Low Surface Brightness Universe**. [S.l.: s.n.], 2021.

2 Domínguez, A. et al. Extragalactic background light inferred from AEGIS galaxy-SED-type fractions. , v. 410, n. 4, p. 2556–2578, fev. 2011.

3 NItU, I. C. et al. An updated estimate of the cosmic radio background and implications for ultra-high-energy photon propagation. **Astropart. Phys.**, v. 126, p. 102532, 2021.

4 PROTHEROE, R. J.; BIERMANN, P. L. A New estimate of the extragalactic radio background and implications for ultrahigh-energy gamma-ray propagation. **Astropart. Phys.**, v. 6, p. 45–54, 1996. [Erratum: Astropart.Phys. 7, 181 (1997)].

5 Bonato, M. et al. Does the evolution of the radio luminosity function of star-forming galaxies match that of the star formation rate function? , v. 469, n. 2, p. 1912–1923, ago. 2017.

6 de Zotti, G. et al. Radio and millimeter continuum surveys and their astrophysical implications. , v. 18, n. 1-2, p. 1–65, fev. 2010.

7 Massardi, M. et al. A model for the cosmological evolution of low-frequency radio sources. , v. 404, n. 1, p. 532–544, maio 2010.

8 AARTSEN, M. G. et al. IceCube-Gen2: the window to the extreme Universe. **J. Phys. G**, v. 48, n. 6, p. 060501, 2021.

9 EVOLI, C. **The Cosmic-Ray Energy Spectrum**. Zenodo, 2020. Disponível em: <https://doi.org/10.5281/zenodo.4396125>.

10 Tatischeff, V.; Gabici, S. Particle Acceleration by Supernova Shocks and Spallogenic Nucleosynthesis of Light Elements. **Annual Review of Nuclear and Particle Science**, v. 68, n. 1, p. 377–404, out. 2018.

11 Montanus, H. An extended Heitler-Matthews model for the full hadronic cascade in cosmic air showers. **arXiv e-prints**, p. arXiv:1311.0642, nov. 2013.

12 The Pierre Auger Collaboration. Inference of the Mass Composition of Cosmic Rays with energies from $\mathbf{10^{18.5}}$ to $\mathbf{10^{20}}$ eV using the Pierre Auger Observatory and Deep Learning. **arXiv e-prints**, p. arXiv:2406.06315, jun. 2024.

13 RIEGER, F. M. Active Galactic Nuclei as Potential Sources of Ultra-High Energy Cosmic Rays. **Universe**, v. 8, n. 11, p. 607, 2022.

14 MOREJON, L. et al. Improved photomeson model for interactions of cosmic ray nuclei. **JCAP**, v. 11, p. 007, 2019.

15 MAZZIOTTA, M. N. et al. Production of secondary particles and nuclei in cosmic rays collisions with the interstellar gas using the FLUKA code. **Astropart. Phys.**, v. 81, p. 21–38, 2016.

16 Dermer, C. D. Binary Collision Rates of Relativistic Thermal Plasmas. II. Spectra. , v. 307, p. 47, ago. 1986.

17 Ackermann, M. et al. The Spectrum of Isotropic Diffuse Gamma-Ray Emission between 100 MeV and 820 GeV. , v. 799, n. 1, p. 86, jan. 2015.

18 FENU, F. The cosmic ray energy spectrum measured using the Pierre Auger Observatory. **PoS**, ICRC2017, p. 486, 2017.

19 ABBASI, R. et al. The IceCube high-energy starting event sample: Description and flux characterization with 7.5 years of data. **Phys. Rev. D**, v. 104, p. 022002, 2021.

20 BEREZINSKY, V.; KALASHEV, O. High energy electromagnetic cascades in extragalactic space: physics and features. **Phys. Rev. D**, v. 94, n. 2, p. 023007, 2016.

21 KACHELRIESS, M.; OSTAPCHENKO, S.; TOMAS, R. ELMAG: A Monte Carlo simulation of electromagnetic cascades on the extragalactic background light and in magnetic fields. **Comput. Phys. Commun.**, v. 183, p. 1036–1043, 2012.

22 AHARONIAN, F. et al. Constraints on the Intergalactic Magnetic Field Using Fermi-LAT and H.E.S.S. Blazar Observations. **Astrophys. J. Lett.**, v. 950, n. 2, p. L16, 2023.

23 MURASE, K.; KIMURA, S. S.; MESZAROS, P. Hidden Cores of Active Galactic Nuclei as the Origin of Medium-Energy Neutrinos: Critical Tests with the MeV Gamma-Ray Connection. **Phys. Rev. Lett.**, v. 125, n. 1, p. 011101, 2020.

24 ATHAR, H.; LIN, G.-L.; TSENG, J.-J. Muon pair production by electron photon scatterings. **Phys. Rev. D**, v. 64, p. 071302(R), 2001.

25 HOOPER, D.; PLANT, K. Leptonic Model for Neutrino Emission from Active Galactic Nuclei. **Phys. Rev. Lett.**, v. 131, n. 23, p. 231001, 2023.

26 CUGNON, J.; VANDERMEULEN, J.; L'HOTE, D. Simple parametrization of cross-sections for nuclear transport studies up to the GeV range. **Nucl. Instrum. Meth. B**, v. 111, p. 215–220, 1996.

27 MAZZIOTTA, M. N. et al. Production of secondary particles and nuclei in cosmic rays collisions with the interstellar gas using the FLUKA code. **Astropart. Phys.**, v. 81, p. 21–38, 2016.

28 BAKER, M. J.; THAMM, A. Probing the Particle Spectrum of Nature with Evaporating Black Holes. 2021.

29 ALBERT, A. et al. Constraining the local burst rate density of primordial black holes with HAWC. **JCAP**, v. 04, p. 026, 2020.

30 HALZEN, F.; KESZTHELYI, B.; ZAS, E. Neutrinos from primordial black holes. **Phys. Rev. D**, v. 52, p. 3239–3247, 1995.

31 DAVE, P.; TABOADA, I. Neutrinos from Primordial Black Hole Evaporation. In: **Contributions to the 36th International Cosmic Ray Conference (ICRC2019)**. [S.l.: s.n.], 2019.

32 ESTEBAN, I. et al. NuFit-6.0: Updated global analysis of three-flavor neutrino oscillations. 10 2024.

33 ESMAEILI, A.; ESMAILI, A.; SERPICO, P. D. Pair production with capture by energetic cosmic ray nuclei in a photon background. **Phys. Rev. D**, v. 111, n. 4, p. 043004, 2025.

34 ESMAEILI, A. et al. Ultrahigh energy neutrinos from high-redshift electromagnetic cascades. **Phys. Rev. D**, v. 106, n. 12, p. 123016, 2022.

35 ESMAEILI, A.; ESMAILI, A.; SERPICO, P. D. Neutrinos from muon-rich ultra high energy electromagnetic cascades: The MUNHECA code. **Comput. Phys. Commun.**, v. 299, p. 109154, 2024.

36 ESMAEILI, A.; ESMAILI, A.; SERPICO, P. D. Closer scrutiny of cosmic ray proton energy losses. **Phys. Rev. D**, v. 109, n. 12, p. 123024, 2024.

37 CAPANEMA, A.; ESMAEILI, A.; ESMAILI, A. Evaporating primordial black holes in gamma ray and neutrino telescopes. **JCAP**, v. 12, n. 12, p. 051, 2021.

38 Biteau, J.; Williams, D. A. The Extragalactic Background Light, the Hubble Constant, and Anomalies: Conclusions from 20 Years of TeV Gamma-ray Observations. , v. 812, n. 1, p. 60, out. 2015.

39 Abeysekara, A. U. et al. Measurement of the Extragalactic Background Light Spectral Energy Distribution with VERITAS. , v. 885, n. 2, p. 150, nov. 2019.

40 ACKERMANN, M. et al. Unresolved Gamma-Ray Sky through its Angular Power Spectrum. **Phys. Rev. Lett.**, v. 121, n. 24, p. 241101, 2018.

41 Giacconi, R. et al. Evidence for x Rays From Sources Outside the Solar System. , v. 9, n. 11, p. 439–443, dez. 1962.

42 Gilli, R.; Comastri, A.; Hasinger, G. The synthesis of the cosmic X-ray background in the Chandra and XMM-Newton era. , v. 463, n. 1, p. 79–96, fev. 2007.

43 Finke, J. D.; Razzaque, S.; Dermer, C. D. Modeling the Extragalactic Background Light from Stars and Dust. , v. 712, n. 1, p. 238–249, mar. 2010.

44 Driver, S. P. et al. Measurements of Extragalactic Background Light from the Far UV to the Far IR from Deep Ground- and Space-based Galaxy Counts. , v. 827, n. 2, p. 108, ago. 2016.

45 de Zotti, G. et al. Radio and millimeter continuum surveys and their astrophysical implications. , v. 18, n. 1-2, p. 1–65, fev. 2010.

46 Fixsen, D. J. et al. ARCADE 2 Measurement of the Absolute Sky Brightness at 3-90 GHz. , v. 734, n. 1, p. 5, jun. 2011.

47 Vernstrom, T.; Scott, D.; Wall, J. V. Contribution to the diffuse radio background from extragalactic radio sources. , v. 415, n. 4, p. 3641–3648, ago. 2011.

48 Murphy, E. J.; Chary, R.-R. Excess in the High-frequency Radio Background: Insights from Planck. , v. 861, n. 1, p. 27, jul. 2018.

49 SANO, K.; MATSUURA, S. Galactic Latitude Dependence of Near-Infrared Diffuse Galactic Light : Thermal Emission or Scattered Light? **Astrophys. J.**, v. 849, n. 1, p. 31, 2017.

50 Mathis, J. S. The Interpretation of the Diffuse Galactic Light. , v. 186, p. 815–830, dez. 1973.

51 Reach, W. T. Zodiacal Emission. II. Dust near the Ecliptic. , v. 369, p. 529, mar. 1991.

52 San, M. et al. COSMOGLOBE: Simulating zodiacal emission with ZodiPy. , v. 666, p. A107, out. 2022.

53 Porter, T. A. Cosmic-Ray induced diffuse emissions from the Milky Way and Local Group galaxies. In: Tuffs, R. J.; Popescu, C. C. (Ed.). **The Spectral Energy Distribution of Galaxies - SED 2011**. [S.l.: s.n.], 2012. (IAU Symposium, v. 284), p. 360–364.

54 Gamow, G. The Evolution of the Universe. , v. 162, n. 4122, p. 680–682, out. 1948.

55 ALPHER, R. A.; HERMAN, R. K. Evolution of the universe. **Nature**, v. 162, p. 774–775, 1948. Disponível em: <https://api.semanticscholar.org/CorpusID:4113488>.

56 Penzias, A. A.; Wilson, R. W. A Measurement of Excess Antenna Temperature at 4080 Mc/s. , v. 142, p. 419–421, jul. 1965.

57 Fixsen, D. J. et al. The Cosmic Microwave Background Spectrum from the Full COBE FIRAS Data Set. , v. 473, p. 576, dez. 1996.

58 Bennett, C. L. et al. Nine-year Wilkinson Microwave Anisotropy Probe (WMAP) Observations: Final Maps and Results. , v. 208, n. 2, p. 20, out. 2013.

59 AGHANIM, N. et al. Planck 2018 results. VI. Cosmological parameters. **Astron. Astrophys.**, v. 641, p. A6, 2020. [Erratum: Astron.Astrophys. 652, C4 (2021)].

60 SAMTLEBEN, D.; STAGGS, S.; WINSTEIN, B. The Cosmic microwave background for pedestrians: A Review for particle and nuclear physicists. **Ann. Rev. Nucl. Part. Sci.**, v. 57, p. 245–283, 2007.

61 HILL, R.; MASUI, K. W.; SCOTT, D. The spectrum of the universe. **Applied Spectroscopy**, v. 72, n. 5, p. 663–688, 2018. PMID: 29617155. Disponível em: <https://doi.org/10.1177/0003702818767133>.

62 TOMPKINS, S. A. et al. The cosmic radio background from 150 MHz to 8.4 GHz and its division into AGN and star-forming galaxy flux. **MNRAS**, v. 521, p. 332–353, 1 2023.

63 Gilmore, R. C. et al. Semi-analytic modelling of the extragalactic background light and consequences for extragalactic gamma-ray spectra. , v. 422, n. 4, p. 3189–3207, jun. 2012.

64 Singal, J. et al. Sources of the radio background considered. , v. 409, n. 3, p. 1172–1182, dez. 2010.

65 WIDROW, L. M. Origin of galactic and extragalactic magnetic fields. **Rev. Mod. Phys.**, American Physical Society, v. 74, p. 775–823, Jul 2002. Disponível em: <https://link.aps.org/doi/10.1103/RevModPhys.74.775>.

66 CHABERT, P.; BRAITHWAITE, N. **Physics of Radio-Frequency Plasmas**. [S.l.: s.n.], 2011.

67 Lacki, B. C. The end of the rainbow: what can we say about the extragalactic sub-megahertz radio sky? , v. 406, n. 2, p. 863–880, ago. 2010.

68 Clark, T. A.; Brown, L. W.; Alexander, J. K. Spectrum of the Extra-galactic Background Radiation at Low Radio Frequencies. , v. 228, n. 5274, p. 847–849, nov. 1970.

69 Ackermann, M. et al. Fermi-LAT Observations of the Diffuse γ-Ray Emission: Implications for Cosmic Rays and the Interstellar Medium. , v. 750, n. 1, p. 3, maio 2012.

70 Antonucci, R. Unified models for active galactic nuclei and quasars. , v. 31, p. 473–521, jan. 1993.

71 Ackermann, M. et al. GeV Observations of Star-forming Galaxies with the Fermi Large Area Telescope. , v. 755, n. 2, p. 164, ago. 2012.

72 Ajello, M. et al. The γ-Ray Emission of Star-forming Galaxies. , v. 894, n. 2, p. 88, maio 2020.

73 Clark, G. W.; Garmire, G. P.; Kraushaar, W. L. Observation of High-Energy Cosmic Gamma Rays. , v. 153, p. L203, set. 1968.

74 Kraushaar, W. L. et al. High-Energy Cosmic Gamma-Ray Observations from the OSO-3 Satellite. , v. 177, p. 341, nov. 1972.

75 Fichtel, C. E. et al. High-energy gamma-ray results from the second Small Astronomy Satellite. , v. 198, p. 163–182, maio 1975.

76 Fichtel, C. E.; Simpson, G. A.; Thompson, D. J. Diffuse gamma radiation. , v. 222, p. 833–849, jun. 1978.

77 Sreekumar, P. et al. EGRET Observations of the Extragalactic Gamma-Ray Emission. , v. 494, n. 2, p. 523–534, fev. 1998.

78 Strong, A. W.; Moskalenko, I. V.; Reimer, O. A New Determination of the Extragalactic Diffuse Gamma-Ray Background from EGRET Data. , v. 613, n. 2, p. 956–961, out. 2004.

79 FERENC, D. The MAGIC gamma-ray observatory. **Nucl. Instrum. Meth. A**, v. 553, p. 274–281, 2005.

80 ABEYSEKARA, A. U. et al. Sensitivity of the High Altitude Water Cherenkov Detector to Sources of Multi-TeV Gamma Rays. **Astropart. Phys.**, v. 50-52, p. 26–32, 2013.

81 SCIASCIO, G. D. The LHAASO experiment: from Gamma-Ray Astronomy to Cosmic Rays. **Nucl. Part. Phys. Proc.**, v. 279-281, p. 166–173, 2016.

82 PACINI, D. **Penetrating Radiation at the Surface of and in Water**. 2010.

83 HESS, V. On the Observations of the Penetrating Radiation during Seven Balloon Flights. 7 2018.

84 ROSSI, B. On the magnetic deflection of cosmic rays. **Phys. Rev.**, American Physical Society, v. 36, p. 606–606, Aug 1930. Disponível em: <https://link.aps.org/doi/10.1103/PhysRev.36.606>.

85 ALVAREZ, L.; COMPTON, A. H. A Positively Charged Component of Cosmic Rays. **Phys. Rev.**, v. 43, n. 10, p. 835–836, 1933.

86 COMPTON, A. H. A geographic study of cosmic rays. **Phys. Rev.**, American Physical Society, v. 43, p. 387–403, Mar 1933. Disponível em: <https://link.aps.org/doi/10.1103/PhysRev.43.387>.

87 JOHNSON, T. H. The Azimuthal Asymmetry of the Cosmic Radiation. **Phys. Rev.**, v. 43, n. 10, p. 834–835, 1933.

88 ROSSI, B. Directional Measurements on the Cosmic Rays Near the Geomagnetic Equator. **Phys. Rev.**, v. 45, n. 3, p. 212–214, 1934.

89 Donati, J. F.; Landstreet, J. D. Magnetic Fields of Nondegenerate Stars. , v. 47, n. 1, p. 333–370, set. 2009.

90 Kronberg, P. P. Extragalactic magnetic fields. **Reports on Progress in Physics**, v. 57, n. 4, p. 325–382, abr. 1994.

91 Fletcher, A. Magnetic Fields in Nearby Galaxies. In: Kothes, R.; Landecker, T. L.; Willis, A. G. (Ed.). **The Dynamic Interstellar Medium: A Celebration of the Canadian Galactic Plane Survey**. [S.l.: s.n.], 2010. (Astronomical Society of the Pacific Conference Series, v. 438), p. 197.

92 Beck, R. Magnetic Fields in Galaxies. , v. 166, n. 1-4, p. 215–230, maio 2012.

93 Kronberg, P. P.; Perry, J. J.; Zukowski, E. L. H. Discovery of Extended Faraday Rotation Compatible with Spiral Structure in an Intervening Galaxy at Z = 0.395: New Observations of PKS 1229-021. , v. 387, p. 528, mar. 1992.

94 BERNET, M. L. et al. Strong magnetic fields in normal galaxies at high redshifts. **Nature**, v. 454, p. 302–304, 2008.

95 Clarke, T. E.; Kronberg, P. P.; Böhringer, H. A New Radio-X-Ray Probe of Galaxy Cluster Magnetic Fields. , v. 547, n. 2, p. L111–L114, fev. 2001.

96 Bonafede, A. et al. The Coma cluster magnetic field from Faraday rotation measures. , v. 513, p. A30, abr. 2010.

97 Feretti, L. et al. Clusters of galaxies: observational properties of the diffuse radio emission. , v. 20, p. 54, maio 2012.

98 XU, Y. et al. A faraday rotation search for magnetic fields in large scale structure. **Astrophys. J.**, v. 637, p. 19–26, 2006.

99 Neronov, A.; Vovk, I. Evidence for Strong Extragalactic Magnetic Fields from Fermi Observations of TeV Blazars. **Science**, v. 328, n. 5974, p. 73, abr. 2010.

100 Dolag, K. et al. Lower Limit on the Strength and Filling Factor of Extragalactic Magnetic Fields. , v. 727, n. 1, p. L4, jan. 2011.

101 PARKER, E. N. Hydromagnetic Dynamo Models. **Astrophys. J.**, v. 122, p. 293, 1955.

102 KULSRUD, R. M. A critical review of galactic dynamos. **Ann. Rev. Astron. Astrophys.**, v. 37, p. 37–64, 1999.

103 BRANDENBURG, A.; SUBRAMANIAN, K. Astrophysical magnetic fields and nonlinear dynamo theory. **Phys. Rept.**, v. 417, p. 1–209, 2005.

104 KULSRUD, R. M.; ZWEIBEL, E. G. The Origin of Astrophysical Magnetic Fields. **Rept. Prog. Phys.**, v. 71, p. 0046091, 2008.

105 KRONBERG, P. P. Extragalactic magnetic fields. **Rept. Prog. Phys.**, v. 57, p. 325–382, 1994.

106 GRASSO, D.; RUBINSTEIN, H. R. Magnetic fields in the early universe. **Phys. Rept.**, v. 348, p. 163–266, 2001.

107 BERTONE, S.; VOGT, C.; ENSSLIN, T. Magnetic Field Seeding by Galactic Winds. **Mon. Not. Roy. Astron. Soc.**, v. 370, p. 319–330, 2006.

108 ENSSLIN, T. A. et al. Cosmic ray protons and magnetic fields in clusters of galaxies and their cosmological consequences. **Astrophys. J.**, v. 477, p. 560, 1997.

109 Akahori, T. et al. Cosmic magnetism in centimeter- and meter-wavelength radio astronomy. , v. 70, n. 1, p. R2, jan. 2018.

110 Jaffe, T. R. Practical Modeling of Large-Scale Galactic Magnetic Fields: Status and Prospects. **Galaxies**, v. 7, n. 2, p. 52, abr. 2019.

111 DURRER, R.; NERONOV, A. Cosmological Magnetic Fields: Their Generation, Evolution and Observation. **Astron. Astrophys. Rev.**, v. 21, p. 62, 2013.

112 Stone, E. C. et al. Voyager 1 Observes Low-Energy Galactic Cosmic Rays in a Region Depleted of Heliospheric Ions. **Science**, v. 341, n. 6142, p. 150–153, jul. 2013.

113 Berezhnev, S. F. et al. The Tunka Experiment: Status 2013. In: **International Cosmic Ray Conference**. [S.l.: s.n.], 2013. (International Cosmic Ray Conference, v. 33), p. 256.

114 BIRD, D. J. et al. Detection of a cosmic ray with measured energy well beyond the expected spectral cutoff due to cosmic microwave radiation. **Astrophys. J.**, v. 441, p. 144–150, 1995.

115 Aartsen, M. G. et al. Measurement of the cosmic ray energy spectrum with IceTop-73. , v. 88, n. 4, p. 042004, ago. 2013.

116 HAUNGS, A. et al. High-energy cosmic rays measured with KASCADE-Grande. **PoS**, EPS-HEP2013, p. 398, 2013.

117 The Pierre Auger Collaboration. The Pierre Auger Cosmic Ray Observatory. **arXiv e-prints**, p. arXiv:1502.01323, fev. 2015.

118 Abu-Zayyad, T. et al. The surface detector array of the Telescope Array experiment. **Nuclear Instruments and Methods in Physics Research A**, v. 689, p. 87–97, out. 2012.

119 TOKUNO, H. et al. New air fluorescence detectors employed in the Telescope Array experiment. **Nucl. Instrum. Meth. A**, v. 676, p. 54–65, 2012.

120 PARKER, E. N. The passage of energetic charged particles through interplanetary space. **Planet. Space Sci.**, v. 13, n. 1, p. 9–49, 1965.

121 GREISEN, K. End to the cosmic ray spectrum? **Phys. Rev. Lett.**, v. 16, p. 748–750, 1966.

122 ZATSEPIN, G. T.; KUZMIN, V. A. Upper limit of the spectrum of cosmic rays. **JETP Lett.**, v. 4, p. 78–80, 1966.

123 ALLARD, D. et al. UHE nuclei propagation and the interpretation of the ankle in the cosmic-ray spectrum. **Astron. Astrophys.**, v. 443, p. L29–L32, 2005.

124 Bird, D. J. et al. The Cosmic-Ray Energy Spectrum Observed by the Fly's Eye. , v. 424, p. 491, mar. 1994.

125 TAKEDA, M. et al. Energy determination in the Akeno Giant Air Shower Array experiment. **Astropart. Phys.**, v. 19, p. 447–462, 2003.

126 ABBASI, R. U. et al. First observation of the Greisen-Zatsepin-Kuzmin suppression. **Phys. Rev. Lett.**, v. 100, p. 101101, 2008.

127 ABBASI, R. U. et al. Measurement of the Flux of Ultra High Energy Cosmic Rays by the Stereo Technique. **Astropart. Phys.**, v. 32, p. 53–60, 2009.

128 **The Pierre Auger Observatory: Contributions to the 36th International Cosmic Ray Conference (ICRC 2019): Madison, Wisconsin, USA, July 24- August 1, 2019**.

129 IVANOV, D. Energy Spectrum Measured by the Telescope Array. **PoS**, ICRC2019, p. 298, 2019.

130 AAB, A. et al. Features of the Energy Spectrum of Cosmic Rays above 2.5×10^{18} eV Using the Pierre Auger Observatory. **Phys. Rev. Lett.**, v. 125, n. 12, p. 121106, 2020.

131 Ostapchenko, S. QGSJET-II: towards reliable description of very high energy hadronic interactions. **Nuclear Physics B Proceedings Supplements**, v. 151, p. 143–146, jan. 2006.

132 d'Enterria, D. et al. Constraints from the first LHC data on hadronic event generators for ultra-high energy cosmic-ray physics. **Astroparticle Physics**, v. 35, n. 2, p. 98–113, set. 2011.

133 GAISSER, T. K.; STANEV, T.; TILAV, S. Cosmic Ray Energy Spectrum from Measurements of Air Showers. **Front. Phys. (Beijing)**, v. 8, p. 748–758, 2013.

134 VERZI, V. Cosmic rays: air showers from low to high energies. **PoS**, ICRC2015, p. 015, 2016.

135 BEREZINSKY, V.; GAZIZOV, A.; GRIGORIEVA, S. On astrophysical solution to ultrahigh energy cosmic rays. **Phys. Rev. D**, American Physical Society, v. 74, p. 043005, Aug 2006. Disponível em: <https://link.aps.org/doi/10.1103/PhysRevD.74.043005>.

136 AAB, A. et al. Measurement of the cosmic-ray energy spectrum above 2.5×10^{18} eV using the Pierre Auger Observatory. **Phys. Rev. D**, v. 102, n. 6, p. 062005, 2020.

137 Verzi, V.; Ivanov, D.; Tsunesada, Y. Measurement of Energy Spectrum of Ultra-High Energy Cosmic Rays. **arXiv e-prints**, p. arXiv:1705.09111, maio 2017.

138 Deligny, O. The energy spectrum of ultra-high energy cosmic rays measured at the Pierre Auger Observatory and at the Telescope Array. **arXiv e-prints**, p. arXiv:2001.08811, jan. 2020.

139 TSUNESADA, Y. et al. Joint analysis of the energy spectrum of ultra-high-energy cosmic rays as measured at the Pierre Auger Observatory and the Telescope Array. **PoS**, ICRC2021, p. 337, 2021.

140 TSUNESADA, Y. et al. Measurement of UHECR energy spectrum with the Pierre Auger Observatory and the Telescope Array. **PoS**, ICRC2023, p. 406, 2023.

141 The Telescope Array Collaboration. Observation of Declination Dependence in the Cosmic Ray Energy Spectrum. **arXiv e-prints**, p. arXiv:2406.08612, jun. 2024.

142 Abbasi, R. U. et al. Indications of Intermediate-scale Anisotropy of Cosmic Rays with Energy Greater Than 57 EeV in the Northern Sky Measured with the Surface Detector of the Telescope Array Experiment. , v. 790, n. 2, p. L21, ago. 2014.

143 Rauch, B. F. et al. Cosmic Ray origin in OB Associations and Preferential Acceleration of Refractory Elements: Evidence from Abundances of Elements $_{26}$Fe through $_{34}$Se. , v. 697, n. 2, p. 2083–2088, jun. 2009.

144 Apel, W. D. et al. Energy spectra of elemental groups of cosmic rays: Update on the KASCADE unfolding analysis. **Astroparticle Physics**, v. 31, n. 2, p. 86–91, mar. 2009.

145 BARTOLI, B. et al. Cosmic ray proton plus helium energy spectrum measured by the argo-ybj experiment in the energy range 3–300 tev. **Phys. Rev. D**, American Physical Society, v. 91, p. 112017, Jun 2015. Disponível em: <https://link.aps.org/doi/10.1103/PhysRevD.91.112017>.

146 Gaisser, T. K.; Hillas, A. M. Reliability of the Method of Constant Intensity Cuts for Reconstructing the Average Development of Vertical Showers. In: **International Cosmic Ray Conference**. [S.l.: s.n.], 1977. (International Cosmic Ray Conference, v. 8), p. 353.

147 Pierre Auger Collaboration. Interpretation of the depths of maximum of extensive air showers measured by the Pierre Auger Observatory. , v. 2013, n. 2, p. 026, fev. 2013.

148 Aab, A.; Pierre Auger Collaboration. Depth of maximum of air-shower profiles at the Pierre Auger Observatory. II. Composition implications. , v. 90, n. 12, p. 122006, dez. 2014.

149 MATTHEWS, J. A Heitler model of extensive air showers. **Astropart. Phys.**, v. 22, p. 387–397, 2005.

150 Linsley, J. Structure of Large Air Showers at Depth 834 G cm^{-2} Applications. In: **International Cosmic Ray Conference**. [S.l.: s.n.], 1977. (International Cosmic Ray Conference, v. 12), p. 89.

151 LINSLEY, J.; WATSON, A. A. Validity of scaling to 10^{20} ev and high-energy cosmic-ray composition. **Phys. Rev. Lett.**, American Physical Society, v. 46, p. 459–463, Feb 1981. Disponível em: <https://link.aps.org/doi/10.1103/PhysRevLett.46.459>.

152 HECK, D. et al. CORSIKA: A Monte Carlo code to simulate extensive air showers. 2 1998.

153 ORTIZ, J. A.; TANCO, G. A. M.; SOUZA, V. de. Longitudinal development of extensive air showers: Hybrid code SENECA and full Monte Carlo. **Astropart. Phys.**, v. 23, p. 463–476, 2005.

154 BERGMANN, T. et al. One-dimensional Hybrid Approach to Extensive Air Shower Simulation. **Astropart. Phys.**, v. 26, p. 420–432, 2007.

155 HALIM, A. A. et al. Testing hadronic-model predictions of depth of maximum of air-shower profiles and ground-particle signals using hybrid data of the Pierre Auger Observatory. **Phys. Rev. D**, v. 109, n. 10, p. 102001, 2024.

156 Telescope Array Collaboration. Mass composition of ultrahigh energy cosmic rays from distribution of their arrival directions with the Telescope Array. , v. 110, n. 2, p. 022006, jul. 2024.

157 Lv, X.-J. et al. Precise measurement of the cosmic-ray spectrum and $\langle \ln A \rangle$ by LHAASO – connecting the Galactic to the extragalactic components. **arXiv e-prints**, p. arXiv:2403.11832, mar. 2024.

158 HILLAS, A. M. The Origin of Ultrahigh-Energy Cosmic Rays. **Ann. Rev. Astron. Astrophys.**, v. 22, p. 425–444, 1984.

159 Fermi, E. On the Origin of the Cosmic Radiation. **Physical Review**, v. 75, n. 8, p. 1169–1174, abr. 1949.

160 Fermi, E. Galactic Magnetic Fields and the Origin of Cosmic Radiation. , v. 119, p. 1, jan. 1954.

161 Axford, W. I.; Leer, E.; Skadron, G. The Acceleration of Cosmic Rays by Shock Waves. In: **International Cosmic Ray Conference**. [S.l.: s.n.], 1977. (International Cosmic Ray Conference, v. 11), p. 132.

162 Bell, A. R. The acceleration of cosmic rays in shock fronts - I. , v. 182, p. 147–156, jan. 1978.

163 Blandford, R. D.; Ostriker, J. P. Particle acceleration by astrophysical shocks. , v. 221, p. L29–L32, abr. 1978.

164 HIROTANI, K. Very High-Energy Emission from the Direct Vicinity of Rapidly Rotating Black Holes. **Galaxies**, v. 6, n. 4, p. 122, 2018.

165 KATSOULAKOS, G.; RIEGER, F. M. Gap-type Particle Acceleration in the Magnetospheres of Rotating Supermassive Black Holes. **Astrophys. J.**, v. 895, n. 2, p. 99, 2020.

166 Chodorowski, M. J.; Zdziarski, A. A.; Sikora, M. Reaction Rate and Energy-Loss Rate for Photopair Production by Relativistic Nuclei. , v. 400, p. 181, nov. 1992.

167 Puget, J. L.; Stecker, F. W.; Bredekamp, J. H. Photonuclear interactions of ultrahigh energy cosmic rays and their astrophysical consequences. , v. 205, p. 638–654, abr. 1976.

168 Stecker, F. W.; Salamon, M. H. Photodisintegration of Ultra-High-Energy Cosmic Rays: A New Determination. , v. 512, n. 2, p. 521–526, fev. 1999.

169 Koning, A.; Hilaire, S.; Goriely, S. TALYS: modeling of nuclear reactions. **European Physical Journal A**, v. 59, n. 6, p. 131, jun. 2023.

170 AGOSTINELLI, S. et al. GEANT4 - A Simulation Toolkit. **Nucl. Instrum. Meth. A**, v. 506, p. 250–303, 2003.

171 KELNER, S. R.; AHARONIAN, F. A.; BUGAYOV, V. V. Energy spectra of gamma-rays, electrons and neutrinos produced at proton-proton interactions in the very high energy regime. **Phys. Rev. D**, v. 74, p. 034018, 2006. [Erratum: Phys.Rev.D 79, 039901 (2009)].

172 Krakau, S.; Schlickeiser, R. Pion Production Momentum Loss of Cosmic Ray Hadrons. , v. 802, n. 2, p. 114, abr. 2015.

173 EVOLI, C. et al. Cosmic-ray propagation with DRAGON2: II. Nuclear interactions with the interstellar gas. **JCAP**, v. 07, p. 006, 2018.

174 GENOLINI, Y. et al. Current status and desired precision of the isotopic production cross sections relevant to astrophysics of cosmic rays: Li, Be, B, C, and N. **Phys. Rev. C**, v. 98, n. 3, p. 034611, 2018.

175 Jackson, J. D. **Classical Electrodynamics, 3rd Edition**. [S.l.: s.n.], 1998.

176 AHLEN, S. P. THEORETICAL AND EXPERIMENTAL ASPECTS OF THE ENERGY LOSS OF RELATIVISTIC HEAVILY IONIZING PARTICLES. **Rev. Mod. Phys.**, v. 52, p. 121–173, 1980. [Erratum: Rev.Mod.Phys. 52, 653–653 (1980)].

177 AARTSEN, M. G. et al. Evidence for Astrophysical Muon Neutrinos from the Northern Sky with IceCube. **Phys. Rev. Lett.**, v. 115, n. 8, p. 081102, 2015.

178 AARTSEN, M. G. et al. Observation and Characterization of a Cosmic Muon Neutrino Flux from the Northern Hemisphere using six years of IceCube data. **Astrophys. J.**, v. 833, n. 1, p. 3, 2016.

179 AARTSEN, M. G. et al. Evidence for High-Energy Extraterrestrial Neutrinos at the IceCube Detector. **Science**, v. 342, p. 1242856, 2013.

180 AARTSEN, M. G. et al. Observation of High-Energy Astrophysical Neutrinos in Three Years of IceCube Data. **Phys. Rev. Lett.**, v. 113, p. 101101, 2014.

181 AARTSEN, M. G. et al. The IceCube Neutrino Observatory - Contributions to ICRC 2015 Part II: Atmospheric and Astrophysical Diffuse Neutrino Searches of All Flavors. In: **34th International Cosmic Ray Conference**. [S.l.: s.n.], 2015.

182 AARTSEN, M. G. et al. The IceCube Neutrino Observatory - Contributions to ICRC 2017 Part II: Properties of the Atmospheric and Astrophysical Neutrino Flux. 10 2017.

183 AARTSEN, M. G. et al. Atmospheric and astrophysical neutrinos above 1 TeV interacting in IceCube. **Phys. Rev. D**, v. 91, n. 2, p. 022001, 2015.

184 AARTSEN, M. G. et al. Characteristics of the diffuse astrophysical electron and tau neutrino flux with six years of IceCube high energy cascade data. **Phys. Rev. Lett.**, v. 125, n. 12, p. 121104, 2020.

185 GLASHOW, S. L. Resonant scattering of antineutrinos. **Phys. Rev.**, American Physical Society, v. 118, p. 316–317, Apr 1960. Disponível em: <https://link.aps.org/doi/10.1103/PhysRev.118.316>.

186 LOEWY, A.; NUSSINOV, S.; GLASHOW, S. L. The Effect of Doppler Broadening on the $6.3\ PeV\ W^-$ Resonance in $\bar{\nu}_e e^-$ Collisions. 7 2014.

187 BUSTAMANTE, M.; AHLERS, M. Inferring the flavor of high-energy astrophysical neutrinos at their sources. **Phys. Rev. Lett.**, v. 122, n. 24, p. 241101, 2019.

188 ABBASI, R. et al. Observation of high-energy neutrinos from the Galactic plane. **Science**, v. 380, n. 6652, p. adc9818, 2023.

189 AARTSEN, M. G. et al. Multimessenger observations of a flaring blazar coincident with high-energy neutrino IceCube-170922A. **Science**, v. 361, n. 6398, p. eaat1378, 2018.

190 AARTSEN, M. G. et al. Neutrino emission from the direction of the blazar TXS 0506+056 prior to the IceCube-170922A alert. **Science**, v. 361, n. 6398, p. 147–151, 2018.

191 ABBASI, R. et al. Evidence for neutrino emission from the nearby active galaxy NGC 1068. **Science**, v. 378, n. 6619, p. 538–543, 2022.

192 AARTSEN, M. G. et al. Time-Integrated Neutrino Source Searches with 10 Years of IceCube Data. **Phys. Rev. Lett.**, v. 124, n. 5, p. 051103, 2020.

193 ALBERT, A. et al. First all-flavor neutrino pointlike source search with the ANTARES neutrino telescope. **Phys. Rev. D**, v. 96, n. 8, p. 082001, 2017.

194 AARTSEN, M. G. et al. Search for steady point-like sources in the astrophysical muon neutrino flux with 8 years of IceCube data. **Eur. Phys. J. C**, v. 79, n. 3, p. 234, 2019.

195 AARTSEN, M. G. et al. Search for Sources of Astrophysical Neutrinos Using Seven Years of IceCube Cascade Events. **Astrophys. J.**, v. 886, p. 12, 2019.

196 GIUNTI, C.; KIM, C. W.; LEE, U. W. When do neutrinos really oscillate? quantum mechanics of neutrino oscillations. **Phys. Rev. D**, American Physical Society, v. 44, p. 3635–3640, Dec 1991. Disponível em: <https://link.aps.org/doi/10.1103/PhysRevD.44.3635>.

197 ELIEZER, S.; SWIFT, A. R. Experimental Consequences of electron Neutrino-Muon-neutrino Mixing in Neutrino Beams. **Nucl. Phys. B**, v. 105, p. 45–51, 1976.

198 FRITZSCH, H.; MINKOWSKI, P. Vector-Like Weak Currents, Massive Neutrinos, and Neutrino Beam Oscillations. **Phys. Lett. B**, v. 62, p. 72–76, 1976.

199 BILENKY, S. M.; PONTECORVO, B. Lepton Mixing and Neutrino Oscillations. **Phys. Rept.**, v. 41, p. 225–261, 1978.

200 Penzias, A. A.; Wilson, R. W. A Measurement of Excess Antenna Temperature at 4080 Mc/s. , v. 142, p. 419–421, jul. 1965.

201 BEREZINSKY, V.; KALASHEV, O. High-energy electromagnetic cascades in extragalactic space: Physics and features. **Phys. Rev. D**, American Physical Society, v. 94, p. 023007, Jul 2016. Disponível em: <https://link.aps.org/doi/10.1103/PhysRevD.94.023007>.

202 BEREZINSKY, V. S.; SMIRNOV, A. Y. Cosmic neutrinos of ultra-high energies and detection possibility. **Astrophys. Space Sci.**, v. 32, p. 461–482, 1975.

203 BERESINSKY, V.; ZATSEPIN, G. Cosmic rays at ultra high energies (neutrino?). **Physics Letters B**, v. 28, n. 6, p. 423–424, 1969. ISSN 0370-2693. Disponível em: <https://www.sciencedirect.com/science/article/pii/0370269369903414>.

204 BREIT, G.; WHEELER, J. A. Collision of two light quanta. **Phys. Rev.**, v. 46, n. 12, p. 1087–1091, 1934.

205 AKHIEZER, A. I.; BERESTETSKII, V. B. Quantum Electrodynamics. In: **Quantum Electrodynamics**. [S.l.: s.n.], 1965.

206 ZDZIARSKI, A. A. Saturated pair-photon cascades on isotropic background photons. **Astrophys. J.; (United States)**, v. 335, 12 1988. Disponível em: <https://www.osti.gov/biblio/6401594>.

207 COPPI, P. S.; BLANDFORD, R. D. Reaction rates and energy distributions for elementary processes in relativistic pair plasmas. **Monthly notices of the Royal Astronomical Society**, Blackwell Science, Oxford, v. 245, n. 3, p. 453–469, 1990. ISSN 0035-8711.

208 CAIRNS, J. A. Developing the Theory of Flux Limits from γ-Ray Cascades. 5 2007.

209 Berezinskii, V. S. et al. **Astrophysics of cosmic rays**. [S.l.: s.n.], 1990.

210 BLANCO, C. γ-cascade: a simple program to compute cosmological gamma-ray propagation. **JCAP**, v. 01, p. 013, 2019.

211 SETTIMO, M.; DOMENICO, M. D. Propagation of extragalactic photons at ultra-high energy with the $EleCa$ code. **Astropart. Phys.**, v. 62, p. 92–99, 2015.

212 CAPANEMA, A.; BLANCO, C. γ-Cascade V4: A semi-analytical code for modeling cosmological gamma-ray propagation. **Comput. Phys. Commun.**, v. 307, p. 109408, 2025.

213 BATISTA, R. A. et al. CRPropa 3.2 — an advanced framework for high-energy particle propagation in extragalactic and galactic spaces. **JCAP**, v. 09, p. 035, 2022.

214 GOULD, R. J.; SCHREDER, G. P. Pair Production in Photon-Photon Collisions. **Phys. Rev.**, v. 155, p. 1404–1407, 1967.

215 Aharonian, F. A.; Coppi, P. S.; Voelk, H. J. Very High Energy Gamma Rays from Active Galactic Nuclei: Cascading on the Cosmic Background Radiation Fields and the Formation of Pair Halos. , v. 423, p. L5, mar. 1994.

216 NERONOV, A.; SEMIKOZ, D. V. A method of measurement of extragalactic magnetic fields by TeV gamma ray telescopes. **JETP Lett.**, v. 85, p. 473–477, 2007.

217 Elyiv, A.; Neronov, A.; Semikoz, D. V. Gamma-ray induced cascades and magnetic fields in the intergalactic medium. , v. 80, n. 2, p. 023010, jul. 2009.

218 ELYIV, A.; NERONOV, A.; SEMIKOZ, D. V. Gamma-ray induced cascades and magnetic fields in intergalactic medium. **Phys. Rev. D**, v. 80, p. 023010, 2009.

219 DAI, Z. G. et al. GeV emission from TeV blazars and intergalactic magnetic fields. **Astrophys. J. Lett.**, v. 580, p. L7–L10, 2002.

220 Plaga, R. Detecting intergalactic magnetic fields using time delays in pulses of γ-rays. , v. 374, n. 6521, p. 430–432, mar. 1995.

221 ICHIKI, K.; INOUE, S.; TAKAHASHI, K. Probing the Nature of the Weakest Intergalactic Magnetic Fields with the High Energy Emission of Gamma-Ray Bursts. **Astrophys. J.**, v. 682, p. 127, 2008.

222 TAKAHASHI, K. et al. Detectability of Pair Echos from Gamma-Ray Bursts and Intergalactic Magnetic Fields. **Astrophys. J. Lett.**, v. 687, p. L5–L8, 2008.

223 NERONOV, A.; SEMIKOZ, D. V. Sensitivity of gamma-ray telescopes for detection of magnetic fields in intergalactic medium. **Phys. Rev. D**, v. 80, p. 123012, 2009.

224 ZATHUL, A. K. et al. An NGC 1068-Informed Understanding of Neutrino Emission of the Active Galactic Nucleus TXS 0506+056. 11 2024.

225 Icecube Collaboration. An absence of neutrinos associated with cosmic-ray acceleration in γ-ray bursts. , v. 484, n. 7394, p. 351–354, abr. 2012.

226 STEIN, R. et al. A tidal disruption event coincident with a high-energy neutrino. **Nature Astron.**, v. 5, n. 5, p. 510–518, 2021.

227 REUSCH, S. et al. Candidate Tidal Disruption Event AT2019fdr Coincident with a High-Energy Neutrino. **Phys. Rev. Lett.**, v. 128, n. 22, p. 221101, 2022.

228 VELZEN, S. van et al. Establishing accretion flares from supermassive black holes as a source of high-energy neutrinos. **Mon. Not. Roy. Astron. Soc.**, v. 529, n. 3, p. 2559–2576, 2024.

229 YUAN, C.; WINTER, W.; LUNARDINI, C. AT2021lwx: Another Neutrino-coincident Tidal Disruption Event with a Strong Dust Echo? **Astrophys. J.**, v. 969, n. 2, p. 136, 2024.

230 FANG, K.; GALLAGHER, J. S.; HALZEN, F. The Milky Way revealed to be a neutrino desert by the IceCube Galactic plane observation. **Nature Astron.**, v. 8, n. 2, p. 241–246, 2024.

231 CAPANEMA, A.; ESMAILI, A.; SERPICO, P. D. Where do IceCube neutrinos come from? Hints from the diffuse gamma-ray flux. **JCAP**, v. 02, p. 037, 2021.

232 CAPANEMA, A.; ESMAILI, A.; MURASE, K. New constraints on the origin of medium-energy neutrinos observed by IceCube. **Phys. Rev. D**, v. 101, n. 10, p. 103012, 2020.

233 ABBASI, R. et al. Updated directions of IceCube HESE events with the latest ice model using DirectFit. **PoS**, ICRC2023, p. 1030, 2023.

234 MURASE, K.; AHLERS, M.; LACKI, B. C. Testing the Hadronuclear Origin of PeV Neutrinos Observed with IceCube. **Phys. Rev. D**, v. 88, n. 12, p. 121301, 2013.

235 FANG, K.; GALLAGHER, J. S.; HALZEN, F. The TeV Diffuse Cosmic Neutrino Spectrum and the Nature of Astrophysical Neutrino Sources. **Astrophys. J.**, v. 933, n. 2, p. 190, 2022.

236 TINYAKOV, P. G.; TKACHEV, I. I. Is astronomy possible with neutral ultrahigh energy cosmic ray particles existing in the Standard Model? **J. Exp. Theor. Phys.**, v. 106, p. 481–487, 2008.

237 JOHNSON, W. R.; BUSS, D. J.; CARROLL, C. O. Single-quantum annihilation of positrons. **Phys. Rev.**, American Physical Society, v. 135, p. A1232–A1235, Aug 1964. Disponível em: <https://link.aps.org/doi/10.1103/PhysRev.135.A1232>.

238 AKHIEZER, A. I.; BERESTETSKII, V. B. **Quantum electrodynamics**. [S.l.: s.n.], 1986.

239 ANCHORDOQUI, L. A. et al. TeV γ^- rays and neutrinos from photodisintegration of nuclei in Cygnus OB2. **Phys. Rev. D**, v. 75, p. 063001, 2007.

240 M.V. Kossov. Approximation of photonuclear interaction cross-sections. **Eur. Phys. J. A**, v. 14, n. 3, p. 377–392, 2002. Disponível em: <https://doi.org/10.1140/epja/i2002-10008-x>.

241 ZHANG, B. T. et al. Ultraheavy Ultrahigh-Energy Cosmic Rays. 5 2024.

242 FARRAR, G. R. Binary neutron star mergers as the source of the highest energy cosmic rays. 5 2024.

243 MURASE, K.; BEACOM, J. F. Very-High-Energy Gamma-Ray Signal from Nuclear Photodisintegration as a Probe of Extragalactic Sources of Ultrahigh-Energy Nuclei. **Phys. Rev. D**, v. 82, p. 043008, 2010.

244 KUSENKO, A.; VOLOSHIN, M. B. A gamma-ray signature of energetic sources of cosmic-ray nuclei. **Phys. Lett. B**, v. 707, p. 255–258, 2012.

245 KALOGERA, V. et al. Deeper, Wider, Sharper: Next-Generation Ground-Based Gravitational-Wave Observations of Binary Black Holes. 3 2019.

246 AARTSEN, M. et al. First observation of PeV-energy neutrinos with IceCube. **Phys.Rev.Lett.**, v. 111, p. 021103, 2013.

247 SCHNEIDER, A. Characterization of the Astrophysical Diffuse Neutrino Flux with IceCube High-Energy Starting Events. In: **36th International Cosmic Ray Conference (ICRC 2019) Madison, Wisconsin, USA, July 24-August 1, 2019**. [S.l.: s.n.], 2019.

248 STETTNER, J. Measurement of the Diffuse Astrophysical Muon-Neutrino Spectrum with Ten Years of IceCube Data. In: **HAWC Contributions to the 36th International Cosmic Ray Conference (ICRC2019)**. [S.l.: s.n.], 2019.

249 AARTSEN, M. G. et al. Characteristics of the diffuse astrophysical electron and tau neutrino flux with six years of IceCube high energy cascade data. 2020.

250 AARTSEN, M. G. et al. Detection of a particle shower at the glashow resonance with icecube. **Nature**, v. 591, p. 220–224, 2021.

251 ABBASI, R. et al. Sensitivity studies for the IceCube-Gen2 radio array. In: **37th International Cosmic Ray Conference (ICRC 2021), Online – Berlin, Germany, July 12-23, 2021**. [S.l.: s.n.], 2021.

252 FANG, K. et al. The Giant Radio Array for Neutrino Detection (GRAND): Present and Perspectives. In: **35th International Cosmic Ray Conference (ICRC 2017), Bexco, Busan, Korea**. [S.l.: s.n.], 2017.

253 BATISTA, R. A. et al. Cosmogenic photon and neutrino fluxes in the auger era. **JCAP**, v. 01, p. 002, 2019.

254 WAXMAN, E.; BAHCALL, J. N. High-energy neutrinos from astrophysical sources: An Upper bound. **Phys. Rev. D**, v. 59, p. 023002, 1998.

255 MANNHEIM, K.; PROTHEROE, R. J.; RACHEN, J. P. On the cosmic ray bound for models of extragalactic neutrino production. **Phys. Rev. D**, v. 63, p. 023003, 2000.

256 KALASHEV, O. E. et al. Ultrahigh-energy neutrino fluxes and their constraints. **Phys. Rev. D**, v. 66, p. 063004, 2002.

257 KUSENKO, A.; POSTMA, M. Neutrinos produced by ultrahigh-energy photons at high red shift. **Phys. Rev. Lett.**, v. 86, p. 1430–1433, 2001.

258 POSTMA, M. Neutrinos as a signature of ultrahigh-energy photons at high red shift. **Phys. Rev. D**, v. 64, p. 023001, 2001.

259 BEREZINSKY, V. Inverse Compton effect, pair production and penetration of high energy electrons and photons through the metagalactics. **Yad. Fiz.**, v. 11, p. 399–410, 1970.

260 WANG, K. et al. Neutrino Production in Electromagnetic Cascades: An extra component of cosmogenic neutrino at ultrahigh energies. **Phys. Rev. D**, v. 95, n. 6, p. 063010, 2017.

261 LI, Z.; WAXMAN, E. EeV neutrinos associated with UHECR sources. In: **32nd International Cosmic Ray Conference**. [S.l.: s.n.], 2007. v. 8, p. 262.

262 DEMIDOV, S. V.; KALASHEV, O. E. Double Pair Production by Ultra High Energy Cosmic Ray Photons. **J. Exp. Theor. Phys.**, v. 108, p. 764–769, 2009.

263 CHENG, H.; WU, T. T. Cross sections for two-pair production at infinite energy. **Phys. Rev. D**, v. 2, p. 2103–2105, 1970.

264 BROWN, R. W. et al. Role of $\gamma+\gamma\rightarrow$e++e−+e++e− in Photoproduction, Colliding Beams, and Cosmic Photon Absorption. **Phys. Rev. D**, v. 8, n. 9, p. 3083, 1973.

265 LEE, S. On the propagation of extragalactic high-energy cosmic and gamma-rays. **Phys. Rev. D**, v. 58, p. 043004, 1998.

266 BELYAEV, A.; CHRISTENSEN, N. D.; PUKHOV, A. CalcHEP 3.4 for collider physics within and beyond the Standard Model. **Comput. Phys. Commun.**, v. 184, p. 1729–1769, 2013.

267 LEPAGE, G. P. A New Algorithm for Adaptive Multidimensional Integration. **J. Comput. Phys.**, v. 27, p. 192, 1978.

268 LEPAGE, G. P. Adaptive multidimensional integration: VEGAS enhanced. **J. Comput. Phys.**, v. 439, p. 110386, 2021.

269 CHENG, H.; WU, T. T. Photon-Photon Scattering close to the Forward Direction. **Phys. Rev. D**, v. 1, p. 3414, 1970.

270 GALANTI, G. et al. Estimating $\gamma\gamma$ absorption for UHE photons with lepton and hadron production. **Phys. Rev. D**, v. 102, p. 123004, 2020.

271 Haug, E. Bremsstrahlung and pair production in the field of free electrons. **Zeitschrift Naturforschung Teil A**, v. 30, p. 1099–1113, set. 1975.

272 Mastichiadis, A.; Marscher, A. P.; Brecher, K. Electron-Positron Pair Production by Ultrarelativistic Electrons in a Soft Photon Field. , v. 300, p. 178, jan. 1986.

273 Mastichiadis, A. Relativistic electrons in photon fields - Effects of triplet pair production on inverse Compton gamma-ray spectra. , v. 253, p. 235–244, nov. 1991.

274 BRODSKY, S. J.; KINOSHITA, T.; TERAZAWA, H. Two Photon Mechanism of Particle Production by High-Energy Colliding Beams. **Phys. Rev. D**, v. 4, p. 1532–1557, 1971.

275 PLANCK-COLLABORATION. Planck 2018 results. I. Overview and the cosmological legacy of Planck. **A&A**, 2018.

276 RAM, M.; WANG, P. Y. Calculation of the total cross-section for double Compton scattering. **Phys. Rev. Lett.**, v. 26, p. 476–479, 1971.

277 GOULD, R. J. SOFT PHOTON EMISSION EFFECTS AND RADIATIVE CORRECTIONS FOR ELECTROMAGNETIC PROCESSES AT VERY HIGH-ENERGIES. **Astrophys. J.**, v. 230, p. 967–973, 1979.

278 LIPARI, P. Lepton spectra in the earth's atmosphere. **Astropart. Phys.**, v. 195, p. 227, 1993.

279 ESTEBAN, I. et al. **NuFIT5.2 (2022)**. Disponível em: <http://www.nu-fit.org>.

280 ESTEBAN, I. et al. The fate of hints: updated global analysis of three-flavor neutrino oscillations. **JHEP**, 2020.

281 ABBASI, R. et al. Sensitivity studies for the IceCube-Gen2 radio array. **PoS**, ICRC2021, p. 1183, 2021.

282 NIZ, J. A.-M. et al. The Giant Radio Array for Neutrino Detection (GRAND): Science and Design. **Sci. China Phys. Mech. Astron.**, v. 63, n. 1, p. 219501, 2020.

283 INAYOSHI, K.; VISBAL, E.; HAIMAN, Z. The Assembly of the First Massive Black Holes. **Ann. Rev. Astron. Astrophys.**, v. 58, p. 27–97, 2020.

284 WOODS, T. E. et al. Titans of the Early Universe: The Prato Statement on the Origin of the First Supermassive Black Holes. **Publ. Astron. Soc. Austral.**, v. 36, p. e027, 2019.

285 HOMOLA, P. et al. Simulation of ultra-high energy photon propagation with PRESHOWER 2.0. **Comput. Phys. Commun.**, v. 184, p. 1468–1475, 2013.

286 SERPICO, P. D. Possible physics scenarios behind cosmic-ray "anomalies". **PoS**, ICRC2015, p. 009, 2016.

287 SERPICO, P. D. Entering the cosmic ray precision era. **J. Astrophys. Astron.**, v. 39, p. 41, 2018.

288 BOEZIO, M.; MUNINI, R.; PICOZZA, P. Cosmic ray detection in space. **Prog. Part. Nucl. Phys.**, v. 112, p. 103765, 2020.

289 MOSKALENKO, I. V. Direct measurements of cosmic rays and their possible interpretations. **PoS**, ICRC2023, p. 020, 2023.

290 WINKLER, M. W. Cosmic Ray Antiprotons at High Energies. **JCAP**, v. 02, p. 048, 2017.

291 BOUDAUD, M. et al. AMS-02 antiprotons' consistency with a secondary astrophysical origin. **Phys. Rev. Res.**, v. 2, n. 2, p. 023022, 2020.

292 CUOCO, A. et al. Scrutinizing the evidence for dark matter in cosmic-ray antiprotons. **Phys. Rev. D**, v. 99, n. 10, p. 103014, 2019.

293 HEISIG, J.; KORSMEIER, M.; WINKLER, M. W. Dark matter or correlated errors: Systematics of the AMS-02 antiproton excess. **Phys. Rev. Res.**, v. 2, n. 4, p. 043017, 2020.

294 MAURO, M. D.; WINKLER, M. W. Multimessenger constraints on the dark matter interpretation of the Fermi-LAT Galactic center excess. **Phys. Rev. D**, v. 103, n. 12, p. 123005, 2021.

295 CALORE, F. et al. AMS-02 antiprotons and dark matter: Trimmed hints and robust bounds. **SciPost Phys.**, v. 12, n. 5, p. 163, 2022.

296 LV, X.-J. et al. Reanalysis of the systematic uncertainties in the cosmic-ray antiproton flux. **Phys. Rev. D**, v. 109, n. 4, p. 043006, 2024.

297 LUQUE, P. De la T.; WINKLER, M. W.; LINDEN, T. Antiproton Bounds on Dark Matter Annihilation from a Combined Analysis Using the DRAGON2 Code. 1 2024.

298 AGUILAR, M. et al. Precision Measurement of the Proton Flux in Primary Cosmic Rays from Rigidity 1 GV to 1.8 TV with the Alpha Magnetic Spectrometer on the International Space Station. **Phys. Rev. Lett.**, v. 114, p. 171103, 2015.

299 Stone, E. C. et al. Voyager 1 Observes Low-Energy Galactic Cosmic Rays in a Region Depleted of Heliospheric Ions. **Science**, v. 341, n. 6142, p. 150–153, jul. 2013.

300 SERPICO, P. D. Cosmic ray interactions with matter and radiation. In: . [S.l.: s.n.], 2023.

301 MOSKALENKO, I. V.; STRONG, A. W.; MASHNIK, S. G. Propagation of cosmic rays: Nuclear physics in cosmic-ray studies. **AIP Conf. Proc.**, v. 769, n. 1, p. 1612–1617, 2005.

302 GENOLINI, Y. et al. Current status and desired precision of the isotopic production cross sections relevant to astrophysics of cosmic rays: Li, Be, B, C, and N. **Phys. Rev. C**, v. 98, n. 3, p. 034611, 2018.

303 GÉNOLINI, Y. et al. Current status and desired accuracy of the isotopic production cross-sections relevant to astrophysics of cosmic rays II. Fluorine to Silicon (and updated LiBeB). 7 2023.

304 ORUSA, L. et al. New determination of the production cross section for γ rays in the Galaxy. **Phys. Rev. D**, v. 107, n. 8, p. 083031, 2023.

305 MAURO, M. D. et al. Novel prediction for secondary positrons and electrons in the Galaxy. **Phys. Rev. D**, v. 108, n. 6, p. 063024, 2023.

306 BERGSTROM, L.; EDSJO, J.; ULLIO, P. Cosmic anti-protons as a probe for supersymmetric dark matter? **Astrophys. J.**, v. 526, p. 215–235, 1999.

307 Moskalenko, I. V.; Strong, A. W. Production and Propagation of Cosmic-Ray Positrons and Electrons. , v. 493, n. 2, p. 694–707, jan. 1998.

308 MAURIN, D. USINE: semi-analytical models for Galactic cosmic-ray propagation. **Comput. Phys. Commun.**, v. 247, p. 106942, 2020.

309 KISSMANN, R. PICARD: A novel code for the Galactic Cosmic Ray propagation problem. **Astropart. Phys.**, v. 55, p. 37–50, 2014.

310 Krakau, S.; Schlickeiser, R. Pion Production Momentum Loss of Cosmic Ray Hadrons. , v. 802, n. 2, p. 114, abr. 2015.

311 MANNHEIM, K.; SCHLICKEISER, R. Interactions of Cosmic Ray Nuclei. **Astron. Astrophys.**, v. 286, p. 983–996, 1994.

312 WEAVER, B. A.; WESTPHAL, A. J. Energy loss of relativistic heavy ions in matter. **Nucl. Instrum. Meth. B**, v. 187, p. 285–301, 2002.

313 Aharonian, F. A.; Atoyan, A. M. Broad-band diffuse gamma ray emission of the galactic disk. **Astronomy and Astrophysics**, v. 362, p. 937–952, out. 2000.

314 KELNER, S. R.; AHARONIAN, F. A.; BUGAYOV, V. V. Energy spectra of gamma-rays, electrons and neutrinos produced at proton-proton interactions in the very high energy regime. **Phys. Rev. D**, v. 74, p. 034018, 2006. [Erratum: Phys.Rev.D 79, 039901 (2009)].

315 GINZBURG, V. L.; PTUSKIN, V. S. On the Origin of Cosmic Rays: Some Problems in High-Energy Astrophysics. **Rev. Mod. Phys.**, v. 48, p. 161–189, 1976. [Erratum: Rev.Mod.Phys. 48, 675–676 (1976)].

316 JONES, F. C. et al. The modified weighted slab technique: models and results. **Astrophys. J.**, v. 547, p. 264, 2001.

317 Ptuskin, V. S.; Jones, F. C.; Ormes, J. F. On Using the Weighted Slab Approximation in Studying the Problem of Cosmic-Ray Transport. , v. 465, p. 972, jul. 1996.

318 Lezniak, J. A. The Extension of the Concept of the Cosmic-ray Path-length Distribution to Nonrelativistic Energies. , v. 63, n. 2, p. 279–293, jul. 1979.

319 ALOISIO, R.; BLASI, P. Propagation of galactic cosmic rays in the presence of self-generated turbulence. **JCAP**, v. 07, p. 001, 2013.

320 GÉNOLINI, Y. et al. Cosmic-ray transport from AMS-02 boron to carbon ratio data: Benchmark models and interpretation. **Phys. Rev. D**, v. 99, n. 12, p. 123028, 2019.

321 WEINRICH, N. et al. Galactic halo size in the light of recent AMS-02 data. **Astron. Astrophys.**, v. 639, p. A74, 2020.

322 EVOLI, C. et al. Cosmic-ray propagation with $DRAGON2$: I. numerical solver and astrophysical ingredients. **JCAP**, v. 02, p. 015, 2017.

323 Salvat, F. Bethe stopping-power formula and its corrections. , v. 106, n. 3, p. 032809, set. 2022.

324 JACKSON, J. D. **Classical Electrodynamics**. [S.l.]: Wiley, 1998. ISBN 978-0-471-30932-1.

325 LINDHARD, J.; SORENSEN, A. H. Relativistic theory of stopping for heavy ions. **Phys. Rev. A**, v. 53, p. 2443–2456, 1996.

326 WEBBER, W. R.; KISH, J. C.; SCHRIER, D. A. Total charge and mass changing cross-sections of relativistic nuclei in hydrogen, helium, and carbon targets. **Phys. Rev. C**, v. 41, p. 520–532, 1990.

327 AGUILAR, M. et al. Properties of Iron Primary Cosmic Rays: Results from the Alpha Magnetic Spectrometer. **Phys. Rev. Lett.**, v. 126, n. 4, p. 041104, 2021.

328 BATTISTONI, G. et al. Overview of the FLUKA code. **Annals Nucl. Energy**, v. 82, p. 10–18, 2015.

329 KALOGERA, V.; BAYM, G. The Maximum Mass of a Neutron Star. **Astrophys. J.**, v. 470, p. L61–L64, 1996.

330 LEUNG, S.-C.; NOMOTO, K.; BLINNIKOV, S. Pulsational Pair-instability Supernovae. I. Pre-collapse Evolution and Pulsational Mass Ejection. **Astrophys. J.**, v. 887:72, p. 27, 2019.

331 CASARES, J.; JONKER, P. G. Mass Measurements of Stellar and Intermediate Mass Black-Holes. **Space Sci. Rev.**, v. 183, n. 1-4, p. 223–252, 2014.

332 SHAHBAZ, T. et al. The mass of the black hole in V404 Cygni. **Monthly Notices of the Royal Astronomical Society**, v. 271, n. 1, p. L10–L14, 11 1994. ISSN 0035-8711. Disponível em: <https://doi.org/10.1093/mnras/271.1.L10>.

333 ABBOTT, B. P. et al. Observation of Gravitational Waves from a Binary Black Hole Merger. **Phys. Rev. Lett.**, v. 116, n. 6, p. 061102, 2016.

334 ZEL'DOVICH, Y. B.; NOVIKOV, I. D. The Hypothesis of Cores Retarded during Expansion and the Hot Cosmological Model. **Soviet Astron.**, v. 10, p. 602, 1967.

335 VILLANUEVA-DOMINGO, P.; MENA, O.; PALOMAREZ-RUIZ, S. A Brief Review on Primordial Black Holes as Dark Matter. **Front. Astron. Space Sci.**, 2021.

336 CARR, B. J. The Primordial black hole mass spectrum. **Astrophys. J.**, v. 201, p. 1–19, 1975.

337 HAWKING, S. W. Black hole explosions? **Nature**, v. 248, p. 30–31, 1974.

338 HAWKING, S. W. Particle Creation by Black Holes. **Commun. Math. Phys.**, v. 43, p. 199–220, 1975.

339 CARR, B. J. et al. New cosmological constraints on primordial black holes. **Phys. Rev. D**, v. 81, p. 104019, 2010.

340 BUGAEV, E. V.; KONISHCHEV, K. V. Cosmological constraints from evaporation of primordial black holes. **Phys. Rev. D**, v. 66, p. 084004, 2002.

341 BUGAEV, E.; KLIMAI, P. Constraints on amplitudes of curvature perturbations from primordial black holes. **Phys. Rev. D**, v. 79, p. 103511, 2009.

342 HE, P.; FANG, L.-Z. Constraints on Primordial Black Holes and Primordial Density Perturbations from the Epoch of Reionization. **Astrophys. J.**, v. 568, p. L1–L4, 2002.

343 MACK, K. J.; WEASLEY, D. H. Primordial black holes in the Dark Ages: Observational prospects for future 21cm surveys. 2008.

344 MACGIBBON, J. H. Can Planck-mass relics of evaporating black holes close the Universe? **Nature**, v. 329, p. 308–309, 1987.

345 BARROW, J. D.; COPELAND, E. J.; LIDDLE, A. R. The cosmology of black hole relics. **Phys. Rev. D**, v. 46, p. 645, 1992.

346 CHEN, P.; ADLER, R. J. Black hole remnants and dark matter. **Nucl. Phys. B, Proc. Suppl.**, v. 124, p. 103–106, 2003.

347 CHAPLINE, G. F. Cosmological effects of primordial black holes. **Nature**, v. 253, p. 251–252, 1975.

348 GREEN, A. M.; KAVANAGH, B. J. Primordial black holes as a dark matter candidate. **J. Phys. G: Nucl. Part. Phys.**, v. 48, p. 043001, 2020.

349 CARR, B.; KüHNEL, F. Primordial Black Holes as Dark Matter: Recent Developments. **Annu. Rev. Nucl. Part. Sci.**, v. 70, p. 355–394, 2020.

350 PAGE, D. N. Particle emission rates from a black hole: Massless particles from an uncharged, nonrotating hole. **Phys. Rev. D**, v. 13, n. 2, p. 198–206, 1976.

351 TAVERNIER, T.; GLICENSTEIN, J.-F.; BRUN, F. Search for Primordial Black Hole evaporations with H.E.S.S. In: **Contributions to the 36th International Cosmic Ray Conference (ICRC2019)**. [S.l.: s.n.], 2019.

352 GLICENSTEIN, J.-F. et al. Limits on Primordial Black Hole evaporation with the H.E.S.S. array of Cherenkov telescopes. In: **33rd International Cosmic Ray Conference (ICRC2013), Rio de Janeiro (Brazil)**. [S.l.: s.n.], 2013.

353 ABDO, A. A. et al. Milagro limits and HAWC sensitivity for the rate-density of evaporating Primordial Black Holes. **Astropart. Phys.**, v. 64, p. 4–12, 2015.

354 ARCHAMBAULT, S. Search for Primordial Black Hole Evaporation with VERITAS. In: **35th International Cosmic Ray Conference - ICRC2017**. [S.l.: s.n.], 2017.

355 ACKERMANN, M. et al. Search for Gamma-Ray Emission from Local Primordial Black Holes with the Fermi Large Area Telescope. **Astrophys. J.**, v. 857, n. 49, p. 11, 2018.

356 WRIGHT, E. L. On the Density of Primordial Black Holes in the Galactic Halo. **Astrophys. J.**, v. 459, p. 487, 1996.

357 LEHUOCQ, R. et al. New constraints on the primordial black hole number density from Galactic gamma-ray astronomy. **Astron. Astrophys.**, v. 502, p. 37, 2009.

358 CARR, B. J. et al. Constraints on primordial black holes from the Galactic gamma-ray background. **Phys. Rev. D**, v. 94, p. 044029, 2016.

359 PAGE, D. N.; HAWKING, S. W. Gamma rays from primordial black holes. **Astrophys. J.**, v. 206, p. 1–7, 1976.

360 ABE, K. et al. Measurement of the Cosmic-Ray Antiproton Spectrum at Solar Minimum with a Long-Duration Balloon Flight over Antarctica. **Phys. Rev. Lett.**, v. 108, p. 051102, 2012.

361 LAHA, R. Primordial Black Holes as a Dark Matter Candidate Are Severely Constrained by the Galactic Center 511 keV γ-Ray Line. **Phys. Rev. Lett.**, v. 123, p. 251101, 2019.

362 BOUDAUD, M.; CIRELLI, M. Voyager 1 $e^{\pm}$ Further Constrain Primordial Black Holes as Dark Matter. **Phys. Rev. Lett.**, v. 122, p. 041104, 2019.

363 DASGUPTA, B.; LAHA, R.; RAY, A. Neutrino and Positron Constraints on Spinning Primordial Black Hole Dark Matter. **Phys. Rev. Lett.**, v. 125, p. 101101, 2020.

364 ARBEY, A.; AUFFINGER, J.; SILK, J. Constraining primordial black hole masses with the isotropic gamma ray background. **Phys. Rev. D**, v. 101, p. 023010, 2020.

365 CLARK, S. J. et al. Planck constraint on relic primordial black holes. **Phys. Rev. D**, v. 95, p. 083006, 2017.

366 COOGAN, A.; MORRISON, L.; PROFUMO, S. Direct Detection of Hawking Radiation from Asteroid-Mass Primordial Black Holes. **Phys. Rev. Lett.**, v. 126, p. 171101, 2021.

367 LAHA, R.; MUñOZ, J. B.; SLATYER, T. R. INTEGRAL constraints on primordial black holes and particle dark matter. **Phys. Rev. D.**, v. 101, p. 123514, 2020.

368 MITTAL, S. et al. Constraining primordial black holes as dark matter using the global 21-cm signal with X-ray heating and excess radio background. 2021.

369 GHOSH, D.; SACHDEVA, D.; SINGH, P. Future Constraints on Primordial Black Holes from XGIS-THESEUS. 2021.

370 RAY, A. et al. Near future MeV telescopes can discover asteroid-mass primordial black hole dark matter. **Phys. Rev. D**, v. 104, p. 023516, 2021.

371 GUO, R. et al. Measuring the local dark matter density with LAMOST DR5 and Gaia DR2. **Mon. Not. Roy. Astron. Soc.**, v. 495, p. 4828–4844, 2020.

372 CARR, B. J. Some cosmological consequences of primordial black-hole evaporations. **Astrophys. J.**, v. 206, p. 8–25, 1976.

373 ARBEY, A.; AUFFINGER, J. BlackHawk: a public code for calculating the Hawking evaporation spectra of any black hole distribution. **Eur. Phys. J. C**, v. 79, n. 8, p. 693, 2019.

374 BAUER, C. W.; RODD, N. L.; WEBBER, B. R. Dark matter spectra from the electroweak to the Planck scale. **JHEP**, v. 06, p. 121, 2021.

375 HECKLER, A. F. Formation of a Hawking-radiation photosphere around microscopic black holes. **Phys. Rev. D**, v. 55, p. 480–488, 1997.

376 HECKLER, A. F. Calculation of the Emergent Spectrum and Observation of Primordial Black Holes. **Phys. Rev. Lett.**, v. 78, p. 3430–3433, 1997.

377 MACGIBBON, J. H.; CARR, B. J.; PAGE, D. N. Do evaporating black holes form photospheres? **Phys. Rev. D**, v. 78, p. 064043, 1997.

378 ABEYSEKARA, A. U. et al. On the sensitivity of the HAWC observatory to gamma-ray bursts. **Astropart. Phys.**, v. 35, n. 10, p. 641–650, 2012.

379 BAI, X. et al. The Large High Altitude Air Shower Observatory (LHAASO) Science White Paper. 5 2019.

380 CAPANEMA, A.; ESMAILI, A.; SERPICO, P. D. Where do IceCube neutrinos come from? Hints from the diffuse gamma-ray flux. **JCAP**, v. 02, p. 037, 2021.

381 ISRAEL, W. Event Horizons in Static Vacuum Space-Times. **Phys. Rev.**, v. 164, n. 5, p. 1776–1779, 1967.

382 ISRAEL, W. Event Horizons in Static Electrovac Space-Times. **Commun. Math. Phys.**, v. 8, p. 245–260, 1968.

383 CARTER, B. Axisymmetric Black Hole Has Only Two Degrees of Freedom. **Phys. Rev. Lett.**, v. 26, n. 6, p. 331–333, 1971.

384 HAWKING, S. W. Black Holes in General Relativity. **Commun. Math. Phys.**, v. 25, p. 152–166, 1972.

385 ROBINSON, D. C. Uniqueness of the Kerr Black Hole. **Phys. Rev. Lett.**, v. 34, n. 14, p. 905–906, 1975.

386 MAZUR, P. O. Proof of uniqueness of the Kerr-Newman black hole solution. **J. Phys. A: Math. Gen.**, v. 15, p. 3173–3180, 1982.

387 ZAUMEN, W. T. Upper bound on the electric charge of a black hole. **Nature**, v. 247, p. 530–531, 1974.

388 CARTER, B. Charge and Particle Conservation in Black-Hole Decay. **Phys. Rev. Lett.**, v. 33, n. 9, p. 558–561, 1974.

389 GIBBONS, G. W. Vacuum Polarization and the Spontaneous Loss of Charge by Black Holes. **Commun. Math. Phys.**, v. 44, p. 245–264, 1975.

390 PAGE, D. N. Particle emission rates from a black hole. II. Massless particles from a rotating hole. **Phys. Rev. D**, v. 14, n. 12, p. 3260–3273, 1976.

391 MACGIBBON, J. H.; WEBBER, B. R. Quark- and gluon-jet emission from primordial black holes: The instantaneous spectra. **Phys. Rev. D**, v. 41, n. 10, p. 3052–3079, 1990.

392 MACGIBBON, J. H. Quark and gluon jet emission from primordial black holes. 2. The Lifetime emission. **Phys. Rev. D**, v. 44, p. 376–392, 1991.

393 BUGAEV, E.; KLIMAI, P.; PETKOV, V. Photon spectra from final stages of a primordial black hole evaporation in different theoretical models. In: **30th International Cosmic Ray Conference**. [S.l.: s.n.], 2007. v. 3, p. 1123–1126.

394 UKWATTA, T. N. et al. Primordial Black Holes: Observational Characteristics of The Final Evaporation. **Astropart. Phys.**, v. 80, p. 90–114, 2016.

395 SJÖSTRAND, T. et al. An introduction to PYTHIA 8.2. **Comput. Phys. Commun.**, v. 191, p. 159–177, 2015.

396 LUNARDINI, C.; PEREZ-GONZALEZ, Y. F. Dirac and Majorana neutrino signatures of primordial black holes. **JCAP**, v. 08, p. 014, 2020.

397 ESTEBAN, I. et al. The fate of hints: updated global analysis of three-flavor neutrino oscillations. **JHEP**, v. 09, p. 178, 2020.

398 ARBEY, A.; AUFFINGER, J.; SILK, J. Evolution of primordial black hole spin due to Hawking radiation. **Mon. Not. Roy. Astron. Soc.**, v. 494, n. 1, p. 1257–1262, 2020.

399 AARTSEN, M. G. et al. Time-integrated Neutrino Source Searches with 10 years of IceCube Data. **Phys. Rev. Lett.**, v. 124, n. 5, p. 051103, 2020.

400 HONDA, M. et al. Atmospheric neutrino flux calculation using the NRLMSISE-00 atmospheric model. **Phys. Rev. D**, v. 92, p. 023004, 2015.

401 ESMAILI, A.; IBARRA, A.; PERES, O. L. Probing the stability of superheavy dark matter particles with high-energy neutrinos. **JCAP**, v. 1211, p. 034, 2012.

402 ABEYSEKARA, A. U. et al. The HAWC Gamma-Ray Observatory: Dark Matter, Cosmology, and Fundamental Physics. In: **33rd International Cosmic Ray Conference (ICRC2013), Rio de Janeiro (Brazil)**. [s.n.], 2013. v. 122, p. 041104. Disponível em: <https://escholarship.org/uc/item/24s550qz>.

403 ADRIAN-MARTINEZ, S. et al. Letter of intent for KM3NeT 2.0. **J. Phys.**, G43, n. 8, p. 084001, 2016.

404 AARTSEN, M. et al. IceCube-Gen2: A Vision for the Future of Neutrino Astronomy in Antarctica. 2014.

405 ISHIHARA, A. The IceCube Upgrade - Design and Science Goals. In: **Contributions to the 36th International Cosmic Ray Conference (ICRC2019)**. [S.l.: s.n.], 2019.